United States Nuclear Regulatory Commission

Protecting People and the Environment

RIL 2023-08

SEISMIC SOURCE CHARACTERIZATION IN CENTRAL AND EASTERN UNITED STATES

Date Published: October 2023

Prepared by:

R. Briggs
R. Gold
J. Thompson Jobe

U.S. Geological Survey
Geologic Hazards Science Center
1711 Illinois St.
Golden, CO 80401 [USA]

Rasool Anooshehpoor, NRC Program Manager

Research Information Letter
Office of Nuclear Regulatory Research

DISCLAIMER

Legally binding regulatory requirements are stated only in laws, NRC regulations, licenses, including technical specifications, or orders; not in Research Information Letters (RILs). A RIL is not regulatory guidance, although NRC's regulatory offices may consider the information in a RIL to determine whether any regulatory actions are warranted. This report was prepared as an account of work sponsored by an agency of the United States Government. Neither the United States Government nor any agency thereof, or any of their employees, makes any warranty, expressed or implied, or assumes any legal liability of responsibility for any third party's use, or the results of such use, or any information, apparatus, product or process disclosed in this report, or represents that its use by such third party would not infringe privately owned rights.

ACKNOWLEDGEMENTS

Many thanks to the individuals who granted access to their property for different aspects of these studies, including: Dustin Faulkner, Kelly McClintock, Paul Miller, Jill Morris, and Jeff Biggs.

This report was reviewed by Alex Hatem, Steve DeLong, and anonymous reviewers, which greatly improved the final report.

Other funding sources: This work was supported by the U.S. Geological Survey (USGS) Earthquake Hazards Program. The seismic reflection study in Chapter 1 was supported by funding from the USGS Earthquake Hazards Program, the National Science Foundation, and the Network for Earthquake Engineering Simulation (NEES) center at the University of Texas. Cooperation and assistance were gratefully received from the Arkansas State Highway Commission and the Arkansas Geological Commission. The USGS Mississippi Alluvial Plain Regional Water Availability project facilitated collection of the airborne electromagnetic data.

Data availability: The 10-m National Elevation Dataset (NED) digital elevation model (DEM) and lidar-derived DEMs or point clouds used in Chapter 1 and 3 are available at https://apps.nationalmap.gov/downloader/. The MATLAB toolbox TopoToolbox used for digital landscape analysis in Chapters 1 and 3 is available for download at https://topotoolbox.wordpress.com/download/. Lidar-derived DEMs and lidar point clouds for Chapter 2 are available at http://tngis.org/lidar and https://opentopography.org/, respectively. All other data are available at the sources cited in this report.

Assistance from Jeff Nekola and Jeff Pigati for identifying snails and Tina Dura for evaluating the presence/absence of diatoms for Chapter 2 was much appreciated. Lidar mapping and database compilation for Chapters 3 and 4 by Camille Collett was invaluable.

TABLE OF CONTENTS

LIST OF FIGURES

LIST OF TABLES

ABBREVIATIONS AND ACRONYMS

2D	two-dimensional
3D	three-dimensional
3DEP	3D Elevation Program
ACS	American Chemical Society
AEM	airborne electromagnetic
AF	Axial fault
AMS	accelerator mass spectrometry
BCEF	Big Creek-Ellendale fault
BF	Bootheel fault
BF	Biggs' Farm site
BMTZ	Bolivar-Mansfield tectonic zone
BP	before present
cal yr BP	calibrated years before present
CCFZ	Crittenden County fault zone
CEUS	central and eastern United States
CEUS-SSC	Central and Eastern United States Seismic Source Characterization model
CF	Cottonwood Grove fault
CGF	Commerce Geophysical Lineament
COCORP	Consortium for Continental Reflection Profiling
CU	Charleston Uplift
CV	Cherry Valley
DEM	digital elevation model
EMF	Eastern Margin fault
ETSZ	Eastern Tennessee seismic zone
GIS	geographic information system
GPR	ground penetrating radar
GPS	global positioning system
JRF	Joiner Ridge fault
HI	hypsometric integral
InSAR	interferometric synthetic aperature radar
ka	thousand years ago
km	kilometers
k.y.	thousand years
L	Levesque
LF	Lanesferry site
m	meters
M	magnitude
M_b	body-wave (p-wave only) magnitude

M_w	moment magnitude
MSF	Meeman-Shelby fault
NE	northeast
NED	National Elevation Dataset
NMNF	New Madrid North fault
NMSZ	New Madrid seismic zone
NMWF	New Madrid West fault
NRC	Nuclear Regulatory Commission
NSHM	National Seismic Hazard Model
NW	northwest
NYAL	New York-Alabama lineament
OSL	optically stimulated luminescence
Qa	Holocene floodplain
Qbr1	beach ridge 1
Qbr2	beach ridge 2
Qbr3	beach ridge 3
QL1	quality level 1 (lidar data)
QL3	quality level 3 (lidar data)
Qtda	Deweyville terrace complex a
Qtdb	Deweyville terrace complex b
Qtfi	Finley terrace
Qtha	Hatchie terrace
Qthe	Henderson terrace
Qthu	Humboldt terrace
REM	relative elevation model
RF	Ridgley fault
RMS	root mean square
SCRF	Southern Crowleys Ridge fault
SfM	structure-from-motion
SRTM	Shuttle Radar Topographic Mission
SW	southwest
USGS	U.S. Geological Survey
WCRF	Western Crowleys Ridge fault
WL	Wilson Loop site
WMF	Western Margin fault
WRFZ	White River fault zone

EXECUTIVE SUMMARY

This report documents earthquake geology studies conducted in the central and eastern United States (CEUS) between 2018 and 2023. The overarching goal of the earthquake geology studies was to identify and characterize fault sources in the New Madrid seismic zone, the eastern Tennessee seismic zone, and the Charleston seismic zone. These studies primarily relied on the interpretation of high-resolution topography, morphotectonic analysis of 10-meter (m) digital elevation models, field reconnaissance, and integration with new and existing subsurface datasets. Results from each study are placed into a seismic hazard framework.

The first two chapters focus on the New Madrid seismic zone, which is the most seismically active region in the CEUS, to better characterize the southern extent of the Reelfoot fault in the Obion River valley, and identify and characterize proposed faults along the margins of Crowleys Ridge in the center of the Mississippi River embayment. Crowleys Ridge is a ~320-kilometer (km) long landform that has been proposed to be formed by intermittent faulting or erosion from the Mississippi River. Legacy seismic reflection data documented Eocene, Mesozoic, and older strata offset by faults on the margins of the ridge (Van Arsdale et al., 1999). A morphotectonic analysis of the topography along Crowleys Ridge indicated southward increases in catchment hypsometric integral and slope. Neotectonic mapping on high-resolution lidar data revealed a series of subparallel linear fault and fold scarps along the margins of Crowleys Ridge. These scarps offset previously mapped fluvial and alluvial surfaces that were <56 thousand years ago (ka) (Rittenour et al., 2007). Integration of new seismic reflection and airborne electromagnetic data, legacy seismic data, with the landscape morphotectonic analysis and neotectonic mapping supports the interpretation that Crowleys Ridge is bound by faults that have been active in the late Quaternary but do not experience modern seismicity. By placing these newly characterized faults into the regional framework, the Crowleys Ridge faults can be interpreted as thrust faults associated with stepovers in the overall dextral fault system, similar to the Reelfoot fault. The results of these studies indicate that seismicity has migrated eastward during the late Quaternary, with the Reelfoot fault accommodating much of the modern-day strain.

The Reelfoot fault ruptured in the 1811-1812 New Madrid earthquake sequence (Fuller, 1912) and has a record of past large earthquakes (Tuttle et al., 2002; 2019). Whereas the northern extent of the fault intersects the Mississippi River and has well-expressed surface deformation, questions remained regarding the southern limit of seismicity, deformation, and overall fault length. Analysis of <25 ka river terraces along the Obion River valley in western Tennessee revealed subtle fold scarps, with increased magnitudes of deformation on progressively older terraces, indicative of a longer record of fault movement than has been documented by paleoseismic and paleoliquefaction studies alone (e.g., Kelson et al., 1996; Gold et al., 2019; Tuttle et al., 2019).

The third chapter integrates surface and subsurface data to assess the landscape record of surface deformation in the eastern Tennessee seismic zone (ETSZ), which is the second most seismically active region in the CEUS. Seismicity in the ETSZ is deep (5-26 km) and focused in the Proterozoic rock below the Paleozoic detachment. Although the region has experienced moderate (≤ M_w 4.8) seismicity in the instrumental record, the lack of a large historical earthquake and limited paleoseismic and paleoliquefaction evidence of prehistoric large ground shaking events have made seismic hazard characterization of the region challenging. Two models have emerged to predict the style and orientation of active surface deformation in the ETSZ. One suggests that surface rupturing earthquakes would exploit pre-existing faults along the regional structural grain (Cox et al., 2022). The second model advocates for primarily strike-

slip motion on east-west or north-south faults, following analyses of recent seismicity (Chapman et al., 1997; Dunn and Chapman, 2006; Daniels and Peng, 2022) and the modern stress field (Levandowski et al., 2018). In our analysis, neotectonic mapping of high-resolution lidar data reveals a concentration of lineaments with east-west orientations, with some corresponding to previously mapped east-west faults that crosscut the northeast-southwest regional structural grain from the Paleozoic orogeny. A morphotectonic analysis of catchments and river segments within the same lithology indicates subtle differences that may be indicative of a longer-term tectonic uplift signal. These changes in morphotectonic metrics spatially correspond to newly mapped lineaments and previously mapped east-west trending faults. Within a regional framework, we suggest that diffuse surface deformation associated with deep seismicity is accommodated on a network on east-west faults. However, further work is needed to better understand the potential late Pleistocene fault activity of these lineaments, and we propose that the ETSZ is still best characterized as an area source in seismic hazard models.

The final chapter presents preliminary work to create a geographic information system (GIS) database of recent studies analyzing surface and subsurface datasets and interpretations in the Charleston seismic zone, South Carolina. This GIS database will serve as a foundation for future work to analyze new quality level 1 (QL1; <0.5 m resolution) lidar data over the 1886 magnitude (M) 7 Charleston epicentral region to identify possible fault source sources responsible for the 1886 or other surface-rupturing events. This chapter briefly summarizes three new subsurface datasets, including seismic reflection (Pratt et al., 2022; Liberty, 2022) and seismicity data (Chapman et al., 2016), and one new surface dataset (Marple and Hurd, 2020), and their interpretations of potentially active lineaments and faults in the region.

1 EVIDENCE FOR LATE QUATERNARY DEFORMATION ALONG CROWLEYS RIDGE, NEW MADRID SEISMIC ZONE

This section of text is reproduced from Thompson Jobe et al. (2020a).

1.1 Abstract

The New Madrid seismic zone has been the source of multiple major (M ~7.0-7.5) earthquakes in the past 2 ka, yet the surface expression of recent deformation remains ambiguous. Crowleys Ridge, a linear ridge trending north-south for 300+ km through the Mississippi River embayment, has been interpreted as either a fault-bounded uplift or a non-tectonic erosional remnant. New and previously published seismic reflection and shallow resistivity data show discontinuities at the ridge margins in Pliocene-Pleistocene strata, yet the timing of most recent faulting and the lateral extent of these faults remains unknown. To assess Pleistocene-to-recent tectonic activity of Crowleys Ridge, we perform landscape-scale geomorphic analyses, such as relief, slope, hypsometry, and drainage basin shape, on a 10-m digital elevation model (DEM). North-to-south variations in geomorphic indices indicate Pleistocene-to-recent tectonic uplift of the southern ridge. Moreover, mapping on a <1-m lidar-derived DEM reveals scarps on late Pleistocene geomorphic surfaces. The scarps are primarily located along the southern ridge, trend parallel to the ridge margin discontinuously for 0.1-1 km, and vertically offset <56-ka surfaces by 0.4 m with up to 6 m of tilting. These landscape-scale patterns and scarps, integrated with discontinuities in the seismic reflection and resistivity data, provide evidence of low-rate (<0.2 mm/yr) late Quaternary tectonic activity along the southern segment of Crowleys Ridge. The interpretations agree with recent tectonic models indicating southern Crowleys Ridge is a compressional step-over in a right-lateral fault system within the Reelfoot rift.

1.2 Introduction

Slow-rate, distributed tectonic deformation in landscapes is often challenging to detect. Although geodesy and historical seismic records can provide information about the location of active faults over decadal timescales, these techniques do not capture the longer-term record of deformation, such as earthquake recurrence intervals or landscape response to active tectonics. Moreover, geodesy and the seismic record work well in high-strain regions, like plate-boundary settings, where deformation may be unambiguously expressed. But in low-strain, intraplate settings, long recurrence intervals on faults (Crone et al., 2003; Tuttle and Atkinson, 2010) and near-zero regional strain accumulation over shorter timescales (Galgana and Hamburger, 2010; Craig and Calais, 2014), in addition to the storage of long-term tectonic strain in intraplate settings (Craig et al., 2016), often mask the activity of potentially-active faults, and may result in underestimating the seismic hazard in the region (Stein et al., 2017).

Digital topographic analysis of the landscape has emerged as a tool to identify regions of uplift and locate individual faults, providing a better understanding of deformation in low rate, intraplate regions. The advent and increasing accessibility of high-resolution topographic datasets, through programs such as the U.S. Geological Survey (USGS) three-dimensional (3D) Elevation Program (3DEP) (Sugarbaker et al., 2017), has facilitated identification of active and potentially active faults that have shaped the landscape (Haugerud et al., 2003; Sherrod et al., 2004; Cunningham et al., 2006; Gold et al., 2013). Furthermore, digital topographic analysis of landscapes using geomorphic indices on lower-resolution digital elevation models (DEM), such as the 30-m Shuttle Radar Topographic Mission (SRTM) and 10-m National Elevation Dataset (NED) DEMs, has identified signatures of low-rate tectonic activity in areas typically thought to be tectonically quiescent or slowly deforming (Pedrera et al., 2009; Font et al., 2010; Giaconia et al., 2012; Ntokos et al., 2016; Marliyani et al., 2016).

We focus on the New Madrid seismic zone (NMSZ), which is one of the most seismically active areas east of the Rocky Mountains in North America (Figure 1-1; Johnston and Schweig, 1996; Petersen et al., 2014, 2018). In general, deformation rates in the region are slow (Craig and Calais, 2014), faults are blind, and surface deformation from recent earthquakes tends to be distributed (Van Arsdale, 2000). Moreover, on-going fluvial modification and anthropogenic activity can mask or remove records of recent tectonic activity, complicating the identification and interpretation of faults outside of the zones of active seismicity and historical earthquakes. Our study centers on Crowleys Ridge, a north-south trending ridge located in the Mississippi embayment whose origin has been debated (Figure 1-1). Whereas some studies interpret the ridge as an erosional remnant created by incision from the paleo-Mississippi and paleo-Ohio Rivers during the Pleistocene (Fisk, 1944; Guccione et al., 1986; Van Arsdale et al., 1995), seismic reflection data reveal that at least part of the ridge is fault-bounded (Van Arsdale et al., 1995), and paleoseismic studies indicate that the northern part of the ridge is active (Baldwin et al., 2006). Recent work supports the interpretation that both erosion and uplift have played a role, with Pleistocene denudation in the Mississippi embayment inferred to have created an isostatic response that has reactivated existing faults within the NMSZ and along the margins of Crowleys Ridge (Van Arsdale et al., 2019). However, the timing of fault activity remains in question, and the limited active seismicity near the ridge is not clearly associated with these faults (Figure 1-1b). Previously published seismic reflection data show vertically offset Cretaceous and Eocene units (Van Arsdale et al., 1995), but the basal Quaternary contact is often poorly imaged, and fault displacements cannot be reliably traced to the surface, preventing identification of faults that were potentially active in the late Pleistocene and Holocene. Moreover, due to the limited seismicity, constraints on recency of faulting, estimates of potential fault slip magnitudes and rates, the faults bounding Crowleys Ridge are not currently included as discrete, independent seismic sources in regional or national seismic hazard models such as the Central and Eastern United States Seismic Source Characterization model (CEUS-SSC; U.S. Department of Energy et al., 2012) or the National Seismic Hazard Model (NSHM; Petersen et al., 2014, 2018). If active, these faults represent a seismic source(s) that warrants consideration for possible inclusion in future seismic hazard models.

We assess potentially active and recent deformation of Crowleys Ridge using a three-pronged approach to interrogate the landscape at different scales and integrate available subsurface data: (1) we use a landscape-scale approach, examining the topography, catchments, and stream networks to detect patterns or signals that may indicate tectonic activity over late Pleistocene timescales; (2) we identify scarps on the landscape near the margins of Crowleys Ridge that offset late Pleistocene geomorphic surfaces using recently available high resolution (<1 m) lidar data; and (3) we integrate our topographic analysis with new and reinterpreted legacy seismic reflection and new airborne resistivity data to assess whether scarps correspond to faults or folds mapped in the subsurface. Together, these datasets support the interpretation that Crowleys Ridge is a tectonically active stepover structure and facilitate a reinterpretation of the regional active fault network and seismic hazard.

1.3 Geologic Setting

The NMSZ is seismically active (Figure 1-1) and considered an area of elevated earthquake hazard (Petersen et al., 2014, 2018), in large part because of a series of large (M>7) earthquakes in 1811-1812 (Johnston and Schweig, 1996) and paleoseismic evidence for M>6

NMSZ earthquakes during the late Holocene (Kelson et al., 1996; Tuttle et al., 2002, 2019; Gold et al., 2019). Historical seismicity occurs at depths of 4 to 14 km within the Cambrian and Precambrian strata (Pujol et al., 1997; Van Arsdale and ten Brink, 2000), and the earthquakes on the Reelfoot fault are thought to be caused by reactivation of the Reelfoot rift basement faults occurring on a compressional left stepover within an overall right-lateral fault system (Schweig and Ellis, 1994; Csontos et al., 2008; Pratt et al., 2013).

Crowleys Ridge extends ~320 km between central Arkansas and southern Missouri and topographically divides the Eastern Lowlands and Western Lowlands of the Mississippi River valley (Figure 1-1, Figure 1-2). The ridge varies in width from 1.6 to 19 km and has an average relief of 60-80 m above the nearby floodplains (Van Arsdale and Cupples, 2013). Stratigraphically, the ridge is composed of Mesozoic, Eocene (Midway and Wilcox Groups), and Pliocene-Pleistocene unconsolidated sediments (Figure 1-2a). The Eocene sedimentary rocks are composed of continental deltaic sand and clay interbedded with lignite and dip ~0.5° to the southeast (Meissner, 1984). Unconformably overlying the Eocene strata are Pliocene-Pleistocene strata of the Upland Complex (Autin et al., 1991; Van Arsdale et al., 2007; Van Arsdale et al., 2019), locally called the Lafayette gravel or Citronelle Formation, composed of fluvial sands, gravels and minor clay that is locally thicker than 50 m (Autin et al., 1991), although it may have been as thick as 150 m (Van Arsdale et al., 2019). The upland complex may be Miocene to early Pleistocene in age (Autin et al., 1991), but recent work indicates it is Pliocene-Pleistocene in age, with a basal unconformity that is ~3.1-4 Ma (Van Arsdale et al., 2007; Van Arsdale et al., 2014a). Overlying the Pliocene-Pleistocene upland complex, Crowleys Ridge is capped by <10 m of a sequence of Pleistocene loess deposits, from oldest to youngest: Crowleys Ridge Loess (200-250 ka), Loveland Loess (120-190 ka), Roxana Silt (27-55 ka), and Peoria Loess (10-25 ka) (Saucier, 1974; Guccione et al., 1986; Markewich et al., 1998; Forman and Pierson, 2002).

Late Pleistocene fluvial terraces composed of glacial outwash flank both sides of Crowleys Ridge in the Eastern Lowlands and Western Lowlands (Figure 1-2a; Saucier, 1974; Rutledge et al., 1990; Autin et al., 1991; Rittenour et al., 2007), recording intervals when the Mississippi River was a proglacial system associated with the Laurentide ice sheet. Geomorphic mapping and optically stimulated luminescence ages have clearly delineated several late Pleistocene fluvial braid belts that are progressively younger away from Crowleys Ridge in both directions (Figure 1-2a; Rittenour et al., 2007). These terraces are locally capped by Peoria Loess (Rutledge et al., 1990; Autin et al., 1991; Forman and Pierson, 2002).

1.3.1 Geomorphic and paleoseismic observations

Because of its enigmatic geomorphic expression and position in the modern landscape, Crowleys Ridge has been studied for decades to better understand its origin. One line of thinking has favored an erosional origin for Crowleys Ridge associated with pulses of glacial melt water and sedimentation associated with Quaternary deglaciation (Fisk, 1944; Guccione et al., 1986; Van Arsdale et al., 1995). A different interpretation assessed Quaternary deformation of Crowleys Ridge using small-scale topographic maps and stratigraphy from well data, and generally concluded that there is a tectonic influence on the landscape and drainage network along Crowleys Ridge (Cox, 1988; Boyd and Schumm, 1995). More recent paleoseismic work has confirmed late Pleistocene-early Holocene thrust, normal, and strike-slip faults bounding the northern part of Crowleys Ridge (Baldwin et al., 2006). Here, we summarize the relevant key findings from previous work, and for purposes of discussion, we divide Crowleys Ridge into three sections based on subtle changes in orientation: northern, central, and southern Crowleys Ridge (Figure 1-2b).

Despite favoring an erosional origin for Crowleys Ridge, Fisk (1944) first reported evidence for possible tectonic control on ridge topography and the fluvial system. Fisk (1944) identified water and wind gaps, or notches cut through the ridge by rivers that either still contain active streams (water gaps) or have been stranded above the modern drainage (wind gaps). Wind and water gaps may imply that the river pathway predates subsequent uplift. Four major water gaps in Crowleys Ridge have been identified: Bell City-Oran, Castor, St. Francis, and Marianna water gaps, in addition to several minor wind gaps north of St. Francis (Figure 1-3). Fisk (1944) primarily attributed the water gaps to avulsions and migration of the fluvial systems within the broader Mississippi River embayment; however, a recent study attributes at least the southernmost Marianna water gap to tectonics based on the drainage patterns, inferred flow of paleochannels, presence of sand blows, and the intersection of multiple previously-mapped faults (Rains and Guccione, 2016).

Cox (1988) built on the observations from Fisk (1944) and also noted that the geomorphology differs markedly to the north and south of the town of Jonesboro and the Bolivar-Mansfield tectonic zone (BMTZ) (Figure 1-1). Cox (1988) documented basin asymmetry along northern Crowleys Ridge, which he attributed to southeast ground tilting and stream migration. Along the southern ridge, drainage basins are largely symmetrical, but do show a preferred valley and channel orientation of N45°-55°E, parallel to the orientation of the underlying Reelfoot rift (Cox, 1988). In addition, Cox (1988) noted that the northern ridge is generally steeper on its western margin, indicating an overall eastward tilt of the topography. Subsequent geomorphic analysis documented three fault-bounded blocks, each approximately 5-10 km wide, that tilt east on the northern part of the ridge (Boyd and Schumm, 1995). Furthermore, the alignment of stream valleys between Cherry Valley (CV on Figure 1-2b) on southern Crowleys Ridge and the salient in the ridge margin near Levesque (L on Figure 1-2b) are considered to be geomorphic evidence of recent faulting (Spitz and Schumm, 1997).

In addition to the surface topography, borehole data from Crowleys Ridge and the surrounding lowlands were used to assess post Pliocene-Pleistocene stratigraphic offsets. A detailed analysis of well data in central Crowleys Ridge indicated that Pliocene-Pleistocene deposits capping the ridge have considerable relief that cannot be explained by one continuous depositional surface; even so, these data indicate that the northern part of the ridge has been down-dropped by 52 m relative to the southern part of the ridge (Cox, 1988). A subsequent interpretation (Van Arsdale et al., 2007) suggests the upper and lower contacts of the Pliocene-Pleistocene upland complex throughout the Mississippi River embayment are relatively parallel and planar, consistent with limited late Quaternary tectonic activity along the margin of Crowleys Ridge (Van Arsdale et al., 2007), although recent work documents a southeast-tilting upland complex contact and speculates that Quaternary reactivation of faults along Crowleys Ridge accompanied by denudation of the upland complex in the Pleistocene (Van Arsdale et al., 2019).

Lastly, paleoseismic studies from the northernmost part of Crowleys Ridge document late Pleistocene to early Holocene tectonic activity. Along the northeastern part of the ridge, paleoseismic trenches in the Idalia Hills fault zone (location of trench sites shown in Figure 1-2), which overlies the Commerce geophysical lineament (Figure 1-1) record late Pleistocene-early Holocene strike-slip faulting (Baldwin et al., 2006). Fault-related geomorphic features including linear troughs, small 2- to 3-m high scarps, deflected drainages, springs, and bedrock notches. Seismic reflection data (HR-1, HR-2, IDAL-1, IDAL-2) reveal near-vertical faults that displace Tertiary and Quaternary reflectors and project into the paleoseismic trenches at the surface (Baldwin et al., 2006). Faulted and warped Eocene, late Pleistocene, and Holocene units within the trench date the most recent event to pre-7.7 ka and a penultimate event dated to 23 to 18 ka

(Baldwin et al., 2006). Furthermore, sand blows and other paleoliquefaction features record mid-Holocene to recent tectonic activity along faults of the eastern and western margins of the Reelfoot rift near the Marianna water gaps and Paragould, respectively, along the Axial fault (Figure 1-1), and northwest of the St. Francis water gap (Figure 1-2b; Tuttle, 2001; Tuttle et al., 2002, 2006, 2019).

1.3.2 Legacy seismic reflection data

Legacy shallow seismic reflection data, collected primarily in the early 1990s, cross the central and southern margins of Crowleys Ridge (Figure 1-2a; Nelson and Zhang, 1991; Van Arsdale et al., 1992, 1995; Stephenson et al., 1999) and show that Crowleys Ridge is fault-bounded. The faults observed in the seismic data vary widely in their orientations and apparent sense of slip. Along the western margin of southern Crowleys Ridge, seismic lines (RV1, RV9, and RV10, Figure 1-2a) indicate down-to-the-west faulting, with limited post-Eocene displacement. Down-to-the-east faulting is observed on the eastern margin of the southern ridge (RV2 and RV11, Figure 1-2a). A deeper, longer seismic line (COCORP AR-6, coincident with RV1 and RV2) supports these interpretations (Nelson and Zhang, 1991). Farther north in central Crowleys Ridge, two seismic lines on the eastern margin (RV5 and RV7, Figure 1-2a) near the town of Jonesboro show more complicated geometries, with horsts, grabens, and broad anticlinal folding present in the pre-Tertiary section, and apparent reverse offset in the post-Eocene section with an apparent vertical offset of 3.5 m of the base of Quaternary reflectors. On the western margin at the same latitude (RV4 and RV8, Figure 1-2a), four to five apparent normal faults offset strata of Cretaceous age, the Paleocene Midway Group, and the Eocene Wilcox Group, with apparent vertical offsets ranging from 12 to 61 m.

Together, the seismic reflection data support the interpretation that the ridge is fault-bounded, with most of the apparent vertical displacement (~90%; 60 of 67 m) Paleocene to Eocene in age (Van Arsdale et al., 1995). Because both apparent normal and reverse displacement are observed over relatively short distances on some of the faults in the seismic reflection profiles, they have been interpreted as the upper portions of flower structures (i.e., RV5 in Van Arsdale et al., 1992, 1995). However, near-surface, post-Eocene strata have been interpreted to have a maximum vertical offset of only 8 m (Van Arsdale et al., 1995) on existing two-dimensional (2D) lines, indicating that the present-day topographic relief of Crowleys Ridge only partially results from faulting. If this is the case, much of the observed relief may be due to Pleistocene incision from the ancestral Mississippi and Ohio Rivers, and Crowleys Ridge is best understood as a tectonic landform that has been heavily modified by major river systems.

1.4 Methods

1.4.1 Landscape analysis

We calculated commonly derived landscape metrics to assess potential tectonic deformation recorded in the geomorphology of Crowleys Ridge. We divided the Crowleys Ridge landform into 194 catchments of >5 km^2 and calculated metrics for each catchment, including average and maximum slope, hypsometry (hypsometric integral and curves; a measure of the distribution of elevation within a catchment), drainage basin elongation, and drainage basin relief, in addition to ridge and topographic asymmetry. These parameters were calculated using TopoToolbox, an open-source toolbox for MATLAB (Schwanghart and Kuhn, 2010; Schwanghart and Scherler, 2014), and QGIS v2.18.9 on the 10-m NED DEM available through the USGS National Map program (https://apps.nationalmap.gov/downloader/). To identify north-to-south variations in these parameters along the ridge, we selected a centerline that extends for ~350 km from north to south through the approximate center of the ridge. The midpoint of each catchment was then projected onto this centerline.

We focus on parameters that have been shown to correlate with tectonic activity, including mean and average slope, hypsometric integral, basin relief ratio, and the basin elongation ratio (Table 1-1), assuming a uniform bedrock lithology, climate, and base-level history (Strahler, 1952; Schumm, 1956; Wobus et al., 2006; Lifton and Chase, 1992; Mahmood and Gloaguen, 2011). Some parameters, such as the hypsometric integral (Strahler, 1952), have been shown to be scale or catchment-size dependent (Willgoose and Hancock, 1998; Hurtrez et al., 1999a; Mahmood and Gloaguen, 2011; Rabii et al., 2017) and sensitive to the catchment bedrock lithology (Hurtrez and Lucazeau, 1999). Regardless, the hypsometric integral has been shown to correlate with tectonic activity for larger catchments (>1000 km^2) but there is a stronger lithologic influence on smaller scales (<100 km^2) (Lifton and Chase, 1992), similar to the scales of catchments along Crowleys Ridge. Numerous studies have successfully used this metric to broadly define areas of uplift and tectonic activity (Hurtrez et al., 1999b; Lifton and Chase, 1992; Mahmood and Gloaguen, 2011; Rabii et al., 2017), even in regions of slightly variable lithology (Rabii et al., 2017). Generally, hypsometric integrals with values >0.6 with convex hypsometric integral (HI) curves are considered youthful landscapes, values between 0.35 and 0.6 with s-shaped curves are considered mature landscapes, and concave curves with HI below 0.35 are considered older, eroding landscapes (Strahler, 1952).

Higher average slope and basin relief ratios have also been found to correlate with higher rates of tectonic activity (Montgomery, 2001; Figueroa and Knott, 2010). Basin elongation ratio may indicate tectonic activity on one side of a mountain range (Bull and McFadden, 1977). Low basin elongation values (<0.6) are generally regarded as an indicator of tectonic activity (Strahler, 1964; Bull and McFadden, 1977).

Previous regional-scale geologic mapping (Meissner, 1984) and well log data indicate that most of Crowleys Ridge is underlain by relatively uniform lithology (Figure 1-2a; Fisk, 1944; Van Arsdale and ten Brink, 2000). We also assume that because all streams draining Crowleys Ridge eventually join the Mississippi River just south of Crowleys Ridge, the streams have experienced a similar regional base level history. Base level is defined as the lower limit of the landscape below which rivers cannot erode (Powell, 1875). If base level changes due to tectonic (i.e., surface elevation change due to faulting) or fluvial (i.e., avulsion) mechanisms/processes, the lower topographic limit of the landscape changes and the hillslopes and channels will respond by either becoming gentler or steeper. Avulsions and migration of the rivers during the latest Pleistocene and Holocene may have a minor effect on the local base level for certain catchments (see “Discussion” Section 1.6).

Channel steepness and the identification of knickpoints are often used to infer tectonic activity on a landscape scale (Kirby and Whipple, 2001; Wobus et al., 2006). We attempted to calculate channel steepness and identify knickpoints along streams draining Crowleys Ridge. The analysis was complicated by substantial anthropogenic modifications to the landscape, including numerous humanmade holding ponds and dams, channel modifications following the construction of roads, and extensive channelization of waterways for agricultural use (e.g., Tarolli and Sofia, 2016). In addition, the overall low relief of the landscape (<100 m) and humid subtropical climate results in channel steepness indices that were too similar to draw any conclusions. Therefore, we do not rely on these common metrics to identify areas of uplift and faulting in the landscape.

1.4.2 Surficial mapping

Lidar has proven to be a powerful tool to identify and analyze faults in the CEUS. However, studies to date have focused on analyzing previously identified faults, such as the Cheraw fault (Ostenaa and Zellman, 2018), Meers fault (Streig et al., 2018), and Reelfoot fault (Delano et al., 2018). Here, we use lidar to map previously unidentified scarps and warps along Crowleys Ridge that may be associated with recent fault ruptures.

To assess possible tectonic deformation and, in particular, surface rupture recorded by fault scarps along the margins of Crowleys Ridge, we mapped suspected fault-related features on the 1-m bare-earth lidar DEM based on the following criteria: (1) the scarp or fold appears to offset correlative surfaces; (2) the scarp or fold is not directly parallel to an active fluvial system or obvious paleo-fluvial system; and (3) the apparent scarp or warp does not appear to be anthropogenic in origin. To determine whether an apparent fault-related feature may be anthropogenic in origin, we compared features mapped from topography with satellite imagery, in addition to visiting several key sites in the field (described below).

Mapped fault-related topographic features are classified into three categories based on their geometry and characteristics (Figure 1-2b; Figure 1-4): (1) fault scarps, where discrete discontinuities offset a surface with similar gradients on either side over a relatively short distance (<50 m); (2) fold scarps, defined as a gentle, broad warping of the surface by 0.5-2 m over a distance of 50-300 m; and (3) scarps or lineaments of unknown origin, where a lineament is clearly present across a surface. This latter class of scarps may be of tectonic origin or may be relict fluvial terrace risers or historical humanmade features that have since been heavily modified and are not obvious in present-day imagery or in the field.

We rely on previously published mapping and age constraints of terrace and braid belts, and we use the channel and braid belt terminology of Rittenour et al. (2007). Geomorphic surfaces, such as alluvial fans or fluvial terraces that appeared to be younger than the adjacent broader braid belt, were mapped in additional detail and were assigned either a maximum or minimum age based on the relationship with the nearby braid belts (Rittenour et al., 2007).

From the surficial mapping, we calculate vertical separation and fault slip rates using a Monte Carlo approach with 50,000 trials, where all variables (linear fits to upper and lower surface, age of surface, position of fault on the scarp, and fault dip) are treated as normal distributions around a mean (Thompson et al., 2002; Amos et al., 2007; Thompson Jobe et al., 2017).

1.4.3 Subsurface data

1.4.3.1 Seismic data collection and processing

To augment previous seismic imaging across the margins of Crowleys Ridge (Nelson and Zhang, 1991; Van Arsdale et al., 1995), we collected an 11.0-km-long high-resolution mini-vibrator P-wave source profile (CRmv line; Figure 1-2) across southern Crowleys Ridge in 2006 (Table S1 in Thompson Jobe et al., 2020a, Table A-1). Five-meter source and receiver intervals with 144 recording channels resulted in 72-fold data. We collocated CRmv with the deep-focused Consortium for Continental Reflection Profiling (COCORP) profile AR6 acquired with 100-m source and geophone group intervals (Nelson and Zhang, 1991) and shallow-focused profiles RV1 and RV2 collected with 15.2-m geophone and source intervals (Van Arsdale et al., 1995). The imaging depth range for CRmv is ~50- to 800-m. The data were collected in time and depth converted and processed using conventional techniques (Table A-2). Compared to earlier seismic imaging, this data acquisition approach improved subsurface imaging of reflector continuity on the margins of the ridge in the upper 800 m.

To tie reflectors to specific geologic formations, we followed the work of previous seismic reflection studies in the NMSZ, which used petroleum test wells in the region, some of which are located near Crowleys Ridge, to assign depths to imaged reflectors (Renfroe, 1949; Dart, 1992; the New Madrid test well 1-W: Crone, 1981; Frederiksen et al., 1982; the Fort Pillow test well in Lauderdale County, Tennessee: Moore and Brown, 1969). In addition, we relied on depths of key reflectors from published seismic lines that pass over Crowleys Ridge (Nelson and Zhang, 1991; Van Arsdale et al., 1995). We used an average velocity function derived from stacking velocities to convert from time to depth.

1.4.3.2 Airborne electromagnetic data collection and processing

Regional-scale airborne electromagnetic (AEM) data were recently acquired as part of a large regional water availability study throughout the Mississippi alluvial plain (Alhassan et al., 2019; Minsley et al., 2019). In coordination with this project, we acquired an additional ~400 km of linear AEM data along 24 17-km-long flight lines with 1.5-km line spacing centered on a portion of southern Crowleys Ridge in early 2019 (Table S4 in Thompson Jobe et al., 2020a). In this study, we show two of the lines that coincide with mapped scarps to highlight the applicability of this new dataset to neotectonic problems. The AEM data were acquired with the CGG Resolve frequency-domain instrument, resulting in high-resolution continuous profiles of electrical resistivity structure to depths of up to about 100 m along flight paths (Siemon et al., 2009). Raw data were averaged to 25-m output intervals, and were inverted for subsurface resistivity structure using the Aarhus Workbench software (Table A-3, Auken et al., 2015). In the neighboring regions of the alluvial plain, high resistivity values in the upper 30-80 m agree with borehole depths to the base of the aquifer in Quaternary units, with low resistivity beneath the aquifer associated with buried Pliocene units.

1.4.4 Field observations

We targeted specific locations to field check the mapped scarps and lineaments. At each site, we assessed the mapped offset correlative surface, checked for recent anthropogenic modification or erosion of the scarps, observed lateral continuity and microtopography along the scarps, and measured topographic profiles using an auto-level and a handheld global positioning system (GPS) unit to estimate the apparent vertical offset and compare against vertical offsets measured from the lidar data.

1.5 Results

1.5.1 Landscape analysis

Our landscape analyses reveal substantial north-to-south changes in the topography and landscape metrics of Crowleys Ridge (Figure 1-3). Swath topographic profiles extracted across Crowleys Ridge illustrate the changing asymmetry of the ridge along its length (Figure 1-3). The northern and central ridge is ~15-km wide on average, and the drainage divide alternates east to west across the ridge whereas topographic asymmetry switches between steeper western and eastern margins (Figure 1-3, profile A). The southern ridge is ~7-km wide on average, and the topography is relatively symmetric in the northern half, with steep eastern and western margins. The southern half of the southern ridge exhibits a pronounced steeper eastern margin (Figure 1-3, profile B).

Hypsometric integrals (HI) vary between 0.24 and 0.61 along the entire length of the ridge, with no obvious dependence on catchment size or shape (Figure A-1). The HI and curves show a consistent increasing trend from north to south, with some noise in the trends (Figure 1-5, Table S6 in Thompson Jobe et al., 2020a). In central and northern Crowleys Ridge, HI are low (<0.4), with a few exceptions of catchments with higher HI (0.5 to >0.55), and the curves generally have a more concave shape. HI in southern Crowleys Ridge are higher (0.45 to >0.55), and the curves are convex in shape. These observations indicate more youthful, tectonically active landscapes in the south, and more mature landscapes in the north, and are consistent with increasing tectonic activity from north to south.

Average and maximum slopes also show consistent north-to-south trend from lower to higher values along the ridge (Figure 1-6a, Table S6 in Thompson Jobe et al., 2020a). Average slopes on the central and northern ridge are between 2 and 8°, whereas average slopes in southern Crowleys Ridge are between 4 and 10° (Figure 1-6a). Slopes in the northern ridge reach a maximum of 45°, with most catchments having maximum slopes between 25 and 35°. In southern Crowleys Ridge, maximum slopes reach 67°, with most catchments having maximum slopes between 35 and 55°. Other parameters, such as the basin elongation ratio or basin relief ratio, did not show obvious north-to-south variations (Figure 1-6). Basin elongation ratios varied between 0.37 and 0.92 along the length of the ridge (Figure 1-6b, Table S6 in Thompson Jobe et al., 2020a). In general, more elongated basins are found along the eastern margin of central Crowleys Ridge. Basin relief ratios are between 0 and 0.08 (Figure 1-6c, Table S6 in Thompson Jobe et al., 2020a). The slope relationships are also consistent with increasing tectonic activity on the southern part of the ridge, whereas the basin elongation ratios may illustrate variable basin development possibly related to the different geometries of faults that bound different ridge margins from north to south (Bull and McFadden, 1977).

Analysis of the drainage network patterns and topography reveals important geomorphic differences between northern, central, and southern Crowleys Ridge (Figure 1-7). The drainage network is considerably modified by humans, both from extensive channelization in lowland areas and the creation of artificial holding ponds. Despite this anthropogenic signal, the underlying unmodified landscape signal can be extracted from the regional topographic dataset. On northern Crowleys Ridge, beheaded channels are observed at the eastern margin of a higher elevation, low-relief surface (Figure 1-7a). Central Crowleys Ridge has elongated drainage basins on its eastern side (Figure 1-6b), and a steeper western margin. Several northeast-southwest (NE-SW) trending ridges divide the largest catchment on the southern end of central Crowleys Ridge, with all ridges characterized by a steeper western margin, gentler eastern margin, and a drainage network that exhibits asymmetry, with the trunk channel on the eastern sides of the valleys (Figure 1-7b). On southern Crowleys Ridge, a sharp, steep escarpment characterizes the eastern margin, and the channel system drains westward. Sharp, 90° turns are observed in the drainage network, and some of the relict channels appear to extend up to the sharp eastern margin (Figure 1-7c). Moreover, we observe an alignment of channels across catchment boundaries, similar to those described by Cox (1988). Approximately 20 km to the south, there is another higher-elevation, low-relief surface, also characterized by beheaded channels along its eastern margin (Figure 1-7d). In general, these drainage network observations support at least some tectonic control on the topographic and drainage network evolution.

1.5.2 Late Pleistocene and Holocene scarps, folds, and warps

We focus on two geomorphic features typically associated with active faults: fault scarps and surficial folds or warps. We describe surficial folds and warps as ‘fold scarps’ to convey their association with near-surface displacement of buried faults and because net vertical displacement of correlative geomorphic surfaces occurs in the far field across these features.

Faults scarps mapped along Crowleys Ridge are typically parallel to the margin of the ridge (Figure 1-2b). In general, scarps show a down-to-the-east sense of displacement on the eastern margin, and a down-to-the-west sense of displacement on the western margin. Fault scarps are mapped with lengths of 300 m to 1 km, with vertical separation of 0.4 to 6.0 m and tilting that has resulted in up to 6 m of vertical separation (Figure 1-3a, Figure 1-8, Figure 1-9, Figure 1-10, Figure 1-11).

Fold scarps are broad with length scales of 50-300 m and amplitudes of 0.3 to 1 m (Figure 1-3a). Fold scarps often extend beyond the ends of fault scarps, which may be interpreted as blind faulting.

Scarps or lineaments of unknown origin can be traced for 100 to 500 m (Figure 1-3b). These scarps are distinguished by the following characteristics that indicate the scarp origin may not be tectonic: questionable correlative surface across the scarp, little to no net displacement of the geomorphic surface, and nearby landscape features (channels, field boundaries, old roads) that may indicate an anthropogenic origin.

To illustrate geomorphic features associated with active faulting along the margins of Crowleys Ridge, we describe four sites in detail (Figure 1-8, Figure 1-9, Figure 1-10, Figure 1-11). Three sites are located near seismic reflection data that clearly show folding or faulting of post-Eocene strata (Van Arsdale et al., 1995). A fourth site in northern Crowleys Ridge records possible deformation of Quaternary surfaces but no subsurface data exist to confirm the presence of faults.

1.5.2.1 Wittsburg area

On the eastern margin of southern Crowleys Ridge, a series of semi-parallel scarps is preserved in a moderately sloping surface (Figure 1-2b, Figure 1-8). Based on surface roughness, distributary drainage pattern, the degree and style of dissection, and the location, geometry, and slope observed in the lidar data, we interpret the faulted surface as an alluvial fan complex deposited on top of the ~15 ka Kennett braid belt (Figure 1-8; Rittenour et al., 2007). This relationship indicates the alluvial fan surfaces must be younger than ~15 ka, providing a maximum age for the fault scarps formed in the fan complex. The scarps are mapped north-to-south for ~4.5 km, and they climb and fall in elevation. The maximum apparent vertical offset measured across the scarps from lidar is ~1 m (Figure 1-8c). Channel incision west of the mapped scarps (~2 m in the hanging wall versus ~1 m in the footwall) is consistent with uplift and subsequent erosion of the western part of the alluvial fan surface. Field mapping confirmed 1-2 m of down-to-the-east apparent vertical offset of the surface at the location of the fault mapped on the lidar (Figure 1-8d).

No seismic data exist in the nearby area. However, previously published seismic reflection data across the eastern margin of Crowleys Ridge ~30 km north of the Wittsburg area (RV2 and RV11, Figure 1-2a), show a steeply west-dipping fault that offsets Paleozoic and Eocene strata into an anticline with ~30 m of structural relief. New AEM data from the eastern margin of the ridge at the same location as the scarps show a sharp discontinuity at the ridge margin, interpreted as a steeply dipping fault, and another discontinuity just inboard of the ridge margin (Figure 1-8e). Although these faults imaged on the AEM data do not align with the scarp observed at the surface, they do support an interpretation of a fault-bounded ridge margin.

1.5.2.2 Harrisburg area

On the western margin of southern Crowleys Ridge, a series of semi-parallel fault and fold scarps offset a surface previously mapped as the ~56-ka Dudley braid belt (Figure 1-2, Figure 1-9; Rittenour et al., 2007). These scarps trend approximately north-south for ~4 km. At the northern end, a series of 3 semi-parallel fold scarps form an en echelon map pattern. These scarps generate a <1-m-high warp of the surface over a distance of 50-150 m. Moreover, stream channels draining Crowleys Ridge to the east are deflected northwest around the scarps.

Less than 1 km to the south, a ~600-m-long fault scarp is bracketed by fold scarps. The surface is offset a maximum of ~2 m across the fault scarp (Figure 1-9c). The fold scarps bounding the fault scarp are subtle; they warp the surface by <1 m over a distance of 40-100 m, but they are distinguishable on lidar. In addition, a stream channel draining Crowleys Ridge is deflected to the northwest around the scarps and is more incised upstream from the scarps (~3 m versus <2 m of incision upstream and downstream, respectively) (Figure 1-9b). The channel planform also changes across the folds and scarps. Upstream, the channel planform is meandering, whereas across and downstream from the fold scarp it is straight.

Previously collected seismic reflection data ~700 m (RV10) and ~2.3 km north (RV1) (Van Arsdale et al., 1995), in addition to the new seismic line CRmv (~2.3 km north) across these scarps, reveal down-to-the-west offset on reflectors in the Paleozoic through Eocene strata. With surficial observations as our guide, we reinterpreted the seismic data as a series of east-dipping reverse faults (Figure 1-9d), which underlie the approximate locations of the scarps along strike.

1.5.2.3 Bono area

On the western margin of central Crowleys Ridge, a series of three semi-parallel scarps cut the lowland adjacent to the bluff (Figure 1-10). The faulted surface has been previously mapped as the ~38-ka Melville Ridge braid belt (Figure 1-3; Figure 1-10; Rittenour et al., 2007). These north-south trending scarps extend across the surface for ~2 km, although individually, each scarp has a maximum length of 1 km. Together, these scarps have a total maximum offset of ~3 m (Figure 1-10c). Some of these scarps are also visible in the field, clearly showing 1-2 m of down-to-the-west apparent vertical offset over two fold scarps.

Previous interpretations of shallow seismic reflection data (RV4) at this site show Cretaceous strata and Eocene Wilcox Group reflectors are offset with apparent normal and reverse displacement that may represent primarily normal faults or flower structures (Van Arsdale et al., 1995). Guided by our surface observations and nearby seismic reflection lines, we reinterpret these mixed-sense displacements as associated with oblique slip on steeply dipping reverse faults (Figure 1-10d). Although reflectors in the upper Eocene Wilcox Group and Quaternary strata are not imaged in the seismic reflection data, the fault scarps mapped at the surface are coincident with deeper subsurface faults, which leads us to conclude that the seismically imaged faults have been active into the late Pleistocene.

1.5.2.4 St. Francis Water Gap

The St. Francis River flows across Crowleys Ridge near the boundary of the central and northern sections (Figure 1-11a). The water gap is ~1.5-km-long and ~0.3-km-wide at its narrowest point (Fisk, 1944). A recently abandoned channel belt with meander cutoffs is still clearly visible in the lidar-derived topography, which marks the natural channel configuration prior to channel diversion in 1900s (Figure 1-11c). Northwest of Crowleys Ridge, the pre-diversion St. Francis River forms a series of high-sinuosity oxbow meanders. Where the St. Francis River crosses Crowleys Ridge, the pre-diversion channel becomes single-thread and less sinuous ('straight') and the channel slope steepens. The natural (pre-diversion), low-sinuosity channel continues downstream from Crowleys Ridge for approximately 3 km, where it is bounded by a series of fluvial terraces (described below). Finally, the channel once again takes a meandering form where it enters the Kennett braid belt (Figure 1-11a), now confined by anthropogenic levees. We interpret the straightening of the channel planform geometry and the steepening of the channel slope as a fluvial response across a zone of uplift (Burbank et al., 1996). In some cases, channel planform changes may be the opposite of what we interpret; a channel may become more sinuous across a zone of uplift and straighten upstream from the uplift (Holbrook and Schumm, 1999). Regardless, we focus on the change in channel planform across Crowleys Ridge. Our interpretation differs from that of Fisk (1944), who suggested the water gap was previously abandoned due to river avulsion and is only currently occupied by the St. Francis River because of anthropogenic diversion of the river in the recent past.

We identified three fluvial terraces at the St. Francis Water Gap based on their geometries and positions relative to the modern St. Francis River, their surface continuity and character, and their relative heights above the modern river and the late Pleistocene braid plains. The highest terrace, T1, is only preserved as a small remnant on the southwestern side of the water gap ~9 m above the modern channel. T2 is the most extensive terrace ~4 m above modern channel that ends abruptly by a sharp fluvial scarp above the ~15-ka Kennett braid plain (Rittenour et al., 2007). Terrace T2 is preserved on both sides (northwest (NW) and SE) of Crowleys Ridge. On the SE side of Crowleys Ridge, the T2 terrace bounds a relatively low-sinuosity reach of the pre-diversion St. Francis channel. Based on mapped relationships to the northwest of the water gap, the T2 terrace is set into the 38-ka Melville Ridge braid plain (Rittenour et al., 2007); we interpret the T2 terrace to be >15 ka but <38 ka. The T3 terrace is equivalent to the modern floodplain and is characterized by levees with heights of 2 m above the surrounding floodplain deposits and 4 m above the modern river channel. The T3 floodplain surface is set into the ~15-ka Kennett braid plain (Rittenour et al., 2007).

We extracted topographic profiles perpendicular to the margins of Crowleys Ridge and parallel to the St. Francis River to assess potential deformation of the terrace surfaces. The T2 surface (Figure 1-11b) tilts ~0.5° away from the ridge for the first ~1.5 km, compared to the modern channel gradient of ~0.01°, before flattening out. The amplitude of the tilting is ~6 m. The 6 m of apparent vertical separation from tilting and concave-up profile could be interpreted as a result of tectonic activity, or colluvial or alluvial deposition on top of T2 close to the higher topography. Based on the available data, we cannot distinguish between these two interpretations.

To the south of the St. Francis Water Gap, a northeast-trending scarp extends ~1 km across the T1 surface (Figure 1-11d). The scarp has a vertical offset of ~2 m, which decreases to the northeast (Figure 1-11e). A channel is deflected to the northeast around the tip of the scarp.

Taken together, observations of St. Francis River sinuosity and steepness, terrace formation and abandonment, apparent tilting of terrace T1, and a late Pleistocene fault scarp indicate that the St. Francis Water Gap records low-rate, progressive late Quaternary tectonic deformation. This interpretation is consistent with previous observations of progressive overall east-southeast migration of the course of the St. Francis River southeast of the water gap towards the modern-day Mississippi River, perhaps caused by southeastward tilting from uplift at Crowleys Ridge (Boyd and Schumm, 1995) or in the Ozark Mountains (McKeown et al., 1988).

1.5.3 Seismic data observations and interpretations from the Harrisburg East site

The observations from the CRmv seismic line are similar to previously published seismic lines across Crowleys Ridge that show discontinuities in the Paleozoic through Eocene strata and upwardly warped reflectors under Crowleys Ridge. On CRmv, there are two main groups of reflections on both sides of Crowleys Ridge separated by a relatively transparent zone underlying the ridge. Figure 1-12 shows the location of the line, interpretations of AEM data long the line, and uninterpreted and interpreted seismic lines from the Harrisburg East site. The Quaternary section is ~70-m and ~50-m thick on the eastern and western sides of the ridge, respectively, as constrained by lignite borehole studies (Csontos and Van Arsdale, 2008; Van Arsdale and Cupples, 2013) and the AEM data (Figure 1-12e). Using the well data and previous interpretations as our guide, we identify the Eocene reflection group at the 200- to 400-m depth interval and the reflective Cretaceous-Paleozoic group from ~500- to 800-m depth. The Paleocene section, from ~400- to 500-m depth, lacks obvious internal reflections.

In general, seismic reflection imaging in the middle part of the profile, over the highest part of Crowleys Ridge, is poor. Here, Pliocene terrace gravels and Pleistocene loess are exposed at the surface and likely contributed to poor coupling and reduced signal penetration because the surficial loess deposits may absorb the seismic energy (Williams et al., 2001). Imaging quality also degrades in this part of the COCORP AR-6 profile even with the use of five industry-sized vibrator trucks as a source (Nelson and Zhang, 1991). Thus, we exclude this portion of the profile from interpretation because we are not confident that apparent reflections beneath the center of Crowleys Ridge represent stratigraphic boundaries.

Across the profile, reflections are primarily deformed by undulating folds with individual 10- to 50-m amplitudes (Figure 1-12e). Reflections are vertically displaced by only a few meters by sharp vertical discontinuities, interpreted as minor steeply dipping faults, primarily in the Cretaceous and Paleozoic section, although some faults extend upwards into the Eocene and Quaternary strata. The largest folds are imaged on the ridge margins extending toward the middle part of the ridge. On the western margin, both the Eocene and Cretaceous-Paleozoic reflection groups are folded upwards ~50 m relative (a in Figure 1-12e) to the adjacent subhorizontal reflections (b in Figure 1-12e) that extend beneath the floodplain to the west. On the eastern side of the ridge, several upward-stepping, 30- to 70-m high folds (c, d, e in Figure 1-12e) coincide with the increasing elevation of Crowleys Ridge, which reaches a maximum elevation of ~40 m above the western alluvial plain and ~60 m above the eastern plain. To guide interpretation across the poor data quality section in the middle part of the ridge and correlate the stratigraphic packages on either side of the ridge, we rely on the previous interpretations from the COCORP AR6 profile, which images the Cretaceous-Paleozoic section and shows that those reflections are relatively flat-lying within the ridge compared to the disruptions at the margins (Nelson and Zhang, 1991).

In the shallow part of the section, several faults cut the Quaternary strata, and may project to the near-surface (f in Figure 1-12e, also shown as dashed lines in Figure 1-12c). The base of the Quaternary appears to be faulted a few meters in an upthrown block (f in Figure 1-12e).

West of this fault, the surface is folded up-to-the-west ~40 m below the eastern edge of the ridge, where the imaging quality degrades.

1.6 Discussion

1.6.1 Is Crowleys Ridge a tectonic landform?

We combine several approaches – tectonic geomorphic analysis, neotectonic mapping on high-resolution lidar, seismic reflection imaging, and resistivity profiling – to test whether Crowleys Ridge is an actively deforming landform. Mapped fault scarps, topographic asymmetry, and drainage network observations indicate that Quaternary-active faults bound most of Crowleys Ridge. Deformation appears to vary north-to-south along Crowleys Ridge: the higher number and continuity of fault scarps, coupled with the higher hypsometric integrals and average slopes, support an interpretation that southern Crowleys Ridge is more tectonically active in the late Quaternary than northern Crowleys Ridge.

We interpret line CRmv, in conjunction with the COCORP AR6 profile, as subsurface evidence that Crowleys Ridge is the surface expression of folding and minor faulting. This interpretation generally agrees with previous interpretations of a tectonic origin for southern Crowleys Ridge (Nelson and Zhang, 1991; Van Arsdale et al., 1995; Stine and Van Arsdale, 2017; Van Arsdale et al., 2019). However, our interpretation shows folding to be more prominent with minor faulting at the margins of the ridge compared to previous interpretations favoring faulting as the primary mode of tectonic deformation on previous, lower resolution data. If folding is a major contributor to net vertical deformation across Crowleys Ridge, as deduced from the seismic data, the surficial expression of Crowleys Ridge integrates the net effects of folding, faulting, and fluvial erosion to produce the topography observed today. The topographic relief on the ridge (~50-90 m) is approximately equal to the cumulative offset and broad folding of Cretaceous, Paleocene/Eocene, and Quaternary units (Figure 1-12), suggesting that Crowleys Ridge is a long-lived tectonic feature but also that incision from the paleo-Ohio and Mississippi Rivers may account for a portion of the present-day topography (Van Arsdale et al., 1995), possibly reactivated by denudation of the Upland Complex in the Quaternary (Van Arsdale et al., 2019).

1.6.2 Geomorphic evidence of active deformation of Crowleys Ridge

We interpret higher hypsometric integrals and average and maximum slopes to indicate that southern Crowleys Ridge may have experienced higher tectonic uplift rates than northern Crowleys Ridge during the Pleistocene to recent (Figure 1-5). Topographic asymmetry, beheaded stream networks, and uplifted, low-relief surfaces (Figure 1-7) are also consistent with tectonic uplift of the ridge. The topographic asymmetry (Figure 1-3) and basin elongation patterns (Figure 1-6) are interpreted to represent active or recent faulting on alternating sides of the ridge.

There are several alternative explanations for the along-ridge variations we observed at the landscape scale, including the effect of regional or local base level and variations in lithology along the ridge. One key assumption in our work is that the base level along the ridge has been the same or changed simultaneously. We assume that the Black and Mississippi Rivers have not been flowing adjacent to Crowleys Ridge since the late Pleistocene, supported by the ages of braid belts that become younger away from the ridge (Rittenour et al., 2007). However, there are exceptions to this assumption. The St. Francis River has been flowing across and close to the eastern margin of Crowleys Ridge during the late Pleistocene and Holocene, and southern Crowleys Ridge is closer to the present-day Mississippi River, which has an overall lower base level than the Black River. The proximity to the lower base level could cause the landscape on the southern ridge to be more sensitive to avulsions. In the lower Mississippi River, the timescales of larger avulsions are ~1300 yr (Aslan et al., 2005), and thus these local base level changes may still be propagating upstream through the landscape. However, we observe that the higher hypsometric integrals and slopes are seen on both sides of the entire length of the southern ridge, so proximity of the Mississippi River and related avulsions to the eastern side of the southern ridge is not clearly influencing the hypsometric or slope data. In addition, the timing of Pleistocene base level falls from sea level fluctuations may also affect the landscape metrics. Previous studies have argued that sea level fluctuations did not extend northward up the Mississippi embayment past Vicksburg, Mississippi (Saucier, 1994; Rittenour et al., 2007). New work indicates that the base of the Quaternary alluvium, mapped from borehole data, is near modern sea level (Csontos et al., 2008; Cupples and Van Arsdale, 2014; Van Arsdale et al., 2014b). This observation, combined with dating of late Pleistocene sediments throughout the Mississippi embayment (Shen et al., 2012) would suggest that possibly several Pleistocene sea-level fluctuations have reached ~600 km inland from the shoreline (Shen et al., 2012) or as far north as 37°N (Van Arsdale et al., 2019), and may have affected the base level near Crowleys Ridge. However, the timescales of response in the Mississippi embayment for these base level changes is estimated to be rapid as ~10 thousand years (k.y.) (Shen et al., 2012); therefore, we might expect that large-scale sea level fluctuations during the Pleistocene may have largely already propagated through the landscape, but acknowledge that the signal we see (higher HI in the south, lower HI in the north) may also reflect the upstream propagation of base-level fall if the timescales are longer. The overall topographic and basin relief along the ridge does not vary considerably (Figure 1-6c); on the northern ridge, the maximum relief is ~90-100 m, whereas along the southern ridge, the maximum relief is ~80 m. We discern that these likely minor differences in base level changes may affect the basin hypsometry, slope, and relief, but because the base level changes affect the entire length of Crowleys Ridge, topographic and basin relief is nearly uniform, and the active fluvial systems are far from the present-day topographic margin of the ridge, their influence is minimal.

Variations in lithology and loess cover may also play a role in the relative erodibility of the ridge, resulting in variations in the landscape parameters. Specifically, lithology has been shown to strongly influence HI for smaller catchments (<100 km^2) (Lifton and Chase, 1992). Because most of the catchments analyzed on Crowleys Ridge are <100 km^2 (Table S6 in Thompson Jobe et al., 2020a), they are likely sensitive to lithologic differences. We assume that lithology does not substantially influence our analyses, because only slight differences in lithology occur along the ridge. The southern ridge has thicker loess deposits (>5 m) than the northern ridge (3-5 m) (Guccione et al., 1986). Eocene sand and clay are exposed along the western margin of the northern ridge, and Pliocene-Pleistocene fluvial sands, gravels, and clays blanket the remainder of the northern ridge (Cox, 1988), but it is not clear that there are any strength differences between these lithologically similar deposits. Along the margins of the southern ridge, Eocene sediments are exposed on both flanks, capped by Pliocene-Pleistocene fluvial sands, gravels, and loess (Guccione et al., 1986; Cox, 1988). Thus, although these minor differences in the lithology capping the northern and southern portions of the ridge may affect the relative erodibility and hence, the measured basin hypsometry (Hurtrez and Lucazeau, 1999), slope, and relief, we do not observe a difference in landscape metrics that clearly correlates with lithology. Because a thin layer of loess blankets the entire ridge and the underlying Eocene sediments are continuous, we assume erodibility is generally the same throughout the study area in the absence of more detailed and local lithologic data.

In summary, we suggest that changes in base-level from the Mississippi River likely affect the entire length of Crowleys Ridge and that minor variations in lithology do not affect the geomorphology of the landscape. We therefore interpret changes in landscape parameters as evidence of Quaternary deformation of Crowleys Ridge.

1.6.3 Neotectonic evidence of active deformation of Crowleys Ridge

In our analysis, we focus on fault and fold scarps that appear to be tectonic in origin. We acknowledge that in a landscape dominated by fluvial processes, identification of tectonic landforms can be difficult. We differentiate fluvial and tectonic scarps in several ways: (1) tectonic scarps show map patterns of en echelon or overlapping tips, and often grade from fault scarps into fold scarps; (2) fault scarps exhibit net vertical displacement across sloping, correlative surfaces; and (3) fault scarps cut up and down slope. We identified discontinuous scarps subparallel to the ridge margin along southern and central Crowleys Ridge. These scarps are discontinuous at the surface, but we infer that the faults responsible for scarp formation continue in the subsurface along the ridge margin even when scarps are not present at the surface (i.e., Harrisburg East area, Figure 1-12). Similar fault-related geomorphic observations from northern Crowleys Ridge were the surface expression of near-vertical faults found in paleoseismic trenches and imaged on seismic reflection data (Baldwin et al., 2006). Discontinuity of the mapped surface scarps may reflect distributed faulting and the competing effects of low-rate surface displacements and relatively high erosion and deposition rates in this setting.

We recognize several regions of mass slope movements and landslides that complicate the interpretation of scarps. Mass movement is clearly an important landscape process along the margins of Crowleys Ridge. We identify and differentiate landslides and mass movements from potential tectonic scarps by arcuate headscarps, the presence of creeks that erode headward and commonly produce a radial drainage pattern, lateral margins that often coincide with creeks, and hummocky and lobate terrain. Moreover, we avoid interpreting scarps in regions of known abundant landslide and lateral spreading features, such as the southernmost tip of Crowleys Ridge, south of Marianna (Doyle, 2005).

1.6.3.1 Slip rates

Because we can measure net vertical displacement of surfaces of approximately known age, we can estimate vertical separation and fault slip rates (Table 1-2). Deformation rates calculated from the scarps along Crowleys Ridge are generally low (<0.2 mm/yr). Vertical separation rates range from 0.03 to 0.08 mm/yr, whereas slip rates range from ~0.04 to 0.09 mm/yr assuming a range of possible fault dips (Table 1-2). We caution that these estimates are highly uncertain due to several dating and measurement issues. For example, some Quaternary surfaces lack precise age dating, (i.e., alluvial fan near Wittsburg, Figure 1-8). Subsequent anthropogenic modification of scarps may alter the total magnitude of offset calculated from the lidar-derived topographic data, leading to under or overestimation of the total offset. Furthermore, the majority of these scarps are small (<0.5 to 2 m), and are likely to only represent 1-2 earthquakes, based on offsets observed during the M>7 1811-1812 earthquakes (5-8 m over 3 earthquake cycles; Kelson et al., 1996; Johnston and Schweig, 1996; Van Arsdale, 2000). Because we do not know if the scarps record a full earthquake cycle, and we are currently in an open interval, any slip rate calculation is subject to substantial uncertainty (Styron, 2019). For example, a near-future event of a similar magnitude and offset could substantially increase the slip rate. Moreover, slip rates rely on estimated fault dips extracted from older, deeper seismic data that may not represent near-surface dips. Finally, the seismic reflection data in the region, including line CRmv, indicates that a substantial amount of tectonic deformation is accommodated as folding. The slip rates we calculate rely only on the fault scarp offsets and fault dips from seismic data and do not include folding, implying that we may be underestimating the total deformation rate. Despite these uncertainties, we conclude that these fault scarps record low rate (<0.2 mm/yr) deformation along the margins of Crowleys Ridge since the late Pleistocene.

1.6.4 Geophysical data

Both seismic reflection and AEM datasets image discontinuities in the strata at the ridge margins, supporting the interpretation that Crowleys Ridge is fault-bounded and has a tectonic origin. Although we cannot directly tie any subsurface fold or fault seen in the seismic reflection data to any specific scarp mapped using the lidar data at the surface due to lack of resolution in the upper ~50 meters, the scarps mapped at the surface have the same overall sense of displacement relative to that seen generally in the subsurface on both sides of the ridge. The youngest faulted and folded reflector clearly imaged on the east side of southern Crowleys Ridge is the base of Quaternary section, supporting the interpretation that deformation on the margins of Crowleys Ridge has persisted into the Quaternary (Figure 1-12). This interpretation is further supported by discontinuities observed in the AEM data, which primarily can image the Quaternary section and uppermost Pliocene strata, at the ridge margin underlying the mapped scarps (Figure 1-8, Figure 1-12). The AEM data demonstrate that the lidar scarps are associated with a subsurface discontinuity that persists for several hundred meters depth and can roughly be tied to discontinuities in the seismic reflection data, thus bridging the gap in the shallow subsurface. We acknowledge that discontinuities in the AEM data may also represent erosion of the Tertiary sediments on either side of Crowleys Ridge, but we discern that the alignment of surface scarps and discontinuities on the seismic reflection data support the interpretation that the discontinuities on the AEM data are faults. Thus, the subsurface and surface data broadly agree with each other.

Based on the seismic reflection data, the two faults observed at the easternmost end of CRmv (c, f in Figure 1-12e) are located ~500 m north of a fold scarp mapped at the surface, supporting the interpretation that the scarp is likely tectonic in origin and that faulting is blind. The offset on these faults (<40 m) is much greater than the offset of the scarp (<0.5 m), indicating that the surface has recorded perhaps only the most recent (<15 ka) fault movement, but that prior movement on the faults has occurred during the Pliocene-Pleistocene.

The elevation of Crowleys Ridge relative to the Eastern Lowlands and Western Lowlands (~50 to 70 m) is comparable to the fold amplitude of ~75 m seen in the subsurface on Eocene to Paleozoic reflectors. There does not appear to be much thickening or thinning of strata in the Paleozoic to Eocene units on either side of the ridge that could be interpreted as growth strata. This observation indicates tectonic activity around Crowleys Ridge is primarily post-Eocene (Van Arsdale et al., 2019), in contrast to previous seismic reflection interpretations that indicate most offset is pre-Eocene (Van Arsdale et al., 1995).

1.6.5 Regional fault network

The seismic reflection and AEM data, landscape analysis, and mapped scarps near Crowleys Ridge indicate that Quaternary faulting in the New Madrid seismic zone is complicated and extends beyond the zone of modern seismicity (Csontos et al., 2008; Van Arsdale and Cupples, 2013). Here, we present an interpretation of how late Quaternary faulting along Crowleys Ridge might fit into a regional kinematic framework (Figure 1-13). In general, our new regional kinematic framework builds on that of Csontos and Van Arsdale (2008) and Van Arsdale and Cupples (2013). The NMSZ is interpreted as an overall dextral transpressive system with documented Quaternary to recent activity on the Commerce fault (Commerce geophysical lineament in previous studies; Stephenson et al., 1999; Baldwin et al., 2006), Charleston Uplift (Martin and Hough, 2019; Pryne et al., 2013), Western Reelfoot Margin fault (Van Arsdale et al., 1995), Axial fault (Pratt et al., 2013), Eastern Reelfoot Margin fault (Tuttle et al., 2006), and the Big Creek-Ellendale fault (Velasco et al., 2005), which trend N30°-50°E (Table 1-3). Other faults, defined by seismicity, seismic reflection data, paleoseismic trenching, and borehole data, generally follow predicted fault orientations for a dextral fault system. The stepover faults trend N15°W to N10°E, creating southern Crowleys Ridge, Joiner Ridge-Manila High, and the Reelfoot fault. A series of subparallel dextral transpressional faults trend N25°-30°E and include the Meeman-Shelby fault, Bootheel fault, and the West Crowleys Ridge fault (Table 1-3).

In our model, we interpret southern Crowleys Ridge as a compressional stepover (Figure 1-13). The orientations of scarps mapped along the margins of southern Crowleys Ridge are parallel to the scarp margin (N10°E), and seismic data indicate faults bound the southern ridge (this study; Van Arsdale et al., 1995). The Axial fault and Blytheville Arch project into the center of the southern part of Crowleys Ridge (Johnston and Schweig, 1996; Pratt et al., 2013) and may offset the ridge laterally by as much as 5 km (Pratt et al., 2013), although evidence for recent offset of landscape features was not observed in the lidar data. Uplift of the Blytheville Arch or movement of the Axial fault over Pleistocene timescales is supported by the alignment of streams at N45°-55°E, parallel to the strike of these structures, which indicates a tectonic influence on the landscape through the Quaternary (Cox, 1988). Notably, the tectonic scarps on the western margin are mostly present to the north of the intersection of the Axial fault, which indicate the fault may also play a role in segmenting faulting along southern Crowleys Ridge.

We interpret central Crowleys Ridge as fault-bounded on its western margin. Although the seismic reflection data and scarp mapping show only down-to-the-west faulting, we speculate that the closely spaced faults with both normal and reverse offset (Van Arsdale et al., 1995) could be indicative of a flower structure. Given that other faults in the NMSZ with similar orientations, such as the Bootheel fault (Guccione et al., 2005) and Meeman-Shelby fault (Hao et al., 2013; Ward et al., 2017), exhibit both dextral and dip-slip movement, it is likely that the West Crowleys Ridge fault is reverse-oblique in slip sense (Stine and Van Arsdale, 2017), but the surficial evidence of dextral movement is poorly preserved or masked by anthropogenic or fluvial activity. Previous studies have indicated that the eastern margin of central Crowleys Ridge is also fault-bounded based on seismic reflection and borehole data (Van Arsdale et al., 1995; Stine and Van Arsdale, 2017). Along the eastern margin, we do not observe scarps at surface and basin elongation ratios would support a tectonically quiescent eastern margin. Offset Quaternary reflectors in seismic reflection data may correspond to part of the Western Margin fault (Van Arsdale et al., 1995) and not necessarily the eastern margin of Crowleys Ridge.

Northern Crowleys Ridge has previously been interpreted as a transpressive flower structure along the Commerce fault (Baldwin et al., 2006). Although we interpret southern Crowleys Ridge as a compressional step-over bounded by the Eastern and Western Margin faults, that does not preclude transpressive movement along the Idalia Hills-Commerce fault at the northernmost end of Crowleys Ridge. Moreover, the orientation and sense of slip of the Commerce fault is similar to the Eastern and Western Margin faults and would likely behave in a similar way in the current central U.S. stress regime.

1.7 Conclusions

We present evidence that Crowleys Ridge is a tectonic landform bounded by late Quaternary active faults based on landscape-scale geomorphic analyses, neotectonic mapping, seismic reflection data, and shallow AEM resistivity data. Geomorphic analyses using modern high-resolution topographic datasets and approaches are consistent with recent tectonic deformation. Neotectonic strip mapping on lidar reveals previously unidentified fault scarps that offset late Pleistocene (<56 ka) geomorphic surfaces. A new seismic reflection and AEM resistivity profiles show faulting that offsets Pliocene-Pleistocene strata and projects near surface scarps mapped on the lidar. The overall rate of deformation is low (<0.2 mm/yr), but evidence for recent (late Pleistocene) surface rupture indicates that Crowleys Ridge may best be incorporated as discrete, independent seismic sources into regional seismic hazard analyses. Our integrated approach demonstrates a way to identify and quantify tectonic deformation in low-strain-rate, high-erosion regions.

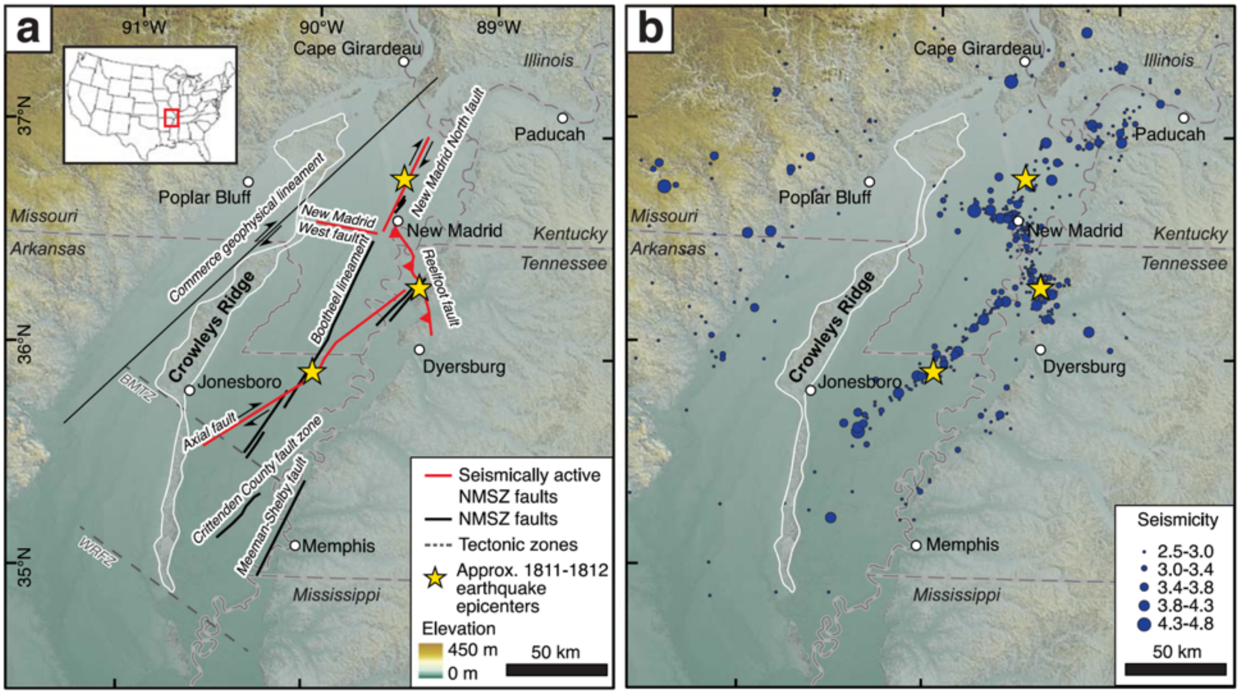

Figure 1-1 **(a) Location map of the New Madrid seismic zone (NMSZ), illustrating major faults and approximate earthquake epicenters of the 1811-1812 earthquake sequence. Inset shows location in central United States. Modified from Delano et al. (2018). (b) Seismicity of the NMSZ from 1900-2019 from the USGS Earthquake Catalog. Crowleys Ridge is outlined in white on both panels. BMTZ – Bolivar Mansfield tectonic zone; WRFZ – White River fault zone.**

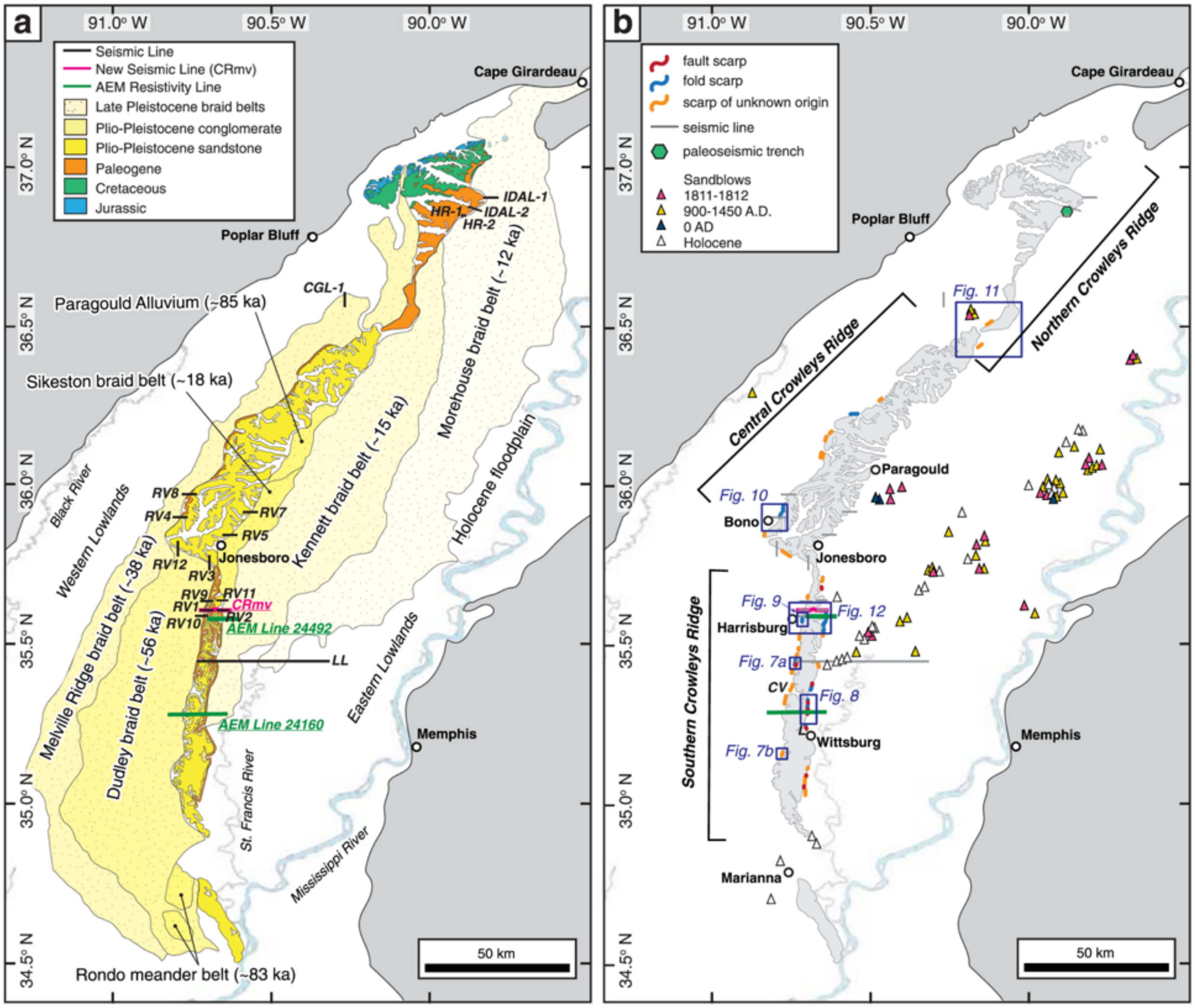

Figure 1-2 (a) Geologic map of Crowleys Ridge, simplified from Haley et al. (1993). Braid belt mapping and ages from Rittenour et al. (2007). Seismic line locations and labels from Van Arsdale et al. (1995), Stephenson et al. (1999), and Baldwin et al. (2006). RV denotes seismic line from Van Arsdale et al. (1995). (b) Scarps mapped along the margins of Crowleys Ridge. Boxes mark locations of detailed scarp mapping in figures. Paleoseismic site along Idalia Hills fault zone from Baldwin et al. (2006). CV – Cherry Valley; L – Levesque. Gray-shaded area represents bluffs and bedrock surrounding the Mississippi embayment (white area).

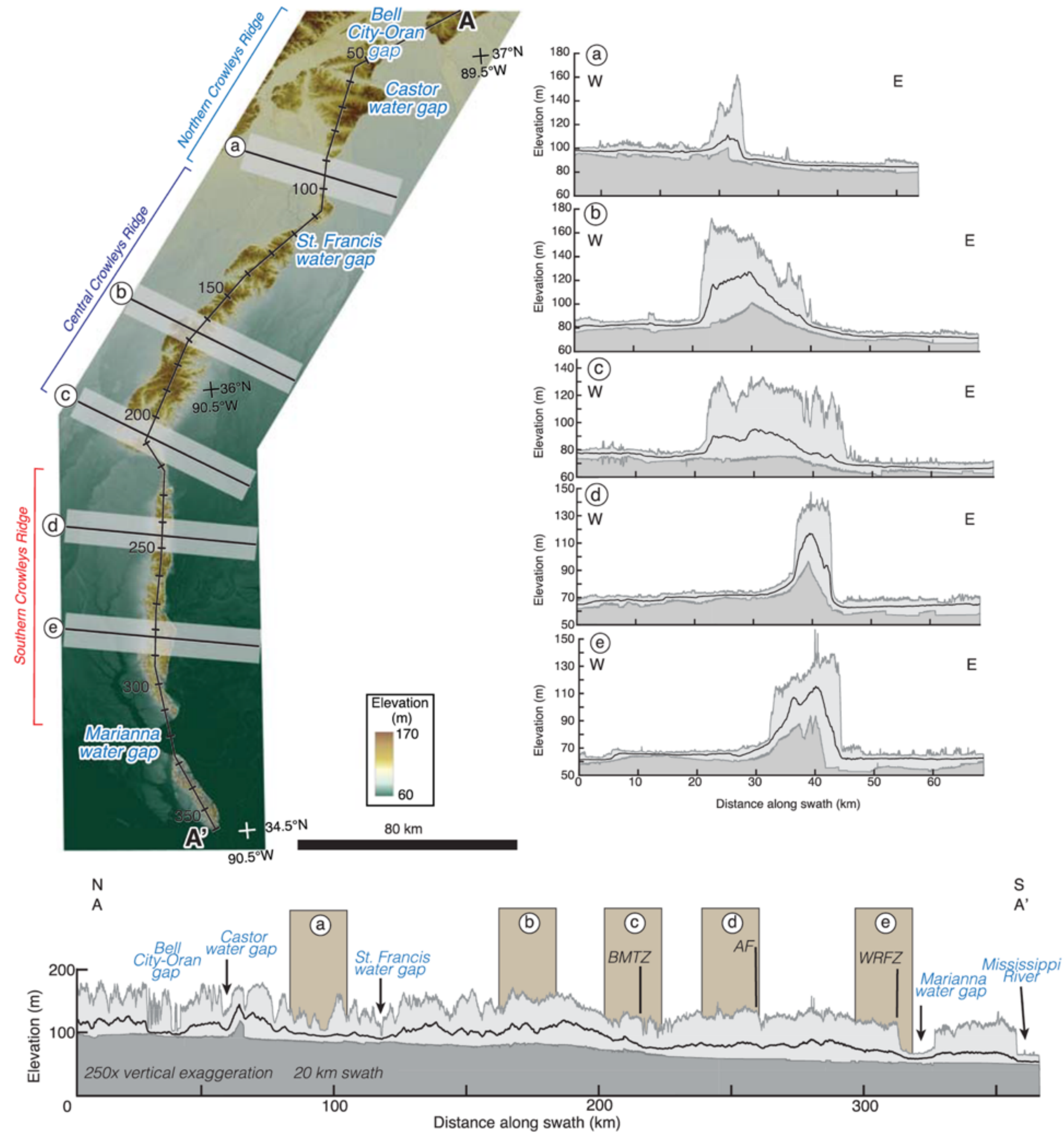

Figure 1-3 **Topographic swath profiles across and along Crowleys Ridge. Swath profiles are extracted from a 10-km window on either side of the profile line, showing minimum (dark gray), mean (black line) and maximum (light gray) elevations within the swath. BMTZ – Bolivar-Mansfield tectonic zone, AF – Axial fault, WRFZ – White River fault zone. Axial fault location is projected from the northeast. Locations of faults shown in Figure 1-1.**

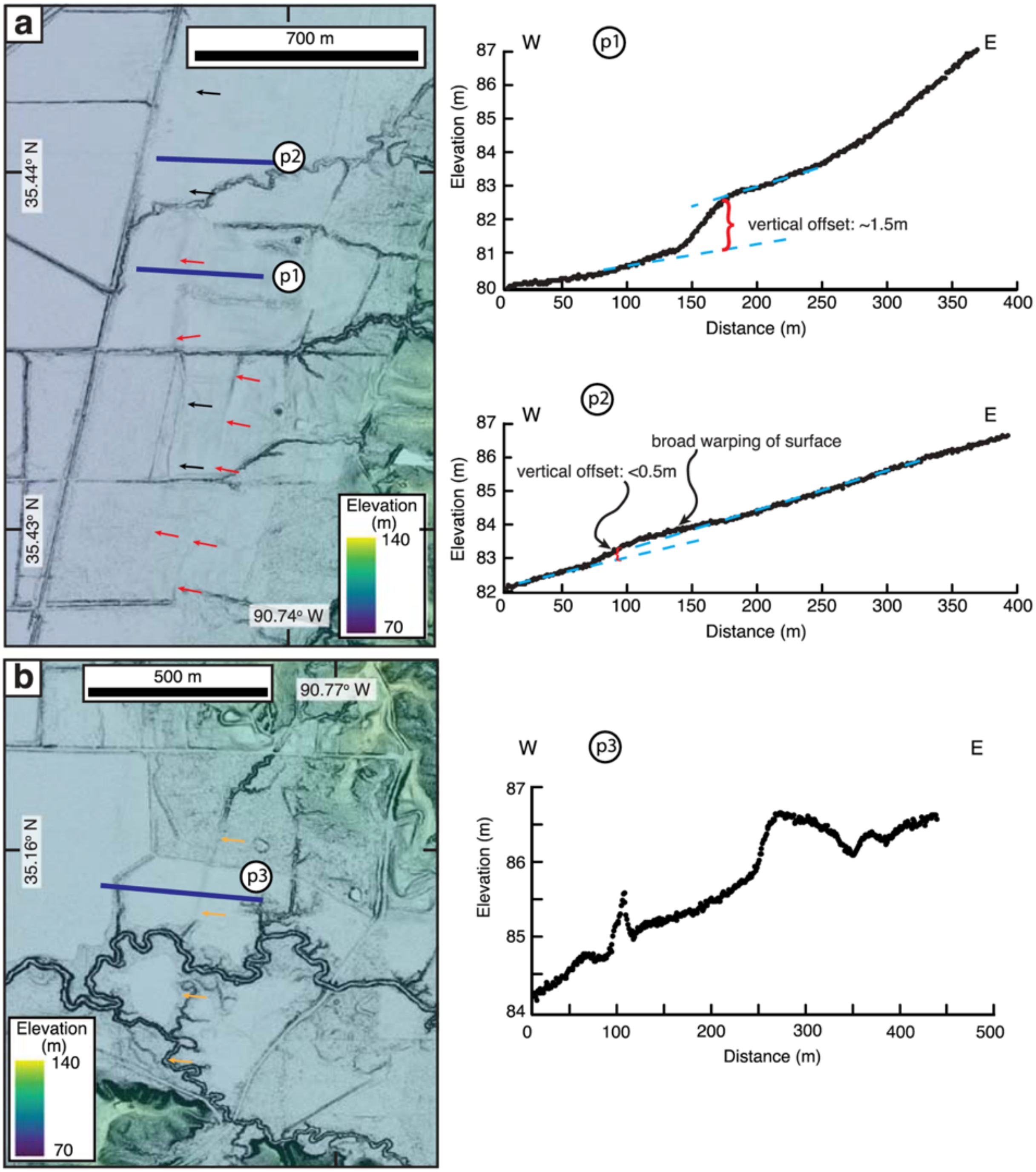

Figure 1-4 Examples of mapped scarps along the western margin of southern Crowleys Ridge. (a) Fault (red arrows) and fold (black arrows). Profile p1 illustrates a sharp discontinuity offsetting a surface with similar slopes above and below the discontinuity. Profile p2 shows a broader warping of the surface. (b) Scarp of unknown origin (yellow arrows), shown in profile p3. Locations shown on Figure 1-2.

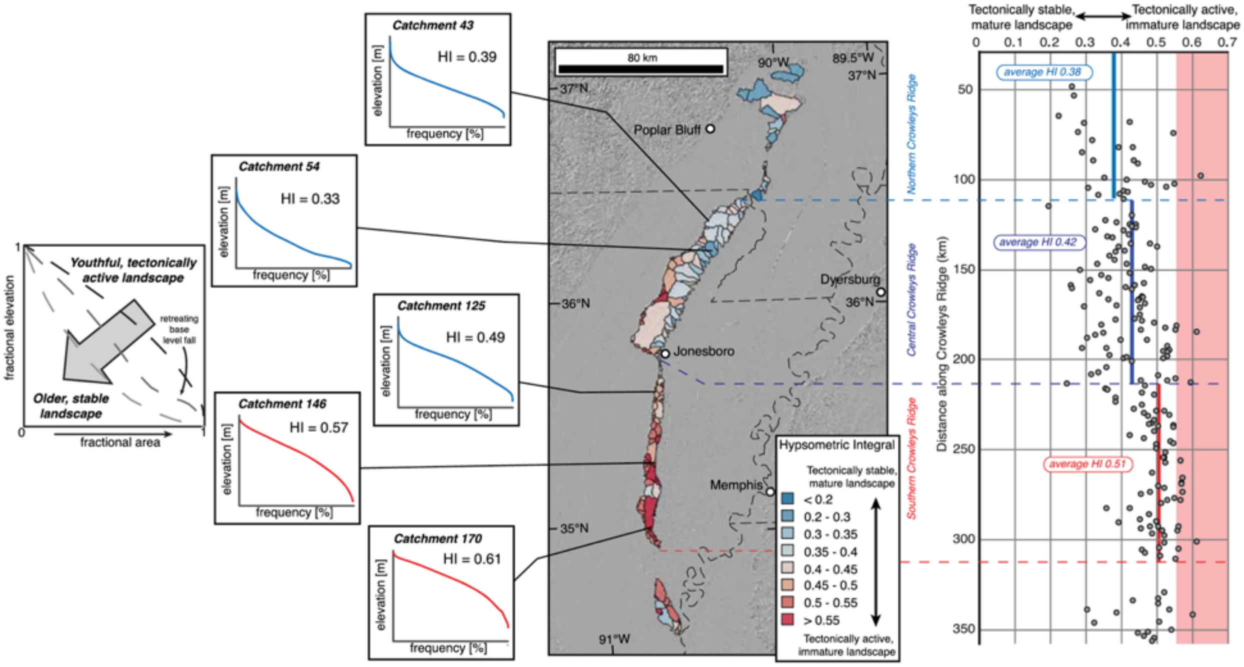

Figure 1-5 Hypsometric integrals (HI) and curves along Crowleys Ridge show evidence for increased tectonic activity from north to south. Right panel illustrates along-ridge variations in HI, with red-shaded area representing HI values that are typically tectonically active. Plots on left show hypsometric curves for five representative catchments, with blue lines representing concave or S-shaped curves of stable or mature landscapes, and red lines representing convex curves of tectonically active or immature landscapes.

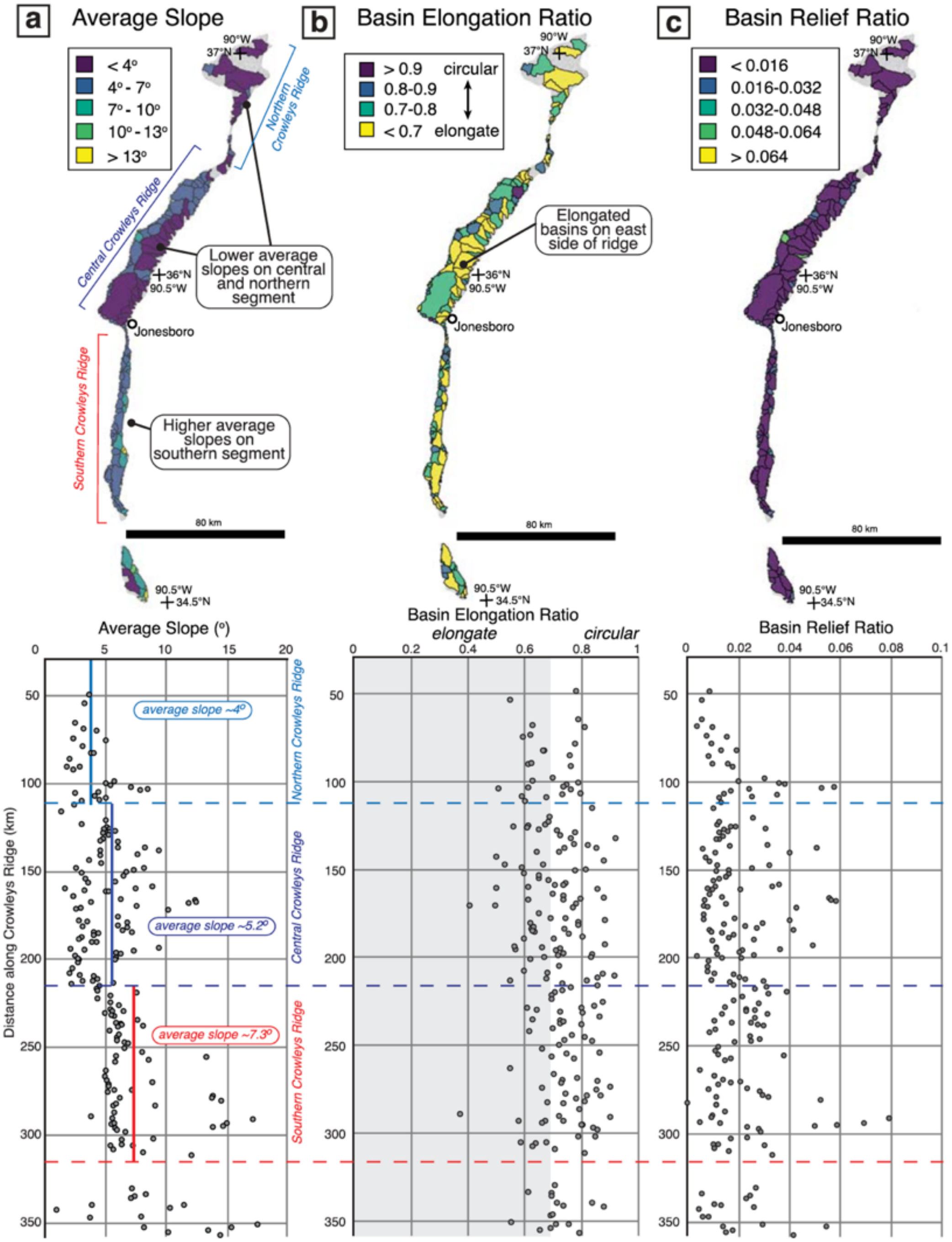

Figure 1-6 (a) Average slope, (b) basin elongation ratio, and (c) basin relief ratio for catchments on Crowleys Ridge. Upper panels illustrate values for each catchment, and lower panels are the same values plotted along the center line. Average slope shows an increase southward along the ridge, illustrated by the average slope for each segment (solid colored lines), whereas the basin elongation and relief ratios do not show a southward increase.

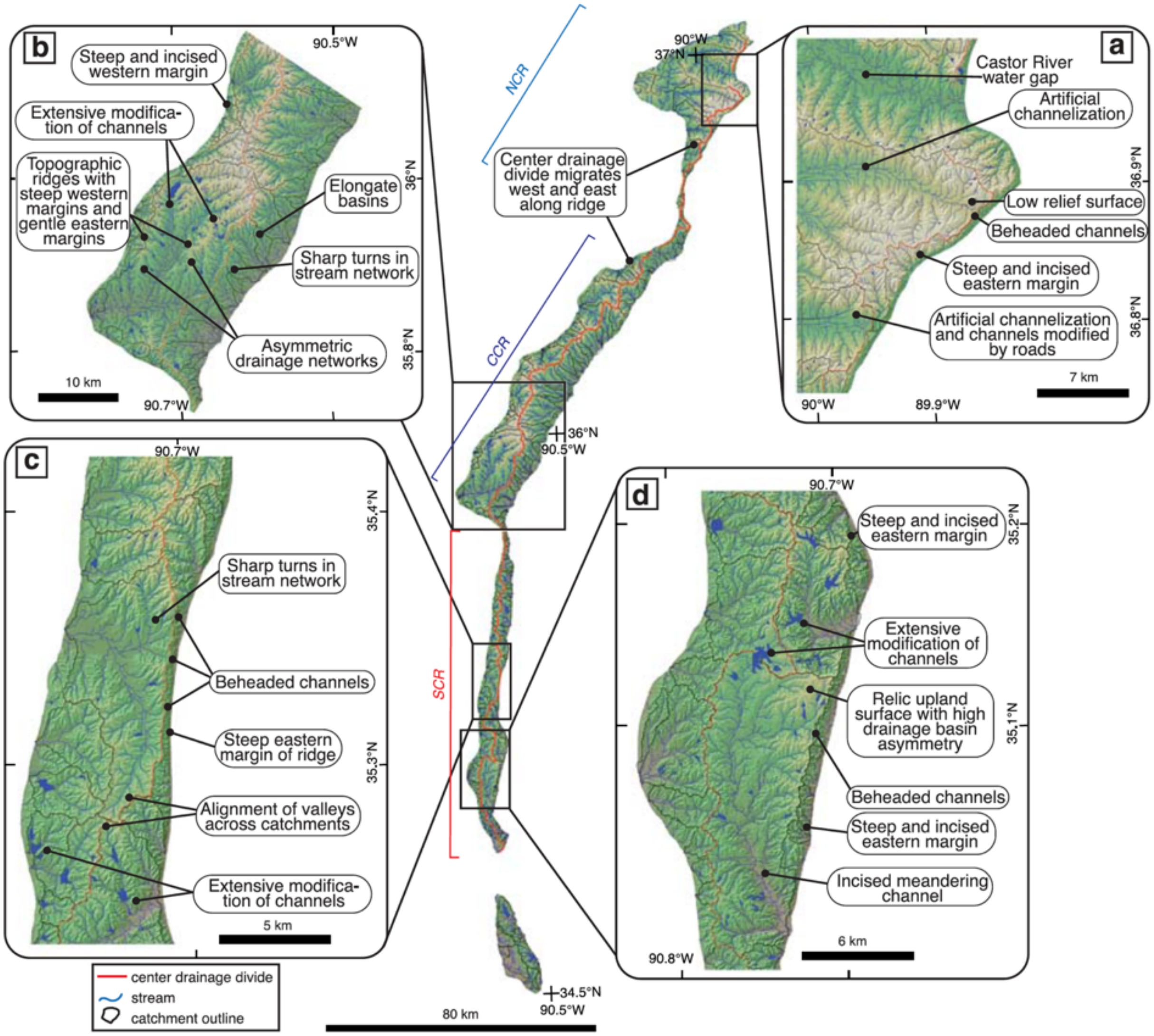

Figure 1-7 **Drainage network and geomorphology at four locations along Crowleys Ridge. (a) northern Crowleys Ridge (NCR), (b) central Crowleys Ridge (CCR), (c) center of southern Crowleys Ridge (SCR), (d) southern end of southern Crowleys Ridge. All locations show extensive anthropogenic modification of the drainage network.**

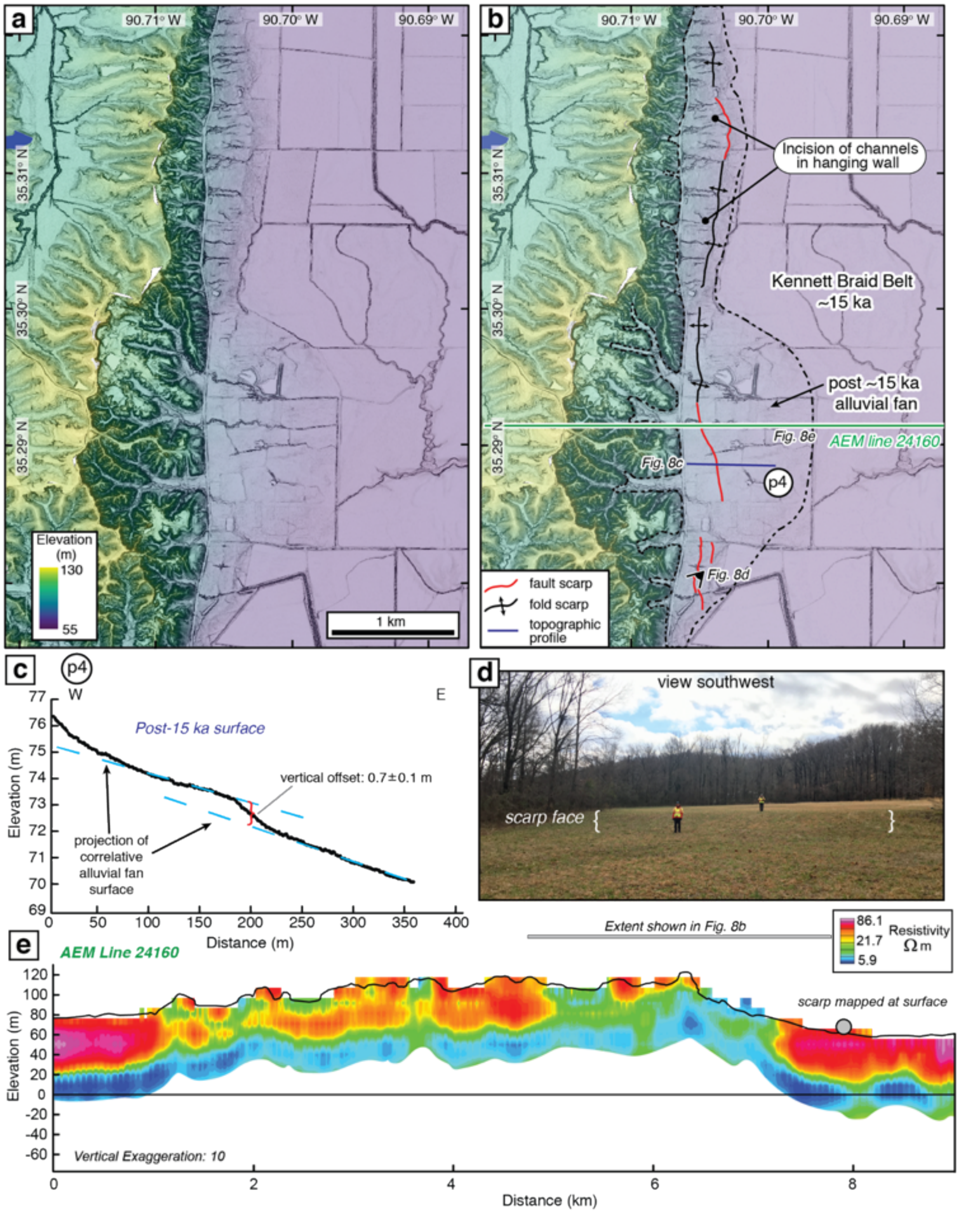

Figure 1-8 (a) Uninterpreted and (b) interpreted lidar digital elevation model (DEM) and slopeshade of the Wittsburg area. Location shown in Figure 1-2b. Age of Kennett braid belt from Rittenour et al. (2007). Dashed line marks extent of alluvial fan surfaces deposited on top of Kennett braid belt. (c) Topographic profile p4 illustrating <1 m of vertical offset of post-15-ka alluvial fan surface. (d) Field photograph of the southern end of the scarps. Location shown in Figure 1-8b. (e) Airborne electromagetic (AEM) profile 24160 across southern Crowleys Ridge close to the southern end of scarps. Topography derived from lidar data. Location of scarp at surface shown on profile by gray dot, which has been projected from north onto AEM profile line. Black dashed lines are interpreted discontinuities and faults on the AEM profile. Location of profile line shown in Figure 1-8b and Table S4 in Thompson Jobe et al. (2020a). Uninterpreted AEM profile 24160 shown in Figure A-2.

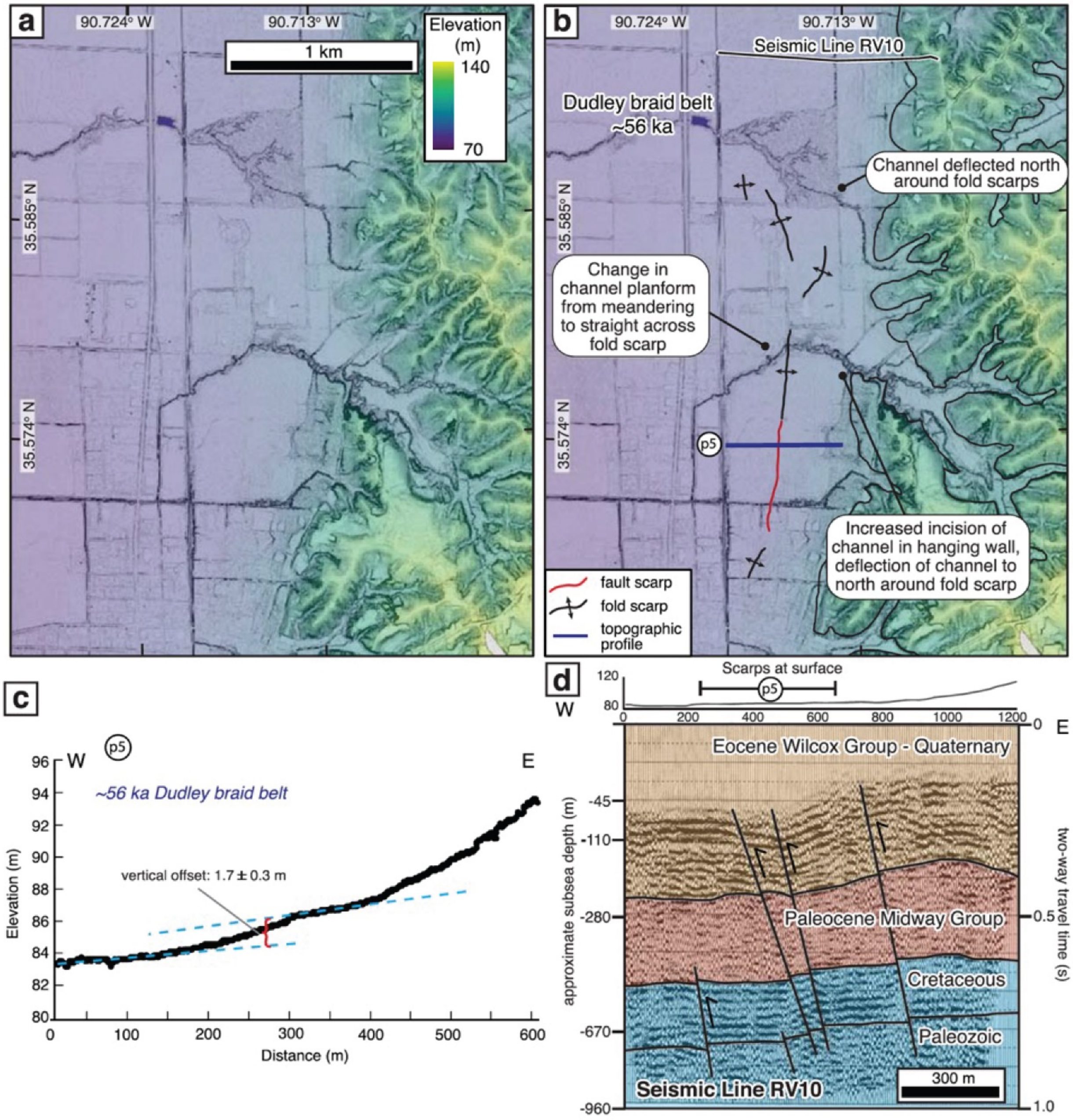

Figure 1-9 (a) Uninterpreted and (b) interpreted lidar digital elevation model (DEM) and slopeshade of the Harrisburg area. Location shown in Figure 1-2b. Age of Dudley braid belt from Rittenour et al. (2007). (c) Topographic profile p5. (d) Reinterpreted seismic line RV10 from Van Arsdale et al. (1995). Location of scarps mapped on the surface are projected north and shown above the seismic line.

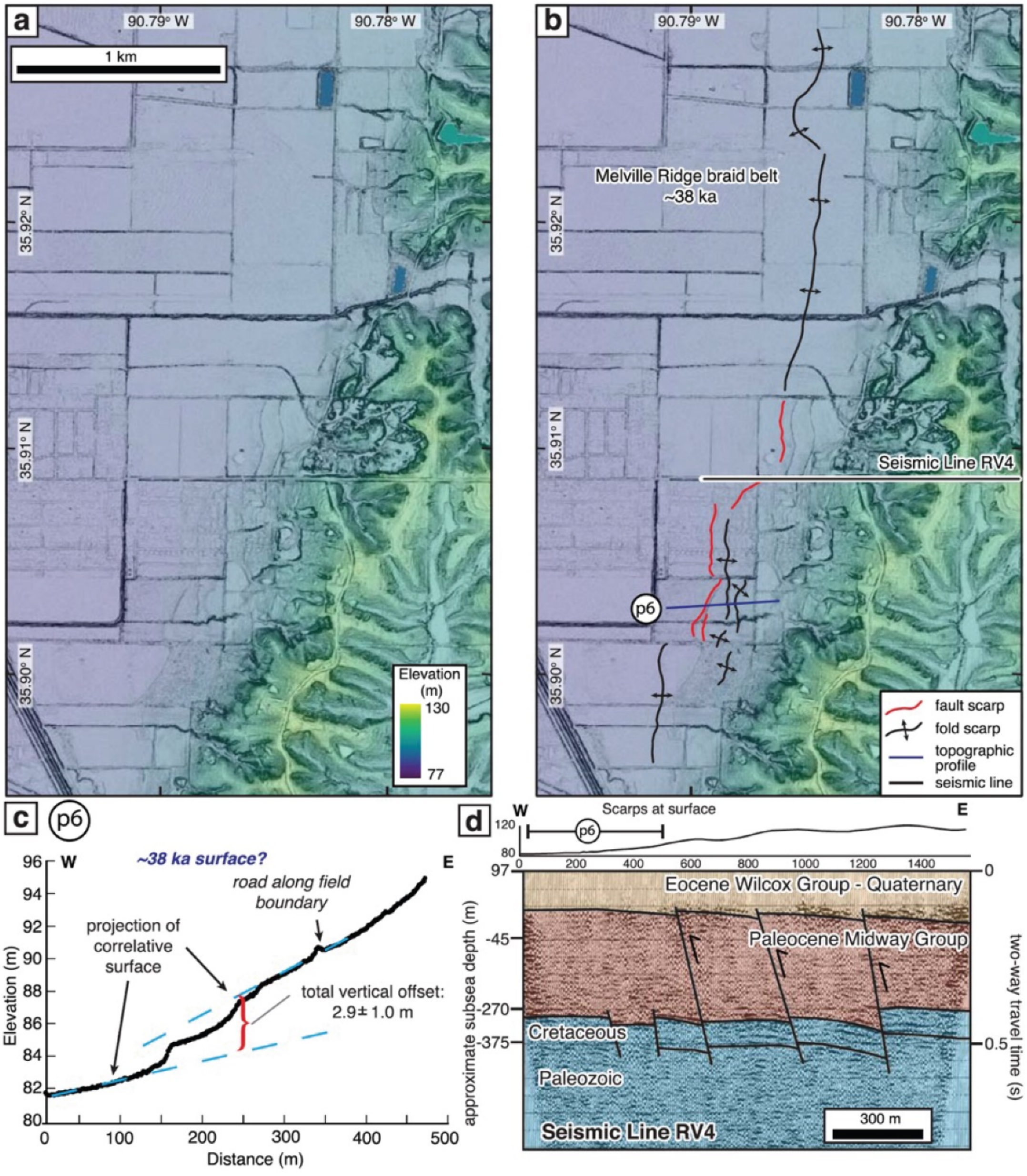

Figure 1-10 (a) Uninterpreted and (b) interpreted lidar digital elevation model (DEM) and slopeshade of the Bono area. Location shown in Figure 1-2b. Age of Melville Ridge braid belt from Rittenour et al. (2007). (c) Topographic profile p6. (d) Reinterpreted seismic line RV4 from Van Arsdale et al. (1995). Location of scarps mapped on the surface are projected from the south.

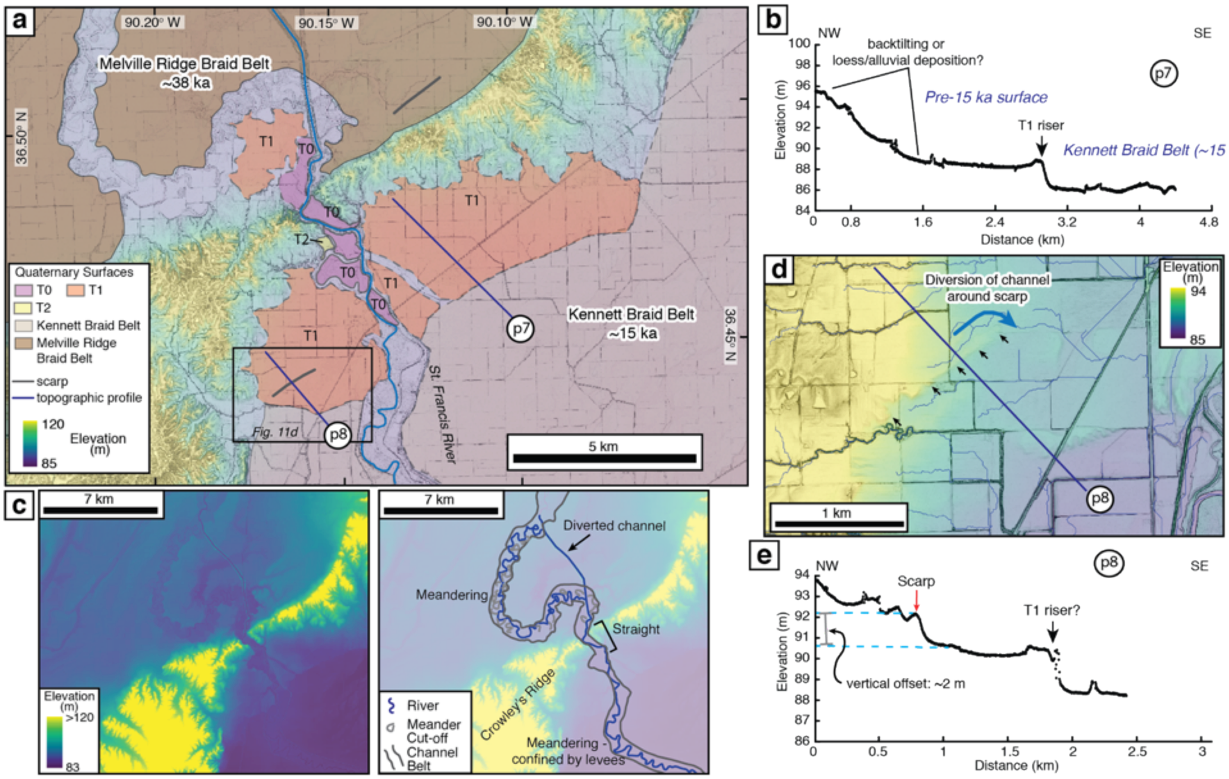

Figure 1-11 (a) Geomorphic map of the St. Francis water gap. Location shown in Figure 1-2b. Age of Melville Ridge and Kennett braid belts from Rittenour et al. (2007). (b) Topographic profile p7 across the pre-15 ka T2 terrace showing 6 m of tilt. (c) Uninterpreted (left) and interpreted (right) geomorphic map illustrating channel planform, which is straighter where the stream passes through Crowleys Ridge, indicating possible tectonic uplift of the ridge. (d) Scarp appears to deflect channel to northeast. (e) Topographic profile p8 across the scarp shown in Figure 1-11d. Apparent vertical offset across scarp is ~2 m.

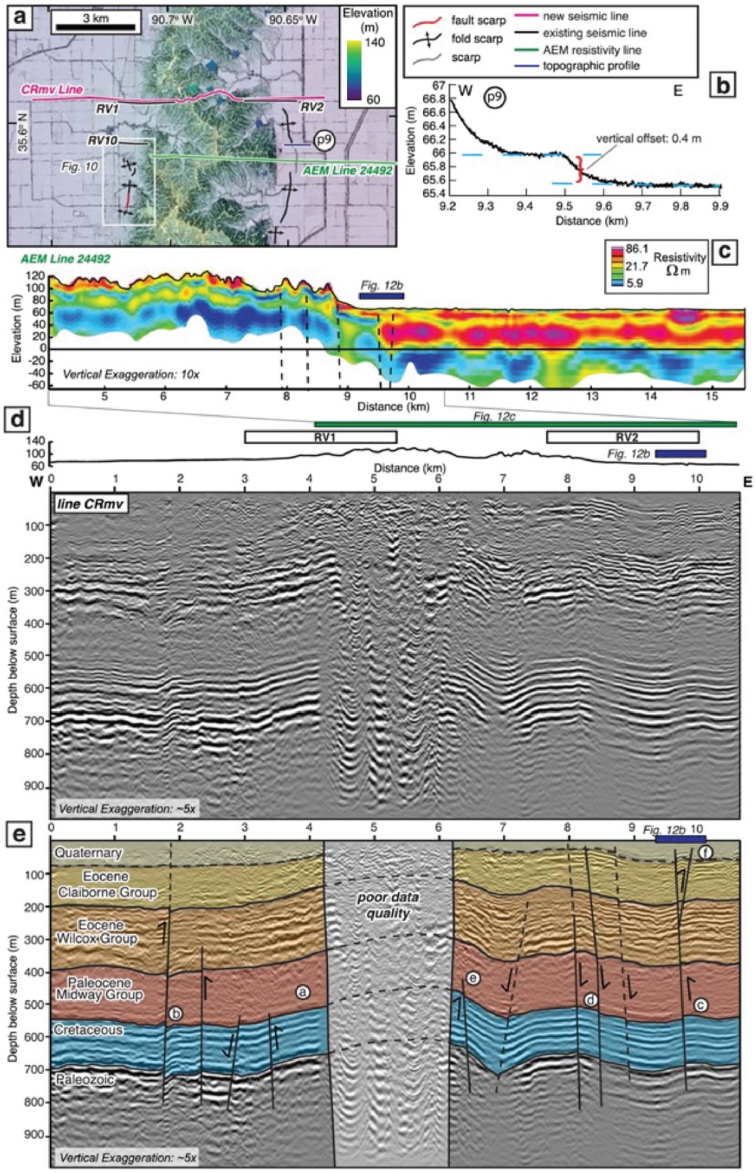

Figure 1-12 (a) Lidar digital elevation model (DEM) of the Harrisburg East site. Location shown in Figure 1-2b. (b) Topographic profile illustrating <0.5 m of vertical offset of ~15-ka Kennett braid belt (Rittenour et al., 2007). (c) Airborne electromagnetic (AEM) profile 24492. Topography derived from lidar data. Black dashed lines are interpreted discontinuities and faults. Location of Figure 1-12b with scarp shown as gray bar. White shaded area is below depth of measurements. Location of profile shown in Figure 1-12a and Table S4 in Thompson Jobe et al. (2020a). (d) Uninterpreted and (e) interpreted seismic reflection data across Crowleys Ridge. Letters on (e) are features described in the text. Location of extent of AEM resistivity profile shown by green bar, and topographic profile of scarp shown by gray bar. Location of seismic line shown in Figure 1-2, Figure 1-12a, and Table S1 in Thompson Jobe et al. (2020a). Uninterpreted AEM profile 24492 and seismic line CRmv shown in Figure A-3 and Figure A-4.

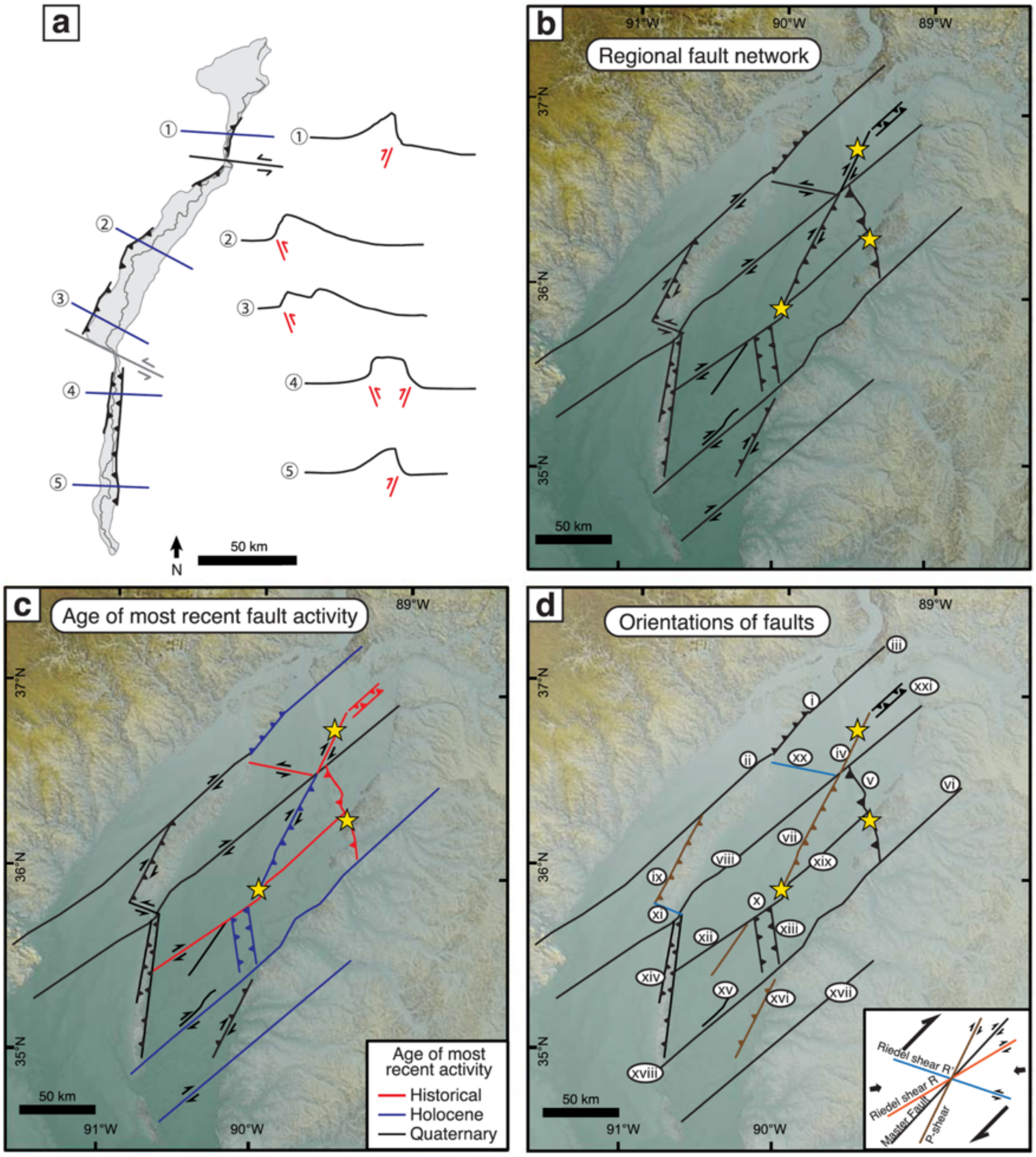

Figure 1-13 (a) Interpreted schematic fault map of Crowleys Ridge, based on surface and subsurface observations. Dark gray line is drainage divide centerline. (b) Regional fault network. Crowleys Ridge is interpreted as a stepover in an overall right-lateral fault zone. Modified from Csontos and Van Arsdale (2008) and Van Arsdale and Cupples (2013). (c) Age of most recent documented fault activity in the New Madrid seismic zone (NMSZ). (d) Orientation of faults in the NMSZ, as compared to an idealized predicted model for fault geometries in an overall right-lateral system. Information for faults can be found in Table 1-3.

Table 1-1 Geomorphic indices analyzed.

Geomorphic index	Equation	Tectonic Interpretation	References
Hypsometric Integral	$\frac{(\text{mean elevation} - \text{minimum elevation})}{(\text{maximum elevation} - \text{minimum elevation})}$	>0.6 = youthful, tectonically active; 0.35-0.6 = mature; <0.35 = older, eroding landscape	Strahler, 1952
Average Slope	Mean slope within a catchment	Higher slopes may indicate higher tectonic activity	Montgomery, 2001
Max Slope	Maximum slope within a catchment	Higher slopes may indicate higher tectonic activity	
Basin Elongation Ratio	$\frac{\text{diameter of a circle with the same area as the drainage basin}}{\text{basin length}}$	<0.6 = tectonically active >0.6 = older, stable landscape	Strahler, 1964; Schumm, 1956; Bull and McFadden, 1977
Basin Relief Ratio[1]	$\frac{\text{basin relief}}{\text{basin length}}$	Higher basin relief ratio may indicate higher tectonic activity	Strahler, 1958; Summerfield and Hulton, 1994

[1] Basin relief is defined as the elevation difference between the highest and lowest points in the catchment (Ohmori, 1993). Basin length is the long axis of the equivalent ellipse of the basin.

Table 1-2 Vertical separation and slip rates[1].

Site Name	Vertical Separation (m)	Age (ka)[2]	Vertical Separation Rate (mm/yr)	Possible fault dip (°)	Slip Rate (mm/yr)
Wittsburg	0.7 ± 0.1	15.1 ± 3.0	0.04 ± 0.01	60 ± 15	$0.05\ ^{+0.04}/_{-0.02}$
Bono	2.9 ± 1.0	38.1 ± 10.8	$0.08\ ^{+0.07}/_{-0.04}$	70 ± 20	$0.09\ ^{+0.10}/_{-0.04}$
Harrisburg	1.74 ± 0.26	56.1 ± 8.5	0.03 ± 0.01	70 ± 20	$0.04\ ^{+0.02}/_{-0.01}$

[1] 6 m of tilt at St. Francis was not included because of uncertainty of vertical separation and lack of subsurface data.

[2] Age of braid belt from Rittenour et al. (2007)

Table 1-3 Summary of faults in the New Madrid seismic zone (NMSZ) region.

Letter	Fault location/name	Fault orientation	Evidence	Most Recent Activity	Reference
i	Idalia Hills – Commerce Fault	N50E-N60E, dextral, flower structure with overall up to west	Paleoseismic trenching, seismic reflection data	Early Holocene (>7.7 ka)	Baldwin et al., 2006
ii	Commerce geophysical lineament	N45E, Dextral oblique, up to west?	Seismic reflection data	Quaternary	Stephenson et al., 1999
iii	Benton Hills – Commerce fault	N45E	Paleoseismic trenching	Holocene (60-50 ka, 35-25 ka, 5 ka, 3660 BP)	Harrison et al., 1999.
iv	New Madrid North fault	N30E, dextral	Seismicity, seismic reflection data, geomorphic mapping, borehole data – geomorphic expression	Historical (1811-1812)	Baldwin et al., 2005
v	Reelfoot fault	N15W	Seismicity, paleoseismic trenching - geomorphic expression	Historical (2350 BC, AD 300, 900, 1450, 1811-1812)	Kelson et al., 1996; Tuttle et al., 2002
vi	Eastern Margin fault	N50E, primarily dextral but also up to west faulting (flower structure?)	Seismic reflection data, cores, paleoseismic trenching	Holocene (2500-2000 BP)	Cox et al., 2006
vii	Bootheel Fault	N24E, dextral oblique (up to east)	Cores – minor geomorphic expression	Holocene (12.5-10.2 ka, 2.7-1.0 ka, AD 1450)	Guccione et al., 2005
viii	Western margin fault	N50E	Seismic reflection data	Quaternary (<19 ka)	Van Arsdale et al., 1995
ix	West Crowleys Ridge fault	N24E	Seismic reflection data, cores, geomorphic mapping	Quaternary (<37 ka)	This study; Van Arsdale et al., 1995; Stine and Van Arsdale, 2017
x	Manilla High	N13W	Cores, geomorphology, geomorphic expression	Historical (11,500-5400 BP, AD 1450 and 1811-1812)	Guccione et al., 2000; Odum et al., 2010

xi	Bolivar-Mansfield fault	N70W	Seismic reflection data	Post-Eocene	Van Arsdale et al., 1995
xii	Marked Tree High		Cores	Holocene (4440-3350 BP)	Guccione et al., 2005
xiii	Joiner Ridge	N10W	seismic reflection data and cores – no surface expression	Holocene (<8.9 ka)	Odum et al., 2010; Ward et al., 2017; Price et al., 2019
xiv	South Crowleys Ridge fault	N10E	Seismic reflection data, geomorphic mapping	Quaternary (<55 ka)	This study; Van Arsdale et al., 1995
xv	Critten County fault	N40E	Seismic reflection data	Quaternary	Crone 1992; Williams et al., 2001
xvi	Meeman Shelby fault	N25E-N33E	Seismic reflection data, cores – no surface expression	Quaternary (<14.3 ka)	Odum et al., 2010; Hao et al., 2013; Ward et al., 2017
xvii	Big Creek-Ellendale fault	N30E	Borehole data, geomorphic expression, seismic reflection data	Holocene (<27 ka, AD 400)	Harris and Sorrells 2006; Velasco et al., 2005
xviii	Eastern Margin fault	N45E	Sand blows	Holocene (7000-5000 BP)	Tuttle et al., 2006
xix	Axial fault	N45E-N55E	Seismicity, seismic reflection data	Historical (1811-1812)	Pratt et al., 2013
xx	New Madrid West fault	N80W	Seismicity	Historical	

2 QUATERNARY REELFOOT FAULT DEFORMATION IN THE OBION RIVER VALLEY, TENNESSEE, USA

This section of text is reproduced from Delano et al. (2021a).

2.1 Abstract

Blind reverse faults are challenging to detect, and earthquake records can be elusive because deep fault slip does not break the surface along readily recognized scarps. The blind Reelfoot fault in the New Madrid seismic zone in the central United States has been the subject of extensive prior investigation; however, the extent of slip at the southern portion of the fault remains unconstrained. In this study, we use lidar to map terraces and lacustrine landforms in the Obion River valley and investigate apparent broad folding resulting from slip on the buried Reelfoot fault. We compare remote surface mapping results with three auger boreholes in the ~24 ka Finley terrace and interpret that apparent warping is due to tectonic folding and not stratigraphic thickening. We combine our results with historical records of coseismic lake formation that indicate surface deformation that dammed the Obion River in the 1812 earthquake. Older terraces (deposited at least 35–55 ka) record progressive fold scarps ≥1 m, ≥2 m, and ≥8 m high indicating a long record of earthquakes predating the existing paleoseismic record. Broad, distributed folding above the Reelfoot fault into the Obion River valley is consistent with a deep active fault tip along the southern reaches of the fault. Our analyses indicate the entire length of the fault (≥70 km) is capable of rupture and is more consistent with longer rupture scenarios.

2.2 Introduction and Motivation

Constraining the source faults of past earthquakes in intraplate settings, such as the New Madrid seismic zone (NMSZ) in the central United States, is key to quantifying seismic hazard (U.S. Department of Energy, 2012; Petersen et al., 2014). The NMSZ most recently produced three M7+ earthquakes during the winter of 1811–1812 (Nuttli, 1973) and at least four other strong shaking events since ~4370 BP (Figure 2-1) (Kelson et al., 1996; Tuttle et al., 2002, 2005, 2019; Holbrook et al., 2006; Gold et al., 2019). Ambiguity in the magnitudes, source faults, rupture lengths, and slip amounts for the 1811–1812 earthquakes is due to both (1) a lack of seismic instrumentation in the region in 1811–1812 and (2) subsequent natural and anthropogenic landscape modification, which obscure geomorphic evidence of faulting and folding. These problems are accentuated for the longer-term earthquake record and hinder traditional paleoseismic investigations, such as fault trenching, in this region. On shorter time scales, multi-decadal regional geodetic observations show near-zero deformation rates (e.g., Calais et al., 2006, Calais and Stein, 2009), which can conceal potential fault activity and further challenge seismic hazard estimates.

The blind Reelfoot reverse fault was one source of the 1811–1812 New Madrid earthquake sequence and is one of the few faults east of the Rocky Mountains with documented Holocene surface expression (Fuller, 1912; Fisk, 1944; Mueller and Pujol, 2001; Russ, 1979, 1982; Van Arsdale et al., 1995). A key outstanding question for NMSZ hazard models is the southern extent of the Reelfoot fault, which has important implications for potential rupture length, slip area, and estimated seismic hazard of the region (Mueller and Pujol, 2001; Petersen et al., 2014). Previous seismological studies recognize modern microseismicity on the Reelfoot fault that extends as far south as Dyersburg, Tennessee (Figure 2-2) (Van Arsdale et al., 1995; Mueller and Pujol, 2001; Greenwood et al., 2016). Evidence of clear coseismic surficial fault deformation has only been observed along the northern extent of the Reelfoot fault near Reelfoot Lake (Van Arsdale et al., 1998; Greenwood et al., 2016) and within the Mississippi River terraces (Figure 2-2) (Holbrook et al., 2006). Farther southeast in the bluffs, geomorphic, geophysical, and geological studies infer broad uplift or slip at depth on the Reelfoot fault in the Tertiary and Holocene but do not identify a fault scarp on the surface (Van Arsdale et al., 1998; Greenwood et al., 2016; Delano et al., 2018; Gold et al., 2019). Near the Obion River (Figure 2-2), sparse observations and inconclusive or conflicting interpretations of surface deformation leave room for debate regarding the southernmost extent of past Reelfoot fault rupture (Rodbell et al., 1997; Van Arsdale et al., 1999).

This study uses newly available airborne lidar to evaluate evidence of fault slip on the Reelfoot fault in western Tennessee (USACE, 2012; USGS, 2014). We combine findings from lidar-derived bare earth digital elevation models (DEMs) and auger-based stratigraphic observations from late Quaternary surfaces with past research and historical records. These data are used to shed light on fault behavior near the southern extent of the Reelfoot fault and to assess the relative contribution of tectonic deformation and climate-driven processes recorded by landforms in the Obion River valley. We interpret the surfaces to record evidence of deformation related to blind slip along the Reelfoot fault in the Obion River.

2.3 Geologic Setting

2.3.1 New Madrid seismic zone

The NMSZ occupies the northern Mississippi embayment spanning northwestern Tennessee, southeastern Missouri, northeastern Arkansas, and southwestern Kentucky (Figure 2-1). The 1811–1812 historical earthquake sequence in the NMSZ is characterized by three main shocks: the first and second earthquakes likely occurred on northeast-striking, right-lateral strike-slip faults (Figure 2-1) (Bakun and Hopper, 2004). The third event on 7 February 1812 occurred on the Reelfoot fault, a southeast-striking reverse fault that accommodates contraction between the two strike-slip faults (Figure 2-1) (Bakun and Hopper, 2004; Pratt, 2012).

Modern seismicity and geophysical surveys indicate that the south-southeast-striking Reelfoot fault extends 60–80 km from approximately 6 km northwest of New Madrid, Missouri, to approximately Dyersburg, Tennessee (Figure 2-2) (Van Arsdale et al., 1999; Greenwood et al., 2016). The Reelfoot fault is commonly split into northern and southern sections, defined by the intersection with the Cottonwood Grove and Ridgely faults (Figure 2-1) (Csontos and Van Arsdale, 2008; Van Arsdale et al., 2013; Greenwood et al., 2016). Previous identification of Quaternary surface deformation along the Reelfoot fault is limited to the northern section of the fault, but preservation is complicated by the migrating Mississippi River. The 1812 earthquake on the Reelfoot fault generated a broad, monoclinal scarp that, together with footwall subsidence, dammed the Reelfoot River, flooded the lowlands upstream, and created Reelfoot Lake (Figure 2-2) (Fuller, 1912; Russ, 1982; Stahle et al., 1992). The fold scarp bounding Reelfoot Lake is typically considered the southernmost extent of surface deformation from the 1812 event on the Reelfoot fault, although the fold scarp may have extended southeast to the bluff margin and has subsequently been eroded (Greenwood et al., 2016).

The southern section of the Reelfoot fault extends southeast from the Mississippi River floodplain margin into a region of elevated, dissected ridges (bluffs) with 35–50 m of relief above the lowlands (Figure 2-1, Figure 2-2a). Prior to this study, evidence for the blind Reelfoot fault southeast of Reelfoot Lake was limited to broader signals of uplift, coseismic sackungen (ridgetop gravitational failures), or folding at depth in seismic surveys. For example, Greenwood et al. (2016) interpret ~6 m of distributed uplift above the Reelfoot fault since ~10 ka from small, abandoned terraces in minor drainages within the bluffs, and Van Arsdale et al. (1999) highlight a local drainage divide that occurs subparallel to the trend, and within the upthrown side, of the southern projection of the Reelfoot fault. Remote mapping studies and trenching investigations of sackungen in the bluffs within 15 km of the Reelfoot fault indicate the southern section of the Reelfoot fault has experienced repeated large earthquakes since 11 ka (Figure 2-2a, Figure 2-3a) (Delano et al., 2018; Gold et al., 2019). Seismic surveys along the bluff margin (Greenwood et al., 2016) and northern edge of the Obion River valley (Van Arsdale et al., 1999) reveal folding in Tertiary sediments within 120 m of the surface (Figure 2-3a). The coseismic sackungen identified in Delano et al. (2018) extend south from the bluff margin to nearly Dyersburg, Tennessee (Figure 2-2a), indicating that recent (<11 ka) movement on the Reelfoot fault extended south of the Obion River valley.

2.3.2 Stratigraphy and geomorphology of the Obion River valley

The Obion River flows westward from the bluffs and enters the Mississippi River floodplain north of Dyersburg, Tennessee (Figure 2-2a, Figure 2-3a). The lower Obion River valley consists of a single, southwest-draining channel; the upper reaches are composed of four smaller tributaries that merge to form the lower Obion River ~35 km northeast of the Mississippi River valley margin. The bluffs flanking the Obion River are underlain by sub-horizontal or gently dipping marine sedimentary Eocene Jackson Formation (Conrad, 1856) and fluvial sand and gravel of the Pliocene-Pleistocene upland complex (Autin et al., 1991). The bluffs are capped by 5–50-m-thick Pleistocene loess derived from successive glacial outwash deposits in the Mississippi River valley (Autin et al., 1991; Rodbell et al., 1997; Markewich et al., 1998). These loess deposits generally decrease in thickness to the east with increasing distance from the Mississippi River valley (Autin et al., 1991; Rodbell et al., 1997). The entire region, both in the valleys and in the bluffs, has long-lived and ongoing agricultural development, such as farming and logging, which has contributed to surface modification since the 1812 earthquake.

Three previously identified terraces in the Obion River valley include the Finley terrace (~24 ka), the Hatchie terrace (older than 35-55 ka), and the Humboldt terrace (pre-Wisconsin), although map depictions of the terraces vary (Saucier, 1987; Rodbell, 1996). These terraces are remapped in this study (Figure 2-3b, Plate 1 in Delano et al., 2021b). An additional older, undated terrace (Henderson terrace) was identified in the adjacent Forked Deer drainage (Figure 2-2) (Saucier, 1987), but it had not been identified in the Obion River valley prior to this study. Three loess deposits in the Obion River valley provide minimum ages for the underlying terraces: the Peoria Loess (10–25 ka) (McKay, 1979; Ruhe, 1983), Roxana Silt (35–55 ka) (Forman et al., 1992; Leigh and Knox, 1993; Rodbell et al., 1997; Markewich et al., 1998), and Loveland Loess (70–120 ka) (e.g., Rodbell et al., 1997; Forman and Pierson, 2002; Markewich et al., 1998). The Finley terrace is mantled by ~2–4 m Peoria Loess, and the Finley terrace abandonment age (~24 ka) was previously constrained by two radiocarbon ages at different locations—charcoal fragments in the overlying Peoria Loess and gastropod shells from the terrace alluvium (Rodbell and Schweig, 1993; Rodbell, 1996). The timing of Hatchie and Humboldt terrace abandonment is constrained by minimum ages from the capping loess deposits—both are mantled Roxana Silt and Peoria Loess, indicating they are both older than 35–55 ka (Forman et al., 1992; Leigh and Knox, 1993; Rodbell et al., 1997; Markewich et al., 1998). Total loess thickness on the Hatchie and Humboldt terraces is spatially variable and poorly constrained; investigations in the Obion River valley did not establish the contact between loess and terrace deposits (Rodbell, 1996; Rodbell et al., 1997).

Terraces in the Mississippi River and Obion River valleys have been interpreted as a series of landforms recording base-level change caused by interrelated processes, including (1) glacio-eustatic variation in sea level; (2) spatiotemporal variation in sediment yield linked to climate change; and (3) regional tectonics, including subsidence (Autin et al., 1991). When viewed in this regional framework, Obion River terraces at the valley mouth may largely record local base-level increase from rapid sedimentation in the adjacent Mississippi River valley resulting in sediment influx and backwater flooding into the Obion River valley (Autin et al., 1991). The observation that each Obion River terrace is mantled by loess from the corresponding Pleistocene glacial retreat (Autin et al., 1991; Rodbell, 1996) provides circumstantial support for the interpretation that lower Obion River terraces are heavily influenced by Mississippi River sedimentation and thus climatically driven changes in local base level (Autin et al., 1991).

Two primary landforms—horizontal-gradient terraces and constructional shorelines—are consistent with pronounced local base-level change at the mouth of the Obion River. It has previously been observed that both the Finley and Hatchie terraces have a near-zero gradient in the lower reaches of the Obion River valley (Saucier, 1987). In addition to the terraces, a series of discontinuous beach ridges were mapped by Saucier (1987) and interpreted as lacustrine shoreline features. The shallow gradient of the Obion river-mouth terraces and shorelines record tributary drowning and lake formation; previously this geomorphic record was interpreted as tied solely to regional base-level changes propagating along the Mississippi River valley (Saucier and Fleetwood, 1970; Saucier, 1987; Autin et al., 1991).

Previous studies also noted that the Finley, Hatchie, and possibly Humboldt terraces have slight reverse gradients near the confluence of the Obion River and the Mississippi River valleys (Saucier, 1987; Rodbell, 1996; Van Arsdale et al., 1999). Here, the terrace elevations deviate vertically from projected river gradients by ~3 m for the Finley terrace (Saucier, 1987; Rodbell, 1996), ~10 m for the Hatchie terrace, and ~12 m for the Humboldt terrace (Rodbell, 1996). These reverse gradients have been interpreted as sediment introduction from the Mississippi River during backwater flooding (Saucier, 1987), a reflection of the regional westward-thickening loess mantle (Rodbell, 1996), or a response to tectonic deformation (Van Arsdale et al., 1999).

In addition to the terrace tread reverse gradients, Van Arsdale et al. (1999) recognized several possible indicators of tectonic deformation in the Obion River valley. A slight reverse gradient in the Holocene floodplain stratigraphy, as interpreted from coring data, might represent broad folding above the blind Reelfoot fault (Van Arsdale et al., 1999). Stream migration vectors and a drainage divide in the surrounding bluffs near the projected trace of the Reelfoot fault are also consistent with distributed tectonic uplift (Van Arsdale et al., 1999). Additionally, the modern Obion River floodplain narrows down valley, which could reflect uplift near the valley mouth (Van Arsdale et al., 1999). Finally, Van Arsdale et al. (1999) noted one historical map (Rhea et al., 1832) that displays a prominent lake within the Obion River valley post-dating the 1812 earthquake on the Reelfoot fault; they suggested that the lake may have formed as a result of river damming from uplift on the hanging wall of the Reelfoot fault, similar to Reelfoot Lake 20–25 km to the northwest. Currently, only portions of the lower Obion River valley flood seasonally and no long-standing lakes exist. The valley floor and river channel, however, have experienced extensive anthropogenic modification over the 20th century, including channelization, widening, dredging, levee creation, and farming (Simon and Hupp, 1992).

2.4 Methods

2.4.1 Geomorphic mapping methods

To more fully explore the hypothesis that the Obion River valley records tectonic deformation (Van Arsdale et al., 1999), we use a combination of lidar-derived DEMs, slope and hillshade maps, and relative elevation models (REMs) to delineate terraces and other landforms. The REM represents elevation as height above the modern Obion River channel and removes elevation changes associated with the modern valley gradient (Olson et al., 2014). The 4-m-resolution REM was generated following the kernel density method outlined in Olson et al. (2014).

Terrace mapping was performed at ~1:10,000 scale (Figure 2-3b, Plate 1 in Delano et al., 2021b). We identify potential terraces by searching for planar surfaces with a gentle slope that contain a scarp at the contact with topographically higher and lower units. Terraces were differentiated by comparing relative tread elevations along and across the Obion River valley, tread elevations above the modern channel, and degree of tread dissection. The mapping extent in this study reaches from the eastern edge of the Mississippi River valley (bluff margin) to the confluence of the major Obion River tributaries ~30 km upstream, where the variable gradients, catchment areas, and discharge complicate terrace formation and preservation. We restrict mapping to the primary Obion River valley and truncate terrace mapping at tributaries on the northern and southern valley flanks.

2.4.2 Topographic analysis methods

To evaluate terrace trends and changes across the length of the lower Obion River valley, we generate valley longitudinal profiles for each mapped unit. We selected the best-preserved locations within each unit by avoiding areas obviously impacted by post-depositional incision, aggradation (e.g., alluvial fan) or anthropogenic modification (e.g., regrading). We then projected these point elevations to a central valley line and plotted the elevations as a function of valley distance upstream (referred to henceforth as “valley distance”) (Figure 2-3, Figure 2-4). Some slight elevation variations within the same unit remain and are caused by incision, alluviation from tributaries, or variation in loess thickness.

We extract 40-m-wide swath elevation profiles from 1-m lidar-derived DEMs using Quick Terrain Modeler to compare the surface expression of the Reelfoot fault monocline along strike (Figure 2-2, Figure 2-5). The final 40-m-wide profile locations were chosen to (1) cross the mapped fault projection approximately orthogonally, (2) minimize effects of post-depositional incision, and (3) avoid anthropogenic alteration such as levees or agricultural regrading. The incised and eroded channel-migration topography leads to uncertainty in which surfaces to reconstruct across the monocline. To better capture this reconstruction uncertainty, we measure vertical separation by repeatedly projecting (~5 times) different combinations of up- and down-thrown surfaces to the scarp midpoint (i.e., DuRoss et al., 2019) (Figure 2-2). This method generates a range of plausible values, as well as a subjective best-fit preferred value, that represent uncertainty caused by several possible reconstructions of surfaces across the fold scarp. The New Madrid and Kentucky Bend profiles (Figure 2-2) in the Mississippi River floodplain, as well as Profiles X and Y on the Hatchie and Finley terraces (Figure 2-5), are drawn orthogonal to the surface projection of the Reelfoot fault trace. Profile Z on the Deweyville A terrace is projected to a line orthogonal to the mapped fault projection, to account for surface modification by a modern levee. We did not include profiles from the Humboldt and Henderson terraces because they either do not cross the surface projection of the Reelfoot fault or are too incised to reveal meaningful values.

2.4.3 Borehole methods

In March 2018, we collected sediment from three 6- to 7-m-deep hand-auger boreholes on the Finley terrace at the Wilson Loop (WL), Lanesferry (LF), and Biggs' Farm (BF) sites (locations in Figure 2-5b). The goal of this limited borehole transect was to determine how subsurface stratigraphy changes across the Reelfoot fault monocline by tracking the loess thickness and underlying contact with the alluvium. We targeted sites along a profile nearly orthogonal to the monocline trend and chose three borehole locations to best capture the apparent inflection in the Finley terrace surface. Specific sites were chosen based on minimal post-depositional incision, low anthropogenic modification (such as significant regrading), and accessibility. We recovered each 20-cm boring increment from the soil auger bit, tracked depths for each increment, and examined sediment in the field. We estimate the uncertainty in depths as half the length of the soil auger bit, or ~10 cm. We made field observations of grain size, Munsell color, texture, structure, soil development, mineral deposits, moisture, and presence of organic/biological material as a function of depth. We also collected samples for additional analyses every 20 cm. We performed grain size analysis on 50 samples using a Malvern Mastersizer 3000. Samples were treated with hydrogen peroxide to remove organics and treated with sodium hexametaphosphate as a deflocculant. We quantified the relative percentages of each Wentworth grain size class (Wentworth, 1922). Complete field observations and analysis results of each auger site can be found in Tables S1–S7 in the companion data repository (Delano et al., 2021b) and Fig. S1 in Delano et al. (2021a).

We attempted to identify mineralogical changes with depth using smear slides under a petrographic microscope, but the mineralogy between the loess and underlying alluvium is nearly identical, as found by previous studies (Snowden and Priddy, 1968). However, we note a sharp increase in carbonate content at 4.0-m depth in all three boreholes. We attribute this change in mineralogy to the pedogenic transition from carbonate leaching to carbonate precipitation, rather than a depositional change, consistent with observations of Snowden and Priddy (1968) at the same depth (13 feet). We also attempted to investigate potential changes in freshwater diatoms between the loess and terrace alluvium. Although the modern floodplain deposits contained freshwater diatoms, the samples retrieved from the boreholes did not preserve diatoms sufficient to use in this stratigraphic analysis (Tina Dura, Virginia Polytechnic Institute and State University, written comm., 2018).

Identifying stratigraphic changes and contacts within the loess and alluvium is complicated by the fact that (i) loess is typically fairly homogenous silt, (ii) alluvium in this low-energy environment is predominantly silt and likely contains reworked loess, (iii) the upper ~0.5 m is disturbed by plowing and other activity, removing near-surface structure, (iv) the high water table masks subtle features such as soil structure. We expect loess should be nearly all silt-sized grains, with potentially some finer-grained material in the near-surface due to soil processes, whereas alluvium could be a mix of bedded clay, silt, and sand. Below, we summarize the observations and identify the most probable contact location using combined observations of subtle changes in grain size, color, structure, and macrofossils. At all three sites, grain size was the primary distinguishing feature between deposit types with additional changes recorded in the other characteristics. In some instances, characteristics other than grain size (such as color, structure, or fossils) were used to infer a contact because they heavily imply a change in depositional environment, even when grain size remained relatively uniform. Because grain size samples were collected at ~20 cm (and occasionally larger) intervals, we use changes in Munsell color and stratigraphic observations (e.g., appearance of laminations or fossils) to estimate contact placement between sample locations and corresponding changes in grain size.

2.4.4 Dating methods

We performed accelerator mass spectrometry (AMS) radiocarbon dating of the snail shells to determine the age of the terrace sediment at the USGS Radiocarbon Laboratory in Denver, Colorado. The clean, dry gastropod shells were broken and examined under a dissecting microscope to ensure that the interior whorls were free of secondary carbonate and detritus. Next, shells were bleached with 30% H_2O_2 to remove organic matter and etched with dilute HCl to remove 30-50% of the total mass prior to hydrolysis (H_2O_2/HCl). Shell carbonate was then converted to CO_2 using American Chemical Society (ACS) reagent grade 85% H_3PO_4 under vacuum at 80ºC until the reaction was visibly complete (~1 hr). Water vapor and other contaminant gases (including SOx, NOx, and halide species) were removed from the sample CO_2 by precise cryogenic separation at -140°C using a variable temperature trap capable of holding temperatures to within 1–2°C of the desired target. The resulting purified CO_2 gas was measured manometrically, converted to graphite using an iron catalyst and the standard hydrogen reduction process (Vogel et al., 1984), and submitted for AMS 14C analysis. We calibrated the radiocarbon ages using Calib v8.2 (Stuiver et al., 2021) and the IntCal20 calibration curve for terrestrial samples (Reimer et al., 2020). Calibrated ages are presented at the 95% (2-sigma) confidence level.

2.5 Results

2.5.1 Fluvial terraces

We mapped the Holocene floodplain, five progressively older terraces, and a series of beach ridges in the Obion River valley (Figure 2-3b, Plate 1 in Delano et al, 2021b). Terrace names are primarily derived from previous mapping within the Obion River valley by Saucier (1987) and newly mapped terraces (e.g., Deweyville Complex and Henderson terrace) are named after equivalent terraces mapped in other nearby drainages. Elevations from the DEMs are reported relative to North American Vertical Datum of 1988. We mapped the following terrace units, listed youngest to oldest: Holocene floodplain (Qa), Deweyville Complex (Qtdb and Qtda), Finley terrace (Qtfi), Hatchie terrace (Qtha), Humboldt terrace (Qthu), and Henderson terrace (Qthe). First, we present results of mapping and boreholes along the Finley (Qtfi) terrace because it provides the clearest evidence for tectonic surface deformation near the mouth of the Obion River valley. We then present mapping and evidence from other terraces from youngest to oldest.

2.5.1.1 Finley Terrace

The Finley terrace surface (Qtfi) is minimally dissected and has distinct, sharp risers (Figure 2-3). At the western edge of the Obion River valley, the Finley terrace tread is 5–8 m above the modern floodplain but gradually decreases in relative height to 1–2 m above the modern floodplain at valley distances >15–18 km (Figure 2-4). The Finley terrace tread does not display migrating channel morphology, such as scroll bars or oxbow lakes, which likely reflects burial by Peoria Loess (Rodbell, 1996). In longitudinal profile, the Finley terrace surface has a reverse (northeast) gradient of 1.4 m/km (0.08°) from 0–3 km up the valley (Figure 2-5), a slight reverse gradient of 0.4 m/km (0.02°) at valley distances 3–10 km, a near-horizontal gradient at 10–24 km valley distance, and parallels the modern floodplain and channel gradient (0.4 m/km [0.02°] to the southwest) at valley distances >24 km (Figure 2-4).

2.5.1.1.1 Wilson Loop (WL) soil auger borehole and subsurface stratigraphy

The Wilson Loop (WL) auger site extended to 6.8-m depth and is the westernmost of the three boreholes on the Finley terrace surface (see Figure 2-5b for location and Figure 2-6 for description). At depths 0–3.50 m in the WL borehole, the largest grain size percentage is medium silt. Sediment grain size is uniform from the surface to 3.5-m depth: the clay, very fine silt, and fine silt fractions decrease slightly with depth and the medium silt and coarse silt increase slightly with depth, consistent with dust infiltration and pedogenesis at the modern surface, but otherwise the grain size is consistent and dominated by medium and coarse silt. Sand is absent from 0–3.5 m except for the upper 1.5 m, which includes <1.5% disseminated medium and coarse sand.

Below ~3.5 m the sediment becomes much more heterogeneous in grain size. There is a slight increase in medium sand at 3.50 m, and a second small 0.5–1% spike in medium, coarse, and very coarse sand at 4.00 m. From 4.00–5.80-m depth, grain size percentages are more variable, do not consistently increase or decrease with depth, and the largest grain size percentage is coarse silt. At ~5.80-m depth, the coarser fractions increase, and the largest percentage is fine sand sized. From 6.00–7.00 m, the largest grain size percentage returns to medium and coarse silt with moderate amounts on clay, very fine silt, and fine silt.

We encountered a disturbed layer extending from the surface to ~0.45-m depth that exhibits a browner color than the auger samples below, which we interpret as the modern disturbed layer or depth of plowing. Below the disturbed layer to 3.65-m depth, the sediment has relatively homogenous color accompanying the massive texture. Colors fluctuate and grade below ~3.65 m, with prominent darker brown horizons near 3.65–3.95 m and 5.65–6.00 m that may represent periods of relative surface stability and incipient soil formation. From 3.65–5.35 m, weak horizontal banding 1–3-mm thick is pervasive and visible as subtle color changes. Notably, at 6.70–6.85-m depth, the auger sample colors transitioned to gleyed (anoxic), rather than the varying shades of reddish, grayish, or yellow-brown (oxidized) seen elsewhere in the auger hole. Because this color transition to gleyed is accompanied by a substantial clay fraction in borehole LF, we interpret this color change as recording a substantial change in depositional setting rather than a modern groundwater signal.

Our preferred interpretation for the location of the loess-alluvium contact at the WL site is at ~3.65-m depth below the terrace tread (Figure 2-6 and Figure 2-7) based on the appearance of sand fractions between 3.50 and 4.00 m as well as prominent changes in texture, color, and banding observed in the field. Above ~3.65-m depth in borehole WL, the sediment is very homogenous in grain size and color, whereas below ~3.65 m the borehole exhibits substantial variability in texture, color, and banding. Variation in color corresponds to shifts in grain size below ~3.65 m in borehole WL. If the transition from loess to alluvium is interpreted on grain size alone, an alternative contact is near 5.6-m depth, where a substantial increase in very fine and fine sand is observed (Figure 2-6). We think this interpretation is unlikely for reasons that incorporate observations from all three boreholes, listed in Alternative Interpretation of loess-alluvium contact, Section 2.5.1.1.4, below. We interpret the massive, stiff, silt-dominated material at the bottom of the borehole (6.3–7.0 m) as lacustrine deposits, which is anoxic (gleyed) at depth and oxidized near a paleosurface in which a soil was formed and subsequently buried.

2.5.1.1.2 Lanesferry (LF) soil auger borehole and subsurface stratigraphy

The Lanesferry (LF) borehole extended to a depth of 7.0 m and was collected from a ditch ~0.3 m below the terrace tread elevation. Similar to the other two boreholes, the grain-size distribution is homogenous in the topmost ~4.20 m of the borehole, with the highest grain size fraction of medium silt. The upper 2.0 m has a slightly higher (0.5–2%) concentration of disseminated fine and medium sand than the underlying stratigraphy. The clay fraction decreases gradually with depth, and the medium and coarse silt fraction gradually increases with depth until 4.30 m, consistent with dust infiltration and incipient soil formation in the modern surface. From 4.30–6.10 m, grain-size percentages fluctuate but generally there are higher percentages of clay, very fine silt, medium silt, and sand fractions than the upper 4.30 m. From 6.10–7.0 m, grain sizes generally fine with depth before an abrupt change to dominantly clay at 7.0 m which prevented further augering.

Below the modern disturbed layer extending to 0.65-m depth, the auger profile color is homogenous light brownish gray and light olive gray with mottled oxidation. The color darkens to grayish brown near ~5.20 m, darkens further to olive brown near 6.10 m and dark gray near 6.70 m, and exhibits gley (anoxic conditions) below 6.80–6.90 m. The color change at 6.10 m coincides with a textural change from (i) variable, fluctuating grain sizes with sporadic laminations and mottled oxidation to (ii) stiff, massive silt and clay with no visible texture (such as laminations) and little to no oxidation until the bottom of the borehole.

Between 4.20 and 5.20 m, we observed small gastropod shells with the densest concentration between 4.20 and 4.35 m (Fig. S1 in Delano et al., 2021a) as well as small, white, precipitated tubes that are interpreted as burrow casts. These were the only shells observed and the only datable carbon material recovered in any of the three auger holes. The gastropod shells were identified as *Pomatiopsis lapidaria* (Jeff Pigati, U.S. Geological Survey, written comm., 2018), a freshwater amphibious (quasi-terrestrial) snail species typically found in flooded riparian forests. The LF site is the closest of our three sites to core OP-21 from Rodbell and Schweig (1993), which was collected from the same Finley terrace surface (Figure 2-5b). Rodbell and Schweig (1993) noted gastropod shells at 4.07–4.40-m depth in the OP-21 core only, although the species was not identified. Other snail species have previously been identified in this region in the Peoria Loess within the bluffs, which caps the Finley terrace, but these are purely terrestrial snails that live in drier environments rather than the semi-aquatic species found here (Pigati et al., 2015). The presence of *Pomatiopsis lapidaria* indicates that the sediment at ~4.20–5.20-m depth was deposited in a wetter, fluvial environment rather than as loess, which drains very well. As noted above, carbonates appear to be leached above 4.00-m depth, which could prevent snail shell preservation at this site (Snowden and Priddy, 1968). However, because we identified snail shells beginning at 4.20-m depth, and snails were discovered nearby at 4.07-m depth (Rodbell and Schweig, 1993), we interpret the appearance of shells as a stratigraphic contact rather than a carbonate leaching boundary. Notably, the first prominent grain-size change occurs slightly below the occurrence of these snail fossils at ~4.30 m rather than at ~4.20-m depth.

The *Pomatiopsis lapidaria* shells (Table 2-1) yielded a calibrated radiocarbon age of 24,457–23,782 cal yrs BP (95% confidence, median probability 24,052 cal yrs BP). The radiocarbon age from Rodbell and Schweig (1993; Table 2-1) is calibrated here to 26,372–25,598 cal yrs BP (95% confidence, median probability 25,905 cal yrs BP). Gastropod shells can yield radiocarbon ages that are slightly too old due to incorporation of old carbon from carbonate rocks or sediment, although the snail taxa previously studied in the Peoria Loess typically incorporate only small amounts of old carbon (1–5%) (Pigati et al., 2015). Although *Pomatiopsis lapidaria* carbon incorporation has not been studied, we assume a similar accuracy to within a few hundred years.

We interpret the most likely depth of the loess/alluvium contact to be ~4.20 m (~4.5 m below terrace tread) (Figure 2-6 and Figure 2-7), based on the appearance of floodplain snail species followed by a pronounced shift in grain size distributions from consistently medium silt to 4.20-m depth to more variable grain sizes and ultimately clay 0.1 m below 4.20 m. The presence of the flooded riparian forest snail species *Pomatiopsis lapidaria* adds robustness to the interpreted location of the loess-alluvium contact at the LF site. We identify a transition to fine grain sizes below 6.10 m and interpret this material as a lacustrine deposit, which is oxidized closer to the paleosurface and not oxidized at depth (gley) (Figure 2-6 and Figure 2-7).

2.5.1.1.3 Biggs' Farm (BF) soil auger borehole and subsurface stratigraphy

The BF borehole extended to 6.8-m depth and is the easternmost of the three boreholes. The shallow sediment recovered from the BF borehole (0–0.3 m) shows the highest percentage of sand found at any depth of the three auger sites (11% medium sand at 0.30 m). We interpret this sand as late-stage flood deposits on the Finley surface, presumably after most of the surface had been abandoned and covered with eolian silt. This sand may have originated from the nearby Biffle Creek, a tributary to the Obion River (Figure 2-5a), or possibly from nearshore reworking of Obion Lake recorded by Crockett (1834) and Lyell (1849), although the extent of that lake is uncertain and no clear diagnostic bedforms could be recovered from the auger. Rodbell (1996) also noted relatively high percentages in sand near the surface at nearby core OP-21 (Figure 2-5), which was attributed to possible coseismic sandblows. Between 0.30- and 3.80-m depth, the largest grain size percentage is medium silt with moderate clay and fine silt but virtually no sand (Figure 2-6). The coarse silt and very fine sand fraction gradually increase with depth while the clay, very fine silt, and fine silt gradually decreases with depth over this section, consistent with other auger sites. At 3.80-m depth, there is a lens with high concentrations (~40%) of clay. Below 3.80-m depth, the grain size fractions fluctuate, but on average, grain size decreases from 3.8 m to the bottom of the borehole at 6.8 m. The lowest sample at 6.60 m is dominated by clay (Figure 2-6).

Sediment collected from the BF borehole was examined in low-light conditions; therefore, observations of color were more uncertain and apparently uniform at this site than the other two auger sites. We repeated Munsell color observations upon returning from the field within two days, but the colors reported here may represent some oxidation that occurred in the days following sample collection.

The topmost layer (to 0.55 m depth) is disturbed, likely from plowing, and is olive brown (Figure 2-6). Below the disturbed layer, recovered sediment becomes mottled and lightens to light brownish gray (0.55–1.20 m). This layer displays intermittent sand lenses associated with the mottled sediment that is lighter in color than the average unit color. At greater depths, the sediment color is typically light yellowish brown (1.2–6.25 m) and darkens slightly to light olive brown near the base of the bore hole (6.25–6.80 m) (Figure 2-6). Importantly, we noted a slight soil textural change near 3.85-m depth that coincided with a change in oxidation mottling in the field (Table S7 in Delano et al., 2021a). Auger sample texture is fairly homogenous and massive from 1.20–4.63 m but shows intermittent liquefied sand lenses below 4.63 m.

We interpret the loess/alluvium contact of the BF borehole at ~3.80-m depth (Figure 2-6 and Figure 2-7), which coincides with a sharp increase of clay, very fine silt, and sand fractions, a decrease in silt-sized grains, and marks the top of a sequence where grain sizes fluctuate. This depth approximately coincides with a field-identified change in texture and prevalence in oxidation mottling at 3.85 m (within auger depth uncertainty). We interpret a relatively abrupt fining grain-size trend near ~5.6 m as a possible contact between alluvium and soil-capped lacustrine deposits, although the contact may be gradational (Figure 2-6 and Figure 2-7).

2.5.1.1.4 Alternative interpretation of loess-alluvium contact

Here, we explore the alternative interpretation that the loess-alluvium contact is deeper in some boreholes based on the observed shift to a relatively coarser grain size (from medium-silt-dominated above to very-fine-sand-dominated below). This scenario implies the loess-alluvium contact across the auger transect occurs at ~5.6 m (WL borehole), ~5.8 m (LF borehole), and ~3.8 m (BF borehole) below the terrace surface from west to east. However, this interpretation requires that we ignore other indicators of depositional environment such as color, texture, and the presence or absence of *P. lapidaria* fossils. Several observations are at odds with the interpretation that the loess-alluvium contact is deeper. First, in the LF borehole, this coarser horizon is clearly below the appearance of the flooded riparian forest snail species *P. lapidaria*. We find the appearance of *P. lapidaria* compelling evidence of the abrupt environmental change accompanying the loess-alluvium transition. Second, we observe a prominent anoxic gleyed silty clay or stiff silt near 7-m depth in all boreholes. These silty clays and stiff silt most likely record a lacustrine setting, but the reinterpretation that the loess-alluvium contact is at ~5.6 m in the WL and BF boreholes but at 4.2 m in the LF borehole – if we accept that *P. lapidaria* marks the loess-alluvium contact – would require substantial thickening of the alluvium upstream from borehole WL (Figure 2-7). Finally, sediment in the uppermost ~3.8–4.2 m of each borehole is very uniform, whereas below these depths there exists substantial color and textural variation in all boreholes, indicating a pronounced shift in depositional environments, which also corresponds with the occurrence of *P. lapidaria* in the LF borehole. With all these factors in mind, we attribute the subtle grain-size changes at the loess-alluvium contact in the WL borehole (and other boreholes) to the high proportion of reworked loess in the drainage, similar to previous findings (Rodbell, 1996).

2.5.1.2 Holocene floodplain (Qa)

The Holocene floodplain (Qa) is consistently 2–4 m above the modern channel (Figure 2-4). Although the surface has been anthropogenically modified, evidence of abandoned oxbow lakes and well-preserved meandering channel morphology is widespread. The Holocene floodplain widens upstream from 0.5–1.3-km wide near the bluff margin (1–2 km valley distance) to 3.0–3.3-km wide at valley distances 18–33 km (Figure 2-3). The Holocene floodplain gradient is approximately zero from valley distances 0–5 km and parallels the modern channel gradient at distances >5 km (Figure 2-4).

2.5.1.3 Deweyville Complex terraces (Qtda and Qtdb)

The Deweyville complex terraces (Qtda and Qtdb) are mapped in the Obion River valley and are interpreted as correlative to terraces observed elsewhere in the Mississippi embayment (Saucier and Fleetwood, 1970; Autin et al., 1991). Where mapped outside the Obion River valley, the Deweyville complex occurs between the Holocene floodplain and Prairie complex (temporally equivalent to Finley and Hatchie terraces). The Deweyville complex elsewhere is characterized by well-preserved, oversized channel migration features compared to Holocene contemporaries and frequently is buried by Holocene deposits at lower elevations (Saucier and Fleetwood, 1970; Autin et al., 1991). These characteristics are consistent with our observations—in the Obion River valley, Deweyville complex terraces are inset below the Finley terrace, nearly merge with the Holocene floodplain, and in some instances preserve migrating channel morphology (e.g., point-bar accretion meander scrolls, or scroll bars) that are oversized compared to the modern Obion River channel (Saucier, 1987) (Figure 2-5). We subdivide the Deweyville complex terraces in the Obion River valley based on relative position and use Deweyville A (Qtda) for the slightly higher elevation, apparently older terraces and Deweyville B (Qtdb) for the slightly lower elevation, younger terraces. The Deweyville complex terrace treads are typically 1–3 m above and smoother than the Holocene floodplain (Figure 2-4). The Deweyville complex terraces are only present in the lower Obion River valley; at ~13 km valley distance, they merge with the Finley terrace tread elevations (Figure 2-4). The longitudinal valley profiles indicate the Deweyville complex terraces may reflect incision from the Finley terrace profile following a base level decrease, consistent with other mapped locations, implying that the highest Deweyville complex terrace surfaces may be nearly contemporaneous (but slightly post-date) with the latest Finley terrace deposition (Autin et al., 1991) (Figure 2-4). The oversized preserved meander scrolls noted by Saucier (1987) indicate deposition when the paleo-Obion River had a different flow rate, annual discharge, or vegetation cover than the modern Obion River (Autin et al., 1991). The crisp expression of these original, oversized meander scrolls indicates that post-depositional surface modification (e.g., recent flood deposits, loess accumulation) on the Deweyville complex terraces is minor. Coring data presented in Van Arsdale et al. (1999) on the Deweyville A surface (mapped there as floodplain) does not mention a loess cap. Limited loess on the Deweyville complex indicates that the terrace deposition post-dates the most recent loess deposit, the Peoria Loess, which may be as young as 10–11 ka (Gold et al., 2019; McKay, 1979; Ruhe, 1983).

2.5.1.4 Hatchie terraces (Qtha)

The Hatchie terrace (Qtha) is the most continuous terrace within the mapping extent and primarily occurs on the northern side of the valley as a single, continuous, somewhat dissected terrace tread (Figure 2-3). The relative height of the Hatchie terrace above the Holocene floodplain (Qa) ranges from 15–29 m near the valley mouth (valley distance 0–3 km) and gradually decreases upstream to ~3 m above Qa near ~30-km valley distance (Figure 2-4). Valley longitudinal profiles reveal a moderate reverse gradient of 3.5 m/km (0.20°) to the northeast at 0–3-km valley distance (Figure 2-5), a slight reverse gradient of 0.4 m/km (0.02°) from 3–15-km valley distance, and a near-zero gradient at distances >15 km (Figure 2-4).

We map the westernmost terrace tread in the Obion River valley (location A in Figure 2-3b, Figure 2-5b) as the Hatchie terrace. Our interpretation differs from others (Saucier, 1987). The abrupt reverse gradient on the western terrace edge, described as a terrace “lip” (Saucier, 1987), was interpreted previously as (1) a remnant of an older, higher terrace that grades into the Hatchie terrace to the east (Saucier, 1987), (2) a continuation of the Hatchie terrace, which contains westward-thickening loess (Rodbell, 1996), or (3) a continuation of the Hatchie terrace that has been uplifted by the Reelfoot fault (Van Arsdale et al., 1999). We interpret this surface as a continuation of the Hatchie terrace observed upstream for the following reasons: the tread is uniformly incised, and the transitional slope is relatively gentle, with no obvious riser to indicate a contact between older and younger terraces as seen elsewhere in the valley.

2.5.1.5 Humboldt (Qthu) and Henderson (Qthe) terraces

Terrace identification, correlation, and differentiation from the surrounding bluffs is more difficult for surfaces older than the Hatchie terrace due to the thick loess cover and a high degree of dissection. Here again, our terrace mapping diverges from previous studies. The Humboldt terrace (Qthu) is the second-oldest identified terrace and is only identified in the upstream extents of the Obion River valley (>15 km valley distance) and does not cross the Reelfoot fault monocline trace (Figure 2-3). The tread is moderately to heavily dissected and resides ~15 m above the modern floodplain (Figure 2-4). The preserved Humboldt terrace surfaces have a gradient that roughly parallels the Holocene floodplain and modern channel (~0.3 m/km [0.02°] to the southwest), although scatter in elevations derived from the dissected loess-covered surface makes the true terrace tread gradient difficult to determine (Figure 2-4).

The Henderson terrace (Qthe), which was previously not mapped in the Obion River valley, is heavily dissected and typically lacks clear indication of a once-planar tread that is visible in the younger surfaces (Figure 2-3). Some of the Henderson terraces identified in this study were previously mapped as Humboldt terrace surfaces (Rodbell, 1996). Differing interpretations here are based on large elevation differences and increased degree of incision between Humboldt terraces mapped by Saucier (1987). These subtle surficial changes are more easily resolved in the high-resolution lidar-derived DEMs than in the original topographic maps used by Rodbell (1996) and Saucier (1987). The Henderson terrace is identified primarily based on elevation and comparing the surface texture to the surrounding bluffs—the Henderson terrace is generally smoother, with overall flatter terrain than the bluffs. Additionally, the contact of the Henderson terrace with the bluffs is typically marked by a steep scarp or slope increase indicative of an inset surface. Due to the degraded condition, the depiction of the Henderson terrace is uncertain (Figure 2-4). Overall, the Henderson terrace gradient (~0.45 m/km [0.025°] to the southwest) is slightly steeper than the Holocene floodplain for all but the lower 5-km valley distance but elevation points have substantial scatter likely due to variation in post-depositional loess cover and erosion (Figure 2-4). The westernmost Henderson terrace tread, closest to the Reelfoot monocline trace, may indicate a reverse gradient as with the younger terrace surfaces (Figure 2-4). However, the unknown amount of post-depositional loess cover and incision complicates identification of the original tread and could influence the apparent gradient.

2.5.2 Shorelines

We map a series of apparent shoreline features, previously identified by Saucier (1987) in the Obion River valley and with additional mapping here. The shoreline landforms manifest as approximately valley-parallel, symmetrical, elongated ridges that we interpret as constructional lacustrine beach ridges (Figure 2-3). Often, these ridges are nested as a series of similar-elevation complexes or decrease in elevation away from the bluff margin. Most beach ridge complexes are concentrated near the confluence of smaller tributaries with the main Obion River valley or along the outer margin of a terrace tread, although some ridges appear isolated on the terrace tread near the riser. We separate these ridge complexes into three groups (beach ridges 3, 2, and 1; Figure 2-3b) based on elevation, lateral ridge continuity, and apparent preservation. We extracted elevation points at the highest point of the best-preserved ridge crests to compare to the terrace longitudinal profiles. The beach ridge units have not been excavated in previous studies or this investigation, and interpretations are based on morphology from the lidar only.

2.5.2.1 Beach ridge 1 (Qbr1)

Beach ridge 1 (Qbr1) is the highest ridge complex and is typically 95–97 m in elevation (Figure 2-4). Beach ridge 1 only appears between 15- and 35-km valley distance and is the most eroded, with smoother peaks and discontinuous ridges (Figure 2-4). The bluff-proximal contact of beach ridge 1 appears to be inset into the Henderson terrace, which indicates beach ridge 1 formed after the Henderson terrace; however, the relationship with the Humboldt and Hatchie terraces is unclear.

2.5.2.2 Beach ridge 2 (Qbr2)

Beach ridge 2 (Qbr2) has the widest distribution and has ridge elevations of 88–92 m at valley distances >10 km and 92–95 m at valley distances <10 km, mimicking the longitudinal profile of the Hatchie terrace tread (Figure 2-4). Beach ridge 2 crests are typically well-defined with relatively sharp peaks that are less incised than beach ridge 1 but show some evidence of post-depositional erosion, which likely contributes to the scatter in elevations. The base of beach ridge 2 is in contact with both the Hatchie and Finley terrace treads, which indicates that beach ridge formation may be decoupled with terrace formation and the associated lake postdates both terraces. At the eastern mapping extent, beach ridge 2 crests are less defined, exhibit less relief above the Hatchie terrace tread, and has been partially buried by tributary alluviation.

2.5.2.3 Beach ridge 3 (Qbr3)

Beach ridge 3 (Qbr3) elevations are typically 85–87 m at valley distances >10 km, 86–99 m at valley distances 4–10 km, and one mapped ridge at 1-km valley distance has elevations of 91–93 m (Figure 2-4). Beach ridge 3 is only found in contact with the Finley terrace or nested in beach ridge 2, indicating it postdates both landforms. The ridges typically occur near the outer Finley terrace contact closest to the bluffs, and crests are typically 2–3 m above the Finley tread. The farthest upstream occurrences of beach ridge 3 are patchy, discontinuous, and have low relief (<2 m) above the Finley terrace indicating partial burial by more recent alluviation. Beach ridge 3 is absent at valley distances >25 km.

2.5.2.4 Origin of beach ridges

There are multiple explanations for lake, beach ridge, and terrace formation in the Obion River valley. One possibility, documented historically (elaborated on in “Historical Data” Section 2.6), is that lakes may form in response to damming of the Obion River due to surface deformation above the Reelfoot fault. It is also possible lakes formed and fluctuated rapidly due to post-glacial sedimentation that blocked Obion River drainage to the Mississippi River (Autin et al., 1991). The more poorly preserved and discontinuous surface expression of beach ridge 1 compared to beach ridges 2 and 3 indicates an older formation age, whereas the surface morphology of beach ridges 2 and 3 are similar, indicating they could be related to the same recessional sequence. We lack absolute age control to accurately constrain beach ridge formation timing; however, depositional relationships and relative sharpness in morphology indicate that beach ridge 1 postdates the Henderson terrace (35-55 ka), and beach ridges 1 and 2 both postdate Finley terrace formation. Based on the map pattern of the shorelines and the complicated depositional relationship with the terraces, we suspect a complex history of shoreline reoccupation has occurred. From a tectonic perspective, the presence of beach ridges in the Obion River valley is important because they represent shorelines that formed at a uniform elevation, unlike the terrace elevations, which are complicated by eolian cover and changing river gradients.

2.5.3 Surface deformation measurements from lidar

2.5.3.1 The northern Reelfoot fold scarp

The northwestern extent of the Reelfoot fold scarp near New Madrid, Missouri, deformed a late Pleistocene (~20–18 ka) (Rittenour et al., 2007) Mississippi floodplain surface and has 1.3–1.7 m of vertical separation with a preferred value of 1.5 m (Figure 2-2). Approximately 5 km north of this profile, the scarp height tapers to zero at the presumed northern extent of the active Reelfoot fault. In the Kentucky Bend of the Mississippi River, we measure 3.4–3.9 m of vertical separation on a folded late Holocene Mississippi floodplain surface (Holbrook et al., 2006), with a preferred value of 3.9 m (Figure 2-2). These vertical separation values are consistent with previous measurements of ~2 m and ~4 m of vertical separation, respectively, by Van Arsdale et al. (1995).

The largest vertical separation measured on the Reelfoot fault is located along the southwestern shore of Reelfoot Lake, where the subaerial side of the monocline was matched with sublacustrine bathymetric data (Carlson and Guccione, 2010). The total vertical separation here is ~11.3 m (Figure 2-2), which records at least two earthquakes offsetting a late Holocene Mississippi alluvial surface. The single event maximum vertical displacement from the 1812 earthquake at this site is estimated at 5.9–8.2 m (Carlson and Guccione, 2010).

2.5.3.2 The southern Reelfoot fold scarp

The most prominent backtilting in terrace surfaces occurs near 3-km valley distance on the Deweyville, Finley, and Hatchie terraces (Figure 2-4, Figure 2-5). The western (downstream) margins of the Deweyville, Finley, and Hatchie terraces have been partially eroded from lateral migration of the Mississippi River (Figure 2-5b). If the terrace treads once returned to the gradient observed upstream, as expected for a broad fold scarp or monocline, this correlative surface no longer exists and cannot be used as a displacement marker. Because correlative surfaces are not available to measure vertical separation in the far field, we can only measure the vertical deviation of the eroded terraces at the mouth of the Obion River with respect to projection of the upstream gradient (Figure 2-5b). We project the mean gradient from the least-disturbed topography on the eastern side of the profile, which approximates the original surface, to the western edge of the fold and measure the vertical difference. This process is repeated several times (as explained in the Methods Section 2.4) to capture a range of plausible correlative surfaces. For shorthand, we refer to these values as apparent vertical separation; these values are minima due to erosion of the terraces from the Mississippi River.

The following vertical separation results are derived from profiles along the least-modified or incised swaths of the Deweyville, Finley, and Hatchie terraces. The minimum apparent vertical separation inferred from the warped terraces is 1.1 m for the Deweyville A terrace (range 0.9–1.1 m), 2.4 m for the Finley terrace (range 2.0–2.6 m), and 8.1 m for the Hatchie terrace (range 7.7–8.1 m) (Figure 2-5b). The pattern of apparent vertical separation is consistent with progressive deformation of increasingly older surfaces. We also measure the gradient of the apparently tilted terrace treads, using negative values to indicate drainage direction up valley (northeast). Upstream from the surface projection of the Reelfoot fault, the Deweyville, Finley, and Hatchie terraces are nearly horizontal to slightly reverse (Figure 2-4, Figure 2-5b). Downstream from the Reelfoot fault projected trace, the terrace gradients are -1.1 m/km for the Deweyville terrace, -1.4 m/km on the Finley terrace, and -3.5 m/km on the Hatchie terrace (Figure 2-5). Similar to the pattern of apparent vertical separation, reverse terrace gradients progressively increase with terrace age.

2.5.3.3 Other possible tectonic features

Other geomorphic features in the Obion River valley could also indicate tectonic deformation but are less reliable. Van Arsdale et al. (1999) first noted that the Obion River floodplain constricts near the projected Reelfoot fault trace. At the mouth of the Obion River valley and near the surface projection of the Reelfoot fault, the Holocene floodplain width is 0.5 km (excluding the

Deweyville terraces). If the definition of the Holocene floodplain is expanded to include the Deweyville terraces, the floodplain is up to 1.5-km wide at valley distances <5 km, compared to 3- to 3.3-km wide farther upstream (Figure 2-3). Van Arsdale et al. (1999) and Rodbell (1996) observed a reverse Holocene floodplain gradient near the Reelfoot fault; however, these profiles lump the Deweyville terraces with the floodplain and are highly generalized. Our measured gradient of approximately zero on the Holocene floodplain could either reflect Mississippi River backwater flooding and sedimentation or a tectonic influence, or both.

Longitudinal valley profiles provide some additional possible insight into tectonic warping after the beach ridges formed (Figure 2-4). Beach ridge 2 and 3 are horizontal within uncertainty at valley distances >10 km, and apparently rise slightly in elevation downstream at valley distances <10 km (Figure 2-4). Beach ridge 3 may record a more substantial elevation increase near the valley mouth, although the record is very sparse (Figure 2-4). These correspond to an apparent vertical separation of 2–3 m, or up to ~5 m for beach ridge 3, although no single ridge is large enough to continuously record deformation across the width of the fold scarp. Because shorelines form horizontally, we interpret the tilting of the profiles of beach ridge 2 and 3 as tectonic.

A final qualitative indicator of terrace deformation, visible in the lidar DEM, is that the incision patterns on the westernmost Hatchie terrace indicate long-lived drainage up valley (to the east), opposite the Obion River valley drainage direction (Figure 2-5). This drainage pattern could reflect uplift above the projection of the Reelfoot fault, potentially accentuated by a wedge of westward-thickening loess. However, we cannot distinguish drainage direction as influenced by tectonic deformation versus non-tectonic processes, such as diversion caused by sedimentation from the Mississippi River valley.

2.6 Historical Data

Several historical records document evidence of a lake in the Obion River valley. Van Arsdale et al. (1999) first noted a lake existed in the Obion River valley as early as 1832 (Rhea et al., 1832) and speculated that this lake had a tectonic origin. However, explicit historical evidence linking the lake to the earthquake sequence of 1811–1812 had remained elusive.

We find additional historical evidence of a lake in the Obion River valley at least as early as 1825 in an autobiography with dated passages. During a bear hunt in the fall of 1825, Davy Crockett (1834) describes his destination as,

"*started to take a hunt between the Obion lake and the Red-foot lake*," further describing that "*The woods were very rough and hilly*."

The "hilly" terrain between the two lakes is consistent with the bluffs between the Obion River valley and Reelfoot Lake (Figure 2-2). The historical map of Russell (1795) shows the modern Reelfoot River, the drainage that was dammed to create Reelfoot Lake during the 1812 earthquake, depicted as the "Red-foot River." This may be a colloquial name that persisted locally through to Crockett's time.

The presence of a lake post-dating 1812 does not necessarily indicate coseismic formation, given the prevalence of backwater flooding in the Obion River valley from the Mississippi River (Shankman and Samson, 1991). However, Lyell (1849) recorded, “*The sunk country is not confined to the region west of the Mississippi; for, on my way up the river, I learnt from Mr. Fletcher, a farmer, who had a wooding station in Tennessee, that several extensive forest tracts in that state were submerged during the shocks of 1811–12, and have ever since formed lakes and swamps, among which are those called Obion and Reelfoot.*”

The second-hand report by Lyell strongly suggests that the Obion River was dammed by vertical surface deformation along the Reelfoot fault similar to the Reelfoot River (and subsequent Reelfoot Lake), creating Obion Lake in 1812. A small change in base level near the mouth of the Obion River valley would have a similar effect of lake formation until the stable river gradient reestablished. The lake referenced by Lyell (1849) may be the same lake depicted by Rhea et al. (1832) and mentioned by Crockett in 1825 (Crockett, 1834). Reelfoot Lake may have outlasted Obion Lake into modern times because it occupied depressions from old Mississippi River meander bends (Fuller, 1912; Russ, 1982), has a high water table (Carlson and Guccione, 2010), and was later anthropogenically regulated with a spillway (U.S. Department of the Interior Fish and Wildlife Service, 1989), whereas the Obion River would eventually breach the natural dam caused by the Reelfoot fold scarp, allowing the lake to drain. Fold scarp heights in the Obion valley are also smaller (1–2 m; Figure 2-5) than scarps bounding Reelfoot Lake (6–8 m in 1812; Figure 2-2) (Carlson and Guccione, 2010), and consequently easier to breach.

2.7 Discussion

2.7.1 Blind faulting

Recent motion on blind reverse faults can be challenging to detect and quantify because deep fault slip does not break the surface along readily recognized scarps. Broad, distributed folding of late Quaternary surfaces and warped and deformed terraces are often the only tectonic signature of blind faults (e.g., Bullard and Lettis, 1993). High-resolution topography, especially bare-earth models derived from lidar, are particularly useful for deciphering subtle signals of landscape deformation from blind faults (e.g., Meigs, 2013; Thompson Jobe et al., 2020a) and these data are especially important in highly vegetated, subtropical, and active landscapes such as the Mississippi embayment. With these new data, we evaluate whether apparently warped landforms in the lower Obion River valley record evidence of tectonic deformation, climate-driven processes, or a combination of both. The landforms studied here contain influences of backwater flooding, changes in base level, and potentially fluctuating lake levels. However, our surficial observations from lidar, subsurface borehole data, and historical accounts of lake formation are also consistent with blind faulting along the Reelfoot fault since the late Pleistocene and potentially in older, late Quaternary surfaces. Disentangling these two signals is challenging but merits investigation, and is elaborated on below.

2.7.2 Surface deformation in the Obion River Valley

Three lines of evidence favor the interpretation that surface folding due to buried faulting is preserved in the landscape at the mouth of the Obion River: (1) increased tilting of progressively older terrace surfaces; (2) the constant thickness of loess on the Finley terrace surface as determined from boreholes; and (3) apparent deformation of previously horizontal shorelines. These geomorphic observations, along with historical records of lake formation following the 1812 earthquake and valley constriction near the Obion River valley mouth, are consistent with uplift above the southern extent of the Reelfoot fault.

2.7.2.1 Deformed terraces

We document progressive deformation of the Deweyville A, Finley, and Hatchie terraces that indicates repeated earthquakes along the southern extent of the Reelfoot fault. At the scale of the entire valley, there appear to be two hingelines where terrace gradient values decrease downvalley: a prominent hinge at ~3-km valley distance seen in the Deweyville, Finley, Hatchie and possibly Humboldt terraces and a subtle hinge at ~12-km distance seen in the Finley and Hatchie terraces (Figure 2-4). Importantly, the terraces that record the subtle hingeline at ~12 km (Finley and Hatchie) also preserve lacustrine landforms, such as horizontal gradients and beach ridges. Therefore, the subtle gradient hinge at ~12-km valley distance may reflect lacustrine or backwater flood influence, such as short-lived upstream deposition from the Mississippi River overbank flow. Alternatively, apparent backtilting between 3- and 12-km valley distance on the Finley and Hatchie terraces may reflect small, meter-scale variation in tread preservation across the valley length since deposition in the late Pleistocene.

The location of the most apparent folding on these three terraces (~3-km valley distance) occurs along a linear trend and coincides with the eastward cessation of modern seismicity (Figure 2-2, Figure 2-3), consistent with colocation with a fault. Reverse gradients from 0-3 km are steeper than the modern or prehistoric river gradients preserved upstream, indicating a non-fluvial origin rather than backwater flooding. Specific evidence for progressive deformation includes increased reverse surface gradient as a function of increasing terrace age and an associated increase in the minimum apparent vertical separation. These observations indicate that older terraces record more tectonic deformation and therefore a longer earthquake record than younger terraces. Assuming all observed tilting is due to tectonic deformation, progressive folding across the three terraces implies earthquake events between deposition of the Hatchie terrace and the Finley terrace (~35–55 ka to 24 ka) (Leigh and Knox, 1993; Rodbell, 1996; Rodbell et al., 1997), between deposition of the Finley and Deweyville terrace (<24 ka), and postdating Deweyville terrace deposition. We cannot, however, estimate the number of events, exact event timing, or slip amount per event.

2.7.2.2 Loess thickness from the auger profile

Three auger boreholes along a 2.6-km-long transect spanning a prominent hingeline of backtilting on the Finley terrace reveals a coherent package of warped loess, alluvium, and lacustrine deposits (Figure 2-7). Across all three boreholes, our interpreted contact between loess and alluvium occurs at 3.7–4.5 m below the terrace tread and mirrors the surface profile (Figure 2-7); therefore, a wedge of decreasing loess thickness extending west-to-east does not appear to explain ~2 m of surface warping over the same distance. Instead, the loess-alluvium contact similarly shows ~2 m of vertical separation, although fewer profile elevations are available due to the limited auger sites compared to elevations extracted from the lidar. This pattern is mirrored with an interpreted lacustrine deposit ~7 m below the surface at all sites (Figure 2-6, Figure 2-7), which likely formed at uniform elevation. We interpret the consistency between warping of the surface and two subsurface contacts as evidence of broad folding related to buried slip on the Reelfoot fault.

Our stratigraphic results from the Finley terrace are consistent with findings from previous studies. The 4.20-m depth to snail fossils in our LF borehole is consistent with the unidentified gastropod fossils found by Rodbell (1996) in OP-21 at 4.07 m (Figure 2-7). Previous work by Van Arsdale et al. (1999) provides generalized stratigraphic context from cores extracted prior to Obion River channelization that parallel our Deweyville A profile (Figure 2-5). They reported patterns of grain size changes that imply the stratigraphic contacts parallel the subtle surface warping at the approximate Reelfoot fault projection (Van Arsdale et al., 1999). Our study provides additional stratigraphic context by focusing on the loess-alluvium contact, which is likely to be less heterogeneous than alluvium stratigraphy.

Although the Obion River has likely flooded the Deweyville surface since deposition, the clear preservation of original oversized scroll bars indicates a lack of loess cover and minimal surface modification since formation of the terrace (Figure 2-5b). We lack loess thickness constraints or stratigraphic information for the Hatchie terrace, and therefore cannot accurately separate differential loess thickness from tectonic deformation on this surface. However, loess has been documented as thinning from west to east in this region over a much larger area (tens of kilometers) but the distribution of thicknesses is sparsely constrained, especially on the Obion River terraces (Rodbell, 1996; Rodbell et al., 1997). We do not expect this regional-scale process to be visible in the few-kilometer-long topographic profiles in this study (Figure 2-5). The results of the auger profile on the Finley terrace show that the effect of loess thickening at this scale is not substantial compared to the coseismic folding, and we extrapolate that inference to the Hatchie terrace as well.

The vertical separation values measured across all three folded terraces are minima. Each deformed terrace represents a fragment of a broad fold, where the original uplifted surface has presumably been removed by erosion from the Mississippi River (Figure 2-5). Without a correlative surface to provide a deformation marker, we cannot calculate true vertical separation and slip or folding rates.

2.7.2.3 Paleolake and shorelines

Geomorphic mapping and historical records indicate that the Obion River valley has been repeatedly occupied by lakes. The most recent Obion Lake likely formed following the 1812 earthquake and is consistent with damming of the Obion River by motion on the Reelfoot fault, or sufficient base level increase, similar to the formation of Reelfoot Lake. Deformation from the 1812 earthquake may still be preserved as the ~1-m-high broad warping on the Deweyville terrace (Figure 2-5c).

Older paleolakes are recorded by the near-zero gradients of portions of the Finley and Hatchie terraces and the presence of beach ridge complexes. These paleolakes may reflect tectonic damming from deformation across the Reelfoot fault, but also could have formed from backwater flooding due to postglacial sediment aggradation on the Mississippi River during glacial retreat (Autin et al., 1991), or both. In either case, landforms from these lakes (Finley and Hatchie terrace treads and beach ridges) provide important horizontal reference frames for later deformation. If each beach ridge unit was originally deposited with uniform elevations, the elevated beach ridges downstream from the Reelfoot fault monocline indicate that the beach ridges have been uplifted by motion on the Reelfoot fault. Additionally, beach ridge profiles parallel the other warped terraces, which could indicate a similar long-term history of folding.

Although the Obion Lake shorelines features are mapped using several criteria, such as morphology and inset relationships, several assumptions are inherent in the interpretation that the shorelines record vertical deformation. First, our mapping is based solely on lidar-based imagery and does not include any absolute age control, field mapping, or stratigraphic data to test correlations. Second, the ridges are not widely or consistently preserved along the length of the Obion River valley, and are especially scarce near the Reelfoot fault monocline, leading to ambiguity in deformation measurements. Finally, the lack of continuous preservation leads to uncertainty in correlating beach ridge complexes over significant distances. An alternative interpretation to tectonic deformation is that beach ridges that appear west and east the Reelfoot monocline scarp are from different lake levels. If multiple lakes formed rapidly, or lake levels fluctuated in short period of time, the differences in age would be nearly indistinguishable without precise age control. In general, because the beach ridge elevations parallel the Finley and Hatchie terraces even where the expressions are sparse, our preferred interpretation is that tilting of originally horizontal shorelines records tectonic deformation near a blind fault.

2.7.3 Implications for fault tip depth

Vertical separation of correlative surfaces above the Reelfoot fault is highest near Reelfoot Lake, the approximate center of the fault, and decreases to the north and south (Figure 2-2, Figure 2-5). The northern half of the Reelfoot fault exhibits more discrete folding at the surface, with deformation over a few 100 m (Figure 2-2), compared to the broad, ~2-km-wide fold within the Obion River valley (Figure 2-5). Vertical separation near the northern Reelfoot fault monocline (1.5 m near New Madrid, Figure 2-2) in 20–18 ka deposits (Rittenour et al., 2007) is similar to the 1.1 and 2.4 m of apparent vertical separation observed in ≤ 24 ka Deweyville and Finley terraces near the southern fault extent (Figure 2-5). These values may indicate that terraces in the Obion River valley have experienced a similar earthquake history to the Mississippi River valley surfaces.

Previous work by Champion et al. (2001) on the Reelfoot fault suggests that changes in deformation character along strike indicates a change in active fault tip depth. Their trishear modeling, constrained by folding at depth, estimates that the active fault tip is twice as deep below the southern section of the fault (~1020-m deep) than along the northern section (~470-m deep), which generates a broader monocline (Champion et al., 2001). The predicted effects of a deeper active fault are consistent with the broader surface folding shown in this study along the southern section of the Reelfoot fault compared to folding in the north (Figure 2-8). This may also indicate that the Reelfoot fault extends south beyond the Obion River valley along seismicity trends to nearly Dyersburg, Tennessee (Figure 2-2), but lacks any identifiable surficial expression.

2.7.4 Implications for rupture length

The historical record of coseismic lake formation and the geomorphic evidence for surface deformation in the Obion River valley indicate that the 1812 earthquake rupture spanned from near New Madrid, Missouri, to at least the Obion River. This rupture length was speculated by Van Arsdale et al. (1999), but conclusive evidence for an 1812 scarp southeast of Reelfoot Lake had not been previously recognized. By combining the northernmost recognized rupture extent (Van Arsdale et al., 1995; Baldwin et al., 2005) with coseismic Obion Lake evidence (Crockett 1834; Lyell 1849; Rhea et al. 1832), the minimum 1812 rupture length is ~58 km. Given the subtle expression of surface deformation in the Obion River valley, and evidence for coseismic sackungen that extend nearly to Dyersberg, Tennessee (Delano et al., 2018), the rupture could have extended farther south of Obion River below the bluffs without preserving tectonic surface deformation. This scenario yields a rupture length of ~70 km (Figure 2-8). Both the 58-km and 70-km estimates substantially exceed the previous 1812 rupture length estimate of 32 km (Van Arsdale et al., 1999). Longer rupture lengths lend themselves to larger earthquake magnitudes and are consistent with recent findings that the Reelfoot fault is continuous across the intersection with the Cottonwood Grove and Ridgeley faults (Figure 2-1) (Greenwood et al., 2016).

2.7.5 Pre-Holocene movement of the Reelfoot fault

The progressive deformation recorded in fluvial terraces indicates that the 1812 earthquake on the Reelfoot fault was not the first earthquake to produce surface deformation in the Obion River valley. The surfaces of the Deweyville, Finley, and Hatchie terraces formed <24 ka, ~24 ka, and 35–55 ka (Leigh and Knox, 1993; Rodbell, 1996; Rodbell et al., 1997) and have minimum vertical separations of 1.1 m, 2.4 m, and 8.1 m, respectively (Figure 2-5). These older, deformed terraces likely indicate slow rates of persistent blind slip on the southern section of the Reelfoot fault postdating at least deposition of the Finley terrace and possibly postdating Hatchie terrace deposition. The Finley terrace age (24 ka) and the approximate age of the Hatchie terrace (35–55 ka) yield minimum vertical deformation rates (using apparent vertical separation; refer to definition in Loess Thickness from the Auger Profile, Section 2.7.2.2) of 0.1 mm/yr and 0.1–0.3 mm/yr, respectively. Deformation rates of the Deweyville terrace are based on the observations that the Deweyville terrace surface postdates Peoria Loess deposition (e.g., preserved scroll bars, coring data presented in Van Arsdale et al. [1999]). Using the latest Peoria Loess age of 11 ka (Gold et al., 2019), the minimum apparent vertical deformation rate on the Deweyville terrace is ~0.1 mm/yr. Paleoseismic records on the Reelfoot fault previously recognized earthquakes as early as ~4 ka (Gold et al., 2019); therefore, this study substantially lengthens the paleoseismic record of fault slip on the southern section of the Reelfoot fault.

Other investigators have speculated that activity along the southern section of the Reelfoot fault initiated with the 1812 event (Csontos and Van Arsdale, 2008), caused by a transition of stress from the southeastern rift margin in the Holocene (Cox et al., 2006). By contrast, our study suggests that pre-1812 slip extends along the southern section of the Reelfoot fault, although apparently as buried slip, and has repeated over more than one earthquake cycle during the late Quaternary.

A history of repeated earthquakes extending southeast of the bluff margin is consistent with recent identification and documentation of coseismic sackungen on bluff ridge tops (Figure 2-2) (Delano et al., 2018; Gold et al., 2019). Gold et al. (2019) demonstrated that these features record at least four earthquakes since 11 ka, including the 1812 event. Delano et al. (2018) suggested that increased shear strain and near-fault deformation may control sackung formation and reactivation. Their mapped distribution of sackungen coincides with the total Reelfoot fault length revealed by modern seismicity, extending south of the Obion River valley. The broad deformation seen in the Obion River terraces likely continues within the bluffs north and south of the river and may contribute to the location of observed coseismic sackungen (Delano et al., 2018); however, the subtle, broad expression would be masked by the thick loess cover and incised topography compared to the relatively smooth and planar terrace surfaces.

2.7.6 Implications for current hazard models

A key component in seismic hazard models is the length and location of the mapped fault trace (U.S. Department of Energy et al., 2012; Petersen et al., 2014). The current fault-based source model maps the Reelfoot fault with two geometries: (1) a shorter, 46-km-long segment and (2) a longer, 83-km-long fault that extends farther south and is composed of 56 km of rupture on the Reelfoot fault and 27 km of rupture along the New Madrid West fault (Fig. S2 in Delano et al., 2021a; U.S. Nuclear Regulatory Commission, 2011).

We estimate that the active Reelfoot fault length and rupture potential is a minimum of ~70 km, given the new minimum length of the 1812 event (58 km), the farthest extent of modern seismicity and coseismic sackungen, and diffuse geomorphic record of displacement (Figure 2-

2, Figure 2-5, Figure 2-8). The revised active fault trace is longer, extends farther south, and is mapped at a slightly different location and orientation than either current model trace (Fig. S2 in Delano et al., 2021a). This longer fault length may impact hazard estimations if the entire 70-km-long Reelfoot fault ruptures, particularly if earthquake rupture continues on to the New Madrid West fault, as is currently depicted in one of the model scenarios (U.S. Department of Energy et al., 2012).

2.8 Conclusions

We document and measure deformed landforms in the Obion River valley in the New Madrid seismic zone using lidar and borehole data to constrain historical and late Quaternary slip along the Reelfoot fault. At least three terraces and two shoreline complexes record broad surficial folding across the projected trace of the blind Reelfoot fault. We compare surface profiles to stratigraphic data from three auger sites to demonstrate that apparent warping is not due to loess thickening and represents folding above a buried fault tip. These findings, combined with historical lake records, show that surface deformation from the 1812 earthquake extended southward through at least the Obion River valley, increasing the minimum 1812 rupture length to 58 km. The broad zone of surficial folding apparent in the Obion River valley dissipates farther south in the incised bluff terrain, but the total fault length is likely ≥70 km based on a continuation of modern seismicity and other geomorphic evidence of strong shaking, like sackungen. Additionally, progressive deformation across multiple terraces indicates a long-lived record of earthquakes that predates the existing paleoseismic record (~4 ka) and likely also predates ~24 ka. The folding observed in the Obion River valley is broader than fold scarps farther north along strike of the Reelfoot fault, which is consistent with models of a deep fault tip along this section of the fault. Together, these observations indicate that slip along the Reelfoot fault is continuous to the south, but slip is deeper and surface deformation is more diffuse and possibly diminished. The record of historical and prehistoric distributed, deep slip south of Reelfoot Lake has important implications for understanding slip potential and seismic hazard from the Reelfoot fault. Improved documentation of subtle tectonic signals from blind faulting, such as with high-resolution topographic data, is critical for characterizing seismic hazard in low strain, high-erosion regions like the New Madrid seismic zone.

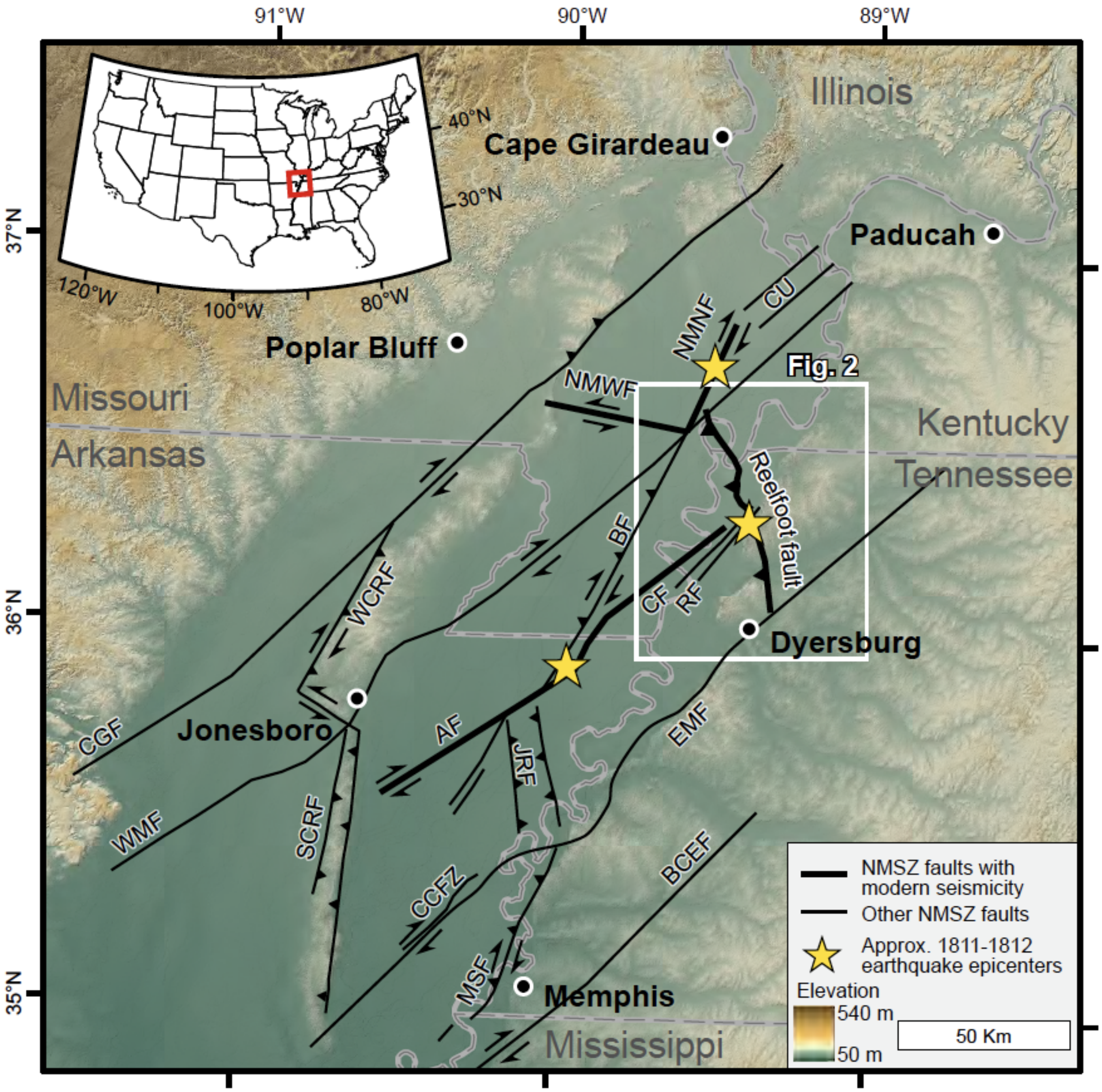

Figure 2-1 **Overview of the New Madrid seismic zone (NMSZ) and major structures in the Mississippi embayment. Largest 1811-1812 earthquake epicenters from Bakun and Hopper (2004). Fault mapping modified from Hao et al. (2013), Johnston and Schweig (1996), Martin and Hough (2019), Stephenson et al. (1995), and Thompson Jobe et al. (2020a). Teeth indicate dip direction of a reverse fault; arrows indicate sense of strike-slip. Gray lines are state boundaries. AF = Axial fault; BCEF= Big Creek - Ellendale fault; BF = Bootheel fault; CCFZ = Crittenden County fault zone; CF = Cottonwood Grove fault; CGF = Commerce Geophysical fault; CU = Charleston Uplift; EMF = Eastern Margin fault; JRF = Joiner Ridge fault; MSF = Meeman-Shelby fault; NMNF = New Madrid North fault; NMWF = New Madrid West fault; RF = Ridgely fault; SCRF = Southern Crowleys Ridge fault; WCRF = Western Crowleys Ridge fault; WMF = Western Margin fault.**

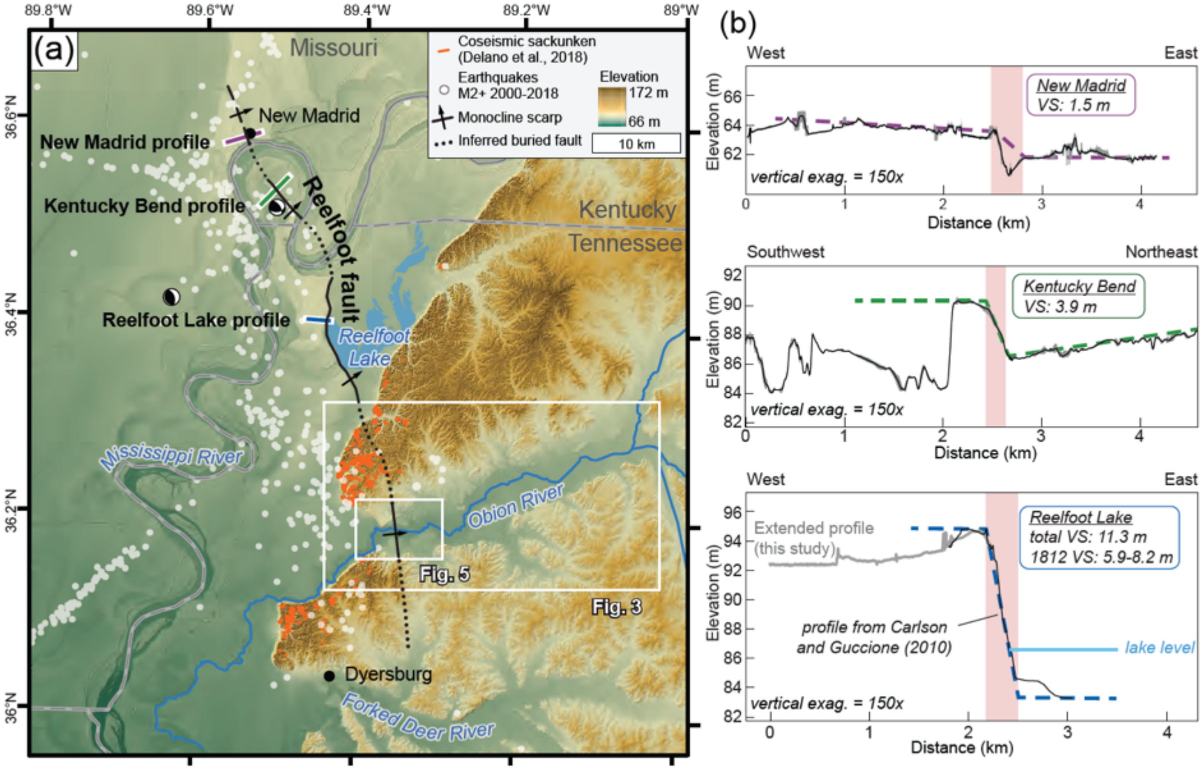

Figure 2-2 Location and expression of the blind Reelfoot fault. (a) Extent of the surface projection of the Reelfoot fault with locations of modern seismicity (CERI, 2019) and example focal mechanisms (Johnson et al., 2014), Reelfoot fault fold-scarp profiles, and coseismic sackungen (Delano et al., 2018). The blind Reelfoot fault is expressed at the surface as a monoclinal fold—solid lines indicate a clear fold scarp, dotted lines indicate eroded fold trace, dashed where location is approximate and diffuse. (b) Topographic profiles of folding above the northern section of the Reelfoot fault. Gray polygon ranges from minimum to maximum values within 40-m-wide swath; black line is the average elevation. Red-shaded boxes represent the location and width of the monocline forelimb, which is relatively narrow along this section of the structure. The fold scarp amplitude increases toward the center of the Reelfoot fault. The Reelfoot Lake profile includes topographic data from Carlson and Guccione (2010) and is extended with lidar digital elevation models (DEMs) from this study. The red-dashed line is approximate projection of the monocline forelimb above the blind Reelfoot fault. VS – vertical separation.

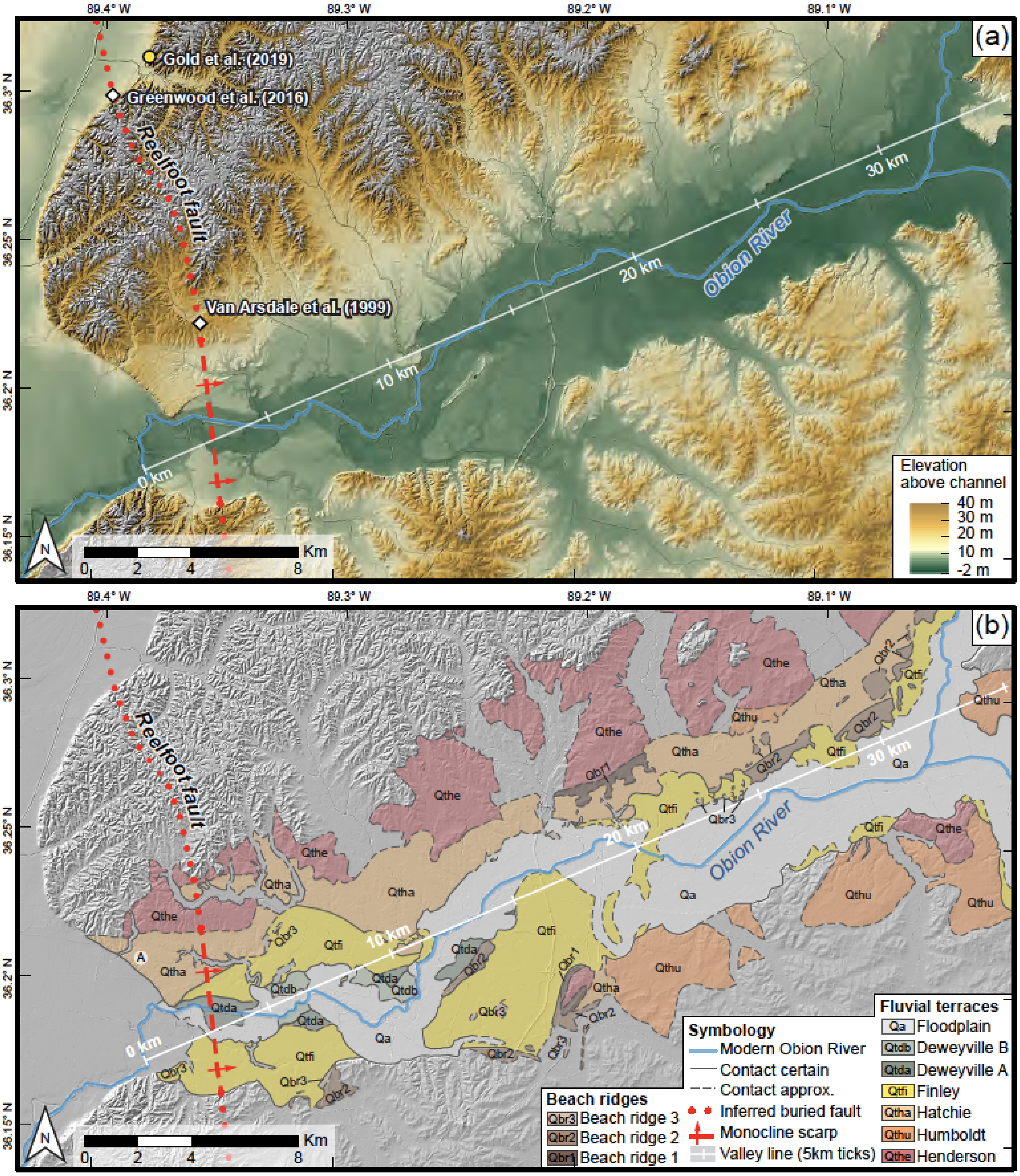

Figure 2-3 Obion River valley and surface projection of the blind Reelfoot fault—dotted lines indicate eroded fold scarp or inferred surface projection, dashed where fold scarp is diffuse. White line shows valley distance used in Figure 2-4. See Figure 2-2 for location. (a) Relative elevation model (REM) of the lower Obion River valley where the modern channel represents base elevation level. The modern flood plain constricts from upstream (east) to downstream (west) indicating uplift in the lower reaches of the valley. Diamonds are seismic surveys that constrain fault location, yellow dot is sackung trench location (Gold et al., 2019). (b) Geomorphic mapping of the lower Obion River valley. Marker A referenced in text.

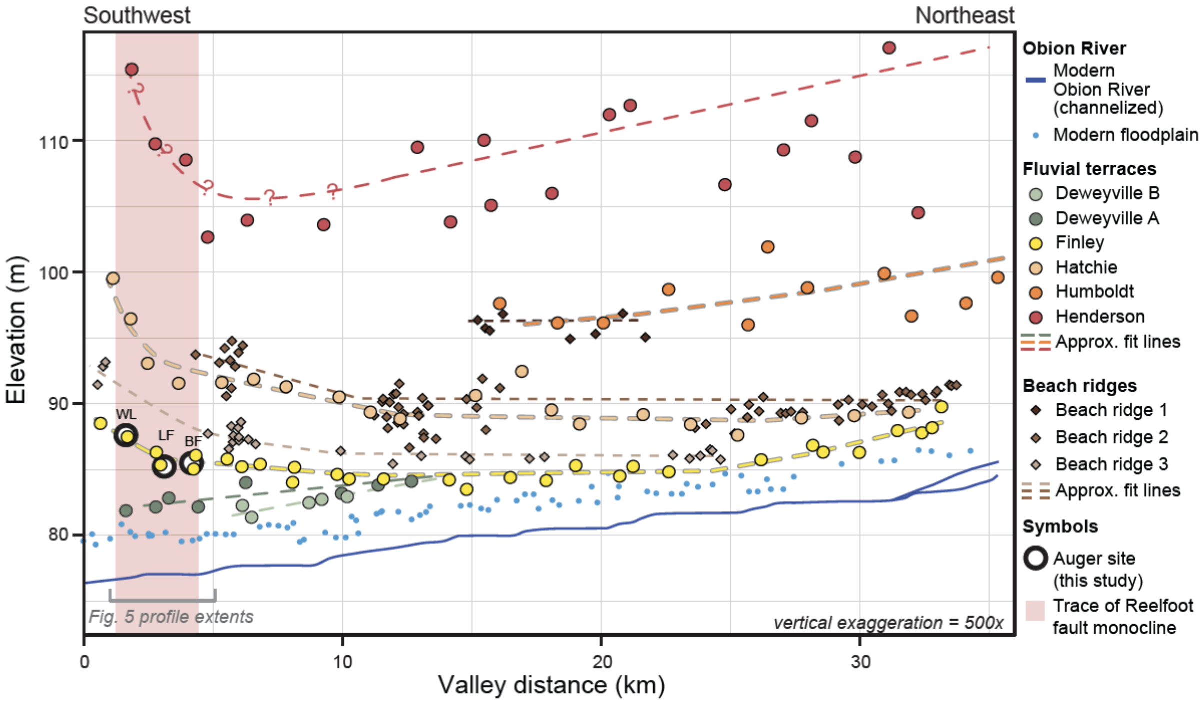

Figure 2-4 Longitudinal valley profiles of Obion River terraces and beach ridge complexes. Geomorphic features are projected orthogonal to a central valley line (see Figure 2-3). The Finley and Hatchie terraces and beach ridges 2 and 3 show apparent folding across the surface trace of the Reelfoot fault. The Henderson terrace may be warped across the fault, but incomplete preservation and post-depositional erosion make the relationship less clear. The horizontal gradients of the Finley and Hatchie terraces indicate a lacustrine-influenced origin. WL= Wilson Loop; LF = Lanesferry; BF = Biggs' Farm.

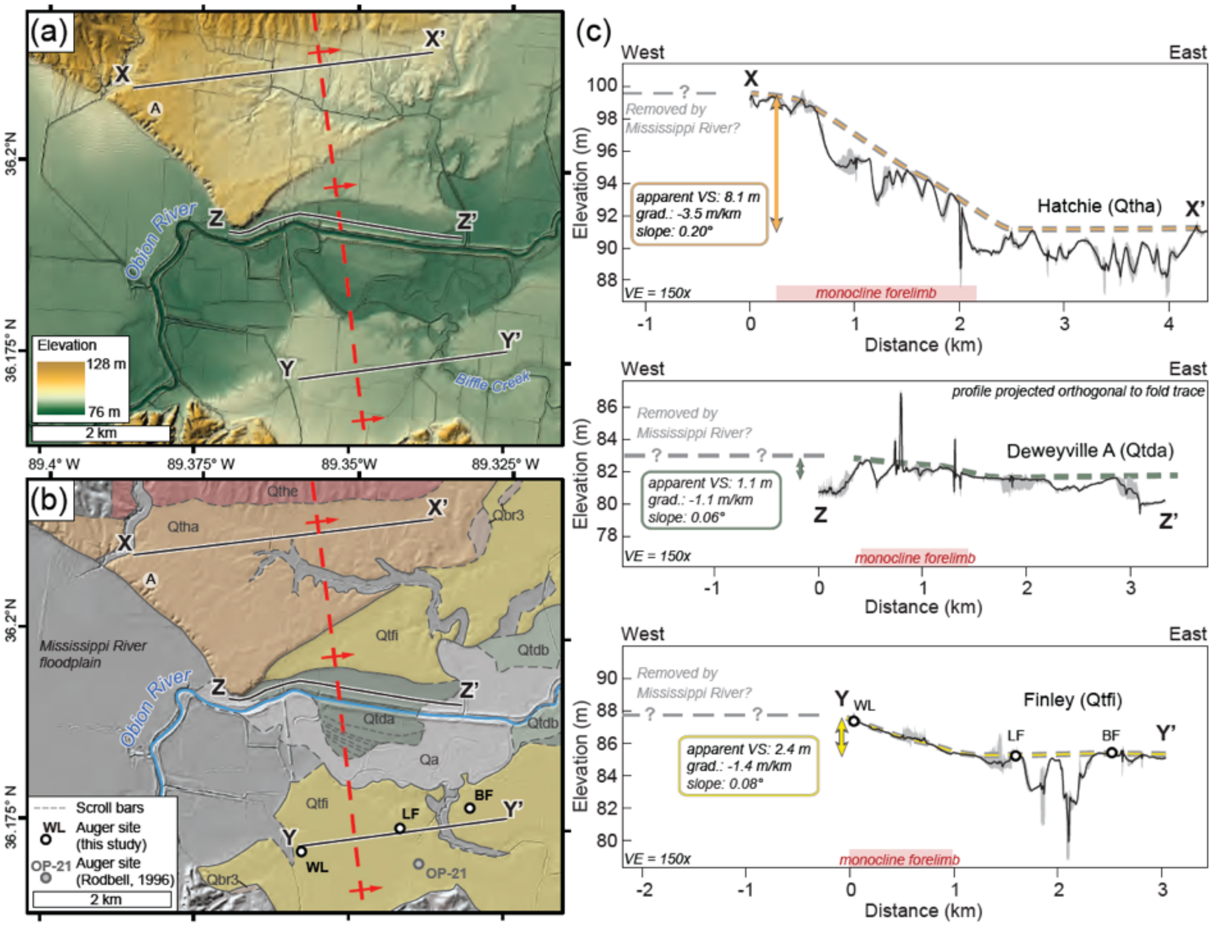

Figure 2-5 Location and expression of apparent warping above the blind Reelfoot fault in the Obion River valley (see Figure 2-2 for location). Marker A referenced in text. (a) Uninterpreted digital elevation model (DEM) of the Obion terraces across the Reelfoot fault monocline. (b) Geomorphic mapping of terraces across the Reelfoot monocline scarp showing auger sites and previous coring locations. (c) Elevation profiles of warped terraces above the blind Reelfoot fault. Gray polygon ranges from minimum to maximum values within 40-m-wide swath; black line is the average elevation. The reverse (flow to the east) gradient/slope and vertical separation (VS) increases with terrace age. The monocline forelimb above the Reelfoot fault is much wider here than farther north (see Figure 2-2). The full extent of deformation is not recorded because the terraces have been truncated by Mississippi River erosion; possible reconstructions of eroded terraces as grey dashed and queried lines. WL= Wilson Loop; LF = Lanesferry; BF = Biggs' Farm.

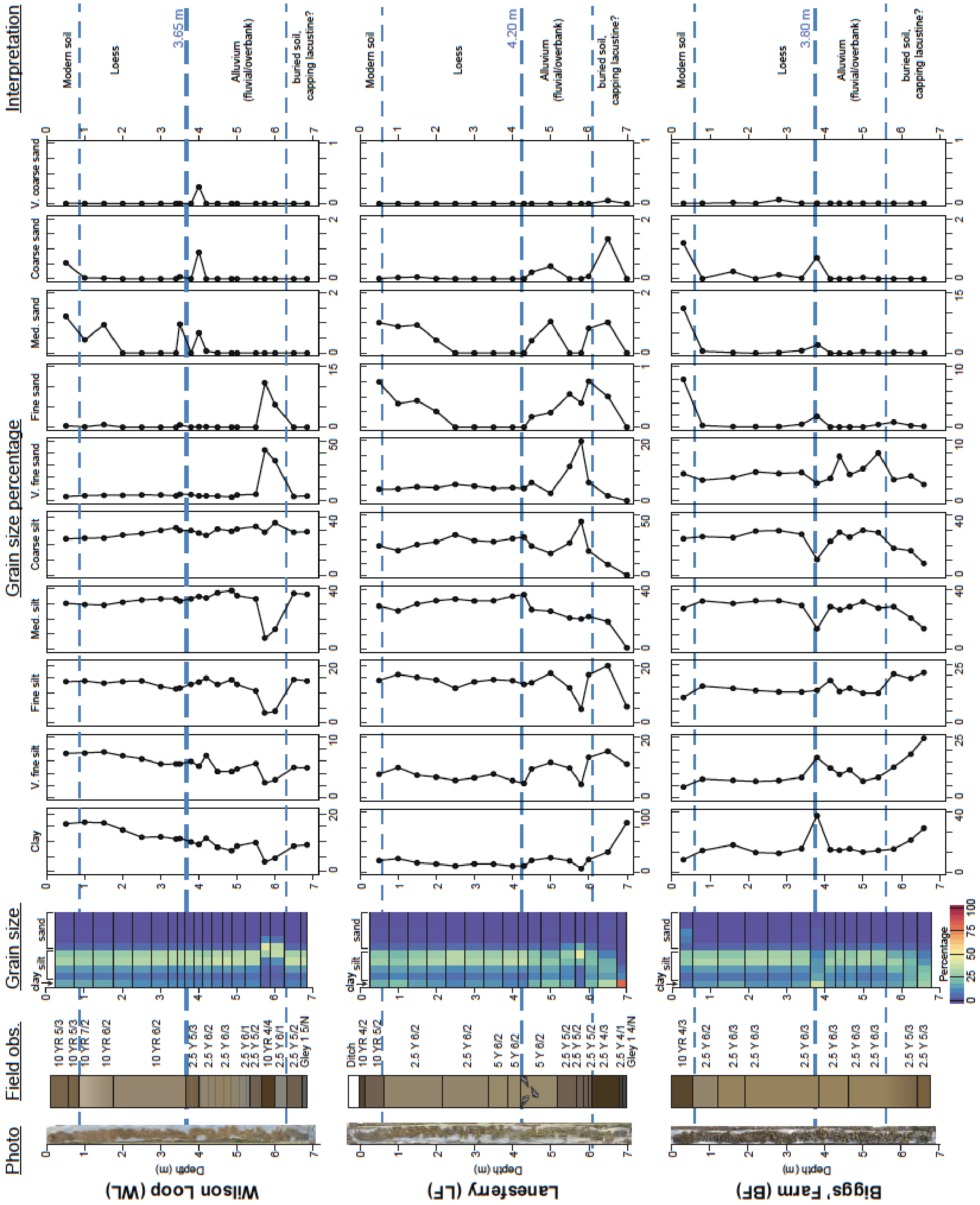
Wilson Loop (WL)
Lanesferry (LF)
Biggs' Farm (BF)
Photo
Field obs.
Grain size
Grain size percentage
Interpretation
Depth (m)
clay
silt
sand
Percentage
0 25 50 75 100
Clay
V. fine silt
Fine silt
Med. silt
Coarse silt
V. fine sand
Fine sand
Med. sand
Coarse sand
V. coarse sand
10 YR 5/3
10 YR 7/2
10 YR 6/2
2.5 Y 5/3
2.5 Y 6/2
2.5 Y 6/3
2.5 Y 6/1
2.5 Y 5/2
10 YR 4/4
Gley 1 5/N
Ditch
10 YR 4/2
10 YR 5/2
5 Y 6/2
2.5 Y 4/3
2.5 Y 4/1
Gley 1 4/N
10 YR 4/3
2.5 Y 5/3
Modern soil
Loess
3.65 m
4.20 m
3.80 m
Alluvium (fluvial/overbank)
buried soil, capping lacustine?

Figure 2-6 Summary of key hand-soil-auger borehole results from the Finley terrace (locations in Figure 2-5, full results in Delano et al., 2021b). Note that horizontal scales vary for each panel to highlight subtle changes in grain size. The "Field Obs." column includes simplified stratigraphic observations such as field-delineated units (black horizontal lines), laminations (grey lines), color changes/gradations, and fossils. The interpreted transition from loess to alluvium occurs between 3.65 m (Wilson Loop) and 4.20 m (Lanesferry) and is marked by a change from homogenous silt to interbedded heterogeneous sand, silt, and clay, and well as the presence of gastropods, laminations, and pronounced color changes due presumably to varying oxidation-reduction conditions. The loess unit has almost no sand below ~1.5-m depth, but notable subtle spikes occur below the interpreted loess/alluvium contact. The base of each auger borehole is marked by a sharp transition to increased fractions of fine to medium silt and/or clay, in some cases gley, which may record paleolakes associated with the horizontal terrace gradient.

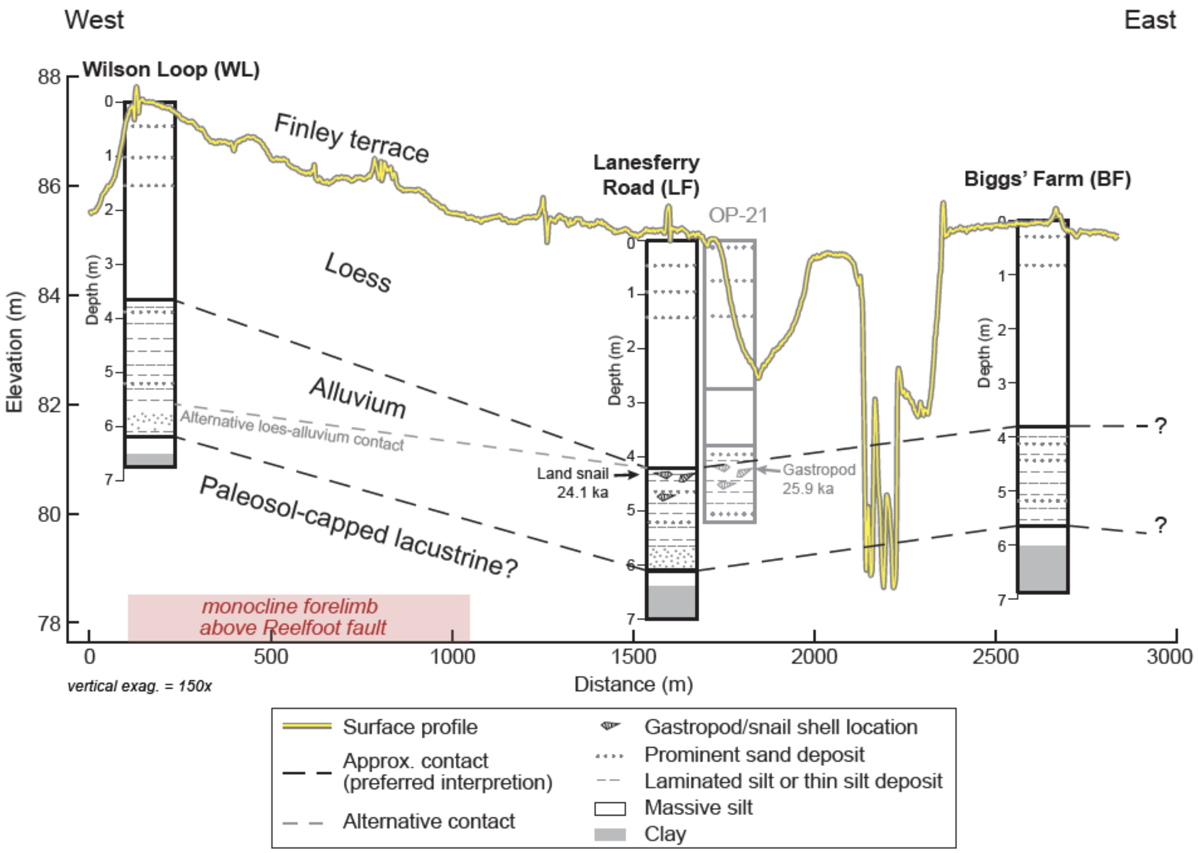

Figure 2-7 Interpreted simplified stratigraphy from auger profile on the Finley terrace across the Reelfoot fault monocline forelimb (red box) (location in Figure 2-5). Yellow line is surface elevation profile. We present two possibilities for the loess-alluvium contact based on uncertainty in the Wilson Loop stratigraphy (3.65-m or 5.6-m depth); however, the alluvium-lacustrine contact parallels the higher contact (3.65 m in Wilson Loop, our preferred interpretation). Stratigraphic contacts parallel the surface and appear warped across the fault projection, indicating fault deformation rather than loess thickening to the west. OP-21 is simplified borehole stratigraphy and recalibrated unidentified gastropod age from nearby core reported by Rodbell (1996), projected to the same profile. OP-21 stratigraphy, depth to gastropod fossils, and gastropod radiocarbon ages agree with findings from this study.

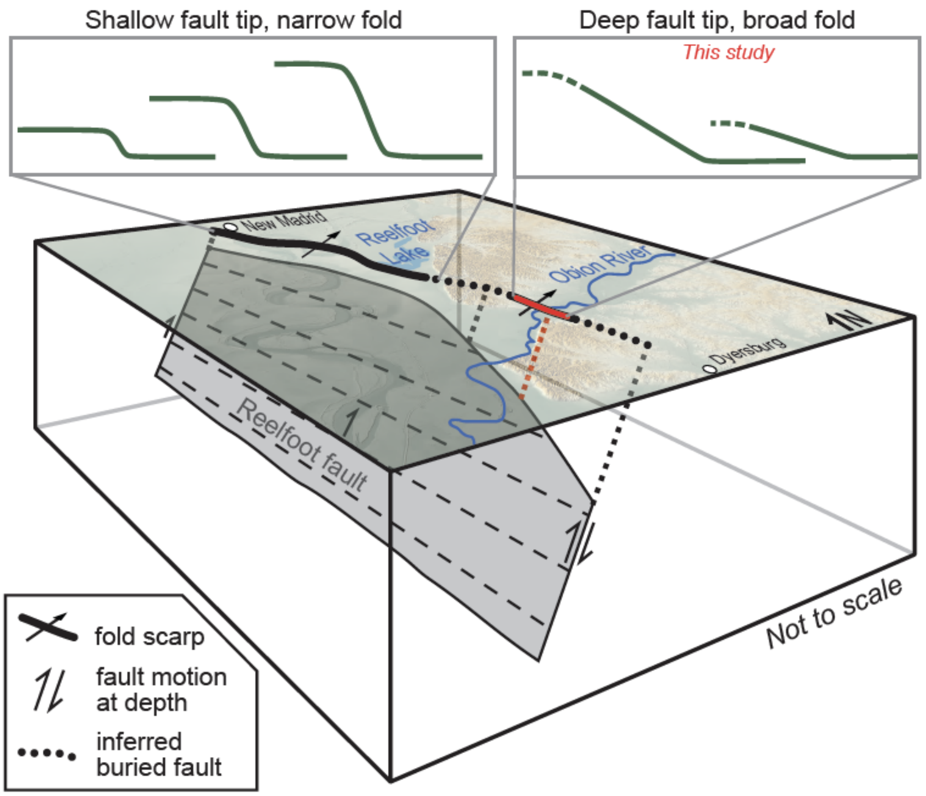

Figure 2-8 Schematic block diagram (not to scale) of the Reelfoot fault at depth demonstrating how changes in fault tip depth affect the surface expression of deformation (black arrows = sense of slip). The active fault tip is closer to the surface along the northern reaches of the Reelfoot fault and plunges deeper along the southern extent (~470-m deep north of Reelfoot Lake, ~1020-m deep in the northern Obion River valley) (Champion et al., 2001). As the active fault tip plunges deeper, folding at the surface widens, making surface deformation more difficult to recognize and measure. Fold scarps reach maximum amplitudes near the center of the fault trace by Reelfoot Lake and taper near the margins. Subtle folding is undetectable in the bluffs between valleys due to the dissected topography which lacks a uniform surface to record deformation.

Table 2-1 Radiocarbon age results of the Finley Terrace.

Sample ID	Location	Material	F14C	14C age [yrs BP]	Calibrated age [cal yrs BP]
OB-LF-420-425	-89.35767, 36.17149	Gastropod shell *Pomatiopsis lapidaria*	0.0827 ± 0.0015	20,030 ± 150	24,457–23,782

3 LIMITED EVIDENCE OF LATE QUATERNARY TECTONIC SURFACE DEFORMATION IN THE EASTERN TENNESSEE SEISMIC ZONE, USA

This section of text is from a draft manuscript in review. Data in this chapter are available in Thompson Jobe et al., 2023.

3.1 Abstract

The ~300-km-long eastern Tennessee seismic zone (ETSZ), USA, is the second-most seismically active region east of the Rocky Mountains. Much of the seismicity occurs below the Paleozoic fold-and-thrust belt within the Mesoproterozoic basement, at depths of 5–26 km, and earthquake magnitudes during the instrumental record have been $M_w \leq 4.8$. Evidence of surface deformation may not exist or be difficult to detect because of the vegetated and soil-mantled landscape, landslides, steep topography, anthropogenic landscape modification, or long and irregular recurrence intervals between surface-rupturing earthquakes. Despite the deep seismicity, analog models indicate that accumulation of strike-slip or oblique-slip displacement at depth would be expected to propagate upward through the Paleozoic section above the decollement, producing a detectable surficial signal of distributed faulting within a broad zone. To identify potential surface deformation, we interrogated the landscape at different spatial scales. We evaluated morphotectonic and channel metrics, such as channel sinuosity and steepness and catchment-scale hypsometry. Additionally, we mapped possible fault-related topographic features on 1-m lidar data. Finally, we integrated our observations with available bedrock and Quaternary surficial mapping and subsurface geophysical data. At a regional scale, most morphotectonic and channel metrics have a strong lithologic control. Within smaller regions of similar lithology, we observe changes in landscape metrics like channel sinuosity and catchment-scale hypsometry that spatially correlate with new lineaments mapped in this study and previously mapped east–west Cenozoic faults in surface and subsurface datasets. These previously mapped faults generally have apparent left-lateral offsets, are optimally oriented to slip in the current stress field, and match kinematics derived from focal mechanisms of recent earthquakes, but do not clearly preserve evidence of Quaternary motion at the surface. Most newly mapped lineaments might also be explained by either tectonic or non-tectonic origins, such as fluvial or karst processes. We also re-evaluated a paleoseismic site described in past studies and interpret that the exposure does not record evidence of late Pleistocene surface faulting but is instead explained by fluvial stratigraphy.

3.2 Introduction

Modern seismicity in these intraplate regions typically drives seismic hazard because potentially active faults are typically un- or under-characterized. These regions are commonly characterized by long earthquake recurrence intervals (e.g., Crone et al., 1992; Bollinger et al., 2021), low or negligible geodetic strain rates (e.g., Calais et al., 2006), and poorly understood drivers of seismicity (e.g., Mazzotti, 2007).

Intraplate seismic zones in the central and eastern United States (CEUS) are no different. This study focuses on the eastern Tennessee seismic zone (ETSZ; Figure 3-1), which stretches for ~300 km along a northeast-trend from northeastern Alabama and northwestern Georgia, through eastern Tennessee and western North Carolina, into southeastern Kentucky and southwestern Virginia (Powell et al., 1994; Hatcher et al., 2012; Carpenter et al., 2014; Levandowski et al., 2023). The ETSZ is the second-most active seismic zone east of the Rocky Mountains; however, it has not hosted a large historical earthquake (Powell et al., 1994). The seismic hazard of the region is estimated largely from instrumental seismicity due to a lack of identified faults at the surface.

Two competing models of expected surface deformation in the ETSZ have emerged (Figure 3-2). One model advocates for reactivation of the Paleozoic structural grain, with dextral strike-slip and thrust motion on northeast–southwest faults during the Quaternary (e.g., Hatcher et al., 2012; Cox et al., 2018; 2022). The second model, based on focal mechanisms and moment tensors from seismicity, predicts strike-slip motion, with either right-lateral motion on north–south fault planes or left-lateral motion on east–west fault planes (e.g., Chapman et al., 1997; Dunn and Chapman, 2006; Daniels and Peng, 2022). An analysis of regional stress integrating recent focal mechanisms indicates that east–west fault (and northeast–southwest) planes are most favorably oriented in the present-day stress field (Levandowski et al., 2023).

In this study, we assessed the landscape at different spatial and temporal scales to identify potential records of surface deformation. We performed a landscape analysis that focused on channel sinuosity and steepness and catchment-scale hypsometric integral to evaluate landscape changes that may correspond with regions of tectonic activity. In addition, we mapped topographic features, such as linear valleys and ridges and scarps that may be indicative of late Pleistocene or Holocene faulting, from 1-m lidar data. We integrated our new observations with previous bedrock and surficial mapping and subsurface datasets to evaluate evidence of recent surface deformation. Finally, we placed our observations in a regional context and compare them to other intraplate settings, expand on limitations of our work, and discuss the implications for seismic hazard.

3.3 Background

3.3.1 Geologic Setting

The ETSZ has a long-lived tectonic history. The Alleghanian orogeny (325–260 Ma) in the Paleozoic created a fold and thrust belt dominated by thin-skinned thrust faults and flexural slip folds with bedding-parallel main thrusts (Harris and Milici, 1977; Cook et al., 1979; Hatcher et al., 2007a). The orogeny resulted in northwest-transported, imbricated thrust sheets of folded Cambrian through Pennsylvanian siliciclastic and carbonate sedimentary rocks in the core of the ETSZ (Woodward, 1957; Secor et al., 1986; Hatcher et al., 2007b; Hatcher et al., 2010). These units overlie a Mesoproterozoic Grenville crystalline basement (Hatcher and Odom, 1980; Wheeler, 1995; Vlahovic et al., 1998; Powell et al., 1994; 2014; Powell and Thomas, 2016; Hatcher et al., 2007a).

East–west faults are present throughout the ETSZ and continue into the Blue Ridge Mountains in western North Carolina (Figure 3-1). Along the Swannanoa lineament, joints and fractures strike generally west–northwest (Hill, 2018). The Boone lineament, near Boone, North Carolina, is a zone of minor faults that typically dip steeply north and south and strike west–northwest (Hill, 2018). These faults exhibit both normal and reverse sense of motion, with a general south-side-up. Paleostress inversions indicate the faults likely formed during the Cenozoic, as it crosscuts the northeast–southwest Paleozoic structural grain (Hill, 2018). Moreover, numerous Cenozoic faults have been recognized throughout the eastern United States in Tennessee and North Carolina, commonly cross cutting the Paleozoic structural trends (Prowell, 1983).

3.3.2 Geomorphology

The ETSZ spans three physiographic provinces: the Blue Ridge, Valley and Ridge, and Appalachian Plateau, with varying rock types that strongly influence the present-day topography. Resistant sandstones, dolomites, and metasedimentary units create ridgetops, while more erodible shales and limestones now form valleys. The region generally has a temperate humid climate, with average precipitation that varies with elevation, from 1016 mm/yr in low elevation areas, to 2286 mm/yr in high elevation areas (Hampson et al., 2000). The landscape is generally soil-mantled with exposed bedrock along ridges and steeper slopes. Land cover is typically forested with cleared fields for agriculture and grazing, and the landscape has been occupied and modified by humans for thousands of years (e.g., Simek et al., 2012).

Several recent studies in the ETSZ have focused on geomorphology to determine if there is a record of surface deformation preserved in the landscape (Gallen and Thigpen, 2018; Lary, 2019). Fluvial erosion has been proposed as a mechanism for seismicity in the New Madrid seismic zone (NMSZ) to the west of the ETSZ due to flexural uplift and decreased fault-normal stresses (Calais et al., 2010). In the ETSZ, Gallen and Thigpen (2018) proposed that erosion from the Upper Tennessee River drainage basin removed a large volume of rock since 9 Ma, driving seismicity in the interior part of the evacuated drainage basin.

In addition to the extensive human modification of the surface (e.g., Cox et al., 2022), it has also been argued that a lack of preservation of surficial deformation results from erosion rates that may substantially outpace, or perhaps keep pace with, deformation rates, at least at a landscape scale (e.g., Spotila and Prince, 2022 and references therein). Erosion rates in the Appalachians are generally low compared to global compilations that include tectonically active areas, but are average for intraplate regions (e.g., Harel et al., 2016). In the Great Smoky Mountains in eastern Tennessee and eastern North Carolina, catchment-averaged ^{10}Be erosion rates are generally between 0.025 and 0.03 mm/yr (Matmon et al., 2003). Farther north in western Virginia, ^{10}Be bedrock erosion rates are even slower (0.0057 mm/yr; Hancock and Kirwan, 2007). In the Central Appalachian Valley and Ridge province farther north along strike of the Appalachians, catchment-averaged erosion rates vary widely from 0.004–0.099 mm/yr (Miller et al., 2013). Modeled long-term erosion rates using landscape analysis in the ETSZ are ~0.027 mm/yr (Gallen, 2018). Although these erosion rates are variable, they require higher vertical deformation rates to preserve any signals of local or regional deformation in the landscape. In at least one location in the eastern United States, the central Virginia seismic zone, deformed fluvial terraces exhibit 0.02–0.03 mm/yr of uplift above a blind thrust fault, at least twice as high as the background erosion rates of 0.008 mm/yr in the Virginia Piedmont (Pavich et al., 1985; Pazzaglia et al., 2021), However, analysis of fluvial scarp degradation in the humid temperate climate of the eastern United States indicates that, if earthquakes produce surface rupture of 1–3 m on low-relief surfaces, fault scarps should be preserved for at least tens of thousands of years (Colman, 1983).

3.3.3 Seismicity

Modern seismicity in the ETSZ is located at depths of 5-26 km, below the Appalachian decollement (Vlahovic et al., 1998; Powell et al., 1994), and is not associated with shallower Paleozoic faults (Bollinger et al., 1991). Instead, colocation of ETSZ seismicity with potential field anomalies indicates the faulting may be associated with ancient basement structure, such as the Proterozoic transform fault the New York-Alabama lineament (NYAL, Figure 3-1; Levandowski and Powell, 2019; Daniels and Peng, 2023), although the lineament is unlikely seismogenic itself (Powell et al., 1994). However, the ETSZ is the only seismically active part of the NYAL. Modern seismicity does not occur on major northeast–southwest-trending structures, but instead focal mechanisms indicate en echelon north–south and east–west-striking faults with primarily strike-slip motion (Chapman et al., 1997; Dunn and Chapman, 2006; Daniels and Peng, 2022). Moreover, an analysis of the seismicity compared against epidemic-type aftershock sequence models indicates the earthquakes within the ETSZ represent long-term strain accrual, not a prolonged aftershock sequence (Levandowski and Powell, 2019). A recent study using template matching also did not find a correlation between seasonal hydrologic changes and seismicity (Daniels and Peng, 2023).

The largest earthquakes on record include the 1987 M_b 4.2 Vonore, Tennessee (Nava et al., 1989), 1973 M4.3 Alcoa, Tennessee (Bollinger et al., 1976), 2018 M_w 4.4 Decatur Tennessee, (Daniels and Peng, 2022) and the 2003 M_w 4.8 Fort Payne, Alabama (Withers et al., 2004), events, although the seismic network in the region has only been established since 1984 (CERI, 2019).

3.3.4 Paleoseismology

Although the historical seismic record is limited to <M_w 4.8 earthquakes, several studies report interpretations of paleoseismic evidence of potentially larger earthquakes during the Holocene. These paleoseismic sites are located at the southeastern margin of the ETSZ, along the Dandridge-Vonore fault zone (Figure 3-1; Hatcher et al., 2012; Warrell et al., 2017; Cox et al., 2018, 2022). Stratigraphy in natural exposures and trenches have been interpreted as faulting along N55°E-striking, southeast-dipping thrust faults in alluvium, dated to the late Pleistocene, with displacements up to 1 m (Warrell et al., 2017). The trenches and exposures are interpreted as preserving ≥3 large late Pleistocene earthquakes. However, there are several discrepancies between these results and other datasets. Primary among these is that these studies do not report geomorphic evidence of surface faulting recorded by Quaternary surfaces anywhere along the Dandridge-Vonore fault zone. Also, the presumed active faults are not optimally oriented in the current stress field, nor are thrust faults expected in the region (Levandowski et al., 2018; Figure 3-1b).

Limited paleoliquefaction features are observed in the ETSZ (Hatcher et al., 2012; Warrell et al., 2017; Cox et al., 2018; 2022), which may be a result of sediments that are not susceptible to liquefaction or to the lack of past ground-shaking events that are strong enough to initiate paleoliquefaction. In addition, the extensive cultural modification of the landscape over the last several hundred years may have removed evidence of some paleoliquefaction.

3.4 Methods

3.4.1 Morphotectonic metrics

We calculated morphotectonic metrics to assess surficial evidence of tectonic deformation on a regional scale. These metrics were calculated using TopoToolbox, an open-source toolbox for MATLAB (Schwanghart and Kuhn, 2010; Schwanghart and Scherler, 2014) and QGIS v3.14 on a 30-m Shuttle Radar Topographic Mission (SRTM) and 10-m National Elevation Dataset (NED) digital elevation model (DEM) available through the U.S. Geological Survey (USGS) National Map program (https://apps.nationalmap.gov/downloader/). We focused on calculating parameters that have been shown to correlate with tectonic activity, usually with an assumption of uniform lithology. Given that lithology may strongly influence the geomorphology in the region (e.g., Gallen, 2018), we assessed channel sinuosity and steepness at a regional scale to identify changes in these parameters that occur within the same lithology and may record a tectonic signal. Then, on a local scale, we assessed morphotectonic metrics of catchments >5 km^2, including normalized channel steepness and hypsometry (hypsometric integral and curves) that may correlate with tectonic activity. In these smaller regions, we selected a centerline extending approximately subparallel to the river and projected the midpoint of each catchment into the centerline to assess trends. For catchment metrics, we assumed that all streams joining the main trunk river experienced a similar base level history. Recent anthropogenic modifications to the landscape, such as damming of rivers to create reservoirs, the creation of holding ponds, or channelization and irrigation for agricultural purposes, may influence the channel profiles and planforms. To avoid these potential issues, we selected catchments that were far enough upstream to not be affected by the creation of reservoirs and that had no clear evidence for anthropogenic modification in the lidar data.

Channel sinuosity, which is the channel thalweg distance divided by the valley straight-line distance, has been shown to be sensitive to subtle slope changes (Holbrook and Schumm, 1999; Holbrook et al, 2006) sometimes created by tectonic activity. Generally, sinuosity will depend on the river-length window over which it is calculated; typically, a range of 30 to 100 times the channel width (e.g., Rosgen, 1996), or at least one order of magnitude larger than the width of the active channel (e.g., Nardini and Brierley, 2021), has been shown to be sufficient to capture a regional signal. In the ETSZ, maximum channel widths are on the order of 100 to 130 m where the channel is not dammed; thus, we used moving windows between 5 and 20 km.

Catchment-scale hypsometry is the distribution of elevation in a catchment (Strahler, 1952). Because the hypsometric integral has been shown to be dependent on the calculated scale or catchment-size (Willgoose and Hancock, 1998; Hurtrez et al., 1999a; Hurtrez et al., 1999b; Mahmood and Gloaguen, 2011) and lithology (Hurtrez and Lucazeau, 1999), we focus on catchments within the same broad lithology.

3.4.2 Lineament mapping

To assess surficial records of possible tectonic deformation, we used high-resolution 1-m lidar data to map previously unidentified topographic lineaments throughout the ETSZ. We use the term “lineament” to broadly define a variety of linear topographic features for convenience. These features include: (1) scarps, where discrete discontinuities offset a Quaternary surface, commonly with a similar gradient on either side of the scarp; (2) linear drainages, where a section of the river valley is straight; and (3) topographic lineaments, which are linear features in the landscape, such as linear ridges or alignments of surfaces, depressions, springs, or sinkholes, that may have a tectonic origin. All lineaments were classified into three categories based on their characteristics and assigned a tectonic confidence (low, medium, or high). Where geologic maps are available, we compared the geologic mapping against the lineaments to assess whether they could result from bedding or lithologic juxtapositions, in addition to using aerial and satellite imagery to assess if the lineament could have a mass wasting, karst, or anthropogenic origin. Distinguishing karst from tectonic origin is challenging in this region due to the prevalence of bedrock units with carbonate and fracturing. Surficial lineaments can be formed by subsidence of sediment into solution-enlarged crevices. In addition, linear drainages or valleys can also represent fracture-controlled drainage (Panno et al., 2011), and surface and subsurface datasets in the region document the extensive karst development (e.g., Doll et al., 2005). Finally, due to a lack of dated Quaternary surfaces in the region, we were unable to assess recency of potential faulting or determine slip rates. We use qualitative observations, such as the sharpness of scarps in the landscape, to broadly discuss recency but acknowledge absolute age control is needed to constrain ages on potentially offset surfaces.

3.4.3 Field observations

We targeted six locations to field check the possible tectonic features and assess channel characteristics. These sites included three sites in the Powell River area, two in the Oak Ridge area, and the Little River site near Alcoa, Tennessee. At each site, we assessed the mapped offset surface, checked for recent anthropogenic modification of the scarps, and documented karst features, bedrock orientations, and mass wasting observations, where applicable. In addition, we created a structure-from-motion (SfM) model to log and interpret the outcrop along the Little River following the workflow outlined in Reitman et al. (2015) and Delano et al. (2021c).

3.5 Results

3.5.1 Regional river channel analysis

Regionally, channel steepness and sinuosity appear to be at least partially lithologically controlled, similar to the findings of past studies in the region (e.g., Gallen, 2018). We do observe broad east–west trends of sinuosity that appear unrelated to sharp lithologic changes (Figure 3-3). However, some meanders in the ETSZ, such as along the upper reaches of the Powell River, appear to be entrenched meanders. Entrenched meanders develop where the meanders of alluvial rivers are superimposed into bedrock during uplift in the absence of significant tilting (Gardner, 1975; Schumm and Brakenridge, 1987).

3.5.2 Lineaments

East–west and north–south subtle lineaments are observed across the ETSZ (Figure 3-3). Most lineaments are <3 km long, but a few are up to ~12 km long. Most lineaments are broadly described as topographic lineaments or linear drainages, with few scarps mapped. We did not find any clear evidence of lateral motion (i.e., no laterally offset geomorphic markers) along any lineaments. In general, mapped lineaments have strikes that are west–northwest–east–northeast or east–west. In the northern ETSZ, mapped lineaments have a similar strike to previously mapped east–west Cenozoic faults and can sometimes be found along strike of a previously mapped east–west fault.

3.5.3 Sites of Interest

3.5.3.1 Powell River area

The Powell River area is located at the northern end of the ETSZ, near the border with Kentucky. The region has experienced moderate seismicity, with focal mechanisms generally indicating either east–west or north–south fault planes. The bedrock in the region has been previously mapped in detail (Brokaw et al., 1966); east–west Cenozoic faults with small offsets are observed. In addition, most of the region comprises the same underlying lithology – carbonates, dolomites, and limestones (Brokaw et al., 1966). We performed a local analysis of catchment-scale metrics in addition to making field observations of two lineaments in the Powell River area located on the Chuck Swan State Forest.

Along the Powell River, channel sinuosity changes as the river flows through the same underlying lithology from the northeast to the southwest (Figure 3-4a). The channel is more sinuous in the northeast and becomes less sinuous as it approaches the reservoir. In addition, catchment-scale hypsometry and normalized channel steepness also change downstream. Higher hypsometric integrals are observed where the channel is more sinuous, whereas lower hypsometric integrals are observed where the channel is less sinuous (Figure 3-4a, b).

The southernmost lineament, called K1, is located north of Levi Springs Road and south of Clear Creek (Figure 3-5a, b). The lineament trends west–northwest–east–southeast for ~600 m. On surface models derived from lidar data, K1 appears as an alignment of linear drainages, a linear trough, and channels that change width across the lineament. Along the lineament, there is not a fresh scarp, but there are subtle 20- to 40-cm depressions and troughs, an uphill-facing scarp, and a linear break in slope (Figure 3-5e). We also observed closed depressions that are oblong and aligned with the lineament. At the western end of lineament K1, we observed limestone bedrock outcrops on other side of the lineament that appeared to be vertically offset. The attitude of local bedrock was oriented highly oblique to the lineament, with a strike/dip of 043/16 and 048/13 on the northern and southern sides, respectively. Together, these observations indicate that (1) the lineament is not a result of bedding or bedrock-controlled; (2) karst or dissolution is a possible explanation for the lineament, given the closed depressions and troughs observed along the lineament; and (3) if the lineament is neotectonic, recent vertical offsets are small (<40 cm) and likely not recent, given that fresh scarps were not observed.

The northern lineament, called K2, is located west of White Road (Figure 3-5c, d). The lineament also trends west–northwest–east–southeast for ~600 m and is observed on both sides of a tributary branch of White Creek. On the eastern side, there is a sharp break in slope along the north side of a tributary drainage. Along the creek, younger fans and terraces do not appear to be deformed. Towards the west up to the next ridgetop, we traced a linear depression to a flattened space. At the ridgetop, there is clearly a depression or saddle with linear scarps on either side, but no observable net vertical across the depression. We speculate this site may be artificially modified to be flattened but did not find definitive evidence. Together, these observations indicate that (1) the lineament is not a result of bedding or bedrock controlled; (2) karst or dissolution along the lineament is a possible explanation; (3) given the lack of scarps or other features observed on the youngest (Holocene?) fans and terraces along White Creek, if neotectonic, there has not been recent vertical movements or vertical movements were small enough to be erased since the last event; and (4) this feature is unlikely to be a sackung, given that it is visible across a hilltop as a small graben-like depression and is also visible at the same orientation across multiple hilltops and slopes that appears to be a continuous lineament.

The changes in hypsometric integral, channel sinuosity, and spatial coincidence of previously mapped east–west faults and newly mapped lineaments are evidence for a possible tectonic control on the landscape, but the lack of scarps in the youngest deposits indicates that either any potential surface deformation associated with tectonic control is not recent or was of a small magnitude. Thus, we interpret that these observations provide equivocal evidence for Quaternary surface deformation.

3.5.3.2 Oak Ridge

Oak Ridge, Tennessee, is located at the western end of the ETSZ and has been studied in detail because of the critical facilities in the region. A recent study used seismic refraction tomography to image the upper 30 m of the subsurface (Atre and Carpenter, 2010). In this study, six lines, coincident with seismic reflection lines from Doll et al. (1998), reveal several joint sets that had been previously mapped and identified by Foreman and Dunne (1991) and Hatcher et al. (1992). Although most fractures are bedding plane fractures (N55°E) or bedding perpendicular strike-parallel joints (N41°E), an east–west joint set that crosscuts the regional fabric was observed (Atre and Carpenter, 2010). These joint sets are consistent with east–west cross-valley faults discovered by Hollon (1997), which vertically and laterally offset subunits within the Nolichucky Shale of Conasauga Group by <10 m and ~50 m, respectively. The data also support the presence of 54-60° dipping apparent faults (Doll et al., 1998) that coincide with lineaments visible on aerial photos of Bear Creek Valley (Atre and Carpenter, 2010).

In the Oak Ridge area, we mapped east–west-trending scarps, topographic lineaments, and linear drainages (Figure 3-6a). We field-checked two of these features, classified as scarps, near the town of Oak Ridge along Poplar Creek and tributaries. The southernmost scarp is ~700-m long and is parallel to a mapped topographic lineament and another scarp in an adjacent creek valley to the east, forming a total length of ~2.5 km if connected. We observed a <2-m-high scarp along Old Harriman Highway. The scarp faces southwest and has scalloped, uneven edges, indicating that it may be fluvially modified or have a fluvial origin. The northern scarp also trends west–southwest–east–northeast and is ~1.9-km long (Figure 3-6b, c). It aligns with a short topographic lineament, for a total length of ~2.4 km. The scarp faces northwest and has a straight, linear character, with Poplar Creek making 90° bends to flow parallel to the scarp and then around the tip. The scarp height decreases from southeast to northwest (~30 m to <10 m) and the terrace surface is backtilted, with younger incised drainages curving to the southwest (Figure 3-6c). At the western end of the Oak Ridge area, near the Emory River, an east-west topographic lineament crosses seismic line ARAL-3 (Figure 3-6a; Hopkins, 1995). There does not appear to be any vertical offset of the base of the Paleozoic, nor any clear vertical offset of the thrust faults above the decollement. However, the seismic data are noisy and have poor reflectivity in the shallow section at this location along the line, perhaps due to the proximity of the Emory River and reservoir.

Although there are surface and subsurface features that are indicative of Quaternary faulting, the origins of these features remain ambiguous. Based on the orientation of the scarps relative to the channels, the scarp origin could be explained by fluvial processes. Similar sharp bends are also observed along other rivers in the region even where lineaments were not mapped. Moreover, the discontinuities in the subsurface data could also be explained by karst development, which has been extensively documented in the Oak Ridge area (e.g., Doll et al., 2005). We interpret these features to be ambiguous evidence for Quaternary faulting and more work is needed to assess a potential tectonic origin.

3.5.3.3 Little River

We revisited the Little River/Alcoa paleoseismic site along the northern bank of the Little River at Brakebill Island (Figure 3-7a; 35.8199°N, 83.8961°W; Cox et al., 2018; 2022). The motivation was to reconcile the interpretations of late Pleistocene faulting with the lack of visible scarps or lineaments on adjacent Quaternary surfaces. Although undercut trees indicate the exposure is slightly different than reported by previous studies (Cox et al., 2018; 2022), the presence of the apparent deepest portion of an optically stimulated luminescence (OSL) sample (Figure 3-7) indicates the bank has been cut back <40 cm. The bank is 4+ m high. We cleaned and photographed an approximately 2.2-m high by 4.5-m wide section of the exposure, created an SfM model, and mapped the outcrop. New observations do not support an interpretation of surface faulting at the Little River site.

Previous work interpreted a low-angle (41°), southeast-dipping thrust fault in the exposure that is subparallel to the regional structural grain and nearby thrust faults (Figure 3-7a; Cox et al., 2018; 2022). In prior studies, a minor channel fill is interpreted to be offset by the fault, with 1.3

m of net slip on the top of the Little River channel fill and 0.65 m of net slip on the overbank sand and gravel-rich colluvium (Cox et al., 2018; 2022). Four OSL samples from this exposure all date to between 10.3 and 12.9 ka, with two surface-faulting events interpreted to have occurred between 10 and 15 ka based on stratigraphic relationships (Cox et al., 2022).

The exposure (Figure 3-7) reveals a bedrock strath overlain by coarse gravels and sand in a series of inset channels extending to ~1.5 m above the strath surface. Above the gravels is a ~2.5-m-thick section of sand and silt (see Table 3-1 for unit descriptions). Observations at this exposure include (1) The bedrock strath surface at the base of the exposure is not vertically offset. Although there is <10 cm of relief on the surface, it is the wrong sense of motion (observed down-to-the-east versus expected down-to-the-west) for the previously interpreted fault. The strath surface was also visible both upstream and downstream at approximately water level, indicating no broad offset of the surface. (2) The coarse basal gravel on top of the strath surface (unit 2, Figure 3-7c, d) is not offset. (3) There is no evidence for shearing in the sandy, laminated unit 8, which appears to be a toppled riverbank block with continuous stratigraphy. (4) The top of the sandy unit 8 is at least 10 cm higher than the tops of the adjacent gravels (units 10 and 11), which are roughly at the same elevation, contrary to apparent thrusting depicted in previous studies (Cox et al., 2018; 2022). (6) The downstream nested channels continue for ~30 m. (7) The site marks a major facies change between clast-supported gravels up river and a set of nested channels of primarily sand, silt, and gravel down river. (8) There is no evidence of colluvium deposited on a stable surface. Although there are some darker horizons in the section, there are not well-developed soils that represent significant depositional hiatuses and subaerial surface soil formation at the site.

Based on the available observations in the lidar and from the exposure, this exposure is interpreted to record a series of cut and fill channels, with some bank collapse features and mass wasting, that were deposited on top of a strath surface composed of the Nolichucky Shale of Conasauga Group. In contrast to previous interpretations, we interpret that the exposure does not record faulted late Pleistocene fluvial and colluvial deposits and instead is more readily explained by fluvial cut and fill stratigraphy.

3.6 Discussion

3.6.1 Expected records of surface deformation

The instrumental seismicity record indicates that the earthquakes in the ETSZ occur at depths between 5 and 26 km, within the Proterozoic basement and not within the overlying Paleozoic fold and thrust belt (Powell et al., 1994; Vlahovic et al., 1998). With such deep seismicity below a regional decollement, how might faulting and deformation be expressed at the surface? As previously explained, there are two competing models for the orientations of faults and surficial expression of tectonic deformation in the ETSZ (Figure 3-2). One model argues for reactivation and recent faulting along the northeast–southwest Paleozoic structural grain (Model A in Figure 3-2; Hatcher et al., 2012; Cox et al., 2018; 2022), whereas the second model indicates recent faulting occurs on faults trending east–west (Model B in Figure 3-2; Chapman et al., 1997; Dunn and Chapman, 2006; Daniels and Peng, 2022). There is no clear seismological evidence for shallow (<5 km) movement along the Paleozoic fold and thrust belt, nor is there any clear expectation that northeast–southwest oriented faults (i.e., Model A in Figure 3-2), if active, would rupture in a reverse sense (Levandowski et al., 2018). Single discrete surface ruptures directly above the basement faults is not supported by the years of surficial and bedrock mapping in the region, nor the regional seismic lines, neither of which clearly document surface rupture nor large-vertical-offset faults that match focal mechanisms.

Analog models can help infer how deformation may manifest at the surface. Although analog models are never an exact match for the geologic settings they represent, scaled models with a thin, previously shortened sedimentary cover over a strike-slip deeper basement fault (e.g., Rosas et al., 2012; 2014; Koyi et al., 2016) are similar to the ETSZ. The results show that movement on basement faults can be expressed at the surface, but that surface expression is complex. The pattern and width of the experimental surface deformation depends on the angle between the fault systems and the relative timing between deformation events. Post-orogenic basement fault movement has less influence on the thickened hinterland in the fold and thrust belt, where pre- and syn-orogenic basement fault movement has the most prominent surficial expression, creating rhombic shapes that may resemble flower structures (Koyi et al., 2016). Regardless of the relative order of initiation of faulting, small lineaments that have similar orientations to the basement faults but may be offset from the actual locations of the basement faults are present in all models (Koyi et al., 2016). In other models, where basement faulting is post- or syn-orogenic, the basement faults may be expressed at the surface through a broad distributed fault zone, with fault traces up to 20° off the primary fault trace and a fault zone width that can be wider than the thickness of the overburden cover (Rosas et al., 2012).

Together, these modeling insights indicate that a single surface trace may not be observed, but instead broad zones (>4–6 km wide) of discontinuous surface traces that may or may not be offset from the basement faults at depth may be present (i.e., Model B in Figure 3-2). These fault traces may exhibit a variety of kinematics; the models predict flower structures at the surface, with dominantly thrust and left-lateral senses of slip on fault traces within 20° of the basement fault strike, but minor normal faults may also be present.

Identifying records of past surface faulting and seismicity in intraplate settings is a global challenge. Historical surface ruptures have occurred during moderate magnitude earthquakes (~M5–6; 2019 M_w 4.9 Le Teil, France, Ritz et al., 2020; 2018 M_w 5.3 Lake Muir, Australia, Clark et al., 2020). These surface ruptures produced small vertical offsets (<60 cm) and have shallow (<5 km) epicenters. For example, the 2019 M_w 4.9 Le Teil, France, earthquake produced 15 cm of vertical offset with a very shallow focal depth of 1–3 km (Ritz et al., 2020). The 2020 M_w 5.1 Sparta, North Carolina, earthquake resulted in <25 cm of vertical offset with a focal depth of less than 4.1 km (Figueiredo et al., 2022). The 2018 M_w 5.3 Lake Muir earthquake sequence in Australia created 20-60 cm of vertical uplift with an epicenter at ~1.7 km depth (Clark et al., 2020). The depths and kinematics of these intraplate earthquakes contrasts with those observed in the ETSZ, where seismicity is much deeper (5–26 km) and kinematics indicate primarily strike-slip faulting (Chapman et al., 1997; Dunn and Chapman, 2006; Daniels and Peng, 2022), which may be more difficult to preserve in vegetated and soil-mantled landscapes in intraplate settings such as the ETSZ (e.g., Reitman et al., 2023).

3.6.2 Limited evidence of tectonic surface deformation in the ETSZ

In general, there is evidence for tectonic features—both previously mapped bedrock faults and younger lineaments on the landscape—that align with slip planes consistent with patterns from moment tensors and focal mechanisms from seismicity. Furthermore, these features are optimally oriented to slip in the modern stress regime (Levandowski et al., 2018; 2023), and some may be capable of surface-rupturing earthquakes, similar to the M_w 5.1 Sparta earthquake (Figueiredo et al., 2022).

Despite their optimal orientation in the modern stress regime and alignment with slip directions predicted from seismicity, lineaments across the ETSZ cannot be definitely linked to an active tectonic origin. The lineaments are not clearly formed by recent tectonic activity, and many of the surficial lineaments could be explained by karst or fluvial processes. Importantly, we did not observe any fresh scarps in the lidar data or landscape, and no conclusive paleoseismic evidence to suggest Holocene or late Pleistocene near-surface ruptures for any features in the region, including along the Dandridge–Vonore fault system (Cox et al., 2018; 2022).

Morphotectonic metrics show that sinuosity changes spatially coincide with groupings of east–west-oriented lineaments, and at least at the Powell River, correspond to changes in the hypsometric integral of catchments within the same lithology. These landscape metric observations are also spatially coincident with previously mapped east–west Cenozoic faults, visible on both surface (this study; Brokaw et al., 1966) and subsurface datasets (Hopkins, 1995; Hollon, 1997; Atre and Carpenter, 2010) that crosscut the regional Paleozoic structural grain. If these features are a record of late Pleistocene or Holocene tectonic activity, perhaps the largest unknowns are the timing and any correlative or causative relationship between observations of lineaments and channel sinuosity. Importantly, the morphotectonic metrics alone do not require recent tectonic uplift (e.g., Woolderink et al., 2021). Given the depth of the entrenched meanders throughout the ETSZ, the changes in channel sinuosity may support broader regional uplift on a longer timescale, but the sinuosity of the river systems are unlikely to record a response to late Pleistocene or Holocene tectonic activity. Sinuosity changes may reflect the regional channel network orientation and impact of anthropogenic activity more so than recent tectonic activity. Many channels within the ETSZ are controlled by the structural grain in the landscape, with an underlying lithologic control on the valleys and ridges. Throughout large parts of the ETSZ, the major streams are flowing parallel to the regional structural grain and often confined by the ridges. Moreover, the low sinuosity in southern ETSZ may reflect damming of the major channels and the subsequent changes to the river planforms. Changes in sinuosity on dammed rivers have been observed throughout the world due to changes in the rivers length from base-level change and ponding behind dams and changes in the water and sediment discharges both upstream and downstream of the dam (e.g., Marston et al., 2005; Kale and Ataol, 2021) However, it is difficult to estimate how far upriver from the dam these impacts may extend and understand the complex interplay and effects of damming and changes in water and sediment discharge without more data.

Our interpretations are limited by the coverage of available and easily accessible geologic mapping (Figure 3-3 inset; Figure B-1). Although much of the region has been mapped, the spatial coverage of easily accessible 1:24,000 geologic maps that depict detailed surficial geology and smaller-scale faulting is limited (Figure B-1, see Appendix B for more details). Thus, we rely heavily on older geologic maps at 1:125,000 scales (Rodgers, 1953) and 1:250,000 maps (Hadley and Nelson, 1971; Rankin et al., 1972), which span the entire region. Thus, the correlations of newly mapped lineaments with previously mapped faults are biased by the available detailed mapping.

Evidence of recent tectonic surface deformation may have been removed from the landscape, but if so, vertical surface deformation rates must be low enough such that meter-scale features have been effectively removed at ten-thousand to hundred-thousand year time scales. As briefly discussed in the Geomorphology section (Section 3.3.2), vertical deformation rates must keep pace with or outpace erosion rates for features to be preserved at local or regional scales. Bedrock and catchment-averaged ^{10}Be erosion rates in the Appalachians vary from 0.008–0.03 mm/yr (e.g., Miller et al., 2013; Pazzaglia et al., 2021), so vertical surface deformation rates may be lower than erosion rates and thus evidence of surficial deformation is not preserved. Moreover, several studies document abrupt landscape change in the Appalachians from stream captures and drainage reorganization (e.g., Johnson, 2020; Spotila and Prince, 2022), which may also lead to rapid incision, erosion, and removal of records of surface deformation.

3.6.3 Regional context

Regionally, west–northwest–east–southeast and east-west lineaments are observed in both eastern Tennessee and western North Carolina (Figure 8; Hack, 1982; Gay 2000; Hill, 2018; Wells-Hull, 2022). In western North Carolina, the lineaments are proposed to be faults that have been active during the Cenozoic and likely post-Miocene, based on paleostress inversions of minor faults along the lineaments that are inconsistent with Paleozoic and Mesozoic paleostress directions, and they crosscut Paleozoic structures (e.g., Hill, 2018). Analysis of channel profiles, planforms, and knickpoints also indicates some differential vertical uplift across the Boone and Swannanoa lineaments (Figure 3-8; Hill, 2018). Moreover, some lineaments align with small to moderate magnitude earthquakes (e.g., Boone lineament and Little River fault; Hill, 2018; Figueiredo et al., 2022). The Little River fault, which ruptured in the 2020 M_w 5.1 Sparta earthquake, has a similar strike from mapping of the surface rupture and interferometric synthetic aperture radar, with limited evidence for repeated activity during the Quaternary from paleoseismic trenching and ground penetrating radar (Figueiredo et al., 2022). Historical moderate magnitude earthquakes within the Blue Ridge province in North Carolina have also been documented, with shaking intensities of MMI V-VII, but the causative faults remain unknown (Reinbold and Johnston, 1987; Stover and Coffman, 1993). These observations indicate there may be an inherited approximately east–west Cenozoic tectonic grain that may be reactivated in the present-day stress regime (Levandowski et al., 2018; 2023). Many of these faults are composed of short en echelon sections with evidence for strike-slip and vertical motion (Wooten et al., 2010; Hill, 2018), similar to what may be recorded in the ETSZ. Notably, however, most of the mapped lineaments in this study and the west–northwest to east–southeast and east–west lineaments from previous mapping do not clearly coincide with modern day seismicity (Figure 3-8), with a few exceptions (e.g., Boone lineament; Hill, 2018). Additional work could help determine the timing of possible paleoearthquakes along these faults.

3.6.4 Seismic Hazard Implications

In past seismic hazard models (Frankel et al., 1996; Petersen et al., 2008; 2014; 2018), the ETSZ was characterized as a zone with modified smoothed seismicity relationships because individual fault sources have not yet been identified. The paleoseismic work published in recent years has not revealed strong evidence of late Pleistocene and Holocene shallow subsurface deformation (Hatcher et al., 2012; Warrell et al., 2017; Cox et al., 2018; 2022). Our reinterpretation of one of these sites is that the proposed Dandridge-Vonore fault zone is not as extensive as previously described. Moreover, the uncertainties regarding the timing of fault activity and the lack of a discrete fault at the surface from the results of lineament mapping from lidar data and morphotectonic analysis do not permit characterization of the ETSZ with fault sources. At present, the ETSZ is best characterized as an area source of modified smoothed seismicity until, or if, future work can more clearly define surficial evidence of a fault trace or demonstrate recurrent Quaternary activity.

3.7 Conclusions

We assessed the landscape in the eastern Tennessee seismic zone for evidence of surface deformation. We mapped lineaments from 1-m lidar data, calculated channel and catchment metrics, and reinterpreted a previously published exposure, integrating our observations at multiple spatial and temporal scales with previously published geologic mapping and subsurface datasets. We find some evidence for late Pleistocene or Holocene surface deformation that may be focused on east–west-trending lineaments rather than northeast–southwest trending thrust faults. These orientations are consistent with recent focal mechanisms (Chapman et al., 1997; Dunn and Chapman, 2006; Daniels and Peng, 2022) and stress fields (Levandowski et al., 2018; 2023). In contrast to other intraplate regions with recent surface-rupturing moderate magnitude events, the region has not experienced a surface-rupturing event. The lack of clear surface expression indicates either the seismicity is too deep to propagate to the surface with a discrete surface rupture, or surficial deformation is not clearly preserved because of the humid temperate climate, vegetated and soil-mantled landscape, and extensive cultural modification. These observations lead us to suggest the ETSZ is best characterized as an area source in seismic hazard models.

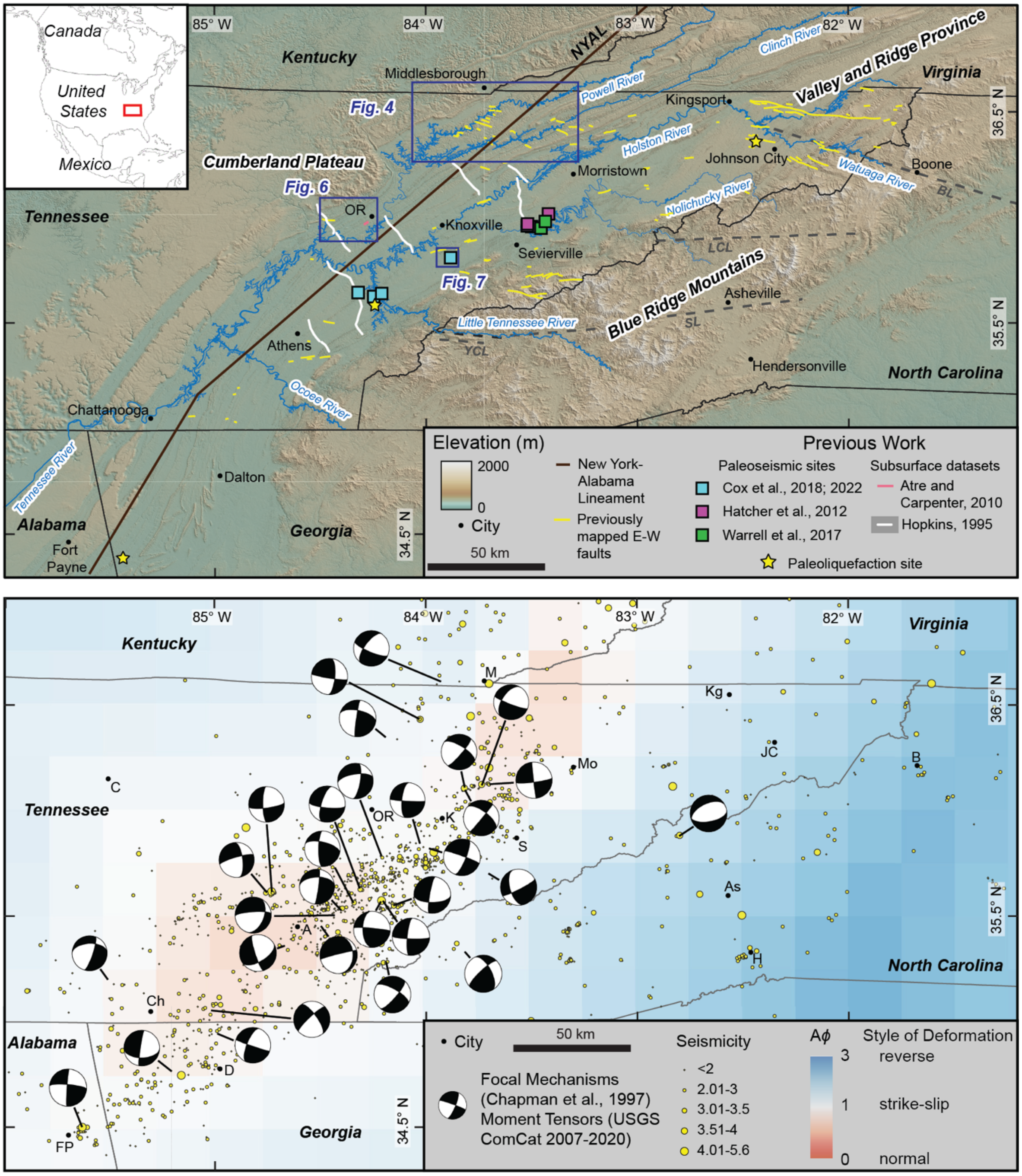

Figure 3-1 (a) Previous paleoseismic and paleoliquefaction sites, geophysical subsurface datasets, and physiographic setting of the Eastern Tennessee seismic zone (ETSZ). Locations of Figure 3-4, Figure 3-6, and Figure 3-7 are shown as purple boxes. Inset shows location of the ETSZ in the eastern United States. See Appendix B for more information on previously mapped east–west faults from geologic maps. (b) Focal mechanisms, moment tensors, and seismicity. Focal mechanisms and moment tensors are from Chapman et al. (1997) and the USGS Comprehensive Catalog (ComCat; USGS EHP, 2017) from 2007–2020. Background image is Aϕ (Simpson, 1997) from Levandowski

et al. (2018) illustrating the expected dominant style of faulting to be oblique-normal in the ETSZ based on inversions of focal mechanisms. Note stretched scale between 0 and 1 to highlight normal and strike-slip styles of deformation. NYAL—New York–Alabama lineament; SL—Swannanoa lineament; BL—Boone lineament; YCL—Yellow Creek lineament, LCL—Laurel Creek lineament. As—Asheville; A—Athens; B—Boone; Ch—Chattanooga; C—Cookville; D—Dalton; FP—Fort Payne; H—Hendersonville; JC—Johnson City; Kg—Kingsport; K—Knoxville; M—Middlesborough; Mo—Morristown; S—Sevierville; OR—Oak Ridge.

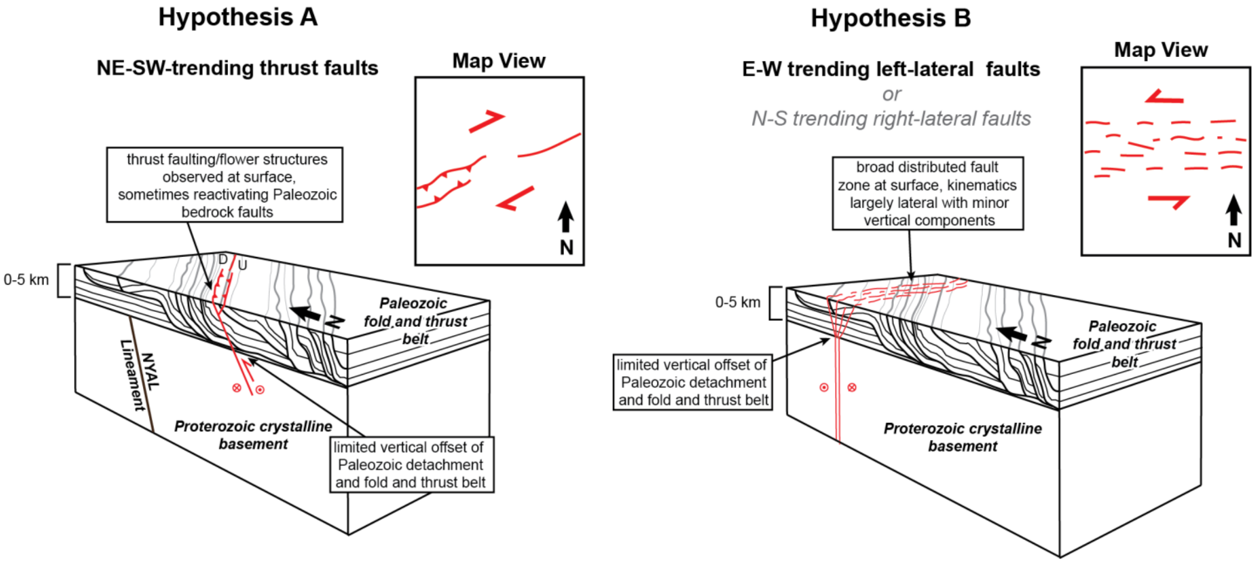

Figure 3-2 Schematic block diagrams illustrating two competing hypotheses for possible surface deformation in the Eastern Tennessee seismic zone (ETSZ). Cross-section is from Whisner (2010), and thin gray lines depict the general northeast–southwest structural grain of the Paleozoic fold and thrust belt. Hypothesis A suggests faults are oriented northeast-southwest and are primarily thrust faults with some strike-slip motion reactivating Paleozoic bedrock faults (after Cox et al., 2018; 2022). Hypothesis B suggests surface deformation should occur on east–west-trending left-lateral faults or north–south-trending right-lateral faults (after Chapman et al., 1997; Levandowski et al., 2023), with a broad zone of surface deformation. North–south-trending faults are less favorably oriented (Levandowski et al., 2023). Both hypotheses would require limited vertical offset of the Paleozoic bedrock faults. NYAL—New York Alabama lineament.

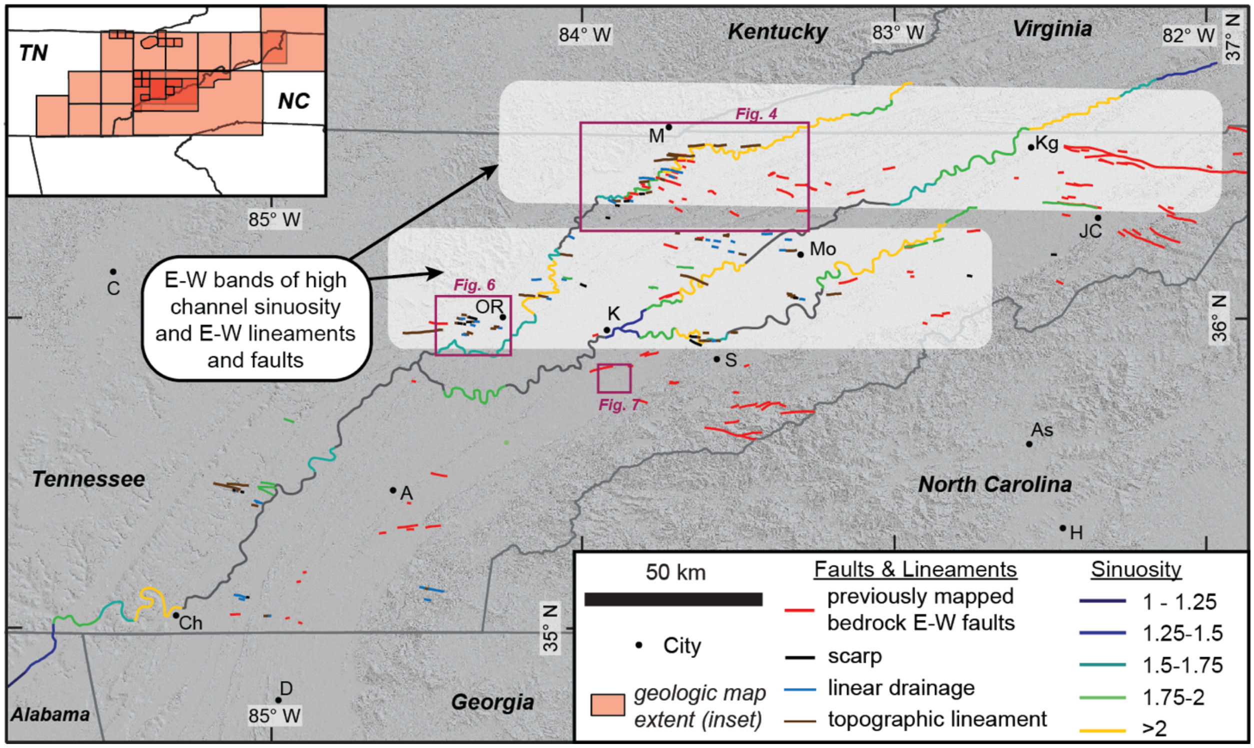

Figure 3-3 Map of channel sinuosity, lineaments mapped in this study (see Thompson Jobe et al., 2023 for shapefiles), and previously mapped east–west faults in the Eastern Tennessee seismic zone (ETSZ). White bands represent east–west trends of higher concentrations of lineaments and faults and higher bands of channel sinuosity. Gray river segments mark the presence of reservoirs along the river and thus the sinuosity measurement may not be a meaningful metric. Inset map shows spatial coverage of 1:24,000 publicly available and easily accessible geologic maps (see Figure B-1 and Appendix B for more details). As—Asheville; A—Athens; B—Boone; Ch—Chattanooga; C—Cookville; D—Dalton; H—Hendersonville; JC—Johnson City; Kg—Kingsport; K—Knoxville; M—Middlesborough; Mo—Morristown; S—Sevierville; OR—Oak Ridge.

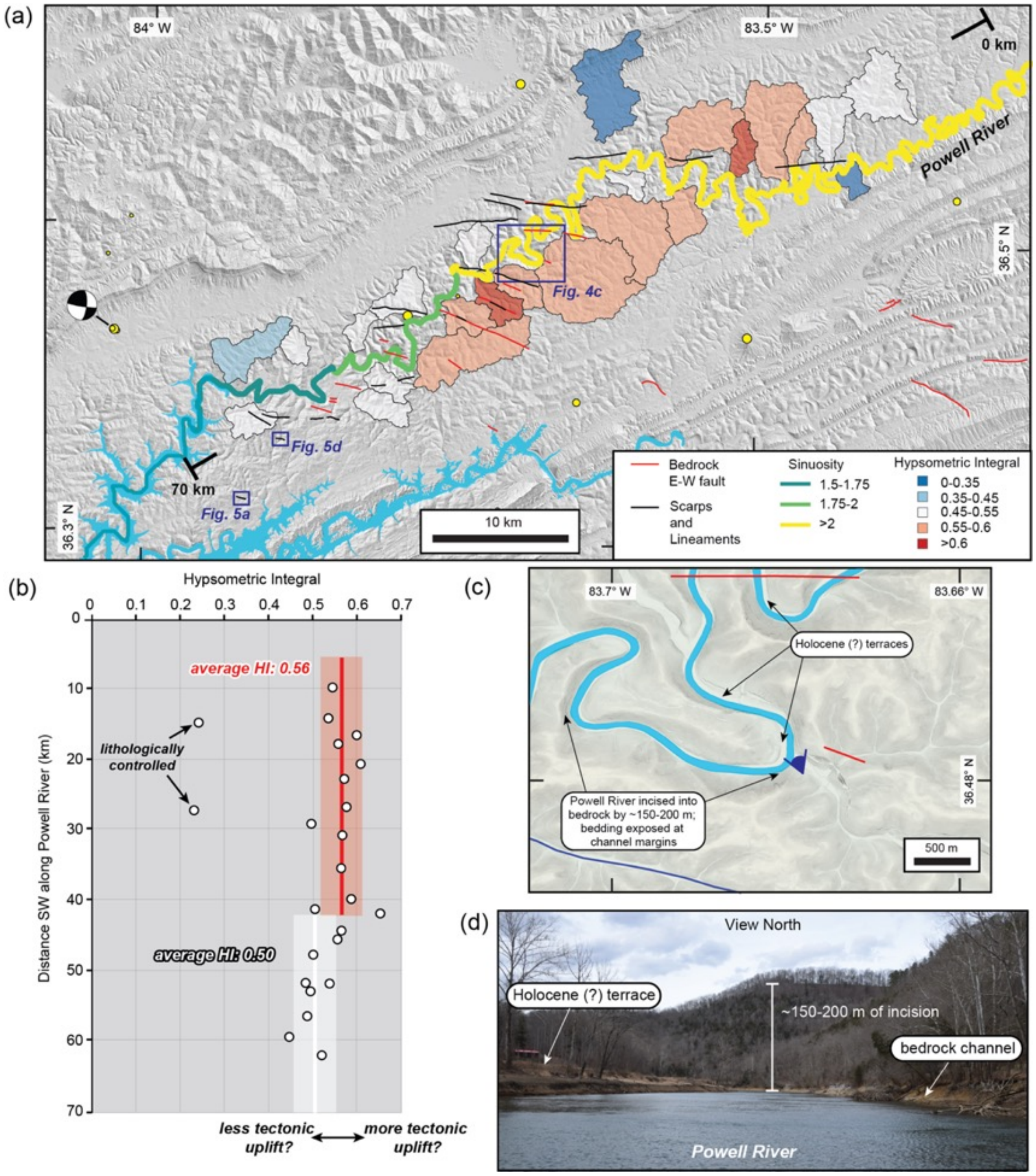

Figure 3-4 **Powell River site. (a) Map illustrating the mapped lineaments in this study, previously mapped east–west faults, channel sinuosity, and hypsometric integral of selected catchments along the Powell River. Yellow circles mark seismicity (see Figure 3-1b for magnitude). Moment tensor marks a 2020 M_w 3.8 earthquake location shown in Figure 3-1 and Figure 3-3 (USGS EHP, 2017). (b) Hypsometric integrals (HIs) of catchments projected in a downstream direction. The average hypsometric integral upstream from the lineaments is 0.56, whereas the average hypsometric integral downstream is 0.50. The two catchments with lower hypsometric integrals have highly variable lithologies. (c) Detailed map of meander bends, illustrating the Powell River is incised 150-200 m into bedrock. Location shown in (a). (d) Field photograph of the Powell River showing the 150-200 m of incision and Holocene (?) terraces. Location shown in (c).**

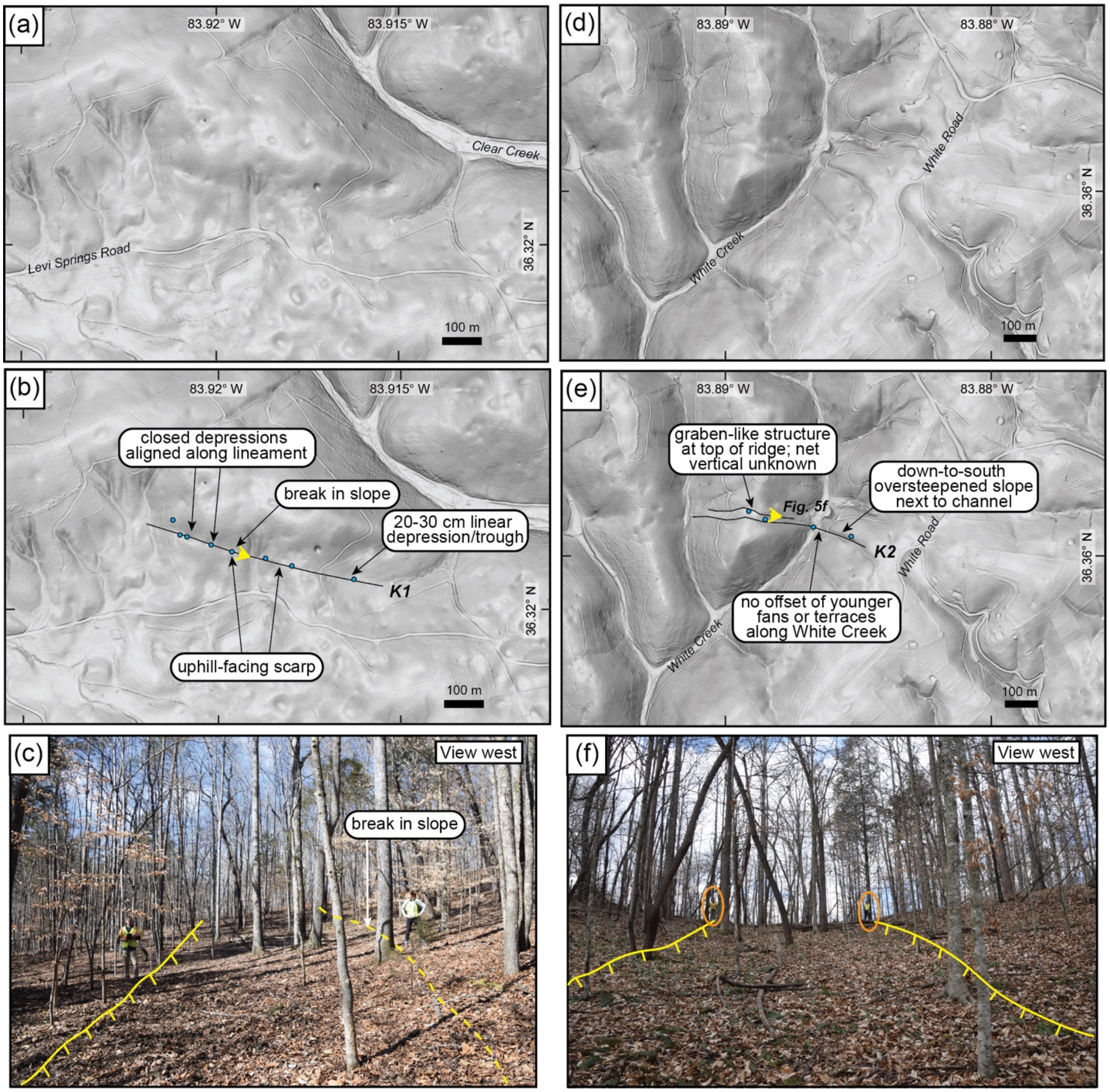

Figure 3-5 (a) Uninterpreted and (b) interpreted slopeshade map of lineament K1. Location in Figure 3-4a. (c) Field photograph of lineament K1. Location shown in (b). (d) Uninterpreted and (e) interpreted slopeshade map of lineament K2. Location shown in Figure 3-4a. (f) Field photograph of lineament K2. Orange circles mark people for scale. Location shown in (d). Yellow lines in (c) and (f) mark scarp across landscape, with hatches on downthrown side.

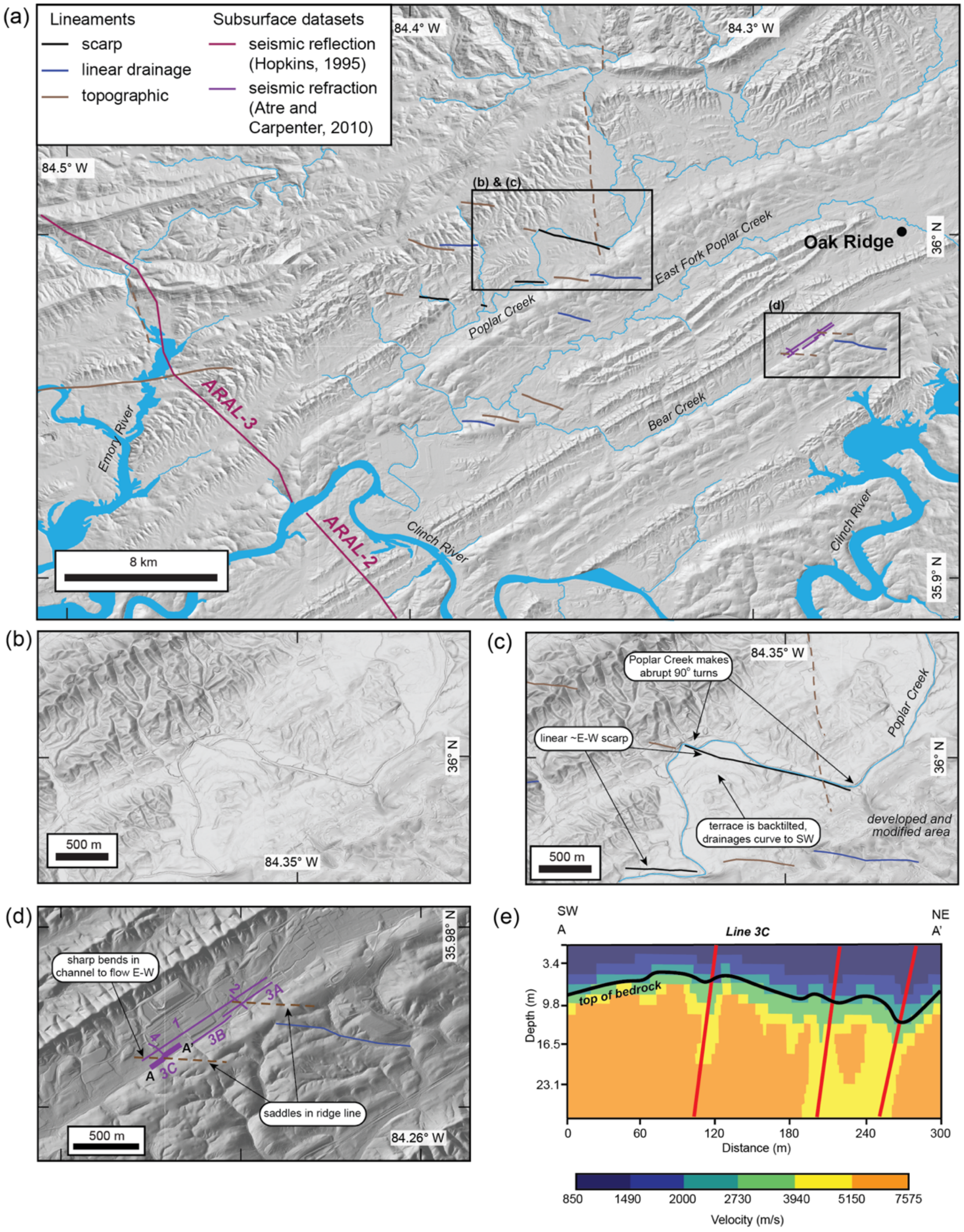

Figure 3-6 (a) Hillshade of the Oak Ridge area illustrating mapped lineaments and subsurface datasets. Most lineaments trend east–west. Location shown in Figure 3-1. (b) Uninterpreted and (c) interpreted slopeshade of a scarp and other lineaments along Poplar Creek, which takes two abrupt 90° turns along the scarp. Location shown in (a). (d) Hillshade of Bear Creek Valley area, showing near-surface seismic refraction lines (purple) from Atre and Carpenter (2010). (e) Interpreted seismic refraction line 3C from Atre and Carpenter (2010). Red lines mark interpreted faults in low-velocity zones.

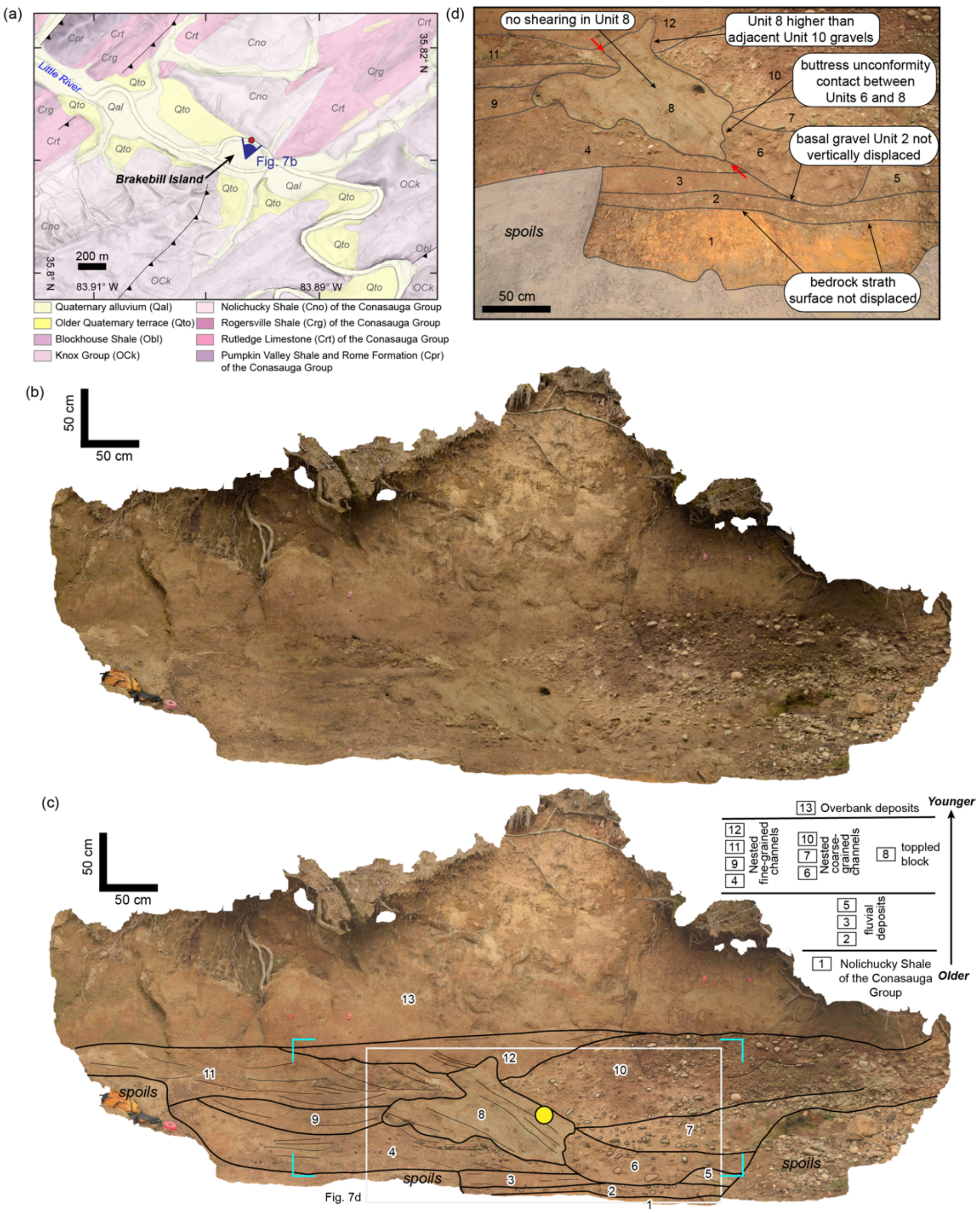

Figure 3-7 Little River site. (a) Geologic map of the area around the Little River site, illustrating the southwest–northeast tectonic grain (Southworth et al., 2012). Red circle marks the Little River exposure north of Brakebill Island. Location shown in Figure 3-1. (b) Uninterpreted and (c) interpreted structure-from-motion (SfM) photomosaics of the Little River exposure. Numbers mark units described and interpreted in the field; see Table 1 for unit descriptions. Yellow circle marks location of optically stimulated luminescence (OSL) sample H from Cox et al. (2022), which yielded an age of 10,310 ± 895 years. Light blue corners mark extent of exposure shown in Cox et al. (2022). White box marks extent shown in (d). (d) Detailed photograph (oblique view) of the previously interpreted fault zone, with alternative observations and interpretations. Red arrows mark the location of the thrust fault interpreted by Cox et al. (2022). Legend for unit numbers in (c).

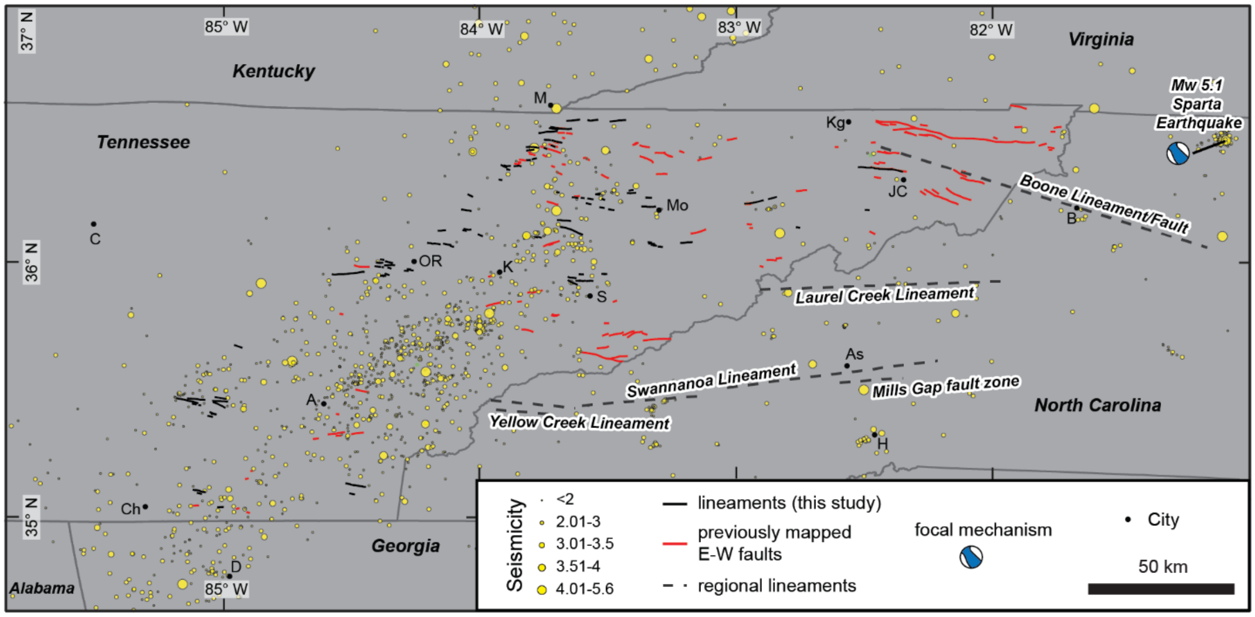

Figure 3-8 Map of seismicity, lineaments mapped in this study, previously mapped east–west faults, and regional lineaments. Seismicity is from the USGS Comprehensive Catalog (ComCat; USGS EHP, 2017) from 1900–2022. Previously mapped east–west faults are from Rodgers (1953), Cattermole (1958), Harris (1965a; 1965b), Brokaw et al. (1966), Harris and Mixon (1970), and Southworth et al. (2012). Regional lineaments are from Hack (1982), Gay (2000), Wooten et al. (2010), and Hill (2018).

Table 3-1 **Brief unit descriptions of the Little River site.**

Unit Number	Description
1	Orange-tan bedrock, highly oxidized, steeply SE-dipping. Interpreted to be Nolichucky Shale of Conasauga Group.
2	Brown-red pebble conglomerate with uncommon cobbles in a sand matrix. Poorly sorted, clasts are rounded to subrounded. Lower contact is wavy, deposited on top of Unit 1.
3	Brown-red granule-pebble conglomerate in a sand matrix. Moderately well sorted, clasts are subrounded. Smooth lower contact.
4	Brown-red pebble-cobble conglomerate in a sand matrix. Matrix-supported, poorly sorted, clasts are subrounded to rounded. Weak bedding and clast imbrication. Grades laterally into tan-gray laminated silty-sand.
5	Tan-light brown silty-sand, weakly bedded. Well sorted. Smooth lower contact.
6	Brown-red cobble conglomerate. Clast-supported with weak bedding. Clasts are subrounded to rounded and moderately sorted within a sand matrix. Wavy upper and lower contacts, appears incised into Unit 5.
7	Brown-red pebble-cobble conglomerate. Clast-supported with weak bedding 5-10 cm thick. Clasts are rounded to subrounded, poorly sorted within a sand-gravel matrix. Wavy upper and lower contacts.
8	Tan-gray thinly laminated silts, dipping to southeast. Irregular undulating contacts with surrounding units. Buttress unconformity with Unit 6.
9	Brown-red granule-pebble conglomerate in a sand matrix. Well sorted, clasts are subrounded. Smooth lower contact.
10	Dark brown-red pebble-cobble conglomerate. Weakly bedded and mostly clast-supported. Clasts are rounded to subrounded, poorly sorted within a sand-gravel matrix. Wavy upper and lower contacts.
11	Brown-red pebble-cobble conglomerate in a sand matrix. Clast-supported, poorly sorted, clasts are subrounded to rounded. Grades laterally into tan-gray laminated silty-sand.
12	Reddish-light brown silt and coarse sand. Irregular lower contact, smooth upper contact.
13	Reddish-tan silt and medium sand, weakly bedded. Smooth lower contact. Red-brown mottling. Soil developed near top of unit.

4 CREATION OF A GEODATABASE OF PREVIOUS FAULT-RELATED STUDIES ON THE CHARLESTON SEISMIC ZONE, SOUTH CAROLINA, USA

4.1 Background and Motivation

The Charleston seismic zone, located in South Carolina, hosted the ~M7 1886 earthquake (Dutton, 1889; Bollinger, 1977). Ongoing seismicity and records of dozens of regional paleoliquefaction features (e.g., Talwani and Schaeffer, 2001) indicate the region has produced large prehistoric earthquakes and has the potential to produce large earthquakes in the future. However, despite the seismicity, seismogenic fault sources have yet to be identified, in part because of the lack of obvious surface expression of active faults. Recent studies have focused on delineating faults from the subsurface data (Figure 4-1; Pratt et al., 2022; Pratt and Counts, 2023; Liberty, 2022), seismicity (Chapman et al., 2016) and geomorphology (Marple and Hurd, 2020), resulting in a complex web of lineaments. For example, lineaments mapped on the ~3-m lidar-derived topography are primarily east-west with vertical offsets (Marple and Hurd, 2020), similar to the orientation of lineaments interpreted from aeromagnetic data (Shah et al., 2023). Legacy and new seismic reflection data (e.g., Pratt et al., 2022; Pratt and Counts, 2023) combined with historical accounts of damaged infrastructure, indicate primarily southwest-northeast faults at depth. In contrast, moment tensors derived from on-going small magnitude earthquakes indicate north-northwest/south-southeast striking faults (Chapman et al., 2016).

New lidar data with ~0.5-m-resolution (QL1) are available over the proposed 1886 M7 epicentral region (Figure 4-1; OCM Partners, 2023a). In advance of a detailed analysis of the new lidar data, we compiled existing datasets and literature to provide a framework for integrating new and existing surface and subsurface observations. These datasets are housed in a geographic information system (GIS) database for ease of spatial comparison. In this chapter, we briefly describe these recent datasets and the key observations. We acknowledge that this database is not meant to be a complete record of all past studies in the Charleston region, and it focuses only on new datasets that have become available since the publication of the Central and Eastern United States Seismic Source Characterization (CEUS-SSC) model in 2012 (U.S. Department of Energy et al., 2012).

4.2 Datasets

4.2.1 Subsurface datasets

New seismic reflection datasets have been collected in recent years and integrated with reprocessed legacy datasets (Figure 4-1; Pratt et al., 2022; Pratt and Counts, 2023; Liberty, 2022). These datasets span the 1886 epicentral region and allow for a reinterpretation of the Cenozoic strata and faulting. The reinterpreted legacy seismic reflection data only image middle Eocene and older strata (Chapman and Beale, 2010), whereas the new ground penetrating radar (GPR) data image the Cooper Group, which is the base of the Miocene and younger strata (Pratt et al., 2022). Interpretations of the seismic reflection data show several northeast (NE)-trending fault zones (Figure 4-2), including the Cypress Swamp, Gants, Cooke, Middleton, and Magnolia fault zones, although Pratt et al. (2022) note that the wide spacing of the seismic reflection data complicates correlation between the profiles and alternative correlations and fault orientation are possible (Pratt et al., 2022). All fault zones image offset and folded Oligocene (and possibly younger strata), and the Cypress Swamp and Gants faults coincide with NE-trending magnetic anomalies on legacy aeromagnetic data (Pratt et al., 2022). A comparison of the interpreted faults with damaged railroad tracks reported by Dutton (1889) suggests the 1886 earthquake may have occurred on the Cooke or Magnolia fault zones (Pratt et al., 2022).

Seismic data were also collected near Summerville to map active faults related to the 1886 and earlier earthquakes (Liberty, 2022). These data include seismic reflection images for the shallow Tertiary stratigraphy and shear-wave velocity images for the uppermost 5-10 m of strata, and sites were selectively chosen to target the Magnolia, Woodstock, Cooke, and Gants fault zones (Liberty, 2022). Interpretations of these data show offset of shallow reflectors (<10 m depth) that correspond with lateral changes in shear wave velocities, indicative of recent faulting of post-middle Pleistocene strata on the Cooke and Magnolia faults (Liberty, 2022).

An analysis of seismicity from a temporary seismic array and relocated earthquakes suggests the seismicity is occurring on a north-striking, west-dipping fault plane (Chapman et al., 2016). The seismicity is interpreted to be aftershocks from the 1886 event, highlighting the potential source fault from near Woodstock to Rantowles. However, this interpretation has only weak evidence in the seismic reflection data, which show <30 m of displacement on post-Cretaceous strata, which indicates either the modern seismicity is in response to stress changes or the 1886 event occurred on fault with infrequent large earthquakes (Pratt et al., 2022).

4.2.2 Geomorphology

High-resolution lidar data (~3 m resolution) have been available over most of the Charleston region since 2017 (OCM Partners, 2023b). Recent lineament mapping by Marple and Hurd (2020) relied on this older lower-resolution (~3 m) lidar data compared to the higher-resolution (~0.5 m) lidar data that can be analyzed in future work. Interpretations of fault-related features from the lidar document numerous lineaments at different orientations, with many lineaments mapped in the east-west or northwest-southeast orientation (Figure 4-2b; Marple and Hurd, 2020). These lineaments include the Middleton Place, Deer Park, and Otranto, which are characterized by linear depressions, troughs, and scarps that can be traced over multiple surfaces and correspond to faults imaged on legacy seismic reflection data (Marple and Hurd, 2020). The Middleton Place lineament, for example, trends east-northeast and is characterized by a 180-m-wide deformation zone at its southwestern end which transitions to a southeast-side-up scarp towards the east-northeast (Marple and Hurd, 2020), where it corresponds to a southeast-side-up fault interpreted on seismic line SC-10 (Chapman and Beale, 2010). Although many of these lineaments are indicative of tectonic origin, improved high-resolution topography and integration with new and reprocessed legacy seismic reflection data may help clarify their origins.

4.3 Future directions

New 0.5-m-resolution lidar data over the 1886 epicentral area were collected in 2020 (Figure 4-1b) and recently released publicly (OCM Partners, 2023b). Lidar data could be analyzed in the future for evidence of surface deformation related to potentially active faults that caused the 1886 or previous earthquakes, in addition to integrating the interpretations from the recent subsurface datasets with any interpretations of surface deformation to assess the long-term history of the fault. The modern stress field indicates that one might expect to observe records of thrust faulting in the Charleston seismic zone; therefore, mapping could focus on searching for vertical surface offsets (e.g., fault scarps) but also include evaluation of any potential lateral offsets of geomorphic markers. In conjunction with neotectonic mapping on the lidar data, changes in channel planform characteristics (i.e., changes in channel sinuosity or width) could be evaluated to broadly identify potential regions of subtle surface deformation, although this type of analysis may be challenging due to the fluctuating sea levels during the late Pleistocene.

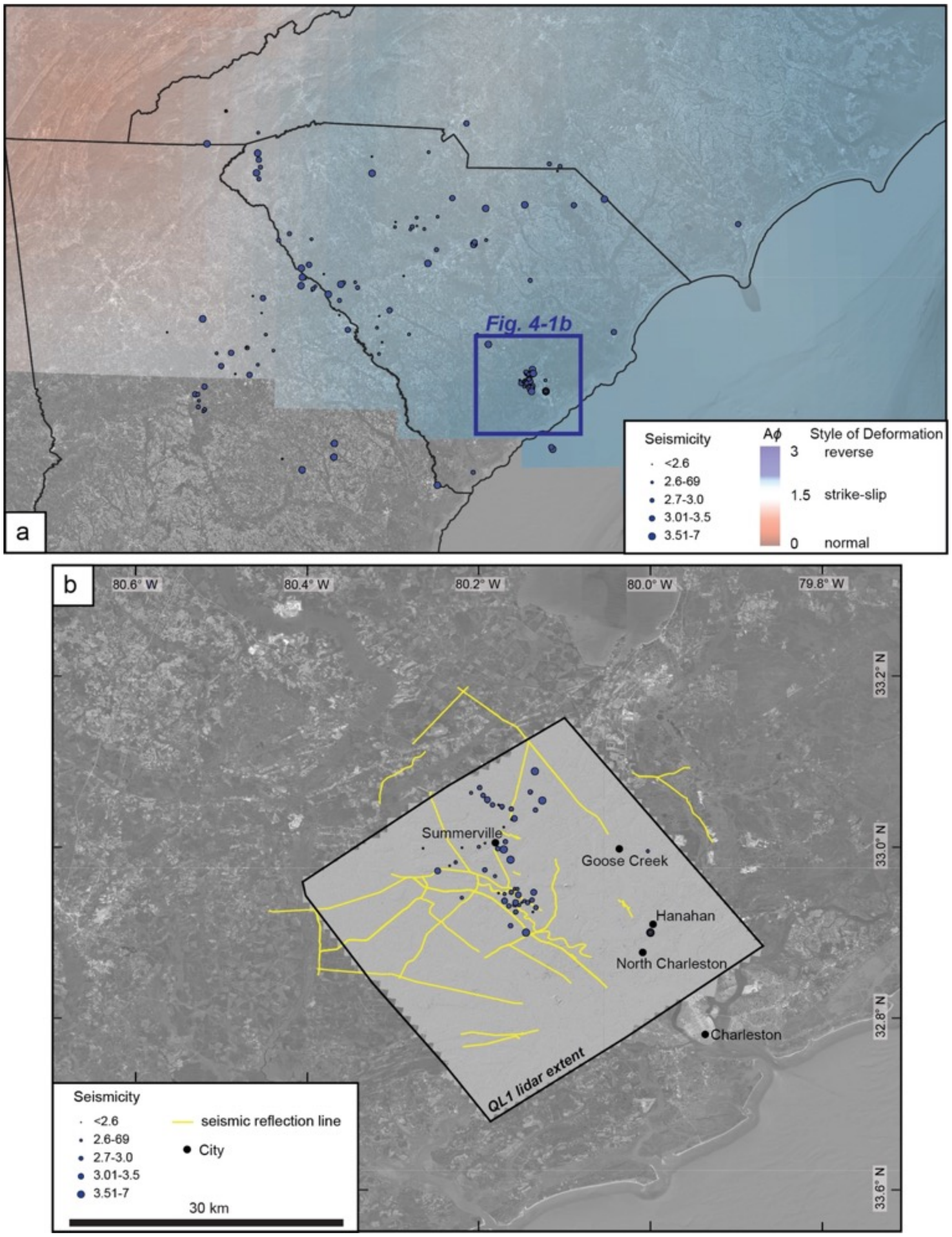

Figure 4-1 **(a) Seismicity (USGS EHP, 2017) and stress field (Levandowski et al., 2018) in the southeast United States. (b) Locations of seismic reflection datasets in the GIS database from Pratt et al. (2022) and Liberty (2022), and legacy seismic reflection data from Chapman and Beale (2010).**

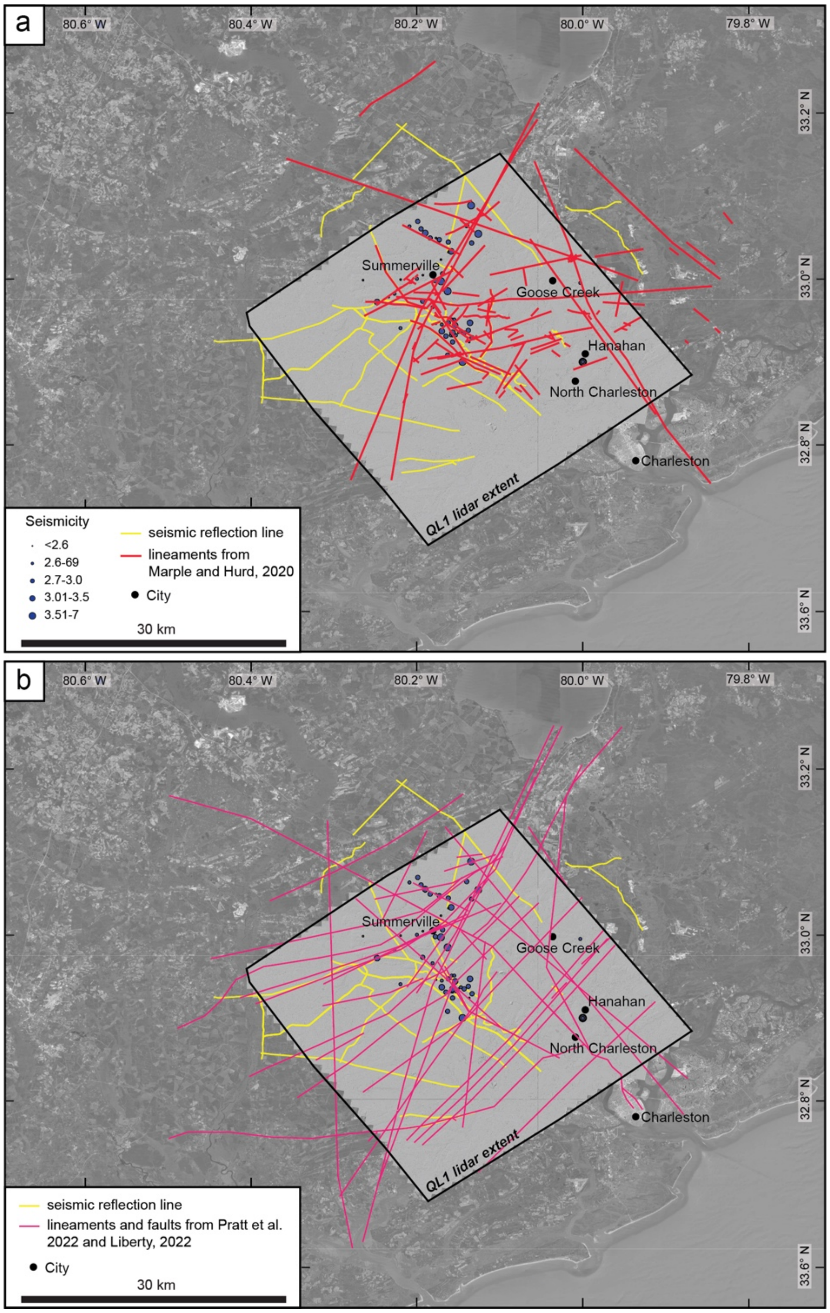

Figure 4-2 **(a) Lineaments mapped on 3-m lidar data from Marple and Hurd (2020). (b) Locations of faults and lineaments interpreted in previous subsurface studies (Pratt et al., 2022; Liberty, 2022). Seismicity on both panels from USGS Compresentive Catalog (ComCat; USGS EHP, 2017) from 1698–2023.**

5 REFERENCES

Alhassan, M., Lawrence, C. B., Richardson, S., and Pindilli, E. J. (2019). The Mississippi alluvial plain aquifers: An engine for economic activity. U.S. Geological Survey Fact Sheet 2019-3003, 4 pp., doi:10.3133/fs20193003.

Amos, C. B., Burbank, D. W., Nobes, D. C., and Read, S. A. (2007). Geomorphic constraints on listric thrust faulting: Implications for active deformation in the Mackenzie Basin, South Island, New Zealand. Journal of Geophysical Research: Solid Earth, 112(B3), B03S11, doi:10.1029/2006JB004291.

Aslan, A., Autin, W. J., and Blum, M. D. (2005). Causes of river avulsion: Insights from the late Holocene avulsion history of the Mississippi River, USA. Journal of Sedimentary Research, 75(4), 650–664, doi:10.2110/jsr.2005.053.

Atre, S. R., and Carpenter, P. J. (2010). Identification of cross-valley faults in the Maynardville Limestone, Oak Ridge Reservation, Tennessee, using seismic refraction tomography. Environmental Earth Sciences, 60(6), 1245–1256, doi:10.1007/s12665-009-0265-4.

Auken, E., Christiansen, A. V., Kirkegaard, C., Fiandaca, G., Schamper, C., Behroozmand, A. A., Binley, A., Nielsen, E., Effersø, F., Christensen, N. B. and Sørensen, K. (2015). An overview of a highly versatile forward and stable inverse algorithm for airborne, ground-based and borehole electromagnetic and electric data. Exploration Geophysics, 46, 223–235. doi:10.1071/EG13097.

Autin, W. J., Burns, S. F., Miller, B. J., Saucier, R. T., and Snead, J. I. (1991). Quaternary geology of the Lower Mississippi Valley. In: Morrison, R. B. (Ed) Quaternary Nonglacial Geology: Conterminous U.S., Volume K-2 (pp. 547–582). Boulder, CO: Geological Society of America, doi:10.1130/DNAG-GNA-K2.

Bakun, W. H., and Hopper, M. G. (2004). Magnitudes and locations of the 1811-1812 New Madrid, Missouri, and the 1886 Charleston, South Carolina, earthquakes. Bulletin of the Seismological Society of America, 94(1), 64–75, doi:10.1785/0120020122.

Baldwin, J. N., Harris, J. B., Van Arsdale, R. B., Givler, R., Kelson, K. I., Sexton, J. L., and Lake, M. (2005). Constraints on the location of the late Quaternary Reelfoot and New Madrid North faults in the northern New Madrid seismic zone, central United States. Seismological Research Letters, 76(6), 772–789, doi:10.1785/gssrl.76.6.772.

Baldwin, J. N., Witter, R. C., Vaughn, J. D., Harris, J. B., Sexton, J. L., Lake, M., Forman, S. L., and Barron, A. D. (2006). Geological characterization of the Idalia Hill fault zone and its structural association with the Commerce Geophysical lineament, Idalia, Missouri. Bulletin of the Seismological Society of America, 96(6), 2281–2303, doi:10.1785/0120050136.

Bollinger, G. A. (1977). Reinterpretation of the intensity data for the 1886 Charleston, South Carolina, earthquake. In: Rankin, D. W. (Ed) Studies Related to the Charleston, South

Carolina Earthquake of 1886: A Preliminary Report (pp. 17–32). U.S. Geological Survery Professional Paper 1028, doi:10.3133/pp1028.

Bollinger, G. A., Langer, C. J., and Harding, S. T. (1976). The eastern Tennessee earthquake sequence of October through December, 1973. Bulletin of the Seismological Society of America, 66(2), 525–547, doi:10.1785/BSSA0660020525.

Bollinger, G. A., Johnston, A. C., Talwani, P., Long, L. T., Shedlock, K. M., Sibol, M. S., and Chapman, M. C. (1991). Seismicity of the southeastern United States; 1698 to 1986. In: Slemmons, D. B, Engdahl, E. R., Zoback, M. D., and Blackwell, D. D. (Eds) Neotectonics of North America, DNAG Continent-scale Map Series, Decade Map 1 (pp. 291–308). Boulder, CO: Geological Society of America, doi:10.1130/DNAG-CSMS-NEO.291.

Bollinger, L., Klinger, Y., Forman, S. L., Chimed, O., Bayasgalan, A., Munkhuu, U., Davaasuren, G., Dolgorsuren, T., Enkhee, B., and Sodnomsambuu, D. (2021). 25,000 Years long seismic cycle in a slow deforming continental region of Mongolia. Scientific Reports, 11(1), 17855, doi:10.1038/s41598-021-97167-w.

Boyd, K. F., and Schumm, S. A. (1995). Geomorphic evidence of deformation in the northern part of the New Madrid seismic zone. U.S. Geological Survey Professional Paper 1538-R, 35 pp., doi:10.3133/pp1538R.

Brokaw, A. L., Rodgers, J., Kent, D. F., Laurence, R. A., and Behre, C. H. (1966). Geology and mineral deposits of the Powell River area, Claiborne and Union Counties, Tennessee. U.S. Geological Survery Bulletin 1222-C, scale 1:48,000, 56 pp., doi:10.3133/b1222C.

Bull, W. B., and McFadden, L. D. (1977). Tectonic geomorphology north and south of the Garlock Fault, California. In: Doehring, D. O. (Ed) Geomorphology in Arid Regions: Binghamton Geomorphology Symposium 8 (pp. 115–138), London: Routledge, doi:10.4324/9780429299230.

Burbank, D., Meigs, A., and Brozović, N. (1996). Interactions of growing folds and coeval depositional systems. Basin Research, 8(3), 199–223. doi:10.1046/j.1365-2117.1996.00181.x.

Bullard, T. F., and Lettis, W. R. (1993). Quaternary fold deformation associated with blind thrust faulting, Los Angeles Basin, California. Journal of Geophysical Research: Solid Earth, 98(B5), 8349–8369, doi:10.1029/93JB00012.

Calais, E., Han, J. Y. , DeMets, C., and Nocquet, J. M. (2006). Deformation of the North American plate interior from a decade of continuous GPS measurements. Journal of Geophysical Research: Solid Earth, 111(B6), B06402, doi:10.1029/2005JB004253.

Calais, E., and Stein, S. (2009) Time-variable deformation in the New Madrid seismic zone, Science, 323(5920), 1442–1442, doi:10.1126/science.1168122.

Calais, E., Freed, A., Arsdale, R., and Stein, S. (2010). Triggering of new Madrid seismicity by late Pleistocene erosion. Nature, 466, 608–611, doi:10.1038/nature09258.

Carlson, S. D., and Guccione, M. J. (2010). Short-term uplift rates and surface deformation along the Reelfoot fault, New Madrid seismic zone. Bulletin of the Seismological Society of America, 100(4), 1659–1677, doi:10.1785/0120100069.

Carpenter, N. S., Woolery, E. W., and Wang, Z. (2014). The Mw 4.2 Perry County, Kentucky, earthquake of 10 November 2012: Evidence of the eastern Tennessee seismic zone in southeastern Kentucky. Seismological Research Letters, 85(4), 931–939, doi:10.1785/0220130221.

Cattermole, J. M. (1958). Geology of the Knoxville quadrangle, Tennessee. U.S. Geological Survey Geologic Quadrangle Map GQ-115, scale 1:24,000, doi:10.3133/gq115.

Center for Earthquake Research and Information (CERI) (2019). New Madrid earthquake catalog: http://folkworm.ceri.memphis.edu/catalogs/html/cat_nm.html (last accessed March 2019).

Champion, J., Mueller, K., Tate, A., and Guccione, M. (2001). Geometry, numerical models and revised slip rate for the Reelfoot fault and trishear fault-propagation fold, New Madrid seismic zone. Engineering Geology, 62(1–3), 31–49, doi:10.1016/S0013-7952(01)00048-5.

Chapman, M. C., and Beale, J. N. (2010). On the geologic structure at the epicenter of the 1886 Charleston, South Carolina, Earthquake. Bulletin of the Seismological Society of America, 100(3), 1010–1030, doi:10.1785/0120090231.

Chapman, M. C., Powell, C. A., Vlahovic, G., and Sibol, M. S. (1997). A statistical analysis of earthquake focal mechanisms and epicenter locations in the eastern Tennessee seismic zone. Bulletin of the Seismological Society of America, 87(6), 1522–1536, doi:10.1785/BSSA0870061522.

Chapman, M. C., Beale, J. N., Hardy, A. C., and Wu, Q. (2016). Modern seismicity and the fault responsible for the 1886 Charleston, South Carolina, Earthquake. Bulletin of the Seismological Society of America, 106(2), 364–372, doi:10.1785/0120150221.

Clark, D. J., Brennand, S., Brenn, G., Garthwaite, M. C., Dimech, J., Allen, T. I., and Standen, S. (2020). Surface deformation relating to the 2018 Lake Muir earthquake sequence, southwest Western Australia: new insight into stable continental region earthquakes. Solid Earth, 11(2), 691-717, doi: 10.5194/se-11-691-2020.

Colman, S. M. (1983). Progressive changes in the morphology of fluvial terraces and scarps along the Rappahannock River, Virginia. Earth Surface Processes and Landforms, 8(3), 201-212, doi:10.1002/esp.3290080303.

Conrad, T. A. (1856). Observations on the Eocene deposit of Jackson, Mississippi, with descriptions of thirty-four new species of shells and corals. Philadelphia Academy of Natural Science, Proceedings, 7, 257–258.

Cook, F. A., Albaugh, D. S., Brown, L. D., Kaufman, S., Oliver, J. E., and Hatcher Jr, R. D. (1979). Thin-skinned tectonics in the crystalline southern Appalachians; COCORP seismic-reflection profiling of the Blue Ridge and Piedmont. Geology, 7(12), 563-567, doi:10.1130/0091-7613(1979)7<563:TTITCS>2.0.CO;2.

Cox, R. T. (1988). Evidence of Quaternary ground tilting associated with the Reelfoot rift zone, northeast Arkansas. Southeastern Geology, 28(4), 211–224.

Cox, R. T., Cherryhomes, J., Harris, J. B., Larsen, D., Van Arsdale, R. B., and Forman, S. L. (2006). Paleoseismology of the southeastern Reelfoot Rift in western Tennessee and implications for intraplate fault zone evolution. Tectonics, 25(3), TC3019, doi:10.1029/2005TC001829.

Cox, R. T., Hatcher Jr, R. D., Counts, R., Gamble, E., Glasbrenner, J., and Warrell, K. (2018). Quaternary faulting along the Dandridge-Vonore fault zone in the Eastern Tennessee seismic zone. In: Summers Engel, A., and Hatcher Jr, R. D. (Eds) Geology at Every Scale: Field Excursions for the 2018 GSA Southeastern Section Meeting in Knoxville, Tennessee (Vol. 50, p. 81), Boulder, CO: Geological Society of America, doi:10.1130/2018.0050(06).

Cox, R. T., Hatcher, R. D., Forman, S. L., Counts, R., Vaughn, J., Gamble, E., Glasbrenner, J., Warrell, K., Adhikari, N., and Pinardi, S. (2022). Synthesis of recent paleoseismic research on quaternary faulting in the Eastern Tennessee Seismic Zone, Eastern North America: Implications for seismic hazard and intraplate seismicity. Bulletin of the Seismological Society of America, 112(2), 1161–1189, doi:10.1785/0120210209.

Craig, T. J., and Calais, E. (2014). Strain accumulation in the New Madrid and Wabash Valley seismic zones from 14 years of continuous GPS observation. Journal of Geophysical Research: Solid Earth, 119(12), 9110–9129. doi:10.1002/2014JB011498.

Craig, T. J., Calais, E., Fleitout, L., Bollinger, L., and Scotti, O. (2016). Evidence for the release of long-term tectonic strain stored in continental interiors through intraplate earthquakes. Geophysical Research Letters, 43(13), 6826–6836. doi:10.1002/2016GL069359.

Crockett, D. (1834). A Narrative of the Life of David Crockett, of the State of Tennessee. Baltimore, MD: Carey, Hart & Co.

Crone, A.J. (1981). Sample description and stratigraphic correlation of the New Madrid test well 1-W, New Madrid Country, Missouri. U.S. Geological Survey Open-File Report 81-426, 26 pp., doi:10.3133/ofr81426.

Crone, A.J. (1992). Structural relations and earthquake hazards of the Crittenden County fault zone, northeastern Arkansas. Seismological Research Letters, 63(3), 249–262, doi:10.1785/gssrl.63.3.249.

Crone, A. J., De Martini, P. M., Machette, M. N., Okumura, K., and Prescott, J. R. (2003). Paleoseismicity of two historically quiescent faults in Australia: Implications for fault behavior in stable continental regions. Bulletin of the Seismological Society of America, 93(5), 1913–1934. doi:10.1785/0120000094.

Csontos, R., and Van Arsdale, R. (2008). New Madrid seismic zone fault geometry. Geosphere, 4(5), 802–813. doi:10.1130/GES00141.1.

Csontos, R., Van Arsdale, R., Cox, R., and Waldron, B. (2008). Reelfoot rift and its impact on Quaternary deformation in the central Mississippi River valley. Geosphere, 4(1), 145–158. doi:10.1130/GES00107.1.

Cunningham, D., Grebby, S., Tansey, K., Gosar, A., and Kastelic, V. (2006). Application of airborne LiDAR to mapping seismogenic faults in forested mountainous terrain, southeastern Alps, Slovenia. Geophysical Research Letters, 33(2), L20308, doi:10.1029/2006GL027014.

Cupples, W., and Van Arsdale, R. (2014). The Preglacial “Pliocene” Mississippi River. The Journal of Geology, 122(1), 1-15, doi:10.1086/674073.

Daniels, C., and Peng, Z. (2022). Fault orientation and relocated seismicity associated with the December 12, 2018, Mw4.4 Decatur, Tennessee earthquake sequence. Seismological Research Letters, 93(6), 3454–3467, doi:10.1785/0220220173.

Daniels, C., and Peng, Z. (2023). A 15-year-Long catalog of seismicity in the Eastern Tennessee Seismic Zone (ETSZ) using matched filter detection. Earthquake Research Advances, 3(1), 100198, doi:10.1016/j.eqrea.2022.100198.

Delano, J. E., Gold, R. D., Briggs, R. W., and Jibson, R. W. (2018). Coseismic sackungen in the New Madrid seismic zone, USA. Geophysical Research Letters, 45(24), 13258–13268, doi:10.1029/2018GL080493.

Delano, J. E., Briggs, R. W., Thompson Jobe, J., Gold, R. D., and Engelhart, S. E. (2021a). Quaternary Reelfoot fault deformation in the Obion River valley, Tennessee, USA. *Tectonics*, *40*(8), e2019TC005990,

Delano, J. E., Briggs, R. W., Thompson Jobe, J., Gold, R. D., and Engelhart, S. E. (2021b). Field data for Quaternary Reelfoot fault deformation in the Obion River valley, Tennessee, USA. U.S. Geological Survey data release, doi:10.5066/P9GDM1VX.

Delano, J. E., Briggs, R. W., DuRoss, C. B., and Gold, R. D. (2021c). Quick and dirty (and accurate) 3D paleoseismic trench models using coded scale bars. Seismological Research Letters, 92(6), 3526–3537, doi:10.1785/0220200246, doi: 10.1029/2019TC005990.

Dart, R. L. (1992). Catalog of pre-Cretaceous geologic drill-hole data from the upper Mississippi Embayment: U.S. Geological Survey Open-File Report 90-260, 253 pp., doi: 10.3133/ofr90260.

Doll, W. E., Nyquist, J. E., Carpenter, P. J., Kaufmann, R. D., and Carr, B. J. (1998). Geophysical surveys of a known karst feature, Oak Ridge Y-12 Plant, Oak Ridge, Tennessee (No. Y/TS-1736). Oak Ridge Y-12 Plant, TN (US).

Doll, W. E., Carr, B. J., Sheehan, J. R., and Mandell, W. A. (2005). Overview of karst effects and karst detection in seismic data from the Oak Ridge Reservation, Tennessee. In: Hammarstrom, J. M., Zientek, M. L., Parks, H. L., Dicken, C. L. ,et al. (Eds) Assessment of Undiscovered Copper Resources of the World, 2015. U.S. Geological Survey Scientific Investigations Report 2005-5160 (pp. 20–28), doi:10.3133/sir20185160.

Doyle, B.C. (2005). Seismically induced lateral spread features in the western New Madrid seismic zone. Environmental and Engineering Geoscience, 11(3), 251–258. doi:10.2113/11.3.251.

Dunn, M. M., and Chapman, M. C. (2006). Fault orientation in the eastern Tennessee seismic zone: A study using the double-difference earthquake location algorithm. Seismological Research Letters, 77(4), 494–504, doi:10.1785/gssrl.77.4.494.

DuRoss, C. B., Bunds, M. P., Gold, R. D., Briggs, R. W., Reitman, N. G., Personius, S. F., and Toké, N. A. (2019). Variable normal-fault rupture behavior, northern Lost River fault zone, Idaho, USA. Geosphere, 15(6), 1869–1892, doi:10.1130/GES02096.1.

Dutton, C. E. (1889). The Charleston earthquake of August 31, 1886. In: Powell, J. W. (Ed) Ninth Annual Report of the U.S. Geological Survey to the Secretary of Interior, 1887-‘88 (pp. 203–528), doi:10.3133/ar9.

Figueiredo, P. M., Hill, J. S., Merschat, A. J., Scheip, C. M., Stewart, K. G., Owen, L. A., Wooten, R. M., Carter, M. W., Szymanski, E., Hotron, S. P., Wegmann, K. W., Bohnenstiehl, D. R., Thompson, G. W., Witt, A., Cattanach, B., and Douglas, T. (2022). The Mw5.1 August 9, 2020 Sparta earthquake, North Carolina: The first documented seismic surface rupture in the eastern United States. GSA Today, 32(3–4), 4–11, doi:10.1130GSATG517A.1.

Figueroa, A. M., and Knott, J. R. (2010). Tectonic geomorphology of the southern Sierra Nevada Mountains (California): Evidence for uplift and basin formation. Geomorphology, 123(1–2), 34–45, doi:10.1016/j.geomorph.2010.06.009.

Fisk, H.N. (1944). Geological investigations of the alluvial valley of the lower Mississippi River. U.S. Army Corps of Engineers, 170 pp.

Font, M., Amorese, D., and Lagarde, J.-L. (2010). DEM and GIS analysis of the stream gradient index to evaluate effects of tectonics: The Normandy intraplate area (NW France). Geomorphology, 119(3–4), 172–180. doi:10.1016/j.geomorph.2010.03.017.

Foreman, J. L., and Dunne, W. M. (1991). Conditions of vein formation in the southern Appalachian foreland: constraints from vein geometries and fluid inclusions. Journal of Structural Geology, 13(10), 1173–1183, doi:10.1016/0191-8141(91)90076-U.

Forman, S. L., Arthur Bettis, E., Kemmis, T. J., and Miller, B. B. (1992). Chronologic evidence for multiple periods of loess deposition during the Late Pleistocene in the Missouri and Mississippi River Valley, United States: Implications for the activity of the Laurentide ice sheet. Palaeogeography, Palaeoclimatology, Palaeoecology, 93(1–2), 71–83, doi:10.1016/0031-0182(92)90184-7.

Forman, S. L., and Pierson, J. (2002). Late Pleistocene luminescence chronology of loess deposition in the Missouri and Mississippi river valleys, United States. Palaeogeography, Palaeoclimatology, Palaeoecology, 186(1–2), 25–46. doi:10.1016/S0031-0182(02)00440-6.

Frankel, A. D., Mueller, C., Barnhard, T., Perkins, D., Leyendecker, E. V., Dickman, N., Hanson, S., and Hopper, M. (1996). National Seismic-Hazard Maps: Documentation June 1996. U.S. Geological Survey Open-File Report 96-532, 110 pp., doi:10.3133/ofr96532.

Frederiksen, N. O., Bybell, L. M., Christopher, R. A., Crone, A. J., Edwards, L. E., Gibson, T. G., Hazel, J. E., Repetski, J. E., Russ, D. P., Smith, C. C., and Ward, L. W. (1982).

Biostratigraphy and paleoecology of Lower Paleozoic, Upper Cretaceous, and lower Tertiary rocks. Tulane Studies in Geology and Palentology, 17(2), 23–45.

Fuller, M.L. (1912). The New Madrid Earthquake. U.S. Geological Survey Bulletin 494, 119 pp. doi:10.3133/b494.

Galgana, G. A., and Hamburger, M. W. (2010). Geodetic observations of active intraplate crustal deformation in the Wabash Valley seismic zone and the southern Illinois basin. Seismological Research Letters, 81(5), 699–714, doi:10.1785/gssrl.81.5.699.

Gallen, S. F. (2018). Lithologic controls on landscape dynamics and aquatic species evolution in post-orogenic mountains. Earth and Planetary Science Letters, 493, 150–160, doi:10.1016/j.epsl.2018.04.029.

Gallen, S. F., and Thigpen, J. R. (2018). Lithologic controls on focused erosion and intraplate earthquakes in the eastern Tennessee seismic zone. Geophysical Research Letters, 45(18), 9569–9578, doi:10.1029/2018GL079157.

Gardner, T. W. (1975). The history of part of the Colorado River and its tributaries: an experimental study. Four Corners of the Geological Society Canyonlands Country 8th field conference, 87–95.

Gay, Parker S., Jr. (2000). Unmapped topographic alignments visible on 3D stereo terrain map of a 2 degrees X 2 degrees segment of the Southern Appalachians. Geological Society of America Abstracts with Programs, Southeastern Section, 32(2), 19.

Giaconia, F., Booth-Rea, G., Martínez-Martínez, J.M., Azañón, J.M., Pérez-Peña, J.V., Pérez-Romero, J., and Villegas, I. (2012). Geomorphic evidence of active tectonics in the Sierra Alhamilla (eastern Betics, SE Spain). Geomorphology, 145–146, 90–106. doi:10.1016/j.geomorph.2011.12.043.

Gold, R. D., DuRoss, C. B., Delano, J. E., Jibson, R. W., Briggs, R. W., Mahan, S. A., Williams, R. A., and Corbett, D. R. (2019). Four major Holocene earthquakes on the Reelfoot fault recorded by Sackungen in the New Madrid seismic zone, USA. Journal of Geophysical Research: Solid Earth, 124(3), 3105–3126, doi:10.1029/2018JB016806.

Gold, R. D., Stephenson, W. J., Odum, J. K., Briggs, R. W., Crone, A. J., and Angster, S. J. (2013). Concealed Quaternary strike-slip fault resolved with airborne lidar and seismic reflection: The Grizzly Valley fault system, northern Walker Lane, California. Journal of Geophysical Research: Solid Earth, 118(7), 3753–3766. doi:10.1002/jgrb.50238.

Greenwood, M. L., Woolery, E. W., Van Arsdale, R. B., Stephenson, W. J., and Patterson, G. L. (2016). Continuity of the Reelfoot fault across the Cottonwood Grove and Ridgely faults of the New Madrid seismic zone. Bulletin of the Seismological Society of America, 106(6), 2674–2685, doi:10.1785/0120150290.

Guccione, M. J., Marple, R., and Autin, W. J. (2005). Evidence for Holocene displacements on the Bootheel fault (lineament) in southeastern Missouri: Seismotectonic implications for the New Madrid region. Geological Society of America Bulletin, 117(3–4), 319–333. doi:10.1130/B25435.1.

Guccione, M. J., Prior, W. L., and Rutledge, E. M. (1986). The Tertiary and Quaternary Geology of Crowley's Ridge: A Guidebook. Arkansas Geological Commission, Guidebook 86–4.

Guccione, M. J., Van Arsdale, R. B., and Hehr, L. H. (2000). Origin and age of the Manila high and associated Big Lake "sunklands" in the New Madrid seismic zone, northeastern Arkansas. Geological Society of America Bulletin, 112(4), 579-590, doi: 10.1130/0016-7606(2000)112<579:OAAOTM>2.0.CO;2.

Hack, J. T. (1982). Physiographic divisions and differential uplift in the Piedmont and Blue Ridge. U.S. Geological Survey Professional Paper 1265, 49 pp., doi:10.3133/pp1265.

Hadley, J. B. and Nelson, A. E. (1971). Geologic map of the Knoxville quadrangle, North Carolina, Tennessee, and South Carolina. U.S. Geological Survey Miscellaneous Geologic Investigations Map 654, scale 1:250,000, doi:10.3133/i654.

Haley, B. R., Glick, E. E., Bush, W. V., Clardy, B. F., Stone, C. G., Woodward, M. B., and Zachry, D. L. (1993). Geologic Map of Arkansas. Arkansas Geological Commission and U.S. Geological Survey, scale 1:500,000, doi:10.3133/70210878.

Hampson, P. S., Treece, Jr., M. W., Johnson, G. C., Ahlstedt, S. A., and Connell, J. F. (2000). Water quality in the Upper Tennessee River Basin, Tennessee, North Carolina, Virginia, and Georgia, 1994-98. U.S. Geological Survey Circular 1205, 32 pp., doi:10.3133/cir1205.

Hancock, G., and Kirwan, M. (2007). Summit erosion rates deduced from ^{10}Be: Implications for relief production in the central Appalachians. Geology, 35(1), 89–92, doi:10.1130/G23147A.1.

Hao, Y., Magnani, M. B., McIntosh, K., Waldron, B., and Guo, L. (2013). Quaternary deformation along the Meeman-Shelby Fault near Memphis, Tennessee, imaged by high-resolution marine and land seismic reflection profiles. Tectonics, 32(3), 501–515. doi:10.1002/tect.20042.

Harel, M. A., Mudd, S. M., and Attal, M. (2016) Global analysis of the stream power law parameters based on worldwide 10Be denudation rates. Geomorphology, 268, 184–196, doi:10.1016/j.geomorph.2016.05.035.

Harris, L. D. (1965a). Geologic map of the Tazewell quadrangle, Claiborne County, Tennessee. U.S. Geological Survey Geologic Quadrangle Map GQ-465, scale 1:24,000, doi:10.3133/gq465.

Harris, L. D. (1965b). Geologic map of the Wheeler quadrangle, Claiborne County, Tennessee and Lee County, Virginia. U.S. Geological Survey Geologic Quadrangle Map GQ-435, scale 1:24,000, doi:10.3133/gq435.

Harris, L. D. and Mixon, R. B. (1970). Geologic map of the Howard Quarter quadrangle, northeastern Tennessee. U.S. Geological Survey Geologic Quadrangle Map GQ-842, scale 1:24,000, doi: 10.3133/gq842.

Harris, L. D., and Milici, R. C. (1977). Characteristics of thin-skinned style of deformation in the southern Appalachians, and potential hydrocarbon traps. U.S. Geological Survey Professional Paper 1018, 40 pp., doi:10.3133/pp1018.

Harrison, R. W., Hoffman, D., Vaughn, J. D., Palmer, J. R., Wiscombe, C. L., McGeehin, J. P., et al. (1999). An example of neotectonism in a continental interior—Thebes Gap, Midcontinent, United States. Tectonophysics, 305(1-3), 399–417, doi: 10.1016/S0040-1951(99)00010-4.

Hatcher Jr, R. D., and Odom, A. L. (1980). Timing of thrusting in the southern Appalachians, USA: Model for orogeny? Journal of the Geological Society, 137(3), 321–327, doi:10.1144/gsjgs.137.3.0321.

Hatcher Jr, R. D., Tollo, R. P., Bartholomew, M. J., Hibbard, J. P., and Karabinos, P. M. (2010). The Appalachian orogen: A brief summary. In: Tollo, R. P., Bartholomew, M. J., Hibbard, J. P., and Karabinos, P. M. (Eds) From Rodinia to Pangea: The Lithotectonic Record of the Appalachian Region. Geological Society of America Memoir 206 (pp. 1–20), Boulder, CO: Geological Society of America, doi:10.1130/2010.1206(01).

Hatcher Jr, R. D., Lemiszki, P. J., Foreman, J. L., Dreier, R. B., Ketelle, R. H., Lee, R. R., and McMaster, W. M. (1992). Status report on the geology of the Oak Ridge Reservation (No. ORNL/TM-12074). Oak Ridge National Lab., TN (United States), 293 pp., doi:10.2172/10131622.

Hatcher Jr, R. D., Bream, B. R., and Merschat, A. J. (2007a). Tectonic map of the southern and central Appalachians: A tale of three orogens and a complete Wilson cycle. In: Hatcher Jr, R. D., Carlso, M. P., McBride, J. H., and Martinez Catalán, J. R. (Eds) 4-D Framework of Continental Crust, Geological Society of America Memoir 200 (pp. 595–622), Boulder, CO: Geological Society of America, doi:10.1130/2007.1200(29).

Hatcher Jr, R. D., Lemiszki, P. J., and Whisner, J. B. (2007b). Character of rigid boundaries and internal deformation of the southern Appalachian foreland fold-thrust belt. In: Sears, J. W., Harms, T. A., and Evenchic, C. A. (Eds) Whence the Mountains? Inquiries into the Evolution of Orogenic Systems: A volume in honor of Raymon A. Price, Geological Society of America Special Paper 433 (pp. 243–276), Boulder, CO: Geological Society of America, doi:10.1130/2007.2433(12).

Hatcher Jr, R. D., Vaughn, J. D., and Obermeier, S. F. (2012). Large earthquake paleoseismology in the East Tennessee Seismic Zone: Results of an 18-month pilot study. In: Cox, R. T., Tuttle, M. P., Boyd, O. S., and Locat, J. (Eds) Recent Advances in North American Paleoseismology and Neotectonics East of the Rockies, Geological Society of America Special Paper 491 (pp. 111–142), Boulder, CO: Geological Society of America, doi:10.1130/2012.2493(06).

Haugerud, R. A., Harding, D. J., Johnson, S. Y., Harless, J. L., Weaver, C. S., and Sherrod, B. L. (2003). High-resolution lidar topography of the Puget lowland, Washington —A bonanza for earth science. GSA Today, 13, 4–10. doi:10.1130/1052-5173(2003)13<0004:HLTOTP>2.0.CO;2.

Hill, J. S. (2018). Post-orogenic uplift, young faults and mantle reorganization in the Appalachian. Ph.D. Dissertation, The University of North Carolina at Chapel Hill, 130 pp. doi:10.17615/rnrd-0d82.

Hill, J. S., Cattanach, B. L., Douglas, T. J., Figueiredo, P. M., Kirby, E., Korte, D. M., Lynn, A. S., Merschat, A. J., Owen, L. A., Scheip, C., Stewart, K. G., Wells, S. B. and Wooten, R. M. (2020). Surface rupture of the Little River fault in response to the August 9, 2020 Mw 5.1 earthquake near Sparta, North Carolina. 2020 SCEC Annual Meeting, abstract.

Holbrook, J. and Schumm, S. A. (1999). Geomorphic and sedimentary response of rivers to tectonic deformation: a brief review and critique of a tool for recognizing subtle epeirogenic deformation in modern and ancient settings. Tectonophysics, 305(1–3), 287–306, doi:10.1016/S0040-1951(99)00011-6.

Holbrook, J., Autin, W. J., Rittenour, T. M., Marshak, S., and Goble, R. J. (2006). Stratigraphic evidence for millennial-scale temporal clustering of earthquakes on a continental-interior fault: Holocene Mississippi River floodplain deposits, New Madrid seismic zone, USA. Tectonophysics, 420(3–4), 431–454, doi:10.1016/j.tecto.2006.04.002.

Hollon, D. M. (1997). The effect of fractures, faults, and sheared shale zones on the hydrology of Bear Creek Burial Grounds A-South, Oak Ridge, Tennessee. Ph.D. Dissertation, Texas A&M University, Available at https://hdl.handle.net/1969.1/ETD-TAMU-1997-THESIS-H656.

Hopkins, D. L. (1995). The New York-Alabama magnetic lineament: its reflection character and relationship to the Grenville Front. Ph.D. Dissertation, Virginia Polytechnic Institute and State University, Available at http://scholar.lib.vt.edu/theses/available/etd-06062008-160240/.

Hurtrez, J. E., and Lucazeau, F. (1999). Lithological control on relief and hypsometry in the Hérault drainage basin (France). Comptes Rendus de l'Académie des Sciences-Series IIA-Earth and Planetary Science, 328(10), 687–694, doi:10.1016/S1251-8050(99)80178-5\.

Hurtrez, J. E., Lucazeau, F., Lavé, J., and Avouac, J. P. (1999a). Investigation of the relationships between basin morphology, tectonic uplift, and denudation from the study of an active fold belt in the Siwalik Hills, central Nepal. Journal of Geophysical Research: Solid Earth, 104(B6), 12779–12796, doi:10.1029/1998JB900098.

Hurtrez, J. E., Sol, C., and Lucazeau, F. (1999b). Effect of drainage area on hypsometry from an analysis of small-scale drainage basins in the Siwalik Hills (Central Nepal). Earth Surface Processes and Landforms, 24(9), 799–808, doi:10.1002/(SICI)1096-9837(199908)24:9<799::AID-ESP12>3.0.CO;2-4.

Johnston, A. C., and Schweig, E. S. (1996). The enigma of the New Madrid earthquakes of 1811–1812. Annual Review of Earth and Planetary Sciences, 24, 339–384, doi:10.1146/annurev.earth.24.1.339.

Johnson, G. A., Horton, S. P., Withers, M., and Cox, R. (2014) Earthquake focal mechanisms in the New Madrid seismic zone. Seismological Research Letters, 85(2), 257–267, doi:10.1785/0220130140.

Johnson, B. (2020). Stream capture and the geomorphic evolution of the Linville Gorge in the southern Appalachians, USA. Geomorphology, 368, 107360, doi:10.1016/j.geomorph.2020.107360.

Kale, M. M., and Ataol, M. (2021). The effects of dams on river channel morphology: A case study at the historical Çarşamba Bridge on the Yeşilırmak River in northern Turkey. Environmental Earth Science, 80(18), 624, doi:10.1007/s12665-021-09935-6.

Kelson, K. I., Simpson, G. D., VanArsdale, R. B., Haraden, C. C., and Lettis, W. R. (1996). Multiple late Holocene earthquakes along the Reelfoot fault, central New Madrid seismic zone. Journal of Geophysical Research: Solid Earth, 101(B3), 6151–6170. doi:10.1029/95JB01815.

Kirby, E., and Whipple, K. (2001). Quantifying differential rock-uplift rates via stream profile analysis. Geology, 29, 415–418, doi:10.1130/0091-7613(2001)029<0415:QDRURV>2.0.CO;2.

Koyi, H., Nilfouroushan, F., and Hessami, K. (2016). Modelling role of basement block rotation and strike-slip faulting on structural pattern in cover units of fold-and-thrust belts. Geological Magazine, 153(5–6), 827–844, doi:10.1017/S0016756816000595.

Lary, B. (2019). Geomorphological Assessment of the Eastern Tennessee Seismic Zone. Ph.D. Dissertation, North Carolina Central University, Available at https://www.proquest.com/openview/f3b46fd43417dd6ce54b32cf95f0cf54/1.

Leigh, D. S., and Knox, J. C. (1993). AMS radiocarbon age of the upper Mississippi Valley Roxana Silt. Quaternary Research, 39(3), 282–289, doi:10.1006/qres.1993.1035.

Levandowski, W., Herrmann, R. B., Briggs, R., Boyd, O., and Gold, R. (2018). An updated stress map of the continental United States reveals heterogeneous intraplate stress. Nature Geoscience, 11(6), 433–437, doi:10.1038/s41561-018-0120-x.

Levandowski, W., and Powell, C. A. (2019). Evidence for strain accrual in the eastern Tennessee seismic zone from earthquake statistics. Seismological Research Letters, 90(1), 446–451, doi:10.1785/0220180052.

Levandowski, W., Powell, C. A., Chapman, M. and Wu, Q. (2023). Anomalous crustal stress in the eastern Tennessee seismic zone. Seismological Research Letters, 94(3), 1643–1655, doi:10.1785/0220220364.

Liberty, L. (2022). Seismic profiling of faults related to the 1886 Charleston earthquake: Summerville survey. USGS Final Technical Report Grant No. G19AP00080, 15 pp.

Lifton, N. A., and Chase, C. G. (1992). Tectonic, climatic and lithologic influences on landscape fractal dimension and hypsometry: Implications for landscape evolution in the San Gabriel Mountains, California. Geomorphology, 5(1–2), 77–114, doi:10.1016/0169-555X(92)90059-W.

Lyell, C. (1849). A second visit to the United States of North America. New York. Harper & Brothers, Publishers. John Murray. [Pdf] Retrieved from the Library of Congress. https://www.loc.gov/item/01026866/.

Mahmood, S. A., and Gloaguen, R. (2011). Analyzing spatial autocorrelation for the hypsometric integral to discriminate neotectonics and lithologies using DEMs and GIS. GIScience & Remote Sensing, 48(4), 541–565, doi:10.2747/1548-1603.48.4.541.

Markewich, H. W., Wysocki, D. A., Pavich, M. J., Rutledge, E. M., Millard, H. T., Rich, F. J., Maat, P. B., Rubin, M., and McGeehin, J. (1998). Paleopedology plus TL, ^{10}Be, and ^{14}C dating as tools in stratigraphic and paleoclimatic investigations, Mississippi River Valley, USA. Quaternary International, 51–52, 143–167, doi:10.1016/S1040-6182(97)00041-4.

Marliyani, G. I., Arrowsmith, J. R., and Whipple, K. X. (2016). Characterization of slow slip rate faults in humid areas: Cimandiri fault zone, Indonesia. Journal of Geophysical Research: Earth Surface, 121(12), 2287–2308, doi:10.1002/2016JF003846.

Marple, R., and Hurd, J. (2020). Interpretation of lineaments and faults near Summerville, South Carolina, USA, using LiDAR data: Implications for the cause of the 1886 Charleston, South Carolina, earthquake. Atlantic Geology, 56, 73–95, doi:10.4138/atlgeol.2020.003.

Marston, R. A., Mills, J. D., Wrazien, D. R., Bassett, B., and Splinter, D. K. (2005). Effects of Jackson Lake Dam on the Snake River and its floodplain, Grand Teton National Park, Wyoming, USA. Geomorphology, 71(1–2), 79–98, doi:10.1016/j.geomorph.2005.03.005.

Martin, S. S., and Hough, S. E. (2019). Where was the 31 October 1895 Charleston, Missouri, Earthquake? Bulletin of the Seismological Society of America, 109(4), 1479–1479. doi:10.1785/0120180328.

Matmon, A., Bierman, P. R., Larsen, J., Southworth, S., Pavich, M., Finkel, R., and Caffee, M. (2003). Erosion of an ancient mountain range, the Great Smoky Mountains, North Carolina and Tennessee. American Journal of Science, 303(9), 817–855, doi:10.2475/ajs.303.9.817.

Mazzotti, S. (2007). Geodynamic models for earthquake studies in intraplate North America. In: Stein, S., and Mazzotti, S. (Eds) Continental Intraplate Earthquakes: Science, Hazard, and Policy Issues, Geological Society of America Special Paper 425 (pp. 17–22), Boulder, CO: Geological Society of America, doi:10.1130/2007.2425(02).

McKay, E. D. (1979). Wisconsin loess stratigraphy of Illinois. Illinois State Geological Survey Guidebook, 13, 95–108.

McKeown, F. A., Jones-Cecil, M., Askew, B. L., and McGrath, M. B. (1988). Analysis of stream-profile data and inferred tectonic activity, Eastern Ozark Mountains Region. U.S. Geological Survey Bulletin, 1807, 39 pp., doi:10.3133/b1807.

Meigs, A. (2013). Active tectonics and the LiDAR revolution. Lithosphere, 5(2), 226–229, doi:10.1130/RF.L004.1.

Meissner, C. R. (1984). Stratigraphic framework and distribution of lignite on Crowley's Ridge: Little Rock, Arkansas. Arkansas Geologic Commission Information Circular 28-B, 32 pp., Available at https://www.geology.arkansas.gov/publication/information-circulars/IC-28B-information-circular.html.

Miller, S. R., Sak, P. B., Kirby, E., and Bierman, P. R. (2013). Neogene rejuvenation of central Appalachian topography: Evidence for differential rock uplift from stream profiles and erosion rates. Earth and Planetary Science Letters, 369–370, 1–12, doi:10.1016/j.epsl.2013.04.007.

Minsley, B. J., Kress, W. H., and Rigby, J. R. (2019). Hidden complexity of the Mississippi River alluvial aquifer illuminated like never before using regional-scale airborne geophysics. In: Thorleifson, L. H. (Ed) Geologic Mapping Forum 2019 Abstracts, Minnesota Geological Survey Open File Report OFR-19-1 (pp. 61-62), Available at https://hdl.handle.net/11299/202386.

Montgomery, D. R. (2001). Slope distributions, threshold hillslopes, and steady-state topography. American Journal of Science, 301(4–5), 432–454, doi:10.2475/ajs.301.4-5.432.

Moore, G. K., and Brown, D. L. (1969). Stratigraphy of the Fort Pillow test well, Lauderdale Country, Tennessee. Tennessee Division of Geology, Report of Investigations, 26.

Mueller, K., and Pujol, J. (2001). Three-dimensional geometry of the Reelfoot blind thrust: Implications for moment release and earthquake magnitude in the New Madrid seismic zone. Bulletin of the Seismological Society of America, 91(6), 1563–1573, doi:10.1785/0120000276.

Nardini, A., and Brierley, G. (2021). Automatic river planform identification by a logical-heuristic algorithm. Geomorphology, 375, 107558, doi:10.1016/j.geomorph.2020.107558.

Nava, S. J., Munsey, J. W., and Johnston, A. C. (1989). First fault plane identification in the southern Appalachians: The mbLg Vonore, Tennessee, earthquake of March 27, 1987. Seismological Research Letters, 60(3), 119–129, doi:10.1785/gssrl.60.3.119.

Nelson, K.D., and Zhang, J. (1991). A COCORP deep reflection profile across the buried reelfoot rift, south-central United States. Tectonophysics, 197(2–4), 271–293. doi:10.1016/0040-1951(91)90046-U.

Ntokos, D., Lykoudi, E., and Rondoyanni, T. (2016). Geomorphic analysis in areas of low-rate neotectonic deformation: South Epirus (Greece) as a case study. Geomorphology, 263, 156–169. doi:10.1016/j.geomorph.2016.04.005.

Nuttli, O. W. (1973). The Mississippi Valley earthquakes of 1811 and 1812: Intenities, ground motion and magnitudes. Bulletin of the Seismological Society of America, 63(1), 227–248, doi:10.1785/BSSA0630010227.

OCM Partners (2023a). 2020 USGS Lidar DEM: Savannah Pee Dee, SC. NOAA National Centers for Environmental Information, Available at https://www.fisheries.noaa.gov/inport/item/65959.

OCM Partners (2023b). 2017 SC DNR Lidar DEM: Coastal Counties (Berkeley, Charleston and Williamsburg Counties). NOAA National Centers for Environmental Information, Available at https://www.fisheries.noaa.gov/inport/item/57112.

Odum, J. K., Stephenson, W. J., and Williams, R. A. (2010). Multisource, high-resolution seismic-reflection imaging of Meeman-Shelby fault and a possible tectonic model for a Joiner Ridge–Manila High stepover structure in the upper Mississippi Embayment region. Seismological Research Letters, 81(4), 647–663, doi: 10.1785/gssrl.81.4.647.

Ohmori, H. (1993). Changes in the hypsometric curve through mountain building resulting from concurrent tectonics and denudation. Geomorphology, 8(4), 263–277, doi:10.1016/0169-555X(93)90023-U.

Olson, P. L., Legg, N. T., Abbe, T. B., Reinhart, M. A., and Radloff, J. K. (2014). A methodology for delineating planning-level channel migration zones. Washington State Department of Ecology Publication 14-06–025, Olympia, WA: Washington State Department of Ecology, 83 pp., Available at https://apps.ecology.wa.gov/publications/SummaryPages/1406025.html

Ostenaa, D. A., and Zellman, M. S. (2018). MI-97 Paleoseismic Investigation of the Cheraw Fault at Haswell, Colorado. Colorado Geological Survey Paleoseismic Miscellaneous Investigations MI–97, Golden, CO: Colorado Geological Survey, Available at https://coloradogeologicalsurvey.org/publications/paleoseismic-investigations-cheraw-fault/.

Panno, S. V., Hackley, K. C., Kelly, W. R., and Luman, D. E. (2011). Illinois' sinkhole plain: Classic karst terrain of the midwestern United States. Geological Field Trip Guidebook for the 12th Multidisciplinary Conference on Sinkholes and the Engineering and Environmental Impacts of Karst, January 10–14, 2011, St. Louis, MO: Illinois State Geological Survey, Guidebook 39, 45 pp., Available at http://hdl.handle.net/2142/32557.

Pavich, M. J., Brown, L., Valette-Silver, J. N., Klein, J., and Middleton, R. (1985). ^{10}Be analysis of a Quaternary weathering profile in the Virginia Piedmont. Geology, 13(1), 39–41, doi:10.1130/0091-7613(1985)13<39:BAOAQW>2.0.CO;2.

Pazzaglia, F. J., Malenda, H. F., McGavick, M. L., Raup, C., Carter, M. W., Berti, C., Mahan, S., Nelson, M., Rittenour, T. M., Counts, R., Willenbring, J., Germanoski, D., Peters, S. C., and Holt, W. D. (2021). River terrace evidence of tectonic processes in the eastern North American Plate interior, South Anna River, Virginia. The Journal of Geology, 129(5), 595–624, doi:10.1086/712636.

Pedrera, A., Pérez-Peña, J. V., Galindo-Zaldívar, J., Azañón, J. M., and Azor, A. (2009). Testing the sensitivity of geomorphic indices in areas of low-rate active folding (eastern Betic Cordillera, Spain). Geomorphology, 105(3–4), 218–231. doi:10.1016/j.geomorph.2008.09.026.

Petersen, M.D., Mueller, C. S., Moschetti, M. P., Hoover, S. M., Rukstales, K. S., McNamara, D. E., Williams, R. A., Shumway, A. M., Powers, P. M., Earle, P. S. and Llenos, A. L. (2018). 2018 One-year seismic hazard forecast for the central and eastern United States from induced and natural earthquakes. Seismological Research Letters, 89(3), 1049–1061. doi:10.1785/0220180005.

Petersen, M. D., Frankel, A. D., Harmsen, S. C., Mueller, C. S., Haller, K. M., Wheeler, R. L., Wesson, R. L., Zeng, Y., Boyd, O. S., Perkins, D. M., Luco, N., Field, E. H., Wills, C. J., and Rukstales, K. S. (2008). Documentation for the 2008 update of the United States

National Seismic Hazard Maps. U.S. Geological Survey Open-File Report 2008-1128, 61 pp., doi:10.3133/ofr20081128.

Petersen, M. D., Moschetti, P. M., Mueller, C. S., Haller, K. M., Frankel, A. D., Zeng, Y., Rezaeian, S., Harmsen, S. C., and Boyd, O. S. (2014). Documentation for the 2014 update of the United States National Seismic Hazard Maps. U.S. Geological Survey Open-File Report 2014-1091, 243 pp., doi:10.3133/ofr20141091.

Pigati, J. S., McGeehin, J. P., Muhs, D. R., Grimley, D. A., and Nekola, J. C. (2015) Radiocarbon dating loess deposits in the Mississippi Valley using terrestrial gastropod shells (Polygyridae, Helicinidae, and Discidae). Aeolian Research, 16, 25–33, doi:10.1016/j.aeolia.2014.10.005.

Powell, J. W. (1875). Exploration of the Colorado River of the West and its tributaries. U.S. Geological Survey Monograph, 291 pp., 2 plates, doi:10.3133/70039238.

Powell, C. A., Bollinger, G. A., Chapman, M. C., Sibol, M. S., Johnston, A. C., and Wheeler, R. L. (1994). A seismotectonic model for the 300-kilometer-long eastern Tennessee seismic zone. Science, 264(5159), 686–688, doi:10.1126/science.264.5159.6.

Powell, C. A., Withers, M. M., Cox, R. T., Vlahovic, G., and Arroucau, P. (2014). Crustal velocity structure associated with the eastern Tennessee seismic zone: Vp and Vs images based upon local earthquake tomography. Journal of Geophysical Research: Solid Earth, 119(1), 464–489, doi:10.1002/2013JB010433.

Powell, C. A., and Thomas, W. A. (2016). Grenville basement structure associated with the Eastern Tennessee seismic zone, southeastern USA. Geology, 44(1), 39–42, doi:10.1130/G37269.1.

Pratt, T. L. (2012). Kinematics of the New Madrid seismic zone, central United States, based on stepover models. Geology, 40(4), 371–374, doi:10.1130/G32624.1.

Pratt, T. L., and Counts, R. C. (2023). Ground-penetrating radar profiles in the epicentral area of the Charleston, SC, earthquake. U.S. Geological Survey data release, doi:10.5066/P9S50R1K.

Pratt, T. L., Williams, R. A., Odum, J. K., and Stephenson, W. J. (2013). Origin of the Blytheville Arch, and long-term displacement on the New Madrid seismic zone, central United States. In: Tom Cox, R., Tuttle, M. P., Boyd, O. S., and Locat, J. (Eds) Recent Advances in North American Paleoseismology and Neotectonics East of the Rockies, Geological Society of America Special Paper 493 (pp. 1–15), Boulder, CO: Geological Society of America, doi:10.1130/2012.2493(01).

Pratt, T. L., Shah, A. K., Counts, R. C., Horton Jr, J. W., and Chapman, M. C. (2022). Shallow faulting and folding in the epicentral area of the 1886 Charleston, South Carolina, earthquake. Bulletin of the Seismological Society of America, 112(4), 2097-2123, doi: 10.1785/0120210329.

Price, A. C., Woolery, E. W., Counts, R. C., Van Arsdale, R. B., Larsen, D., Mahan, S. A., and Beck, E. G. (2019). Quaternary displacement on the Joiner Ridge fault, eastern Arkansas. Seismological Research Letters, 90(6), 2250–2261, doi:10.1785/0220190149.

Prowell, D. C. (1983). Index of faults of Cretaceous and Cenozoic age in the eastern United States. U.S. Geological Survey Miscellaneous Field Studies Map 1269, scale 1:2,500,000, doi:10.3133/mf1269.

Pryne, D., van Arsdale, R. B., Csontos, R., and Woolery, E. (2013). Northeastern extension of the New Madrid north fault, New Madrid seismic zone, central United States. Bulletin of the Seismological Society of America, 103(4), 2277–2294, doi:10.1785/0120120241.

Pujol, J., Johnston, A., Chiu, J.-M., and Yang, Y.-T. (1997). Refinement of thrust faulting models for the Central New Madrid seismic zone. Engineering Geology, 46(3–4), 281–298. doi:10.1016/S0013-7952(97)00007-0.

Rabii, F., Achour, H., Rebai, N., and Jallouli, C. (2017). Hypsometric integral for the identification of neotectonic and lithology differences in low tectonically active area (Utica-Mateur region, north-eastern Tunisia). Geocarto International, 32(11), 1229–1242, doi:10.1080/10106049.2016.1195890.

Rains, D. S., and Guccione, M. J. (2016). Formation of the Marianna Gap, a transverse stream valley, through Crowley's Ridge, northern Mississippi alluvial valley, U.S.A. Seismological Research Letters, 87(6), 1442–1452. doi:10.1785/0220160083.

Rankin, D. W., Espenshade, G. H., and Neuman, R. B. (1972). Geologic map of the west half of the Winston-Salem quadrangle, North Carolina, Virginia, and Tennessee. U.S. Geological Survey Miscellaneous Geologic Investigations Map 709-A, scale 1:250,000, doi:10.3133/i709A.

Reimer, P. J., Austin, W. E. N., Bard, E., Bayliss, A., Blackwell, P. G., Bronk Ramsey, C., et al. (2020). The IntCal20 northern hemisphere radiocarbon age calibration curve (0–55 cal kBP). Radiocarbon, 62(4), 725–757, doi:10.1017/RDC.2020.41.

Reinbold, D. J., and Johnston, A. C. (1987). Historical seismicity in the southern Appalachian seismic zone. U.S. Geological Survey Open-File Report 87-433, 862 pp., doi:10.3133/ofr87433.

Reitman, N. G., Bennett, S. E. K., Gold, R. D., Briggs, R. W., and DuRoss, C. B. (2015). High resolution trench photomosaics with structure from motion: Workflow and accuracy assessment. Bulletin of the Seismological Society of America, 105(5), 2354–2366, doi:10.1785/0120150041.

Reitman, N. G., Klinger, Y., Briggs, R. W., and Gold, R. D. (2023). Climatic influence on the expression of strike-slip faulting. Geology, 51(1), 18–22, doi:10.1130/G50393.1.

Renfroe, C. A. (1949). Petroleum exploration in eastern Arkansas with selected well logs. Arkansas Resource and Development Commission, Division of Geology Bulletin 14, 159 pp., 2 plates, Available at https://www.geology.arkansas.gov/publication/bulletins/b14-bulletin.html.

Rhea, M., Tanner, H. S., Knight, J., and Dawson, E. B. (1832). A map of the state of Tennessee taken from survey. Columbia, TN: Matthew Rhea, Available at https://www.loc.gov/item/2011588000/.

Rittenour, T. M., Blum, M. D., and Goble, R. J. (2007). Fluvial evolution of the lower Mississippi River valley during the last 100 k.y. glacial cycle: Response to glaciation and sea-level change. Geological Society of America Bulletin, 119(5–6), 586–608. doi:10.1130/B25934.1.

Ritz, J. F., Baize, S., Ferry, M., Larroque, C., Audin, L., Delouis, B., and Mathot, E. (2020). Surface rupture and shallow fault reactivation during the 2019 Mw 4.9 Le Teil earthquake, France. Nature Communications Earth & Environment, 1(1), 10, doi: 10.1038/s43247-020-0012-z.

Rodgers, J. (1953). Geologic map of east Tennessee with explanatory text. Tennessee Division of Geology Bulletin 58 Part 2, 167 pp., 14 plates, scale 1:125,000, Available at https://www.tn.gov/environment/program-areas/tennessee-geological-survey/geology-redirect/maps-publications/out-of-print-publications-on-line.html.

Rodbell, D. T. (1996). Subdivision, subsurface stratigraphy, and estimated age of fluvial-terrace deposits in northwestern Tennessee. U.S. Geological Survey Bulletin 2128, 24 pp., doi:10.3133/b2128.

Rodbell, D. T., Forman, S. L., Pierson, J., and Lynn, W. C. (1997). Stratigraphy and chronology of Mississippi Valley loess in western Tennessee. Geological Society of America Bulletin, 109(9), 1134–1148, doi:10.1130/0016-7606(1997)109<1134:SACOMV>2.3.CO;2.

Rodbell, D. T., and Schweig, E. S. (1993). The record of seismically induced liquefaction on late Quaternary terraces in northwestern Tennessee. Bulletin of the Seismological Society of America, 83(1), 269–278, doi:10.1785/BSSA0830010269.

Rosas, F. M., Duarte, J. C., Neves, M. C., Terrinha, P., Silva, S., Matias, L., Garcia, E., and Bartolomé, R. (2012). Thrust–wrench interference between major active faults in the Gulf of Cadiz (Africa–Eurasia plate boundary, offshore SW Iberia): Tectonic implications from coupled analog and numerical modeling. Tectonophysics, 548–549, 1–21, doi:10.1016/j.tecto.2012.04.013.

Rosas, F. M., Terrinha, P., Duarte, J., Baptista, L., Kullberg, C., Almeida, J., Barata, F., Carvalho, B. N., Grigorova, V., Tomas, R., and Almeida, P. (2014). Analog modelling of strike-slip fault (lateral) propagation from an elastic to a viscous medium: Insights from trial experiments. Communicações Geológicas, 101(3), 1429–1432.

Rosgen, D. L. (1996). Applied River Morphology. Pagosa Springs, CO: Wildland Hydrology, 378 pp.

Ruhe, R. V. (1983). Depositional environment of late Wisconsin loess in the midcontinental United States. In: Porter, S.C. (Ed) Late-Quaternary Environments of the United States, the Late Pleistocene Volume 1 (pp. 130–137), Minneapolis, MN: University of Minnesota Press.

Russ, D. P. (1979). Late Holocene faulting and earthquake recurrence in the Reelfoot Lake area, northwestern Tennessee. Geological Society of America Bulletin, 90(11), 1013–1018, doi:10.1130/0016-7606(1979)90<1013:LHFAER>2.0.CO;2.

Russ, D. P. (1982). Style and significance of surface deformation in the vicinity of New Madrid, Missouri. In: McKeown, F. A., and Pakiser, L. C. (Eds) Investigations of the New Madrid, Missouri, earthquake region, U.S. Geological Survey Professional Paper 1236 (pp. 95–114), doi:10.3133/pp1236.

Russell, J. (1795). Map of the southern states of America: Comprehending Maryland, Virginia, Kentucky, Territory sth. of the Ohio, North Carolina, Tennessee Government, South Carolina, & Georgia, Available at https://dlg.usg.edu/record/guan_hmap_hmap1795r7.

Rutledge, E. M., West, L. T., and Guccione, M. J. (1990). Loess deposits of northeast Arkansas. In: Guccione, M. J., and Rutledge, E. M. (Eds) Field Guide to the Mississippi Alluvial Valley, Northeast Arkansas and Southeast Missouri (pp. 57–98). Friends of the Pleistocene - South Central Cell 8th Annual Field trip, Fayetteville, Arkansas.

Saucier, R. T. (1974). Quaternary geology of the lower Mississippi Valley. Arkansas Archaeological Survey Research Series No. 6, 26 pp.

Saucier, R. T. (1987). Geomorphological interpretations of late Quaternary terraces in western Tennessee and their regional tectonic implications. U.S. Geological Survey Professional Paper 1336, 19 pp., doi:10.3133/pp1336A.

Saucier, R. T. (1994). Geomorphology and Quaternary Geologic History of the Lower Mississippi Valley, Volume 1. Vicksburg, MS: U.S. Army Corps of Engineers Waterways Experiment Station, 414 pp .

Saucier, R. T., and Fleetwood, A. R. (1970). Origin and chronologic significance of late Quaternary terraces, Ouachita River, Arkansas and Louisiana. Geological Society of America Bulletin, 81(3), 869–890, doi:10.1130/0016-7606(1970)81[869:OACSOL]2.0.CO;2.

Schumm, S. A.,(1956). Evolution of drainage systems and slopes in badlands at Perth Amboy, New Jersey. Geological Society of America Bulletin, 67(5), 597–646, doi:10.1130/0016-7606(1956)67[597:EODSAS]2.0.CO;2.

Schumm, S. A., and Brakenridge, G. R. (1987). River responses. In: Ruddiman, W. F., and Wright, Jr., H. E. (Eds) North America and Adjacent Oceans During the Last Deglaciation, DNAG Geology of North America Volume K-3 (pp. 221–240), Boulder, CO: Geological Society of America, doi:10.1130/DNAG-GNA-K3.221.

Schwanghart, W., and Kuhn, N. J. (2010). TopoToolbox: A set of Matlab functions for topographic analysis. Environmental Modelling & Software, 25(6), 770–781. doi:10.1016/j.envsoft.2009.12.002.

Schwanghart, W., and Scherler, D. (2014). Short Communication: TopoToolbox 2 – MATLAB-based software for topographic analysis and modeling in Earth surface sciences. Earth Surface Dynamics, 2(1), 1–7, doi:10.5194/esurf-2-1-2014.

Schweig, E. S., and Ellis, M. A. (1994). Reconciling short recurrence intervals with minor deformation in the New Madrid seismic zone. Science, 264(5163), 1308–1311. doi:10.1126/science.264.5163.1308.

Secor Jr., D. T., Snoke, A. W., and Dallmeyer, R. D. (1986). Character of the Alleghanian orogeny in the southern Appalachians: Part III. Regional tectonic relations. Geological Society of America Bulletin, 97(11), 1345–1353. doi:10.1130/0016-7606(1986)97<1345:COTAOI>2.0.CO;2.

Shah, A. K., Pratt, T. L., and Horton Jr, J. W. (2023). Rift Basins and Intraplate Earthquakes: New High-Resolution Aeromagnetic Data Provide Insights Into Buried Structures of the Charleston, South Carolina Seismic Zone. Geochemistry, Geophysics, Geosystems, 24(5), e2022GC010803, doi:10.1029/2022GC010803.

Shankman, D., and Samson, S. A. (1991). Channelization effects on Obion River flooding, western Tennessee. Journal of the American Water Resources Association, 27(2), 247–254, doi:10.1111/j.1752-1688.1991.tb03129.x.

Shen, Z., Törnqvist, T. E., Autin, W. J., Mateo, Z. R. P., Straub, K. M., and Mauz, B. (2012). Rapid and widespread response of the Lower Mississippi River to eustatic forcing during the last glacial-interglacial cycle. Bulletin, 124(5–6), 690–704, doi:10.1130/B30449.1.

Sherrod, B. L., Brocher, T. M., Weaver, C. S., Bucknam, R. C., Blakely, R. J., Kelsey, H. M., Nelson, A. R., and Haugerud, R. (2004). Holocene fault scarps near Tacoma, Washington, USA. Geology, 32(1), 9–12, doi:10.1130/G19914.1.

Siemon, B., Christiansen, A. V., and Auken, E. (2009). A review of helicopter-borne electromagnetic methods for groundwater exploration. Near Surface Geophysics, 7(5–6), 629–646. doi:10.3997/1873-0604.2009043.

Simek, J. F., Blankenship, S. A., Cressler, A., Douglas, J. C., Wallace, A., Weinand, D., and Welborn, H. (2012). The prehistoric cave art and archaeology of Dunbar cave, Montgomery County, Tennessee. Journal of Caves and Karst Studies, 74(1), 19–32, doi:10.4311/ 2011AN0219.

Simon, A., and Hupp, C. R. (1992). Geomorphic and vegetative recovery processes along modified stream channels of West Tennessee. U.S. Geological Survey Open-File Report 91–502, 142 pp., doi:10.3133/ofr91502.

Simpson, R. W. (1997). Quantifying Anderson's fault types. Journal of Geophysical Research: Solid Earth, 102(B8), 17909–17919, doi:10.1029/97JB01274.

Snowden, J. O., and Priddy, R. R. (1968). Loess investigations in Mississippi. Mississippi Geological, Economic, and Topographic Survey Bulletin 111, 267 pp., Available at https://www.mdeq.ms.gov/geology/work-areas/publications-and-map-sales/categories/bulletins/loess-investigations-in-mississippi-19386/

Southworth, S., Schultz, A., Aleinikoff, J. N., and Merschat, A. J. (2012). Geologic Map of the Great Smoky Mountains National Park and Region, Tennessee and North Carolina. U.S. Geological Survey Scientific Investigations Map 2997, 54 pp., 1 plate, scale 1:100,000, doi:10.3133/sim2997.

Spotila, J. A., and Prince, P. S. (2022). Geomorphic complexity and the case for topographic rejuvenation of the Appalachian Mountains. Geomorphology, 417*,* 108449, doi:10.1016/j.geomorph.2022.108449.

Spitz, W. J., and Schumm, S. A. (1997). Tectonic geomorphology of the Mississippi Valley between Osceola, Arkansas and Friars Point, Mississippi. Engineering Geology, 46(3–4), 259–280, doi:10.1016/S0013-7952(97)00006-9.

Stahle, D. W., Van Arsdale, R. B., and Cleaveland, M .K. (1992). Tectonic signal in baldcypress trees at Reelfoot Lake, Tennessee. Seismological Research Letters, 63(3), 439–447, doi:10.1785/gssrl.63.3.439.

Stein, S., Liu, M., Camelbeeck, T., Merino, M., Landgraf, A., Hintersberger, E., and Kübler, S. (2017). Challenges in assessing seismic hazard in intraplate Europe. In: Landgraf, A., Kübler, S., Hintersberger, E., and Stein, S. (Eds) Seismicity, Fault Rupture and Earthquake Hazards in Slowly Deforming Regions (pp. 13–28). Geological Special Publication 432, London: The Geological Society, doi:10.1144/SP432.7.

Stephenson, W. J., Shedlock, K. M., & Odum, J. K. (1995). Characterization of the Cottonwood Grove and Ridgely faults near Reelfoot Lake, Tennessee, from high-resolution seismic reflection data. (Report No. 1538I). https://doi.org/10.3133/pp1538I.

Stephenson, W. J., Odum, J. K., Williams, R. A., Pratt, T. L., Harrison, R. W., and Hoffman, D. (1999). Deformation and Quaternary faulting in southeast Missouri across the Commerce geophysical lineament. Bulletin of the Seismological Society of America, 89(1), 140–155, doi:10.1785/BSSA0890010140.

Stine, T. A., and Van Arsdale, R. B. (2017). Faulting within and bounding northern Crowley's Ridge, Northeastern Arkansas. Southeastern Geology, 52(3), 117–133.

Stover, C. W., and Coffman, J. L. (1993). Seismicity of the United States, 1568–1989. U.S. Geological Survey Professional Paper 1527, 417 pp., doi:10.3133/pp1527.

Strahler, A. N. (1952). Hypsometric (area-altitude) analysis of erosional topography. Geological Society of America Bulletin, 63(11), 1117–1142, doi:10.1130/0016-7606(1952)63[1117:HAAOET]2.0.CO;2.

Strahler, A. N. (1964). Quantitative geomorphology of drainage basins and channel networks. In: Chow, V. T. (Ed) Handbook of Applied Hydrology (pp. 439–476). New York: McGraw-Hill.

Streig, A., Bennett, S., Hornsby, K., Chang, J., and Mahan, S. (2018). Recent paleoseismic and tectonic geomorphic Studies of the Meers Fault, Oklahoma reveal longer rupture lengths and more Surface deforming earthquakes in the last 6,000 years. Abstract S41D-0576 presetned at the 2018 American Geophysical Union Fall Meeting, 10-14 December, Washington, DC.

Stuiver, M., Reimer, P. J., and Reimer, R. W. (2021). CALIB Radiocarbon Calibration, Version 8.2, Radiocarbon, 35(1), 215–230, doi:10.1017/S0033822200013904, WWW program available at http://calib.org.

Styron, R. (2019). The impact of earthquake cycle variability on neotectonic and paleoseismic slip rate estimates. Solid Earth, 10(1), 15–25. doi:10.5194/se-10-15-2019.

Sugarbaker, L. J., Eldridge, D. F., Jason, A. L., Lukas, V., Saghy, D. L., Stoker, J. M., and Thunen, D. R.,(2017). Status of the 3D Elevation Program, 2015. U.S. Geological Survey Open-File Report 2016-1196, 13 pp., doi:10.3133/ofr20161196.

Summerfield, M.A., and Hulton, N.J. (1994). Natural controls of fluvial denudation rates in major world drainage basins. Journal of Geophysical Research: Solid Earth, 99(B7), 13871–13883, doi:10.1029/94JB00715.

Talwani, P., and Schaeffer, W. T. (2001). Recurrence rates of large earthquakes in the South Carolina Coastal Plain based on paleoliquefaction data. Journal of Geophysical Research, 106(B4), 6621–6642, doi:10.1029/2000JB900398.

Tarolli, P., and Sofia, G. (2016). Human topographic signatures and derived geomorphic processes across landscapes. Geomorphology, 255, 140–161. doi:10.1016/j.geomorph.2015.12.007.

Thompson, S. C., Weldon, R. J., Rubin, C. M., Abdrakhmatov, K., Molnar, P., and Berger, G. W. (2002). Late Quaternary slip rates across the central Tien Shan, Kyrgyzstan, central Asia. Journal of Geophysical Research: Solid Earth, 107(B9), ETG 7-1–ETG 7-32, doi:10.1029/2001JB000596.

Thompson Jobe, J. A., Li, T., Chen, J., Burbank, D. W., and Bufe, A. (2017). Quaternary tectonic evolution of the Pamir-Tian Shan convergence zone, Northwest China. Tectonics, 36(12), 2748–2776, doi: 10.1002/2017TC004541.

Thompson Jobe, J. A., Gold, R. D., Briggs, R. W., Williams, R. A., Stephenson, W. J., Delano, J. E., Shah, A., and Minsley, B. (2020a). Evidence for late Quaternary deformation along Crowleys Ridge, New Madrid seismic zone. Tectonics, 39, e2019TC005746, doi:10.1029/2019TC005746.

Thompson Jobe, J. A., Gold, R. D., Briggs, R. W., Williams, R. A., Stephenson, W. J., Delano, J. E., Shah, A., and Minsley, B. (2020b). Digital datasets documenting subsurface data locations, topographic metrics, fault scarp mapping, and revised fault network for Crowley's Ridge. New Madrid Seismic Zone. U.S. Geological Survey data release, doi:10.5066/P9TFRP5D.

Thompson Jobe, J. A., Briggs, R. W., Gold, R. D., Bauer, L., and Collett, C. (2023). Datasets documenting limited evidence of Late Pleistocene tectonic surface deformation in the Eastern Tennessee Seismic Zone, Tennessee, USA. U.S. Geological Survey data release, doi:10.5066/P9R5NSAI.

Tuttle, M.P., Wolf, L. W., Starr, M. E., Villamor, P., Lafferty III, R. H., Morrow, J. E., Scott Jr., R. J., Forman, S. L., Hess, K., Tucker, K., and Dunahue, J. (2019). Evidence for large New Madrid earthquakes about A.D. 0 and 1050 B.C., central United States. Seismological Research Letters, 90(3), 1393–1406, doi:10.1785/0220180371.

Tuttle, M. P. (2001). The use of liquefaction features in paleoseismology: Lessons learned in the New Madrid seismic zone, central United States. Journal of Seismology, 5(3), 361–380, doi:10.1023/A:1011423525258.

Tuttle, M. P., Al-Shukri, H., and Mahdi, H. (2006). Very large earthquakes centered southwest of the New Madrid seismic zone 5,000-7,000 years ago. Seismological Research Letters, 77(6), 755–770, doi:10.1785/gssrl.77.6.755.

Tuttle, M. P., and Atkinson, G. M. (2010). Localization of large earthquakes in the Charlevoix seismic zone, Quebec, Canada, during the past 10,000 years. Seismological Research Letters, 81(1), 140–147, doi:10.1785/gssrl.81.1.140.

Tuttle, M. P., Schweig, E. S., Campbell, J., Thomas, P. M., Sims, J. D., and Lafferty, R. H. (2005). Evidence for New Madrid earthquakes in A.D. 300 and 2350 B.C. Seismological Research Letters, 76(4), 489–501, doi:10.1785/gssrl.76.4.489.

Tuttle, M. P., Schweig, E. S., Sims, J. D., Lafferty, R. H., Wolf, L. W., and Haynes, M. L. (2002). The earthquake potential of the New Madrid seismic zone. Bulletin of the Seismological Society of America, 92(6), 2080–2089, doi:10.1785/0120010227.

U.S. Army Corps or Engineers (USACE) (2012). Western Tennessee Lidar. Available at https://www.tn.gov/finance/sts-gis/gis/gis-projects/gis-projects-elevation.html.

U.S. Department of Energy, Electric Power Research Institute, and U.S. Nuclear Regulatory Commission (2012). Central and Eastern United States Seismic Source Characterization for Nuclear Facilities: NUREG-2115, 6 volumes, 3798 pp., Available at https://www.nrc.gov/reading-rm/doc-collections/nuregs/staff/sr2115/index.html.

U.S. Department of the Interior Fish and Wildlife Service (1989). Reelfoot Lake water level management: Final environmental impact statement.

U.S. Geological Survey (USGS) (2014). Central U.S. ARRA lidar, New Madrid seismic zone, doi:10.5069/G9N014G4.

U.S. Geological Survey (USGS) Earthquake Hazards Program (EHP) (2017). Advanced National Seismic System (ANSS) Comprehensive Catalog of Earthquake Events and Products, doi:10.5066/F7MS3QZH.

Van Arsdale, R. (2000). Displacement history and slip rate on the Reelfoot fault of the New Madrid seismic zone. Engineering Geology, 55(4), 219–226, doi:10.1016/S0013-7952(99)00093-9.

Van Arsdale, R., Bresnahan, R., McCallister, N., and Waldron, B. (2007). Upland Complex of the central Mississippi River valley: Its origin, denudation, and possible role in reactivation of the New Madrid seismic zone. In: Stein, S., and Mazzotti, S. (Eds) Continental Intraplate Earthquakes: Science, Hazard, and Policy Issues Geological Society of America Special Paper 425 (pp. 177–192), Boulder, CO: Geological Society of America, doi: 10.1130/2007.2425(13).

Van Arsdale, R. B., and ten Brink, R. K. (2000). Late Cretaceous and Cenozoic geology of the New Madrid seismic zone. Bulletin of the Seismological Society of America, 90(2), 345–356, doi:10.1785/0119990088.

Van Arsdale, R. B., Cox, R. T., and Lumsden, D. N. (2019). Quaternary uplift in the lower Mississippi River valley. The Journal of Geology, 127(1), 1–13, doi:10.1086/700405.

Van Arsdale, R.B., and Cupples, W. (2013). Late Pliocene and Quaternary deformation of the Reelfoot rift. Geosphere, 9(6), 1819–1831, doi:10.1130/GES00906.1.

Van Arsdale, R. B., Balco, G., Bierman, P. R., Rood, D. H., Rovey, C., Cox, R. T., Lumsden, D. N., and Parks, A. (2014a). The Pliocene Mississippi River. Geological Society of America Abstracts with Programs, 46, 288.

Van Arsdale, R.B., Cox, R.T., Johnston, A.C., Stephenson, W.J., and Odum, J.K. (1999). Southeastern extension of the Reelfoot fault. Seismological Research Letters, 70(3), 348–359, doi:10.1785/gssrl.70.3.348.

Van Arsdale, R. B., Cupples, W. B., and Csontos, R. M. (2014b). Pleistocene–Holocene transition in the central Mississippi River valley. Geomorphology, 214, 270–282, doi:10.1016/j.geomorph.2014.02.011.

Van Arsdale, R. B., Schweig, E. S., Kanter, L. R., Williams, R. A., Shedlock, K. M., and King, K. W. (1992). Preliminary shallow seismic reflection survey of Crowleys Ridge, northeast Arkansas. Seismological Research Letters, 63(3), 309–320, doi:10.1785/gssrl.63.3.309.

Van Arsdale, R. B., Williams, R. A., Schweig, E. S., Shedlock, K. M., Odum, J. K., and King, K. W. (1995). The origin of Crowley's Ridge, northeastern Arkansas: Erosional remnant or tectonic uplift? Bulletin of the Seismological Society of America, 85(4), 963–985, doi:10.1785/BSSA0850040963.

Van Arsdale, R. B., Kelson, K. I., and Lumsden, C. H. (1995). Northern extension of the Tennessee Reelfoot scarp into Kentucky and Missouri. Seismological Research Letters, 66(5), 57–62, doi:10.1785/gssrl.66.5.57.

Van Arsdale, R., Pryne, D., and Woolery, E. (2013). Northwestern extension of the Reelfoot North fault near New Madrid, Missouri. Seismological Research Letters, 84(6), 1114–1123, doi:10.1785/0220130067.

Van Arsdale, R., Purser, J., Stephenson, W., and Odum, J. (1998). Faulting along the southern margin of Reelfoot Lake, Tennessee. Bulletin of the Seismological Society of America, 88(1), 131–139, doi:10.1785/BSSA0880010131.

Velasco, M., Van Arsdale, R., Waldron, B., Harris, J., and Cox, R. (2005). Quaternary faulting beneath Memphis, Tennessee. Seismological Research Letters, 76(5), 598–614, doi:10.1785/gssrl.76.5.598.

Vlahovic, G., Powell, C. A., Chapman, M. C., and Sibol, M. S. (1998). Joint hypocenter-velocity inversion for the eastern Tennessee seismic zone. Journal of Geophysical Research: Solid Earth, 103(B3), 4879–4896, doi:10.1029/97JB01891.

Vogel, J. S., Southon, J. R., Nelson, D. E., & Brown, T. A. (1984). Performance of catalytically condensed carbon for use in accelerator mass spectrometry. Nuclear Instruments and Methods in Physics Research B 5, 289–293, doi:10.1016/0168-583x(84)90529-9.

Ward, A., Counts, R., Van Arsdale, R., Larsen, D., and Mahan, S. (2017). Quaternary displacement rates on the Meeman-Shelby fault and Joiner Ridge horst, eastern

Arkansas: Results from coring Mississippi River alluvium. Seismological Research Letters, 88(2A), 442–455. doi:10.1785/0220160171.

Warrell, K. F., Cox, R. T., Hatcher Jr, R. D., Vaughn, J. D., and Counts, R. (2017). Paleoseismic evidence for multiple Mw≥ 6 earthquakes in the Eastern Tennessee Seismic Zone during the Late Quaternary. Bulletin of the Seismological Society of America, 107(4), 1610–1624, doi:10.1785/0120160161.

Wells-Hull, S. B. (2022). Pre-Alleghanian extension and post-Alleghanian brittle deformation in the southern Appalachians. M.S. Thesis, University of North Carolina at Chapel Hill, 40 pp., doi:10.17615/yhhj-5e71.

Wentworth, C.K. (1922). A scale of grade and class terms for clastic sediments. The Journal of Geology, 30(5), 377–392, doi:10.1086/622910.

Wheeler, R. L. (1995). Earthquakes and the cratonward limit of Iapetan faulting in eastern North America. Geology, 23(2), 105–108, doi:10.1130/0091-7613(1995)023<0105:EATCLO>2.3.CO;2.

Whipple, K. X., and Tucker, G. E. (1999). Dynamics of the stream-power river incision model: Implications for height limits of mountain ranges, landscape response timescales, and research needs. Journal of Geophysical Research Solid Earth, 104(B8), 17661–17674, doi:10.1029/1999JB900120.

Whisner, J. K. (2010). Surface and subsurface structures of the western Valley and Ridge in Tennessee and geometry and kinematics that permit reconstruction of the Tennessee salient, southern Appalachians. Ph.D. Dissertation, University of Tennessee, Knoxville, 263 pp., Available at https://trace.tennessee.edu/utk_graddiss/857.

Willgoose, G., and Hancock, G. (1998). Revisiting the hypsometric curve as an indicator of form and process in transport-limited catchment. Earth Surface Processes and Landforms, 23(7), 611–623, doi:10.1002/(SICI)1096-9837(199807)23:7<611::AID-ESP872>3.0.CO;2-Y.

Williams, R. A., Stephenson, W. J., Odum, J. K., and Worley, D. M. (2001). Seismic-reflection imaging of Tertiary faulting and related post-Eocene deformation 20 km north of Memphis, Tennessee. Engineering Geology, 62(1–3), 79–90, doi:10.1016/S0013-7952(01)00052-7.

Withers, M., Horton, S., Powell, C., Bodin, P., Munsey, J., and Herrmann, R. (2004). Preliminary analysis of aftershocks of the April 29, 2003 4.6 Mw Fort Payne, Alabama, earthquake [Abstract]. Seismological Research Letters, 75(3), 445, doi:10.1785/gssrl.75.3.435.

Wobus, C., Whipple, K. X., Kirby, E., Snyder, N., Johnson, J., Spyropolou, K., Crosby, B., and Sheehan, D. (2006). Tectonics from topography: Procedures, promise, and pitfalls. In: Willett, S. D., Hovius, N., Brandon, M. T., and Fisher, D. M. (Eds) Tectonics, Climate, and Landscape Evolution. Geological Society of America Special Paper 398 (pp. 55–74), Boulder, CO: Geological Society of America, doi:10.1130/2006.2398(04).

Woodward, H. P. (1957). Chronology of Appalachian folding. American Association of Petroleum Geologists Bulletin, 41(10), 2312–2327, doi:10.1306/0BDA5993-16BD-11D7-8645000102C1865D.

Woolderink, H. A. G., Cohen, K. M., Kasse, C., Kleinhans, M. G., and Van Balen, R. T. (2021). Patterns in river channel sinuosity of the Meuse, Roer and Rhine Rivers in the Lower Rhine Embayment rift-system, are they tectonically forced? Geomorphology, 375, 107550, doi:10.1016/j.geomorph.2020.107550.

Wooten, R. M., Cattanach, B. L., Gillon, K. A., and Bozdog, G. N. (2010). Geology of the Mills Gap area, Buncombe County, North Carolina. North Carolina Geological Survey Report of Special Investigation 2010-09-30, Technical Memorandum to the U.S. Environmental Protection Agency, U.S. Geological Survey, and the North Carolina Department of Environment and Natural Resources, Division of Waste Management, 19 pp., 2 plates, scale 1:12,000.

APPENDIX A
SUPPORTING INFORMATION FOR CHAPTER 1

This Appendix provides Figure A-1 of catchment characteristics versus hypsometric integral, Figures A-2 to A-4 of high-resolution uninterpreted images of the seismic reflection data (shown in Figure 1-12 in main text) and airborne electromagnetic (AEM) resistivity profiles (shown in Figure 1-8 and Figure 1-12 in main text), Tables A-2 and A-3 containing information for the seismic reflection processing parameters and the velocity model, Table A-3 containing information for the AEM processing parameters. Shapefiles of scarps mapped from the lidar data (s01, shown in Figure 1-2b in the main text) and New Madrid seismic zone faults (s02, shown in Figure 1-13 in main text) can be found at Thompson Jobe et al. (2020b).

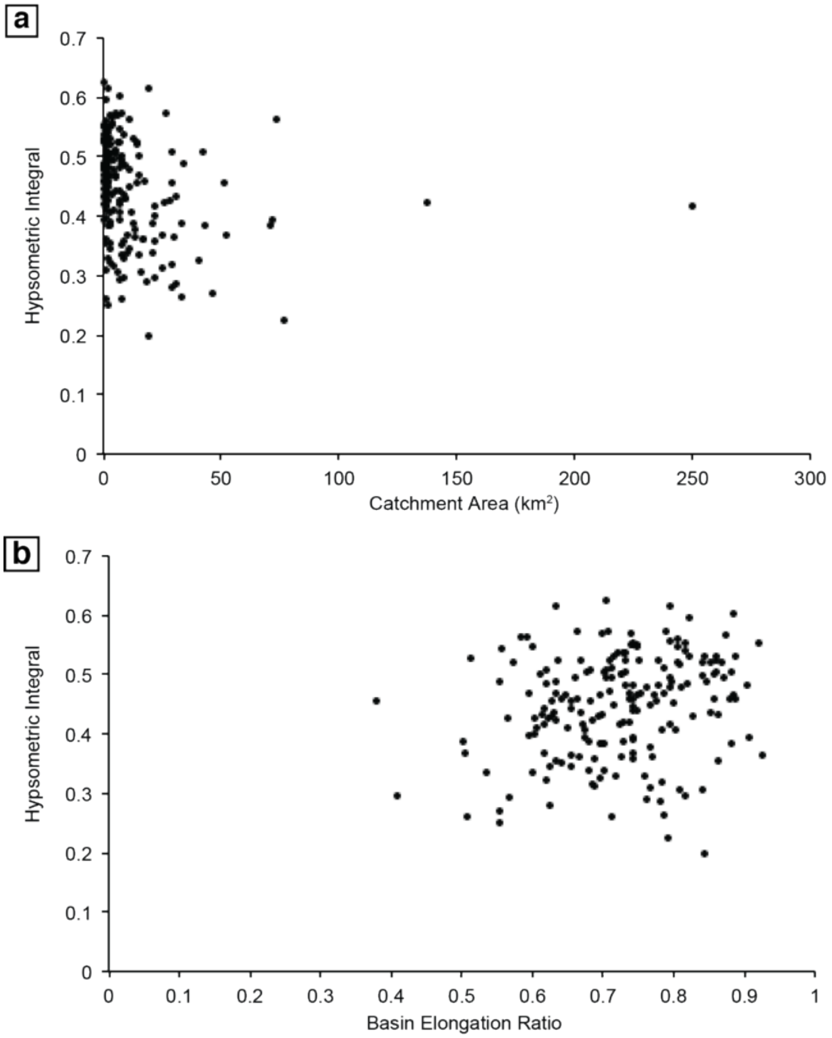

Figure A-1: (a) Catchment area and (b) basin elongation ratio (as a proxy for basin shape) vs. hypsometric integral for the 194 catchments analyzed. There is no clear correlation between catchment area and hypsometric integral or basin shape and hypsometric integral.

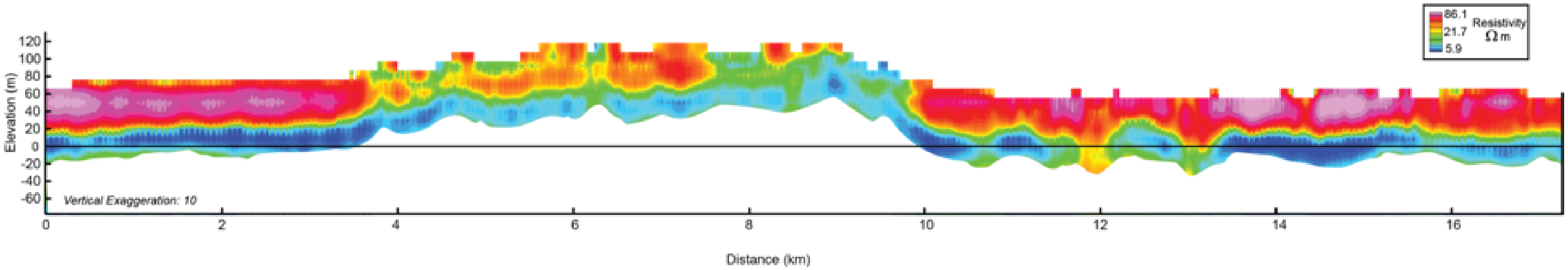

Figure A-2: Uninterpreted AEM profile 24160. Only part of line is shown in Fig. 8. Location information in Table S4 in Thompson Jobe et al. (2020a).

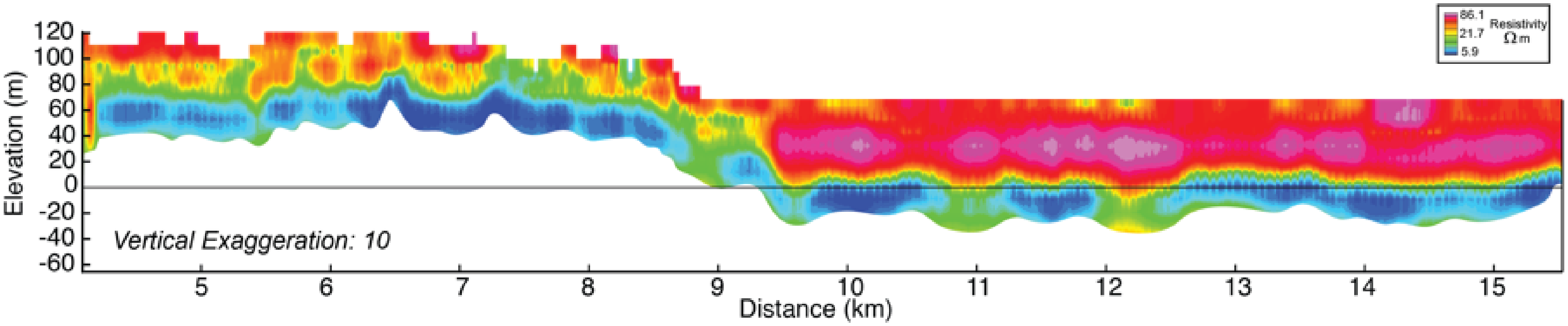

Figure A-3: Uninterpreted AEM profile 24492. Location information in Table S4 in Thompson Jobe et al. (2020a).

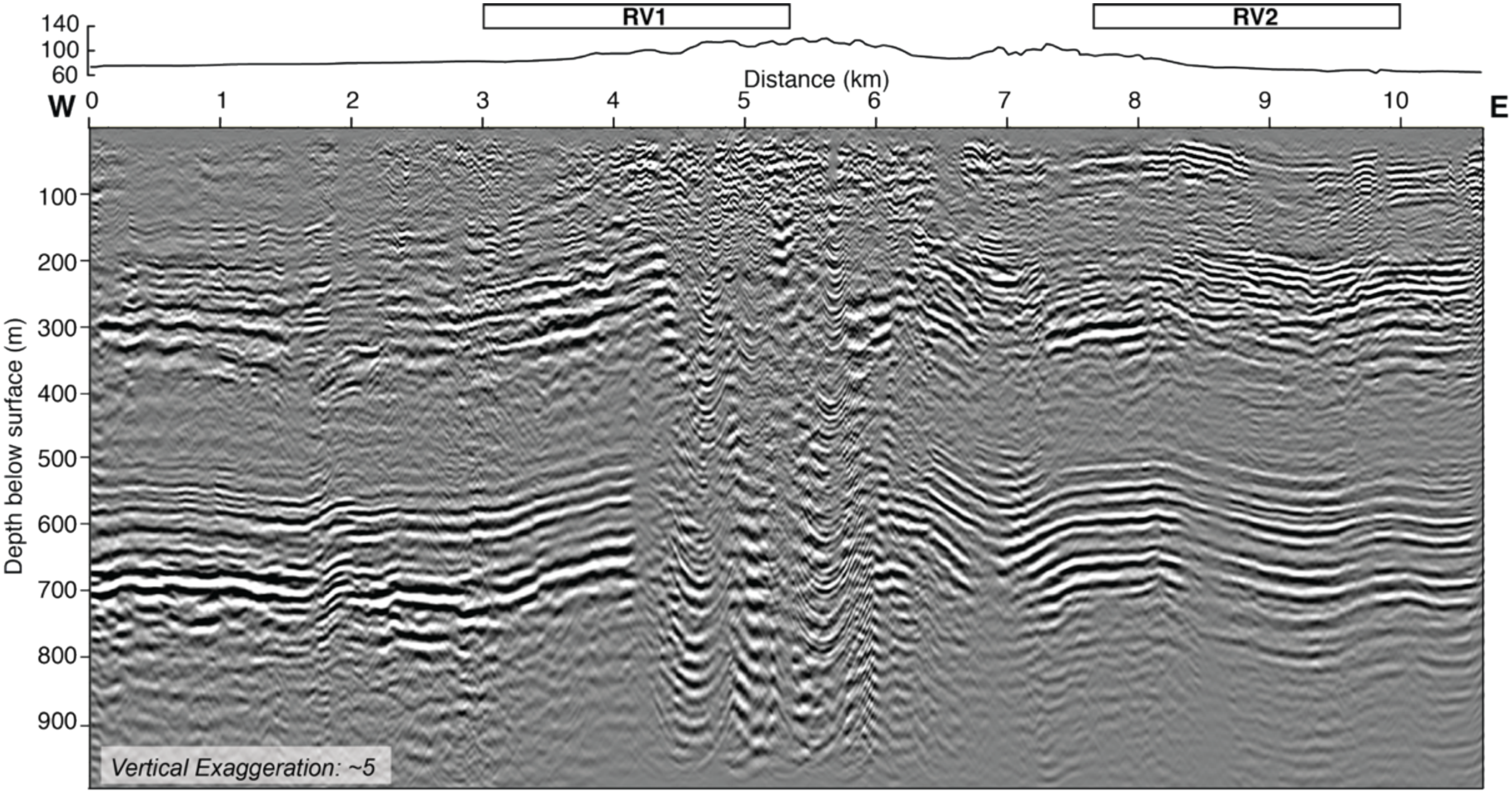

Figure A-4: Uninterpreted seismic line CRmv. Location information in Table S1 in Thompson Jobe et al. (2020a).

Table A-1: CRmv seismic profile Data Acquisition Parameters – November 2006

Acquisition Parameter
Source array: Single 9990-kg IVI Minivib I (Thumper; P-wave)
For more source details, see: http://nees.utexas.edu/Equipment-Thumper.shtml
Number of sweeps per station: up to 4
Vibe point interval: 5 m
Geophones: Single 8 Hz
Geophone group interval: 5 m
Recording geometry: 144 channels, usually off-end, some walk-throughs
Near trace offset: usually 10 m
Recording filters: none
Recording system: 24-channel Geometrics Geodes
Sampling interval: 0.002 s
Sweep length: 14.0 s
Listen time: 12.0 s
Sweep frequencies: 15-120 Hz (linear)
Output Record length: 2.0 s
Data format: SEG-2

Data Processing sequence:
Data reformat: convert from SEG-2 to ProMAX internal
AGC 200 ms; pre-correlation
Trace edit: delete noisy traces
Top mute
Zero all data amplitudes in the surface-wave arrival zone
Common midpoint (CMP) sort: 72 fold
Automatic Gain Control (AGC): operator length 0.5 ms
Elevation statics; 65 m datum
Normal moveout correction (NMO), 50% stretch mute
Band-pass filter: 20-30-90-120 Hz and 60-Hz notch
Predictive deconvolution filter: 20 ms pred. distance
Residual statics
Surface wave mute
CMP stack
Freq/distance (F/X) deconvolution filter
Eigenvector filter: 51 trace window, retain 0-10%
Time-to-depth conversion: smoothed velocity function

Table A-2: RMS Velocity Model.

Time (ms)	Velocity (m/s)
250	1600
650	1800
1200	2000

Table A-3. AEM Data Acquisition and Processing/Inversion Parameters – March 2019

Acquisition Parameter	
AEM instrument:	CGG Resolve Frequency-domain electromagnetic sensor
Helicopter:	AS350 B2
Coil frequencies (Hz):	383; 1,820; 3,315; 8,488; 40,835; 133,528
Coil dipole orientations:	z, z, x, z, z, z
Coil separations (m):	7.93, 7.95, 9.06, 7.93, 7.92, 7.97
Nominal instrument height:	30 m
Nominal flight speed:	80 km/hr
Recording rate:	10 Hz
Digital Acquisition:	CGG HeliDAS
Laser Altimeter:	Optech ADMGPA100 mounted in EM bird
EM Bird Positional Data:	NovAtel OEM4 with Aero Antenna mounted on EM bird

Data Processing sequence:
(CGG)
0.8 second lag correction
0.9 second median filter
0.9 second Hanning filter
Drift correction
Levelling correction (if needed)

(USGS)
Imported CGG-provided Geosoft.gdb to Aarhus Workbench GERDA database
Data assigned 3% relative error and 5 ppm absolute error
Running mean filter applied to each coil, filter widths (m) = 100, 80, 60, 40, 30, 25
Original 10 Hz data averaged and resampled to 25 m output sounding intervals
Total data error calculated from assigned errors and averaging variability
Laterally constrained inversion (LCI) for resistivity model in Aarhus Workbench

# layers:	30
1st layer depth:	1m
Last layer depth:	125 m
Starting resistivity:	40 ohm-m
Resistivity prior constraint:	99
Vertical smoothness constraint:	5
Horizontal smoothness constraint:	2

Parameter uncertainty estimates calculated for each model location.
Depth of investigation calculated for each model location.

APPENDIX B
SUPPORTING INFORMATION FOR CHAPTER 3

Compilation of faults from previous geologic maps

We digitized approximately east–west oriented faults from existing geologic maps. We focused on faults that crosscut the southwest–northeast Paleozoic structural grain. These faults generally have an orientation between 90°–270° ± 20°. Although some of these faults likely formed as tear faults during the Alleghanian orogeny, other faults are suspected to have formed during Neogene deformation events (e.g., Hill et al., 2020).

We relied on geologic maps that were easily accessible and publicly available. Geologic map PDFs and tiff files were georeferenced using QGIS if an existing georeferenced map was unavailable. Eastern Tennessee has been mapped at various scales and levels of detail in previous studies; the entire region is covered by 1:100,000 (e.g., Southworth et al., 2012), 1:125,000 (e.g., Rodgers, 1953), 1:250,000 (e.g., Hadley and Nelson, 1971; Rankin et al., 1972) scale maps (Figure B-1). However, many of these studies focused on mapping larger-offset faults and stratigraphy, often with a focus on the Paleozoic structures, with limited high-resolution surficial or Quaternary mapping. When available, we relied on 1:24,000-scale geologic maps, which commonly mapped Quaternary deposits in more detail.

Our analysis is limited by the availability and detail of the geologic mapping; if and when promising Quaternary offsets are identified, more detailed geologic mapping would be beneficial.

Catchment-averaged Normalized Channel Steepness

We assessed catchment-averaged normalized channel steepness (ksn) in the Powell River area following the equations and methods outlined in Whipple and Tucker (1999) and TopoToolbox workflows described in Schwanghart and Kuhn (2010) and Schwanghart and Scherler (2014). We used a value of θ_{ref} =0.45. Catchment-averaged hypsometric integrals and ksn are reported in Table B- 1.

Table B- 1 Catchment mouth locations, hypsometric integrals (HI), and normalized channel steepness (ksn) values for catchments in the Powell River area. UTM coordinates are in Zone 17N, WGS 84.

Catchment Number	UTM Easting	UTM Northing	HI	ksn
1	268863	4048386	0.5698	64.26
2	274106	4047308	0.6066	82.09
3	277948	4046723	0.5561	66.90
4	287727	4051268	0.5435	45.79
5	281251	4047326	0.5338	77.98
6	282187	4047360	0.2409	12.16
7	278661	4047875	0.5979	91.62
8	269688	4045878	0.5749	78.51
9	266933	4052412	0.3046	55.64
10	264608	4047362	0.4955	59.15
11	262803	4043618	0.5656	64.96
12	260051	4040793	0.5628	69.02
13	254957	4040034	0.5037	70.10
14	256465	4039859	0.5856	84.13
15	255249	4039788	0.6511	111.73
16	252661	4037693	0.5634	93.49
17	250877	4033530	0.5545	55.24
18	248049	4033479	0.5366	72.14
19	246353	4034150	0.4823	85.31
20	237202	4031926	0.4455	62.85
21	236788	4029532	0.5190	61.99
22	251324	4036722	0.4861	49.84
23	241864	4033337	0.4995	72.08
24	246256	4030712	0.4935	51.92

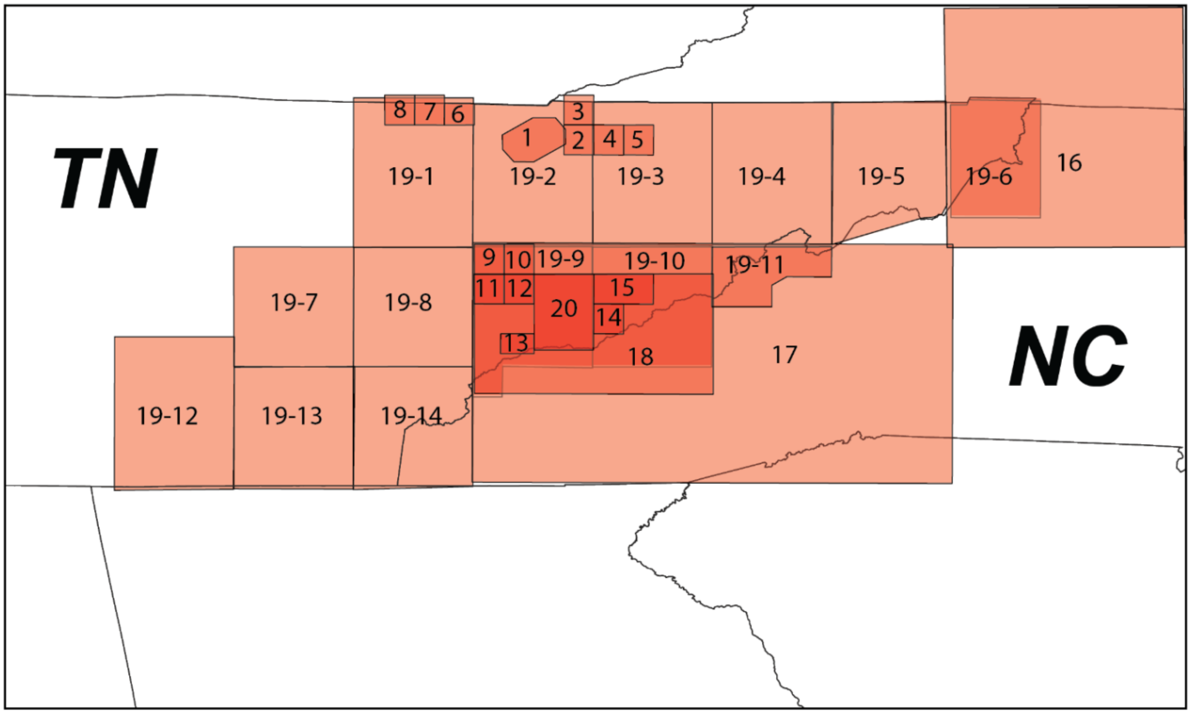

Figure B-1: Geologic maps referenced in this study. Numbers correspond to the references listed below. Numbers with a "-*X*", where "X" is a number, represent the plate number for geologic maps in Rodgers (1953).

Geologic Map references

1. Brokaw, A. L., Rodgers, J., Kent, D. F., Laurence, R. A., and Behre Jr., C. H. (1966). Geology and mineral deposits of the Powell River area, Claiborne and Union Counties, Tennessee. U.S. Geological Survey Bulletin 1222-C, 56 pp., 4 plates, scale 1:48,000, doi:10.3133/b1222C.
2. Harris, L. D. (1965a). Geologic map of the Tazewell quadrangle, Claiborne County, Tennessee. U.S. Geological Survey Geologic Quadrangle Map GQ-465, scale 1:24,000, doi:10.3133/gq465.
3. Harris, L. D. (1965b). Geologic map of the Wheeler quadrangle, Claiborne County, Tennessee and Lee County, Virginia. U.S. Geological Survey Geologic Quadrangle Map GQ-435, scale 1:24,000, doi:10.3133/gq435.
4. Harris, L. D. and Mixon, R. B. (1970). Geologic map of the Howard Quarter quadrangle, northeastern Tennessee. U.S. Geological Survey Geologic Quadrangle Map GQ-842, scale 1:24,000, doi:10.3133/gq842.
5. Mixon, R. B. and Harris, L. D. (1971). Geologic map of the Swan Island quadrangle, northeastern Tennessee. U.S. Geological Survey Geologic Quadrangle Map GQ-878, scale 1:24,000, doi:10.3133/gq878.
6. Rice, C. L. and Newell, W. L. (1990). Geologic map of part of the Jellico East quadrangle, Campbell and Claiborne Counties, Tennessee. U.S. Geological Survey Geologic Quadrangle Map GQ-1674, scale 1:24,000, doi:10.3133/gq1674.
7. Englund, K. J. (1969). Geologic map of the Jellico West quadrangle, Kentucky-Tennessee. U.S. Geological Survey Geologic Quadrangle Map GQ-855, scale 1:24,000, doi:10.3133/gq855.
8. Englund, K. J. (1966). Geologic map of the Ketchen quadrangle, Tennessee-Kentucky. U.S. Geological Survey Geologic Quadrangle Map GQ-500, scale 1:24,000, doi:10.3133/gq500.
9. Cattermole, J. M. (1958). Geology of the Knoxville quadrangle, Tennessee. U.S. Geological Survey Geologic Quadrangle Map GQ-115, scale 1:24,000, doi:10.3133/gq115.
10. Cattermole, J. M. (1955). Geology of the Shooks Gap quadrangle, Tennessee. U.S. Geological Survey Geologic Quadrangle Map GQ-76, scale 1:24,000, doi:10.3133/gq76.

11. Cattermole, J. M. (1962). Geology of the Maryville quadrangle, Tennessee. U.S. Geological Survey Geologic Quadrangle Map GQ-163, scale 1:24,000, doi:10.3133/gq163.
12. Neuman, R. B. (1960). Geology of the Wildwood quadrangle, Tennessee. U.S. Geological Survey Geologic Quadrangle Map GQ-130, scale 1:24,000, doi:10.3133/gq130.
13. Southworth, S., Chirico, P. G., and Putbrese, T. (2000). Geologic map of Cades Cove and Calderwood quadrangles, Tennessee and North Carolina, Great Smoky Mountains National Park. U.S. Geological Survey Open-File Report 99-175, scale 1:24,000, doi:10.3133/ofr99175.
14. Schultz, A., Southworth, S., Fingeret, C., and Weik, T. (2000). Geology of the Mount Le Conte 7.5-minute quadrangle, Great Smoky Mountains National Park, Tennessee and North Carolina. U.S. Geological Survey Open-File Report 2000-261, scale 1:24,000, doi:10.3133/ofr00261.
15. Hamilton, W. (1961). Geology of the Richardson Cove and Jones Cove quadrangles, Tennessee. U.S. Geological Survey Professional Paper 349-A, 55 pp., 1 plate, scale 1:24,000, doi:10.3133/pp349A.
16. Rankin, D. W., Espenshade, G. H., and Neuman, R. B. (1972). Geologic map of the west half of the Winston-Salem quadrangle, North Carolina, Virginia, and Tennessee. U.S. Geological Survey Miscellaneous Geologic Investigations Map 709-A, scale 1:250,000, doi:10.3133/i709A.
17. Hadley, J. B. and Nelson, A. E. (1971). Geologic map of the Knoxville quadrangle, North Carolina, Tennessee, and South Carolina. U.S. Geological Survey Miscellaneous Geologic Investigations Map 654, scale 1:250,000, doi:10.3133/i654.
18. Southworth, S., Schultz, A., Aleinikoff, J. N., and Merschat, A. J. (2012). Geologic map of the Great Smoky Mountains National Park region, Tennessee and North Carolina. U.S. Geological Survey Scientific Investigations Map 2997, 54 pp. 1 plate, scale 1:100,000, doi:10.3133/sim2997.
19. Rodgers, J. (1953). Geologic map of east Tennessee with explanatory text. Tennessee Division of Geology Bulletin 58 Part 2, 167 pp., 14 plates, scale 1:125,000, Available at https://www.tn.gov/environment/program-areas/tennessee-geological-survey/geology-redirect/maps-publications/out-of-print-publications-on-line.html.
20. King, P. B. (1964). Geology of the central Great Smoky Mountains, Tennessee. U.S. Geological Survey Professional Paper 349-C, 148 pp., 13 plates, doi:10.3133/pp349C.

SEISMIC SOURCE CHARACTERIZATION IN CENTRAL AND EASTERN UNITED STATES DATE December 15, 2023

DISTRIBUTION:
BHayes, NRR/DEX/EXHB
CMunson, NRR/DEX
JMcKirgan, RES/DE
TWeaver, RES/DE/SGSEB
AAnooshehpoor, RES/DE/SGSEB
LBauer, NRR/DEX/EXHB

ADAMS Accession No.: ML23339A121; ML23339A123

OFFICE	RES/DE/SGSEB	NRR/DEX/EXHB	NSIR/DPCP/RSB	
NAME	AAnooshehpoor *AA*	LBauer *LB*	MSampson *MS*	
DATE	Dec 5, 2023	Dec 5, 2023	Dec 15, 2023	

OFFICIAL RECORD COPY